MULTISCALE MODELS IN BIOELECTROCHEMICAL ENGINEERING

By

Christina M. Wark

A DISSERTATION

Submitted to
Michigan State University
in partial fulfillment of the requirements
for the degree of

Chemical Engineering - Doctor of Philosophy

2025

ABSTRACT

Future technological progress will increasingly rely on biomaterials and bioinspired mechanisms. We can draw inspiration from nature to meet industrial needs because biological materials and mechanisms are often highly efficient and superior to other synthesized materials. Overall, the work herein strives to advance understanding of bio-inspired materials for a versatile set of engineering challenges and solutions.

First, we study the highly efficient reaction cascade of the tricarboxylic acid (TCA), or Krebs, cycle, which converts nutrients in food to usable energy in fractions of seconds. Of particular interest in the TCA cycle is the conversion of oxaloacetate (OAA) between malate dehydrogenase (MDH) and citrate synthase (CS). Based on previous experimental and computational studies of recombinant and mutant MDH-CS complexes, a time-dependent finite difference model was developed to predict each complex's transfer efficiency and determine the surface's reaction pathways. Utilizing the kinetic parameters of recombinant and mutant complexes determined experimentally and surface transition probabilities of OAA from a Markov state model, the lag time of MDH-CS was determined computationally for recombinant and mutant complexes. Additional implications of the reaction path and reversible reaction at MDH are also considered. This model study furthers the understanding of dynamic enzymatic cascades and points toward approaches to cascade design.

Second, we address the upgrading of bio-oil from pyrolyzed lignocellulosic biomass. Bio-oils yield a complex mixture of organic constituents that can be used as feedstock for valuable chemicals. However, these molecules are often oxygenated with low energy density. Recently, electrocatalytic hydrotreatment (ECH) of bio-oil was used to reduce oxygen content and increase energy density. Mechanistic understanding of interaction effects in mixtures is required for effective process design. Here, the mechanisms by which ECH of bio-oil constituent 4-

propylphenol (4-PP) is inhibited by furfural (FF) are studied computationally. Inhibition is elucidated through potential dependent studies of adsorption and reaction mechanisms on a platinum/ruthenium electrocatalyst. Thermodynamic studies suggest that the FF pathways are competitive in adsorption and more favorable in reactions due to fewer barriers and smaller limiting potentials than the 4-PP pathways. Prediction of activation barriers by reaction energy scaling techniques found the FF pathways also to be favored kinetically over the 4-PP pathways. Reaction thermodynamics and kinetics models suggest that FF inhibits 4-PP hydrotreatment because the FF pathways are more favorable than 4-PP pathways on a platinum/ruthenium catalyst.

Finally, a new biomaterial is evaluated as a high performance substrate in tissue regeneration applications. A biomaterial was previously developed where gelatin was modified by methacrylic anhydride (GelMA) for stability at physiological conditions and silver-bioactive glass (Ag-BG) was added for antibacterial properties. Chemically linked GelMA and Ag-BG (GAB) was hypothesized to exhibit superior structural and cell viability behavior to GelMA in extrusion printed applications, which we seek to validate. Scaffold printing parameters were optimized for acellular GelMA, GAB, and a GelMA + Ag-BG composite bio-ink. Then, cell-laden media was introduced to the bio-ink to generate scaffolds. The viability of the cells within the scaffold was observed over time after printing. Ultimately, bio-ink performance and cell viability were poor for the selection of materials during cellular printing. These challenges suggest further optimization steps are needed within the material synthesis and printing processes, which is a point of more recent work that shows promising results.

To my parents, Joe, Ayla, and Lily...

ACKNOWLEDGMENTS

First and foremost, I would like to express my deepest gratitude to my advisor, Dr. Scott Calabrese Barton, for his unwavering support and encouragement to persist throughout the years. The person and researcher that I am today is undoubtably due to his guidance and mentorship. I was always challenged to ask "why?" which has made a lasting impression that will help me to push the edge of science throughout the rest of my career and life. I am a better person and scientist from my time here. I would also like to extend my appreciation and gratitude to my committee members: Dr. James (Ned) Jackson, Dr. Jose Mendoza Cortes, Dr. Michael Murillo, and Dr. Chris Saffron. Though my research trajectory made some substantial shifts throughout my time at MSU, each of my committee members have been figures of guidance and expertise on a versatile set of theoretical and physical concepts. They have all made a lasting impact on how I think about and execute my pursuit of science.

Additionally, I want to thank my current and past groupmates, and collaborators. To Brandon, Yunlu, Yan, Kanchan, Manali, Alex, Mindy, Pranavi, and Meiers: I am so thankful for all of our chats, research related and otherwise. I was lucky to learn alongside so many wonderful people. I was also fortunate to collaborate with many incredible people throughout my research work. Thank you to the MTRAC and beyond team members: Dr. Xanthippi Chatzistavrou, Dr. Adam Marsh, Dr. Nuredin Ashammakhi, Dr. Chris Contag, Dr. Victoria Toomajian, and Anthony Tundo, all of whom have taught me so many things about materials engineering and how to probe the interface between design and application. Further thanks to Dr. Per Askeland, Emily Pawlowski, Amy Albin, and Dr. Dan Holmes who helped me in access to equipment necessary to the work and analysis of the results. I also want to acknowledge Johannes Schavikin and Romila Manchanda who I've been able to continue learning through as they pursue further development of these biomaterials. I am also grateful

to the other members of the NSF-DFG team: Dr. Meheryar Kasad, Dr. Uwe Schröder, Dr. Keyvan Malaie, and Jannelle Casanova. It has been an absolute pleasure to work alongside all of you. Finally, I want to thank the entire Schröder group at the University of Greifswald for their kindness, friendship, and all of the things I learned during my visit.

I am so thankful for the friends that have been around to support me for a long time and the new friends that I made along the way. To Sarah, who has been my buddy in all things academic and otherwise since our time as undergrads through working on our PhDs together. This was easier knowing I was never alone. To Kyra and Allie, two of the friends I made along the way, thank you for being such wonderful pillars of emotional support and reminders to take care of my wellbeing when the going got rough. To the rest of my core friend groups: Tim, Bre, Brad, Lacie, Chris, Sean, Ryan, Andrew, Greg, Dan, Robert, Ben, Jeremy, and the Mega Group, thank you all for standing with me for all of these years. Even at the lowest points, time with you all made things brighter. Thank you for always reminding me of who I am and what I'm working toward, but also being so fun when I needed a break.

I am deeply grateful to my family: Joe, mom, dad, Michelle, and my in-laws-to-be: Tim, Marsha, Ben, and Maggie. They all have been nothing but supportive and encouraging throughout my life. There are not enough words to express how thankful I am for my soon-to-be husband, Joe, for all that he has done to support me through this process, and constantly encouraging me to be my best and keep pushing toward my dreams. This accomplishment was made possible because he stood with me through all of the highs and lows by making sure everything else was taken care of so that I could focus during the busy times, tagging along when I had to check on my syntheses at odd hours, and celebrating every accomplishment along the way. My parents have worked so hard to give me the opportunities to continue learning and pursue science. I wouldn't have made it this far without their support. To my

sister, Michelle, thank you for indulging me as my assistant in all the times I wanted to play "Science Lab" as kids. She helped me find my passion in science. Thank you to the family I gained when I met Joe. I am so lucky to have been welcomed in to their family from the start. They all have been such a strong source of support, encouragement, and love through this process and in life. Lastly, to my cats, Ayla and Lily, who sat with me through all of the early mornings, late nights, and Zoom lectures and meetings. Their emotional support helped me through a lot of the challenges of grad school and their presence made it easier to talk out my code logic when debugging.

With many thanks and a lot of caffeine,

Christina

TABLE OF CONTENTS

Chapter 1

Introduction

Technical industries constantly pursue more efficient solutions to engineering problems. Several sectors of industry seek sustainable materials due to climate change and diminishing resources.[1] Recently, a trend emerged in engineering toward sustainability aspects that often rely on efficient processes and clean materials. One aspect focuses on understanding the efficiency of biological processes.[2,3] Another aspect investigates use of renewable and alternative resources to generate supplies that meet current demands.[4] A third application lies in the design of bio-compatible materials in medical technologies.[5] Versatile solutions can be explored through exploiting mechanisms and functions of bio-derived and bio-inspired materials. The ability to apply bio-inspired materials to meet diverse needs relies on advancements in computational modeling, material performance optimization, and an improved fundamental understanding of mechanisms. The research summarized herein aims to advance understanding of bio-inspired materials for a versatile set of engineering challenges and efficient, sustainable solutions.

1.1 Enzyme-inspired Efficient Reaction Cascades

Complex living organisms utilize highly efficient metabolic pathways to execute several vital functions required for survival.[6,7] Biological cycles and naturally occurring mechanisms efficiently convert chemicals into energy sources and other materials needed to complete the metabolon, or metabolic cycle.[6] The desire to generate novel chemicals (i.e. biofuels) at high yields has placed focus on understanding biochemical mechanisms.[3,7] A cascade of reactions is required to mimic the various steps in these metabolon.[6,7] However, the inclusion of biocatalytic surfaces in the form of enzymes adds complexity to reaction systems.

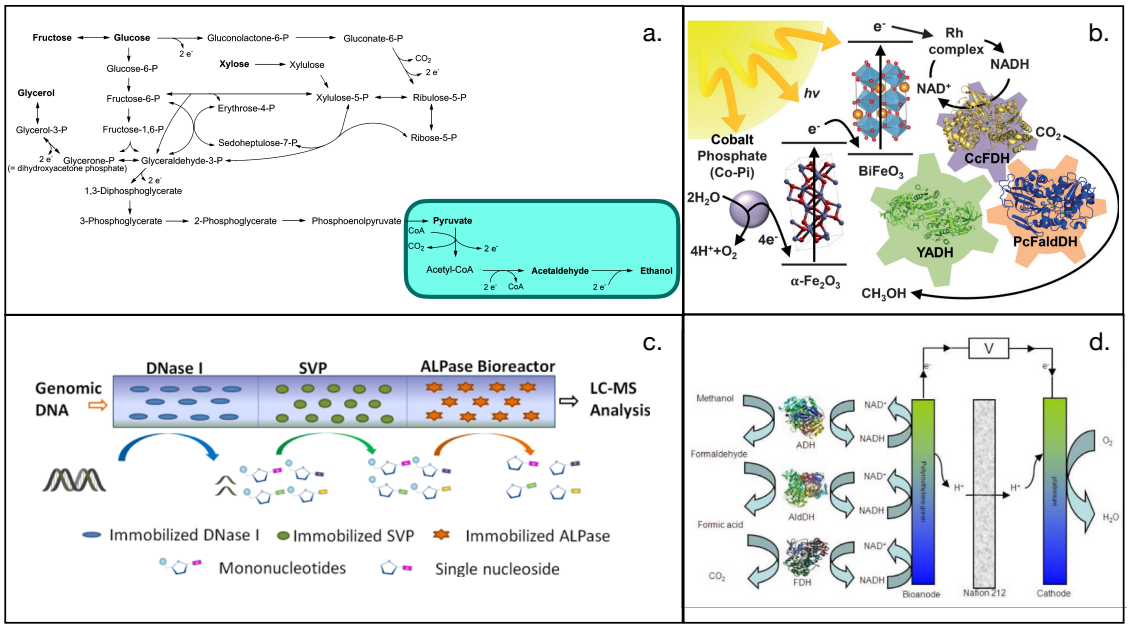

Figure 1.1: Enzyme cascades in (a) ethanol production from biomass(adapted from Ref 8[9]), (b) methanol generation from CO_2 from Ref[10]), (c) DNA processing for cancer detection from Ref[11]), and (d) biofuel cells (adapted from Ref[12]).

This complexity can be overcome with computational methods that can reveal phenomena influencing the yield of the cascade.[3,8]

Enzymatic cascades are broadly implemented in various applications for efficient chemical processes. Some examples of these applications are summarized in Figure 1.1. In the commodity chemical sector, enzymatic cascades are under development to convert biomass and carbon dioxide into platform chemicals. Specific examples include the production of ethanol from biomass-derived pyruvate (Fig. 1.1a)[9] and methanol from carbon dioxide (Fig. 1.1b)[10]. Pyruvate is formed via a glycolysis pathway on α-amylase and glucoamylase.[9] The pyruvate is first converted to acetaldehyde on pyruvate decarboxylase. Then, ethanol is formed by the reduction of acetaldehyde by alcohol dehydrogenase. This pathway is observed in yeasts utilized for fermentation. The conversion of CO_2 to methanol is similarly inspired by nature through a photo-electrochemical process consisting of a three-enzyme cascade designed to mimic photosynthesis.[10] Here, carbon dioxide is first reduced to formate on formate dehydrogenase (FDH), formaldehyde is produced from formate on formaldehyde dehydrogenase(FaldDH), and finally, methanol is formed on alcohol dehydrogenase (ADH).

Enzymatic cascades are also utilized in technological applications, including medical di-

agnostics[11] and biofuel cells[12]. In medical diagnostics, a three-enzyme cascade for DNA conversion to single nucleosides exposes DNA damage due to the onset of cancer (Fig. 1.1c).[11] The DNA is first broken into smaller mono-nucleotide and oligonucleotide fragments by deoxyribonuclease I (DNase I). The resulting oligonucleotides are broken into mono-nucleotides via snake venom phosphodiesterase (SVP). Finally, the mono-nucleotides are broken down into single nucleosides by alkaline phosphatase(ALPase). Biofuel cells utilize enzyme cascades to electrochemically oxidize fuel sources such as methanol (Fig. 1.1d).[12] A process similar to the reverse of the CO_2 to methanol conversion is used here. Methanol is first converted to formaldehyde via ADH. Then formic acid is generated on aldehyde dehydrogenase (AldDH). Finally, CO_2 is generated from formic acid on FDH. These examples illustrate the versatility of enzyme-catalyzed reaction cascades for chemical processes and in technology. The processes can be inspired by natural phenomena or utilize the selectivity of enzymes to develop new, efficient processes.

1.1.1 Enzymatic Reaction Mechanisms

In enzyme-catalyzed reactions, the mechanisms must account for the interaction of reactants, or substrates, and intermediates with the enzyme's active site and the reaction at the active site. For single-substrate reactions, this is accomplished via a Michaelis-Menten rate law, which captures the formation of an enzyme-substrate complex, $E \cdot S$, as depicted below.

$$E + S \rightleftarrows E \cdot S \rightarrow E + P \tag{1.1}$$

Where the enzyme is denoted by "E", a simple diagram of the Michaelis-Menten mechanism is shown in Figure 1.2a. Also in this figure (Fig. 1.2a-b) are two forms of Bi-Bi mechanisms for dual-substrate reactions. These mechanisms are discussed in more detail in Section 1.1.1.1.

For a simple Michaelis-Menten mechanism, the overall reaction rate or reaction velocity, ν, can be defined as the rate of increase in the product concentration, C_{P}. Reaction velocity

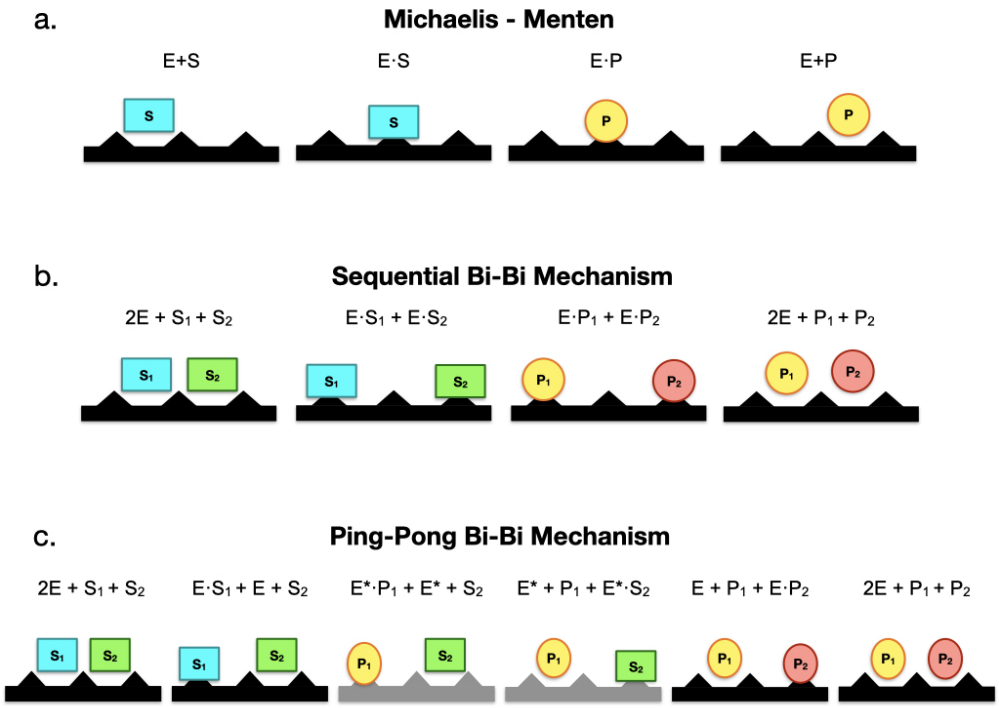

Figure 1.2: Schematic of enzyme reaction mechanisms: (a) standard Michaelis - Menten, (b) Sequential Bi - Bi, and (c) Ping - Pong Bi - Bi mechanisms.

depends on the substrate concentration (C_S) plus other terms for active site interactions.[13–15]

$$\nu = \frac{V_{max} C_S}{K_M + C_S} \tag{1.2}$$

Where V_{max} represents the maximum rate of product generation when the enzyme is saturated with substrate as a function of turnover frequency (k_{cat}) and enzyme concentration(C_{enz}).

$$V_{max} = k_{cat} C_{enz} \tag{1.3}$$

The Michaelis-Menten coefficient, K_M, describes the adsorption equilibrium between the substrate and the enzyme as a function of k_{cat}. Further, at a product generation rate of one-half of V_{max}, the substrate concentration will be equivalent to K_M.

$$K_M = \frac{k_{des} + k_{cat}}{k_{ads}} \tag{1.4}$$

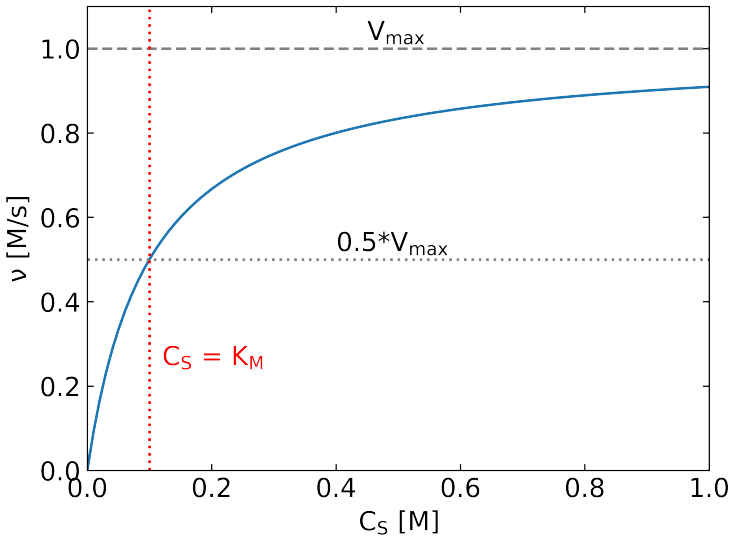

Figure 1.3: Example Michaelis-Menten Plot where $k_{\text{cat}} = 10$ s^{-1}, $K_{\text{M}} = 10^{-1}$ M, and $C_{\text{enz}} = 10^{-1}$ M.

The rate constant of substrate adsorption is k_{ads} and desorption is represented by k_{des}. An example of a Michaelis-Menten plot is provided in Figure 1.3.

The rate law can be further simplified in the case of very large Michaelis-Menten constant relative to the substrate concentration. Here, the generation of the product would be pseudo-first order and take the form of:

$$\nu = \frac{V_{\text{max}}}{K_{\text{M}}} C_{\text{S}} \tag{1.5}$$

1.1.1.1 Bi-Bi Mechanisms

The rate law becomes more complex when multiple substrates are consumed in an enzymatic reaction. This is often the case in naturally occurring enzymatic reactions like those within the Krebs cycle.[16] The bi-bi mechanism describes a reaction in which two substrates (S_1 and S_2) are consumed to produce two products (P_1 and P_2).

$$S_1 + S_2 \underset{\longleftarrow}{\overset{\text{Enz}}{\longrightarrow}} P_1 + P_2 \tag{1.6}$$

Within a bi-bi reaction system, the reaction may proceed as either a sequential mechanism or a ping-pong mechanism, as shown in Figs 1.2b-c.[17,18] In the sequential mechanism, the binding of substrates and release of products are classified as ordered sequential, where

substrates bind and react in a specific order, or random sequential, where the substrates bind at different times in either order before the dissociation of products. One cycle of substrate consumption and product dissociation must occur before a new cycle occurs. The same forward rate law describes both categories of sequential mechanisms, as the kinetics are indistinguishable for the two categories of sequential mechanisms[17]:

$$\nu_{\mathrm{f}} = \frac{V_{\max} C_{\mathrm{S}_1} C_{\mathrm{S}_2}}{K_{\mathrm{M,S}_2} C_{\mathrm{S}_1} + K_{\mathrm{M,S}_1} C_{\mathrm{S}_2} + C_{\mathrm{S}_1} C_{\mathrm{S}_2} + K_{\mathrm{i,S}_1} K_{\mathrm{M,S}_2}} \tag{1.7}$$

This expression considers the Michaelis-Menten kinetics for each substrate and an inhibition factor of S_1, K_{i,S_1}, to describe the likelihood of inhibition of the second substrate reaction by the first substrate.[13] Only one inhibition term is necessary because there is no inhibition of whichever substrate that binds first. For a reversible reaction, the reverse rate law would be:

$$\nu_{\mathrm{r}} = \frac{V_{\max} C_{\mathrm{P}_1} C_{\mathrm{P}_2}}{K_{\mathrm{M,P}_2} C_{\mathrm{P}_1} + K_{\mathrm{M,P}_1} C_{\mathrm{P}_2} + C_{\mathrm{P}_1} C_{\mathrm{P}_2} + K_{\mathrm{i,P}_1} K_{\mathrm{M,P}_2}} \tag{1.8}$$

The ping-pong mechanism describes a case in which the first substrate reaction occurs by chemically modifying the enzyme, and then the second reaction occurs, renewing the enzyme. Since the second reaction is dependent on the first reaction, there is no inhibition, and the rate law does not consider an inhibition term.

$$\nu = \frac{V_{\max} C_{\mathrm{S}_1} C_{\mathrm{S}_2}}{K_{\mathrm{M,S}_2} C_{\mathrm{S}_1} + K_{\mathrm{M,S}_1} C_{\mathrm{S}_2} + C_{\mathrm{S}_1} C_{\mathrm{S}_2}} \tag{1.9}$$

The system may be saturated with one of the two substrates to probe just one of the two reactions within a bi-bi mechanism.[16] In this case, the bi-bi rate law may be simplified to the single-substrate Michaelis-Menten equation because the saturated substrate's concentration change is negligible within the context of the reaction environment. For example, if the system is saturated with S_2, the rate law in Eq. 1.8 can be written as:

$$\nu = \frac{V_{\mathrm{m,app}} C_{\mathrm{S}_1}}{K_{\mathrm{M,app}} + C_{\mathrm{S}_1}} \tag{1.10}$$

For both simultaneous and ping-pong bi-bi mechanisms, the applicable maximum rate,

$V_{\mathrm{m,app}}$, is the same for a fixed concentration of the second substrate, $C^0_{\mathrm{S}_2}$:

$$V_{\mathrm{m,app}} = \frac{V_{\max} C^0_{\mathrm{S}_2}}{K_{\mathrm{M,S}_2} + C^0_{\mathrm{S}_2}} \tag{1.11}$$

The applicable Michaelis-Menten constant, $K_{\mathrm{M,app}}$, varies for the two subsets of bi-bi mechanisms. In a simultaneous mechanism, the applicable constant is:

$$K_{\mathrm{M,app}} = \frac{K_{\mathrm{i,S}_1} K_{\mathrm{M,S}_2} + K_{\mathrm{M,S}_1} C^0_{\mathrm{S}_2}}{K_{\mathrm{M,S}_2} + C^0_{\mathrm{S}_2}} \tag{1.12}$$

In the ping-pong mechanism, applicable Michaelis-Menten constant is:

$$K_{\mathrm{M,app}} = \frac{K_{\mathrm{M,S}_1} C^0_{\mathrm{S}_2}}{K_{\mathrm{M,S}_2} + C^0_{\mathrm{S}_2}} \tag{1.13}$$

Similar to the standard expression of the Michaelis-Menten equation, and in the case of a $K_{\mathrm{M,app}}$ that is much larger than the concentration of S_1, the rate expression may be simplified to a pseudo-first order rate law:

$$\nu = \frac{V_{\mathrm{m,app}}}{K_{\mathrm{M,app}}} C_{\mathrm{S}_1} \tag{1.14}$$

1.1.2 Reaction Cascades and Lag Time

A reaction cascade is a general classification for reaction systems in which a reactant is converted to a stable intermediate, then a product without substantial side reactions.[3] These "one-pot synthesis" processes can be highly efficient with minimal byproducts or competing side reactions.[3,19] The efficiency of such systems is evaluated by the system lag time, or the time that the systems requires to achieve steady state. Steady state is defined by constant bulk intermediate concentration and linearly increasing product generation.[7] For an example of lag time calculation, consider an arbitrary system in which intermediate generation follows a zeroth order rate law and its consumption to form product follows a first order rate law.

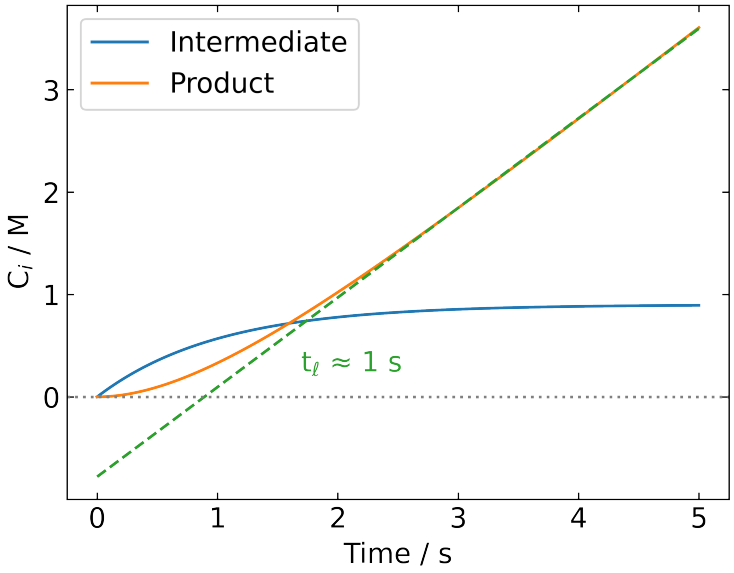

Figure 1.4: Example product and intermediate concentration curves with lag time fit to product curve (green dashed line) for $k_1 = 0.9$ s^{-1} and $k_2 = 1$ s^{-1}.

The rates of intermediate (C_I) and product (C_P) generation are:

$$\frac{dC_\mathrm{I}}{dt} = k_1 - k_2 C_\mathrm{I} \tag{1.15}$$

$$\frac{dC_\mathrm{P}}{dt} = k_2 C_\mathrm{I} \tag{1.16}$$

where k_1 and k_2 are the rate constants of the intermediate and product generation, respectively, and k_2 is larger than k_1. The time dependent solutions to the two differential equations are:

$$C_\mathrm{I}(t) = \frac{k_1}{k_2}\left(1 - e^{-k_2 t}\right) \tag{1.17}$$

$$C_\mathrm{P}(t) = k_1 t\left(1 - e^{-k_2 t}\right) \tag{1.18}$$

The resulting concentration curves are plotted in Figure 1.4 where the lag time is approximately 1 second. At steady state, the concentration of intermediate is constant ($C_\mathrm{I} = C_{\mathrm{I,ss}}$).

The lag time is proportional to the intermediate concentration.[20]

$$t_\ell = \frac{C_{\mathrm{I,ss}}}{k_1} \tag{1.19}$$

From this relationship, one can deduce that lower steady-state bulk concentrations of intermediate will reduce the lag time. Since this is also indicative of a faster approach to steady state, a lower lag time and lower bulk intermediate concentration result from more efficient systems. Therefore, a well-designed catalyst with favorable intermediate transport properties, thus reducing the intermediate lost to the bulk, is imperative for highly efficient reaction cascade processes.

1.1.3 Transport Mechanisms in Enzymatic Reaction Cascades

The design of such catalysts is inspired by enzymatic cascades occurring in natural biochemical processes. In particular, the highly efficient intermediate transport mechanisms from the reactant consumption site to the product generation site are of interest. Two mechanisms found in enzymatic reaction cascades are electrostatic channeling and tunneling as exemplified in Figure 1.5a-b.[2,21–23] Electrostatic channeling utilizes an electrostatic interaction between the oppositely charged enzyme surface and a charged stable intermediate to keep the intermediate very close to the surface, preventing losses to the bulk.[20,21,24–27] Molecular tunneling occurs when the proteins of the enzyme complex form a tunnel between intermediate generation and consumption sites to force the intermediate to the next step of the reaction.[22,23,28–31] The relationship between surface transport and surface charge on a catalyst makes the electrostatic channeling mode especially intriguing for reaction cascade engineering and will be the focus of the remaining discussion on this topic.

In the study of enzymatic systems that exhibit electrostatic channeling, three design cases can be explored, as visualized in Figure 1.6. The first represents one of the extreme cases in which intermediate does not channel on the surface, which we refer to as "free enzymes" (Fig. 1.6a). In the case of free enzymes, the intermediate and product generation sites are not physically connected. Thus, the intermediate can only reach the product generation site by desorbing from the first site, traversing the bulk, then adsorbing on to the second site.

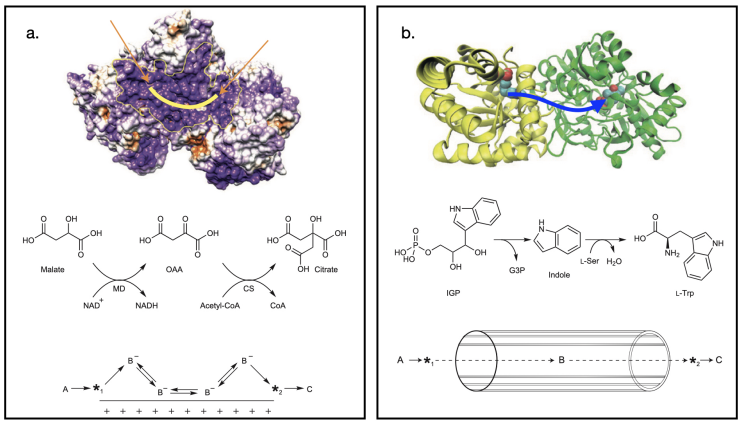

Figure 1.5: Transport mechanisms in enzyme cascades: (a) electrostatic channeling on malate dehydrogenase - citrate synthase where the intermediate traverses the surface along the highlighted line and (b) molecular tunneling in tryptophan synthase where intermediate is tunneled along the blue line to the second active site. Figures are adapted from Ref[2].

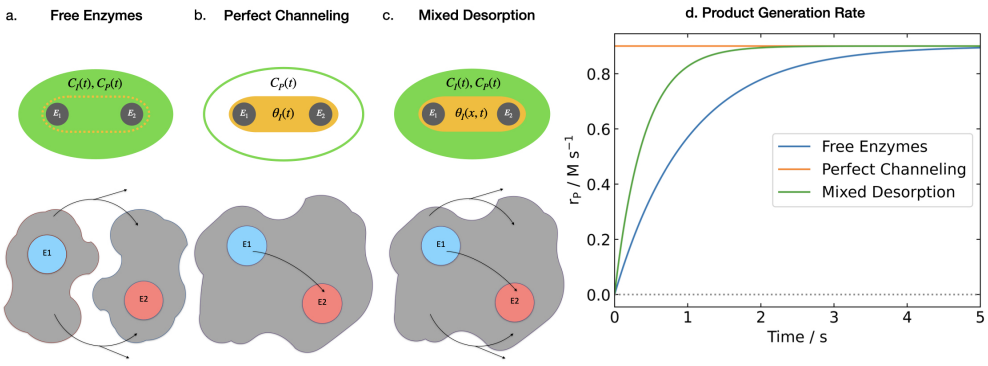

Figure 1.6: Electrostatic channeling design cases (a-c) and (d) product generation rates for each case.

This case represents a lag time maximum for a given system, with lag times on the order of 1 to 10 seconds.[16,32] In Fig 1.6d, the free enzymes exhibit the lowest product generation rates at early times.

The other cases represent a system where the intermediate generation and consumption sites are connected by some surface on which the intermediate can be electrostatically channeled. Such a surface may be formed by an enzyme complex or a peptide bridge connecting the two enzymes. The second extreme case is where intermediate is perfectly channeled on the surface, *i.e.*when no intermediate is released to the bulk but is completely consumed to create product (Fig. 1.6b). Surface transport occurs very quickly at rates several orders of

magnitude faster than chemical reactions.[26,33,34] Because of the timescale difference between transport and reactions, and lack of intermediate bulk concentration, the perfect channeling case results in nearly zero lag time and constant product generation, as depicted in Fig. 1.6d.

The final case in Fig. 1.6c represents the more realistic middle ground of channeling systems. In this mixed desorption case, a mixture of intermediate channeling and desorption occurs. Lag time and product generation rate (Fig. 1.6d) in this case reside somewhere between that of the free enzymes and perfect channeling. The resulting transfer efficiency of the system describes how close the mixed desorption lag time is to the free enzyme lag time. A more efficient system with a higher tendency to channel would have a lower lag time and greater transfer efficiency.

1.1.4 Experimental Studies of Enzymatic Cascades

Enzymatic reaction cascades of recent interest that utilize electrostatic channeling include the engineered cascade of Hexokinase - Glucose-6-Phosphate Dehydrogenase (HK-G6PDH)[7,24,27,32] and naturally-occurring Malate Dehydrogenase - Citrate Synthase (MDH-CS).[16,26,35] Some recent works also suggest that mechanisms of electrostatic channeling exist within the metabolism of E. Coli, but mechanistic studies for this system are not yet available.[36,37] HK-G6PDH is an example of a bridging system, as shown in Figure 1.7a. Details of the peptide bridge, colored green in the Figure, such as length and protein have been engineered to maximize transfer efficiency.[7,24,27,32] MDH-CS, responsible for the conversion of malate to citrate via an oxaloacetate intermediate in the Tricarboxylic acid (TCA) or Krebs cycle[38], is a complexed enzyme system, as shown in Fig. 1.7b. Several variations of the MDH-CS complex structure have been studied to determine the implications on transfer efficiency.[16]

In 2017, Liu et al. studied electrostatic channeling within the transformation of glucose to 6-phospho-gluconolactone via a glucose-6-phosphate (G6P) intermediate on HK-G6PDH.[32] The bridge, where the channeling of negatively-charged G6P occurs, was anchored to cysteine residues on each enzyme. In addition to the free enzyme systems, two peptide bridges were probed experimentally: the first with 5 positively-charged lysine residues and the second with 5 neutral glycine residues. The glycine bridged system exhibited a comparable lag time

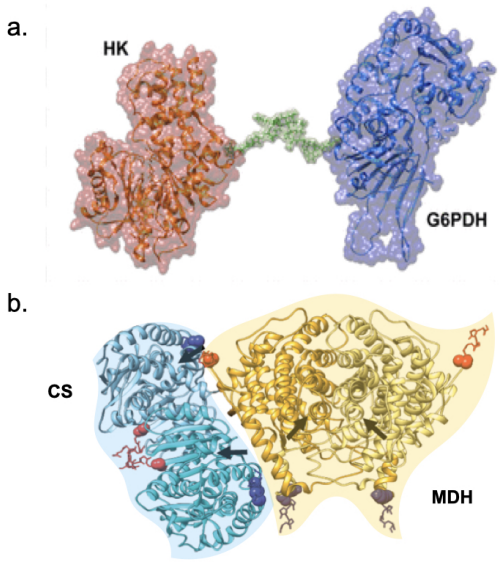

Figure 1.7: Electrostatic channeling enzyme systems of interest include (a) HK-G6PDH (adapted from Ref[32]) and (b) MDH-CS (adapted from Ref[16]).

to the free enzymes at around 100 s. The lysine bridge afforded a shorter lag time of 70 s, exemplifying the advantage of engineered electrostatic channeling. This affect is observed across a range of enzyme concentrations with lower, and more similar, lag times at higher enzyme concentrations. Additionally, the lag time of the charged lysine bridge decreased with lower ionic strength, more so than the neutral glycine bridge. This suggests that electrostatic channeling of a negatively charged intermediate on a positively charged bridge is particularly efficient under low enzyme concentration and low ionic strength conditions.

The conversion of malate to citrate via an oxaloacetate (OAA) intermediate on MDH-CS was experimentally studied by Bulutoglu et al. in 2016.[16] In this work, complexed MDH-CS was found to exhibit electrostatic channeling. The efficiency of a complex, and the impact of channeling, varied for a variety of different MDH-CS complexes. The variants included native bovine, commercial wild-type porcine, recombinant porcine, and a mutation of the recombinant. Implications of electrostatic channeling were determined via transient analysis of product concentration, resulting in lag times for each variant. Native bovine and recombinant porcine complexes were the most efficient, with lag times for both almost ten fold lower than the commercial. The mutant exhibited the longest lag time, nearly 30 fold that of the recombinant. In addition to lag time analysis, Bulutoglu et al.'s work also

parameterized the kinetics at MDH and CS for the recombinant and mutant complexes. This study indicates that OAA transport and overall system efficiency is reliant on effective surface transport modulated by consistent surface charge.

1.1.5 Computational Studies of Enzymatic Cascades

Various computational methods have been developed to address and model complex reaction systems. Molecular and atomistic level simulations have been employed to advance the understanding of mechanisms that occur in complex chemical reaction environments, particularly catalytic systems.[8,27,39] Transport of an intermediate on a complex or bridge has been studied via Brownian dynamics, Molecular Dynamics (MD), and Markov State Models (MSM). The implications of chemical reactions and diffusion on a system's efficiency has been probed via some Kinetic Monte Carlo (KMC) models. However, use of these techniques for biological systems is limited to short time scales.[40] Time scale limitations compromise a simulation's ability to capture transport events and some nuances of chemical reactions.[40,41]

In focusing computational efforts on the bridge of HK-G6PDH for simplicity, multiple studies have combined the previously mentioned computational methods to exploit design parameters within our group. The 2017 work of Liu et al. complemented experiments with MD simulations to determine the thermodynamics of adsorption and transport of G6P, and to screen peptide bridges.[32] Upon determining that a lysine bridge would sufficiently channel the intermediate, the adsorption energy, desorption probability, and diffusivity of G6P on the lysine bridge were calculated. Subsequently, MD and KMC methods were utilized in continuation of the previous work to determine rates of adsorption, desorption, and diffusion of G6P on the lysine bridge while considering chemical reaction rate constants calculated from their previous experimental data.[7] Here, the lag time of HK-G6PDH was simulated as a function of ionic strength, bridge length, and desorption on G6PDH after transport across the bridge. Although the "hopping rate" of transport from one bridge residue to the next was higher for a longer bridge, the desorption rate was also higher, resulting in longer lag times for the longer bridge. Lag times were further extended when desorption on G6PDH was also considered. The previously reported increase of lag time with ionic strength was also captured in these simulations. Both effects can be observed in Figure 1.8.

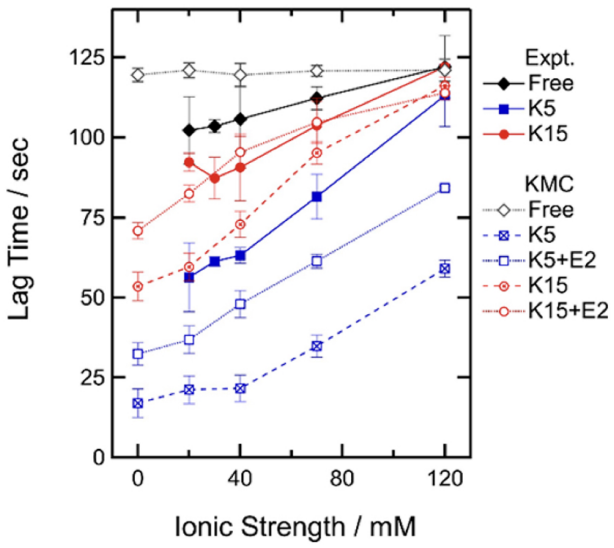

Figure 1.8: Lag time as a function of bridge length and ionic strength for a lysine bridge in the HK-G6PDH system (from Ref[7]).

The implications of desorption on both enzymes and the bridge were further probed by MSM and KMC models in 2019.[24] These simulations most closely matched experimental lag times when desorption was considered on the bridge and both enzymes instead of only in other smaller segments of the system. MD and KMC methods were later utilized to assess the arginine bridge, which was predicted to yield lower lag times across a range of ionic strengths than the lysine bridge.[27]

While the HK-G6PDH system can be simplified to enable macroscopic simulations in alignment with experiment (Figure 1.9a), the same methods are not as easily applied to MDH-CS, which has a much larger network of intermediate positions (Fig 1.9b). As a result, models of MDH-CS to date primarily focus on capturing the details of surface transport within this network. Surface transport of OAA was first studied computationally with Brownian dynamics.[35] Similar to HK-G6PDH, increasing ionic strength negatively impacted the transfer of the intermediate. Negatively charged OAA was found to interact with the surface, but charge-neutral OAA did not. More recently, our group used metadynamics and a MSM to analyze the transfer efficiency of OAA on a recombinant and mutant variation of MDH-CS.[26] Metadynamics enabled long-time MD simulations by introducing a bias energy that forces OAA to visit states near the active site in shorter MD simulations. These states

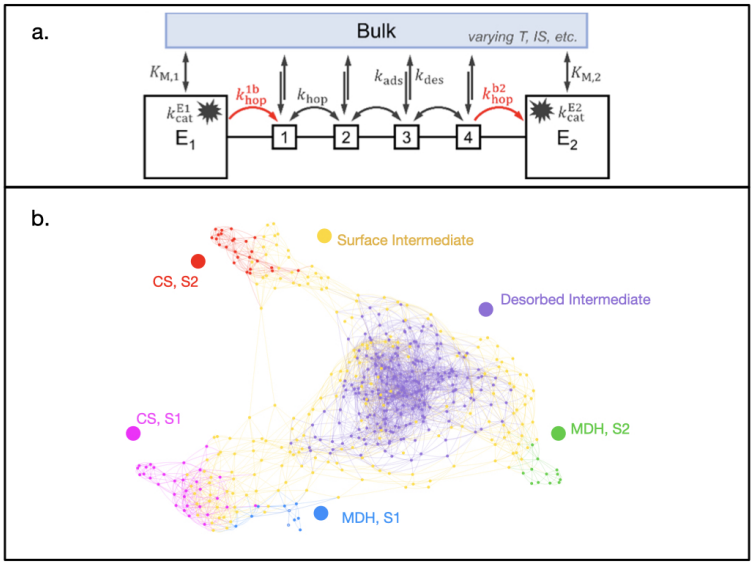

Figure 1.9: Network models of (a) HK-G6PDH (from Ref[24])and (b) MDH-CS. The HK-G6PDH system may be modified to this simple model representing each enzyme as a single node with additional nodes for residuals on the bridge. The MDH-CS system consists of a much more complex network with 500 sites depicting the four active sites, additional surface site, and bulk positions of intermediate.

were then used to initiate longer simulations. The collection of these trajectories was analyzed by a MSM to produce state transition probabilities for states categorized as one of the four active sites, other surface states, or desorbed intermediate states (Fig. 1.9b). Here, the mutation, which disrupts the positive charge on the surface, had a transfer efficiency less than half that of the recombinant.

Previous models of MDH-CS consider surface transport, but are incapable of including chemical reactions due to the size of the network combined with large differences in time scale. To overcome the limitations of other methods to handle transport and reaction events, finite difference models can observe longer time scales while handling the complexities of the reaction environments.[42–45] The work in Chapter 2 utilizes a finite difference model to study the transient behavior of MDH-CS, as summarized in Figure 1.19a.[46]

1.2 Multi-scale Modeling of Electrochemical Conversion of Biomass

Bio-derived materials are also capable of providing alternative solutions as value added materials. With threats of global warming and diminishing supplies of fossil fuels, there exists a strong need for sustainable and clean means for energy production.[1] Although advancements in alternative energy technology have been made, society still relies on liquid fuels to supply energy, particularly for transportation applications.[47] As such, we turn to nature to supply alternative resources for fuels and related value-added chemicals. The use of bio-oils from plant-derived lignin has become a popular solution in addressing the world energy crisis.[4,47] Extraction of usable chemicals from lignocellulosic biomass first requires pyrolysis to produce the bio-oil. Pyrolysis is an energy and heat-intensive process that yields highly oxygenated molecules with low energy density.[48] Recent work suggests electrochemically upgrading bio-oils to more value added chemicals may be a viable secondary processing method.[49–51] However, deconvoluting and understanding the plethora of reaction mechanisms that can take place in these systems is a complex task that remains to be explored in depth.

1.2.1 Bio-oils from Pyrolyzed Lignocellulosic Biomass

Bio-oils are extracted from biomass via pyrolysis.[48] During fast pyrolysis processes, temperatures around 500C are applied to small biomass particles for approximately 1 second to separate volatile chemicals from the undesired mass, which forms biochar. Fast pyrolysis is advantageous because it yields higher liquid content with shorter residence times and less biochar content than slow or intermediate pyrolysis.[4,48,52] After the reaction, the volatile output is cooled to form bio-oil. These oils are rich with a variety of molecules. The pyrolysis process and composition of lignocellulosic bio-oil is depicted in Figure 1.10. The constituents, however, are often oxygenated and low in energy density. Pyrolyzed oils must be further processed in order to achieve a greater variety of molecules with characteristics such as high energy density.

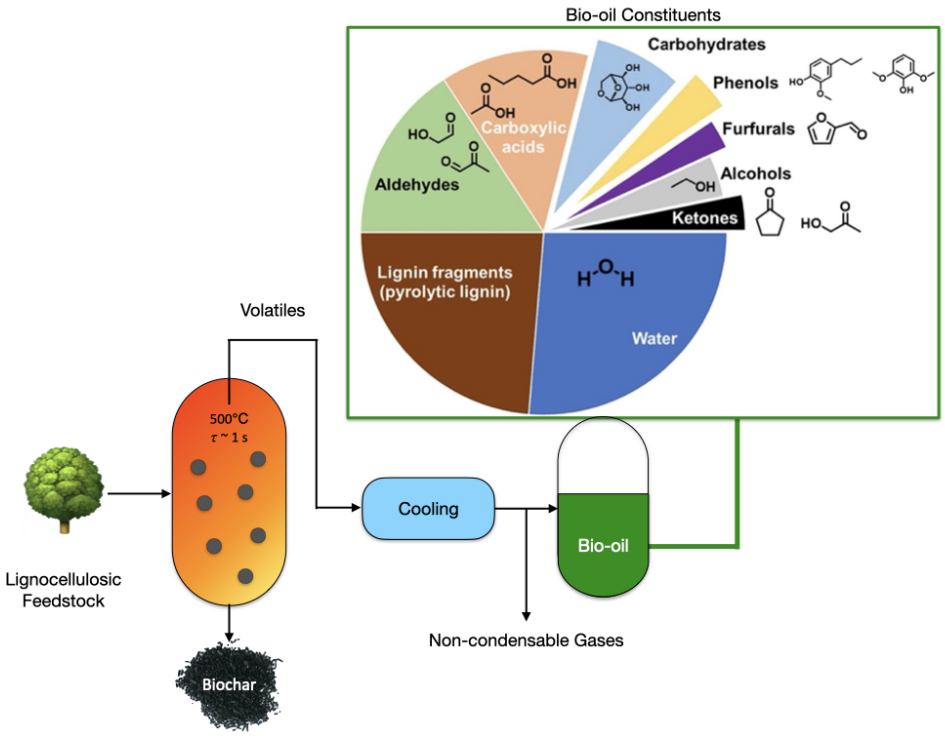

Figure 1.10: Schematic of lignin pyrolysis and composition of bio-oils.[4,48]

While there is a vast array of applications for all of the constituents types, furfurals and phenols are of particular interest.[53–57] Phenol-type molecules can be used in fuels owed to the high carbon density. Specifically, 4-propylphenol has been shown to yield favorable products that can be directly implemented in sustainable jet fuels.[55–57] Furans and furfural-derived compounds are of interest because of their versatile applications, including solvents, polymer substrates, fuels, fuel additives, and textiles.[53,54] To achieve the derivates of the platform molecules in bio-oil, further treatment is required, which comes with a set of engineering challenges. In fuel applications, the high oxygen content of the molecules creates the first challenge in efficient post-treatment, or "upgrading", of pyrolysis oils. The second challenge arises in the complexity of the bio-oil mixtures with many different molecules that can potentially inhibit processing of other molecules. An understanding of molecular interactions is vital to engineering efficient upgrading processes, regardless of application.

1.2.2 Electrocatalytic Hydrotreatment of Bio-oil

Electrocatalytic hydrotreatment (ECH) has been utilized to remove the oxygen from the bio-oil molecules using applied electric potential to drive the hydrogenation reactions.[50,51,58–62] This approach is preferred over the traditional method of thermocatalytic hydrogenation (TCH) because, in addition to the high temperatures utilized to drive reactions, pressurized hydrogen gas provides the hydrogen for reactions.[63] ECH is a more favorable approach than TCH because it can be operated in ambient conditions, and the aqueous electrolyte supplies hydrogen.

1.2.2.1 Electrochemical Reactions

During ECH processes, many mechanisms are involved in processing even a single molecule. For an illustration of the steps involved, consider some reversible reduction reaction where the equilibrium of an oxidized species (Ox) and a reduced species (Red) exists at some equilibrium potential, E_0, and n moles of electrons are involved.

$$\mathrm{Ox} \; + \; n\mathrm{e}^- \; + \; n\mathrm{H}^+ \; \rightleftharpoons \; \mathrm{Red} \tag{1.20}$$

First, the oxidized species must diffuse through the bulk electrolyte to arrive near the surface and react. As the molecules approach the electrode surface, the electrolyte and oxidized molecules must be oriented to favor interaction with the surface. This regime is called the double layer or diffuse layer, with the oxidized species concentration gradient dependent on whether the reaction rate is electron transfer or mass transfer controlled, as shown in Figure 1.11.[64]

For the reversible electrochemical reaction, the net reaction rate, ν_{net}, is proportional to the current in response to an applied potential, divided by the number of electrons, n, Faraday's Constant, F, and the surface area of the electrode, A.[64]

$$\nu_{\mathrm{net}} = \frac{I_{\mathrm{net}}}{nFA} \tag{1.21}$$

In the electron transfer controlled regime, the net reaction rate is a function of the forward

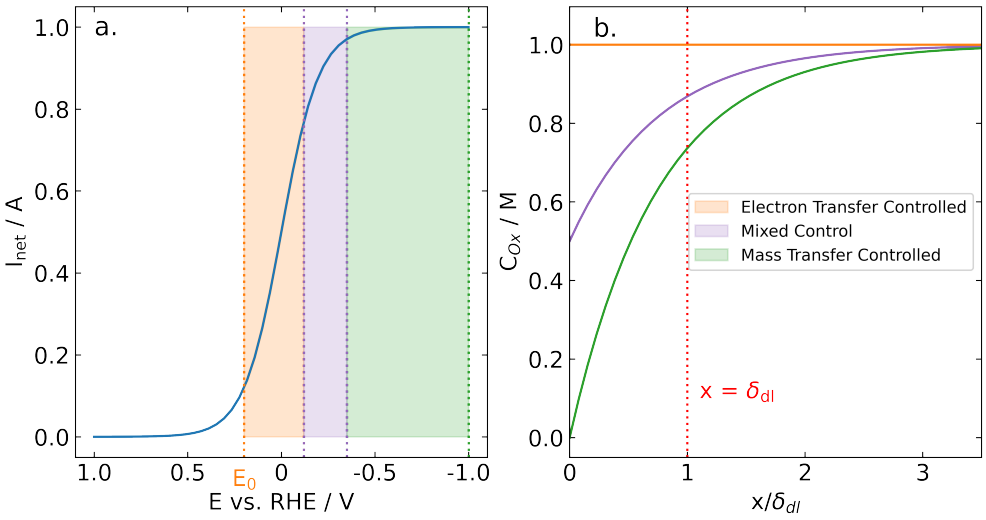

Figure 1.11: (a) Current versus Potential curve and (b) Oxidized species concentration profile in the diffusion layer with the distance from the electrode interface, x, normalized to the width of the diffusion layer for a reversible reduction reaction. The electron transfer controlled regime is colored orange, the mass transfer controlled regime is colored green, and the mixed control region is colored purple.

and reverse electron transfer rate. Assuming that the electron transfer reactions are first-order with respect to the reactant concentration (C_{Ox} & C_{Red}) at the electrode interface, the net reaction rate is the difference between the forward, or reduction, reaction rate, ν_{f}, and the reverse, or oxidative, reaction rate, ν_{r}.

$$\nu_{\mathrm{net}} = \nu_{\mathrm{f}} - \nu_{\mathrm{r}} = k_{\mathrm{f}} C_{\mathrm{Ox}} - k_{\mathrm{r}} C_{\mathrm{Red}} \tag{1.22}$$

The Butler-Volmer equation relates the electron transfer rates to the observed current[64]:

$$I_{\mathrm{net}} = nFA\left[k_{\mathrm{f}} C_{\mathrm{Ox}} - k_{\mathrm{r}} C_{\mathrm{Red}}\right] \tag{1.23}$$

where, the rate constants are related to the over potential, η, or the difference between applied potential and the equilibrium potential, by an electron transfer constant, α, which describes the change in free energy barrier with polarization.

$$k_{\mathrm{f}} = k^0 \exp\left(-\alpha n F \eta / RT\right) \tag{1.24}$$

$$k_{\mathrm{r}} = k^0 \exp\left((1-\alpha) n F \eta / RT\right) \tag{1.25}$$

where k^0 is the standard rate constant which describes the rate when the interface and solution are at equilibrium and $k_{\mathrm{f}} = k_{\mathrm{r}}$.

Although the net current at equilibrium is zero, there is still a need to balance the electrochemical, or faradaic, activity at the electrode. From this arises the exchange current where electrons are exchanged at equal rates between the electrode and oxidized or reduced species. Often the current is normalized to the area of the electrode to yield the exchange current density. This exchange current density is:

$$j_0 = \frac{I_0}{A} = F k^0 C_{\mathrm{Ox}}^{1-\alpha} C_{\mathrm{Red}}^{\alpha} \tag{1.26}$$

In the mass transfer controlled regime, the reaction rate is equivalent to the diffusion rate of the oxidized species.

$$\nu_{\mathrm{net}} = m_{\mathrm{Ox}} C_{\mathrm{Ox}} = \frac{D_{\mathrm{Ox}}}{\delta_{\mathrm{dl}}} C_{\mathrm{Ox}} \tag{1.27}$$

The mass transfer coefficient, m_{Ox}, is the diffusion coefficient, D_{Ox}, divided by the thickness of the diffusion layer, δ_{dl}.

1.2.2.2 Adsorption Mechanisms in Electrochemical Reactions

Although adsorption of an organic (Ox species) occurs much faster than electron transfer or mass transfer and does not impact the reaction rate, the orientation of the oxidized species on the electrode can affect the details of the reaction mechanism.[65–67] Determination of organic adsorption configuration is complicated by molecule size and coverage of the surface. The possibilities of adsorption configuration are expansive, and at moderate coverages, the configurations change from one in which the ring is parallel to the surface to a vertical one in which the ring is perpendicular to the surface.[66,67] This shift can affect the reactivity of the organic due to less interaction with the surface.

Organic ECH further requires a proton presence. Most commonly, a Langmuir-Hinshelwood

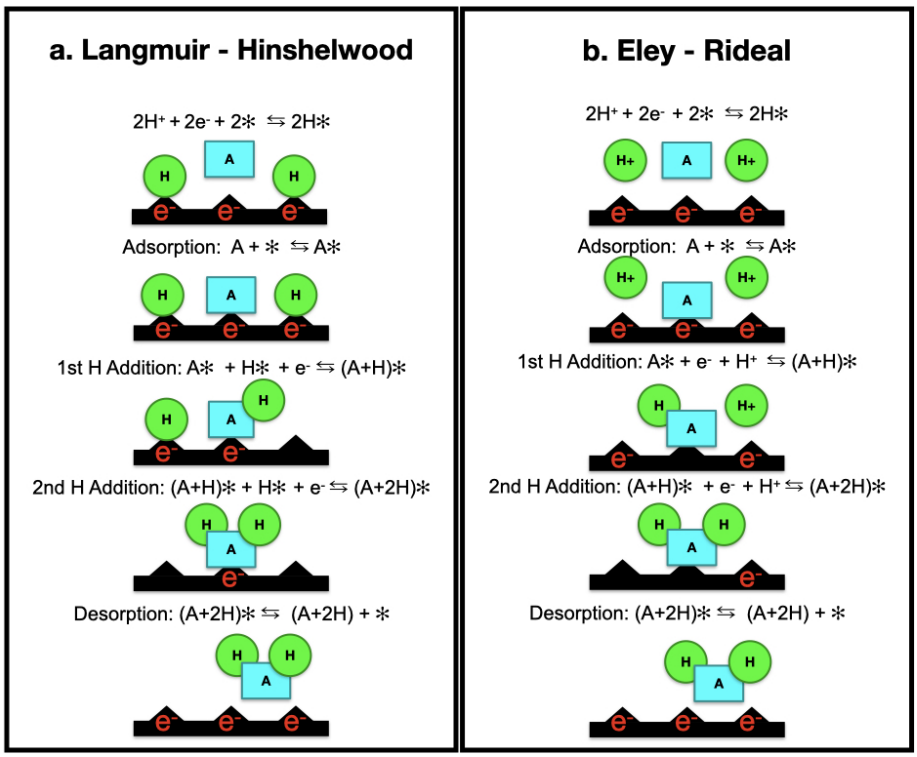

Figure 1.12: Depictions of (a) a Langmuir-Hinsehlwood mechanism of organic and hydrogen co-adsorption and reaction and (b) an Eley-Rideal mechanism of organic adsorption and reaction with protons in solution.[13,68,69]

mechanism is assumed in which the adsorbed organic reacts with co-adsorbed hydrogen.[68] However, in practice, it is possible that the adsorbed organic could also be hydrogenated by protons in solution, per an Eley-Rideal mechanism.[69] The two mechanisms are illustrated in Figure 1.12 for some organic molecule A.

1.2.2.3 Hydrogen Evolution Reaction

In electrochemical processes, the reducing potentials required for the hydrogenation of most organics occur near that of hydrogen deposition and the hydrogen evolution reaction (HER).[70] While the presence of hydrogen aids in more efficient hydrogenation, it also enhances the competition for the active sites necessary for organic hydrogenation. The net reaction of HER is:

$$2H^+ + 2e^- \rightleftharpoons H_2 \tag{1.28}$$

The equilibrium potential of HER is a function of the standard hydrogen electrode potential, E_0, which is zero when utilizing a reversible hydrogen reference electrode.[70] The activities of protons in solution (α_{H^+}) and hydrogen gas (α_{H_2}) are also accounted for:

$$E_{\mathrm{eq}} = E_0 + \frac{1}{2f} ln \left(\frac{\alpha_{\mathrm{H}^+}^2}{\alpha_{\mathrm{H}_2}} \right) \tag{1.29}$$

where $f = \frac{F}{RT}$, the ratio of Faraday's constant to the gas constant - temperature product.

During HER, protons can interact with the electrode through a Volmer, Heyrovsky, or Tafel mechanism.[70,71] The Volmer and Heyrovsky mechanisms (Eqs. 1.30 & 1.31) entail electrochemical adsorption where the former exhibits only proton adsorption and the latter exhibits the dissociation of H_2 and adsorption of a proton. An Eley-Rideal mechanism is comparable to the Heyrovsky step. A Tafel mechanism (Eq. 1.32) represents the dissociative chemisorption of H_2.

$$\text{Volmer}: \quad \mathrm{H}^+ + * + \mathrm{e}^- \rightleftarrows \mathrm{H}* \tag{1.30}$$

$$\text{Heyrovsky}: \quad \mathrm{H}* + \mathrm{H}^+ + \mathrm{e}^- \rightleftarrows * + \mathrm{H}_2 \tag{1.31}$$

$$\text{Tafel}: \quad 2\mathrm{H}* \rightleftarrows 2* + \mathrm{H}_2 \tag{1.32}$$

In acidic media, and assuming a Langmuir adsorption isotherm, the reaction rates of Volmer, Heyrovsky, and Tafel steps in units of $\mathrm{mol} \cdot \mathrm{cm}^{-2} \cdot \mathrm{s}^{-1}$, are a function of the fraction of free surface sites, θ, and the fraction of active sites covered with hydrogen, θ_{H}.[70]

$$\nu_{\mathrm{Volmer}} = k_{\mathrm{vf}} C_{\mathrm{H}+} \theta (1 - \theta_{\mathrm{H}}) e^{-\beta_{\mathrm{v}} f (\mathrm{E} - \mathrm{E}_{\mathrm{v}}^0)} - k_{\mathrm{vr}} \theta \theta_{\mathrm{H}} e^{(1-\beta_{\mathrm{v}}) f (\mathrm{E} - \mathrm{E}_{\mathrm{v}}^0)} \tag{1.33}$$

$$\nu_{\mathrm{Heyrovsky}} = k_{\mathrm{hf}} C_{\mathrm{H}+} \theta \theta_{\mathrm{H}} e^{-\beta_{\mathrm{h}} f (\mathrm{E} - \mathrm{E}_{\mathrm{h}}^0)} - k_{\mathrm{hr}} C_{\mathrm{H}_2} \theta (1 - \theta_{\mathrm{H}}) e^{(1-\beta_{\mathrm{h}}) f (\mathrm{E} - \mathrm{E}_{\mathrm{h}}^0)} \tag{1.34}$$

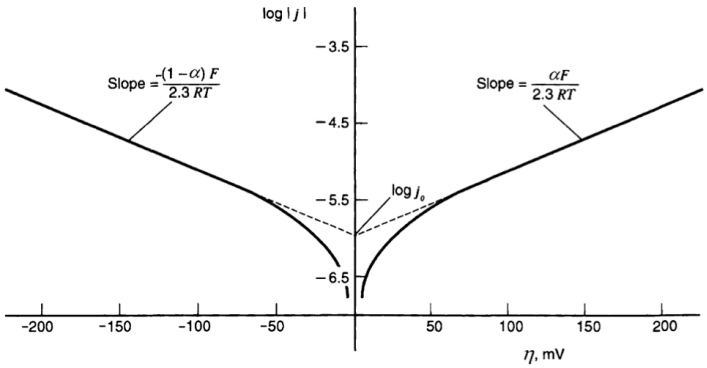

Figure 1.13: A generic Tafel plot of current density vs. overpotential from Ref[73].

$$\nu_{\text{Tafel}} = k_{\text{tf}}\theta^2\theta_{\text{H}}^2 - k_{\text{tr}}\theta^2(1-\theta_{\text{H}})^2 C_{\text{H}_2} \tag{1.35}$$

In these expressions, the forward and reverse rate constants are represented by k_{if} and k_{ir}, respectively. The standard potentials of the Volmer and Heyrovsky mechanisms are denoted by E_{v}^0 and E_{h}^0. The symmetry coefficients of the Volmer and Heyrovsky mechanisms are β_{v} and β_{h}.

The Volmer and Heyrovsky mechanisms are differentiated by analysis of a Tafel plot, as shown in Figure 1.13. The value of the slope of the linear portion can suggest the utilized mechanism. A slope of 30 mV dec^{-1} suggests a Volmer-Tafel mechanism and a slope of 40 mV dec^{-1} suggests a Volmer-Heyrovsky mechanism.[72] If the slope is 120 mV dec^{-1}, then the rate-limiting step is dependent on surface coverage of hydrogen where, at low coverages, the Volmer step is rate-limiting and at saturation, either the Volmer or Heyrovsky mechanism can be rate-limiting.

During electrochemical hydrotreatment of organic molecules, the hydrogen and organics are in competition for adsorbed sites. The number of remaining free sites, θ_*, and those occupied by either hydrogen (θ_{H}) or an organic (θ_{org}), all relative to the total number of sites, sum to unity:

$$1 = \theta_* + \theta_{\text{org}} + \theta_{\text{H}} \tag{1.36}$$

Therefore, there will be competition between the organic reactions and hydrogen evolution because the available number of active sites for organic adsorption is dependent on hydrogen coverage. Additionally, the standard potentials of the Volmer and Heyrovsky steps are 0 V versus a standard hydrogen electrode. If the applied potential is positive against the same reference, favoring oxidation instead of HER, protons in solution will be favored for the Volmer step, and adsorbed hydrogen will be favored in a Heyrovsky mechanism due to the negative exponent in the exponential factor for the forward reactions. When the applied potential is reduced to negative values against the standard hydrogen electrode, the favorability of the Volmer and Heyrovsky steps is reversed, favoring adsorbed protons and hydrogen gas, respectively. In either case, the Tafel mechanism presents a competitive hydrogen pathway due to hydrogen coverage at positive potentials and hydrogen gas presence at negative potentials.

1.2.3 Thermodynamic Evaluation

Reaction mechanisms in the conversion of bio-oil molecules to value added chemicals may be explored by quantum modeling. Energetics and thermodynamics of reactions in comparison to other mechanisms drive the outcome of the reaction system. Using quantum level simulations, we can identify rate limiting steps and reaction pathways based on the reaction barrier, adsorption energy, and reaction energy. Further work may extend modeling to multiple scales to enable further comparison to experiment.

1.2.3.1 Density Functional Theory

Quantum-level simulations may be executed with Density Functional Theory (DFT) to understand the electronic structures of atoms within a molecular system. Specifically, since the electron clouds of an atom are much more sensitive to environmental changes than the nucleus, the electron density and changes therein in response to external factors are the focus.[74] The Born-Oppenheimer approximation describes this separate treatment of electrons and nuclei when searching for the electrons' lowest energy state, or the ground state. The ground state is the electronic structure that yields the lowest energy while solving the

Schrödinger equation. Using the variation of Kohn and Sham, a set of Schrödinger's equations are written for single electrons in the form of[74,75] :

$$\left[\frac{h^2}{2m}\nabla^2 + V(r) + V_{\mathrm{H}}(r) + V_{\mathrm{XC}}(r)\right]\psi_i(r) = E_i\psi_i(r) \tag{1.37}$$

where h is Planck's constant, m is the electron mass, r describes the coordinates of an electron, ψ_i is the wave function of an electron i, which describes the probability of an electron being at some position, r, and E_i is the electronic energy. The four terms within the square brackets represent the potentials to be considered in the solution.[74,75] The first term, $\frac{h^2}{2m}\nabla^2$, represents the kinetic energy of the electron. The interaction between the electron and the nuclei around it is described by $V(r)$. The Hartree potential, $V_{\mathrm{H}}(r)$, accounts for repulsion between the electron and the remaining electron density. The final term, $V_{\mathrm{XC}}(r)$corrects for exchange and correlation contributions within the single-electron equations, such as the non-physical self-interaction energy that results from the Hartree potential. In practice, Kohn-Sham equations are solved in four steps[74]:

1. Select an initial electron density.
2. Solve the single electron Schrödinger equation for the electrons from Step 1.
3. Calculate an electron density from the solution determined in Step 2.
4. Compare the initial electron density to the one calculated in Step 3.

If the two electron densities from Steps 1 and 3 are the same, then the ground state has been found. If not, the process should be repeated with a different guess at electron density in Step 1 until the ground state is found. System attributes such as total energy can be calculated once the electron densities have been described as a function of nuclear positions. Changes in the electronic structure and factors like total energy, due to the movement of nuclei, can also be described through this process.

1.2.3.2 Adsorption Thermodynamics

To probe adsorption thermodynamics by DFT, three states must be assessed including a bare surface slab with some vacuum layer perpendicular to the top layer, the free organic

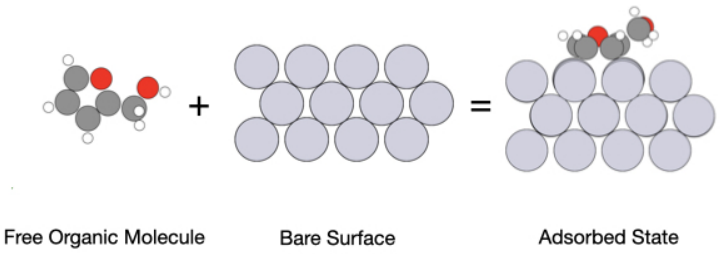

Figure 1.14: Three states considered in calculation of adsorption energy: free organic molecule, bare slab, and the adsorbed state.

in vacuum, and an adsorbed state in which the organic is bound to the surface slab. A schematic depicting the states is in Figure 1.14. Energy prediction for the first two states, the bare slab and organic in vacuum, is relatively straightforward. The lattice parameters of various facets of many surface crystals are available in databases and are experimentally determined.[76,77] The slab size used varies somewhat in literature, but a 4x4 atom surface with 3 to 5 layers is commonly used to model a surface.[77–80] Similarly, the atomic positions of organic molecule isomers in vacuum are available through PubChem.[81] Both the bare slab and the free organic undergo complete geometric optimization, or relaxation, in which the energy and force are both optimized to a given threshold.

Calculation of the adsorbed state energy is a more tedious task. Using the relaxed geometry of the surface slab, layers beneath the top 2 are fixed to represent the bulk surface that would not react to an adsorbate.[82–86] The adsorbate is then placed near the top of the surface. The exact configuration of the adsorbate relative to the surface can vary, resulting in substantial differences in adsorption energy.[85] Consequently, when working with a new system, one must test an array of possible adsorption configurations. The horizontal, or "ring-down", configuration exhibits stronger binding than a vertical configuration and is the focus of most studies.[85] Even still, the placement of the ring and substituent group(s) can vary. The center of the ring and substituent group(s) can take atop, hollow, or bridge configurations on most surfaces.[87] Combination of ring and substituent group(s) positions relative to the surface can lead to an expansive list of possibilities that must all be assessed. An example of possible positions for a five member ring with one substituent on an FCC(111)

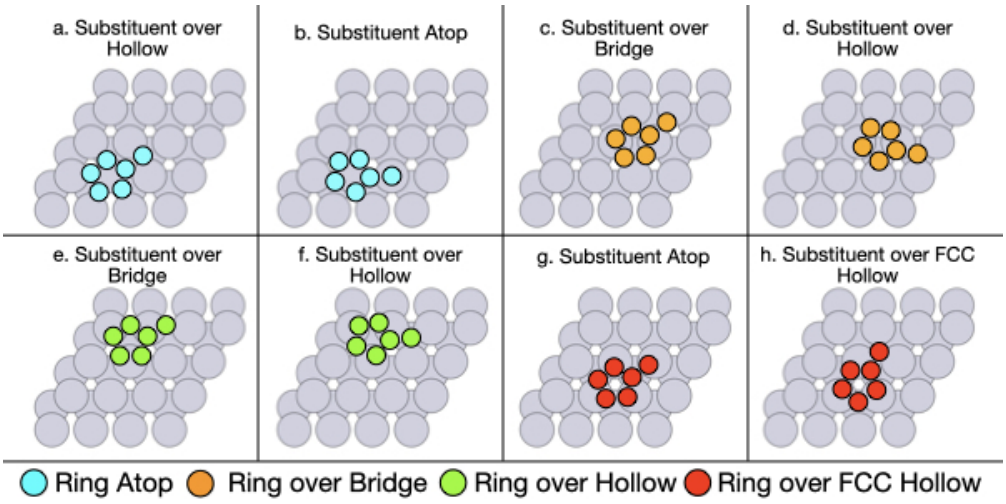

Figure 1.15: Surface-parallel adsorption configurations of a five member ring with one substituant group. Ring positions are color coded and each have two substituent positions. The substituant positions are (a) hollow and (b) atop for an atop ring, (c) bridge and (d) hollow for a ring over a bridge, (e) bridge and (f) hollow for a ring over a hollow, and (g) atop and (h) FCC hollow for a ring over a FCC hollow.

slab is shown in Figure 1.15. Whichever adsorption configuration, upon relaxation, that yields the lowest energy is considered the preferred state. The adsorption energy of some organic, i, is:

$$i(g) + * \rightarrow i* \tag{1.38}$$

$$E_{\text{ads},i} = E_{i*} - E_{i(\text{g})} - E_{*} \tag{1.39}$$

where the adsorbed state energy is E_{i*}, the energy of the free organic is $E_{i(\text{g})}$, and the slab is represented by E_{*}.

1.2.3.3 Reaction Energy

The thermodynamics of reactions are similarly predicted by the comparison of state energies. However, this will focus more on successive hydrogenation steps that occur on the surface. As such, the relaxed states of the various hydrogenation products are required. The product state can initially assume the positions of the reactant state to enhance computational

efficiency. The energy of reaction, for some reactant, $i*$, and some product, $(i + \mathrm{H})*$, is:

$$i* + H* \rightarrow (i + H)* + * \tag{1.40}$$

$$E_{rxn} = E_{(i+\mathrm{H})*} + E_* - E_{i*} - E_{\mathrm{H}*} \tag{1.41}$$

1.2.3.4 Gibbs Free Energy Corrections in Adsorption and Reaction

The internal energies calculated in the geometric optimization process represent that at absolute zero temperature and zero pressure. To assess the thermodynamics of these systems in line with experimental conditions, steps must be taken to align the energies with what would occur at some non-zero temperature and pressure. Computationally, this is accomplished by prediction of Gibbs free energy through vibrational corrections to the electronic energies previously discussed. For a given state, j, the Gibbs free energy is[88,89]:

$$G_j = E_j + E_{\mathrm{ZPE}} - TS + H_{0\rightarrow \mathrm{T}} \tag{1.42}$$

where E_j is the electronic energy calculated in the relaxation, E_{ZPE} is the zero point energy, or the accounting of vibrational energy of a system at absolute zero, TS is the entropic contribution, and $H_{0\rightarrow \mathrm{T}}$ are additional enthalpic contributions beyond $E_j + E_{\mathrm{ZPE}}$ due to heating the system from 0K to some arbitrary temperature, T.

The Gibbs free energy of some elementary reaction step would then be:

$$\Delta G_{\mathrm{rxn}} = G_{\mathrm{FS}} - G_{\mathrm{IS}} \tag{1.43}$$

where G_{FS} and G_{IS} are the free energies of the final state and the initial state, respectively. This can be applied to reactions and adsorption or desorption.

1.2.3.4.1 Potential Dependence To apply the thermodynamic evaluation to electrocatalytic processes, one must further account for the impact of applied potential. The presence of protons and electrons in solution are accounted for by the Computational Hydrogen

Electrode (CHE) method.[90] Here, the chemical potential of a proton-electron pair ($H^+ + e^-$) in solution is assumed to be equivalent to half the chemical potential of a hydrogen gas molecule ($H_2(g)$) at 0 V vs. RHE (0 U_{RHE}) and any value of pH. At any value of U_{RHE}, the resulting relationship is described by Eq. 1.44.

$$\mu(H^+ + e^-) = 0.5\mu(H_2(g)) - |e|U_{RHE} \tag{1.44}$$

Here, $|e|$ is the elementary charge in units of coulombs and the term $|e|U_{RHE}$ is converted from units of joules to eV.

Elementary electrochemical steps, assumed to include proton-coupled electron transfer (PCET)[91,92], are also corrected for applied potential. The product of elementary charge and applied potential are similarly accounted for in the change in free energy expression, such that Eq. 1.42 is expanded to be[93] :

$$\Delta G = \Delta E + \Delta E_{ZPE} - T\Delta S + \Delta H_{0\rightarrow T} + n|e|U_{RHE} \tag{1.45}$$

where the $|e|U_{RHE}$ is again converted to have units of eV and n is the number of electrons used in the reaction.

1.2.3.5 Experimental Adsorption Thermodynamics

The free energy and heat of adsorption of an organic species on a Pt electrode can be probed experimentally through organic-blocked hydrogen electrochemical under potential deposition (H_{upd}).[94,95] In the reductive window during a cyclic voltammogram or linear voltage sweep, the amount of adsorbed hydrogen is a function of the sum of peaks, as highlighted in Figure 1.16. When organic adsorption blocks hydrogen adsorption, the sum of peaks will decrease and enables the calculation of fraction of Hupd blocked, which is equivalent to the amount of organic adsorbed.

The relationship between fraction H_{upd} blocked (θ) and the heats of adsorption of the organic is described by a Frumkin isotherm. Here, the fraction of H_{upd} inhibited as a function of concentration is fit to the isotherm to determine the saturation coverage, θ_{sat}, the free

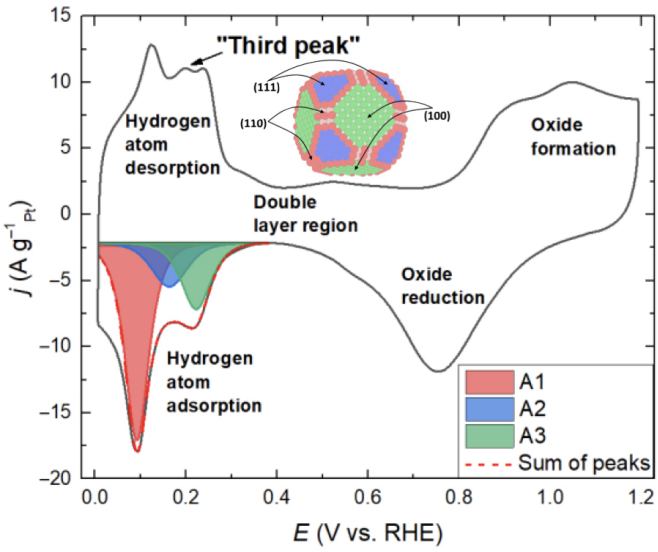

Figure 1.16: Example of hydrogen adsorption peaks in a CV. The inset particle presents the various facets of a Pt nanoparticle, which correspond to the 3 sub peaks highlighted in the CV. Adapted from Ref[94].

energy of adsorption at zero coverage, $\Delta G^{\text{aq}}_{\text{ads},\theta=0}$, and the linear scaling slope for free energy of adsorption, α.[95]

$$\frac{C}{C_0} = \frac{\frac{\theta}{\theta_{\text{sat}}}}{1-\frac{\theta}{\theta_{\text{sat}}}} \exp\left[\frac{-\Delta G_{\text{ad,aq},\theta=0}}{RT} - \frac{\alpha\frac{\theta}{\theta_{\text{sat}}}}{RT}\right] \tag{1.46}$$

For the aqueous phase experiment, the Gibbs free energy ($\Delta G_{\text{ad,aq}}$) and heat of adsorption ($\Delta H_{\text{ad,aq}}$) are related to $K_{\text{eq,aq}}$ with an assumed entropy of adsorption value ($\Delta S_{\text{ad,aq}}$).

$$K_{\text{eq,aq}} = e^{-\Delta G_{\text{ad,aq}}/RT} = e^{-\Delta H_{\text{ad,aq}}/RT} e^{-\Delta S_{\text{ad,aq}}/R} \tag{1.47}$$

To compare with the gas phase free energies calculated by DFT, the aqueous phase relationships are extrapolated to the gas phase through Henry's Law. Here, $K_{\text{eq,gas}}$ is determined from the aqueous equilibrium coefficient and Henry's constant, K_{H}, which becomes unitless when multiplied by RT, and used in Eq. 1.47 to determine the values of $\Delta G_{\text{ad,gas}}$ and $\Delta H_{\text{ad,gas}}$.[95]

$$K_{\text{eq,gas}} = \frac{K_{\text{eq,aq}}}{K_{\text{H}}} \tag{1.48}$$

Henry's Law enables estimation of the solvation of the organic from gas to aqueous phases. The resulting isotherms are a function of θ, and therefore, can be evaluated at a given coverage to correspond to the coverages used in DFT models. Chapter 3 employs H_{upd} analysis in comparison to a potential dependent thermodynamic assessment by DFT to understand mechanisms involved in the electrochemical hydrotreatment of a furfural and 4-propylphenol binary mixture (Fig. 1.19b).

1.2.4 Kinetic Evaluation

Thermodynamic evaluation of hydrogenation reactions provide a substantial amount of information toward understanding competing mechanisms. However, the varied rates of reaction can also affect the competition between reactions and, therefore, must also be assessed.

1.2.4.1 Activation Barrier

Prediction of reaction kinetics requires information about the activation barriers. Computationally, several methods are utilized to search the reaction path and find the transition state (TS), as summarized in Figure 1.17. The TS with the highest energy represents the highest barrier in the reaction. Some common methods include nudged elastic band (NEB, Fig. 1.17a) or the climbing image (CI-NEB) variation, and the dimer method (Fig. 1.17b).[96,97] However, the TS search methods are computationally demanding, especially for large systems representing heterogenous catalysis. More recently, linear scaling relationships have been developed to correlate the energy of an activation barrier (Fig. 1.17c) or TS (Fig 1.17d) with that of the initial and/or final states.[98] This approach offers the advantage of quick estimation of transition state energetic information where the relationship has been defined for a specific reaction type using a method like NEB, CI-NEB, or the dimer method.

Elastic band methods search for a TS along a pathway between an initial state (IS) and final state (FS). The subsequent images are connected via "springs" with spring constants to set the forces that determine how stiff the pathway is, or how far apart images are from each other.[96] The primary difference between NEB and CI-NEB is that, in the climbing image variation, the optimized TS is found by moving the highest energy image to the appropriate

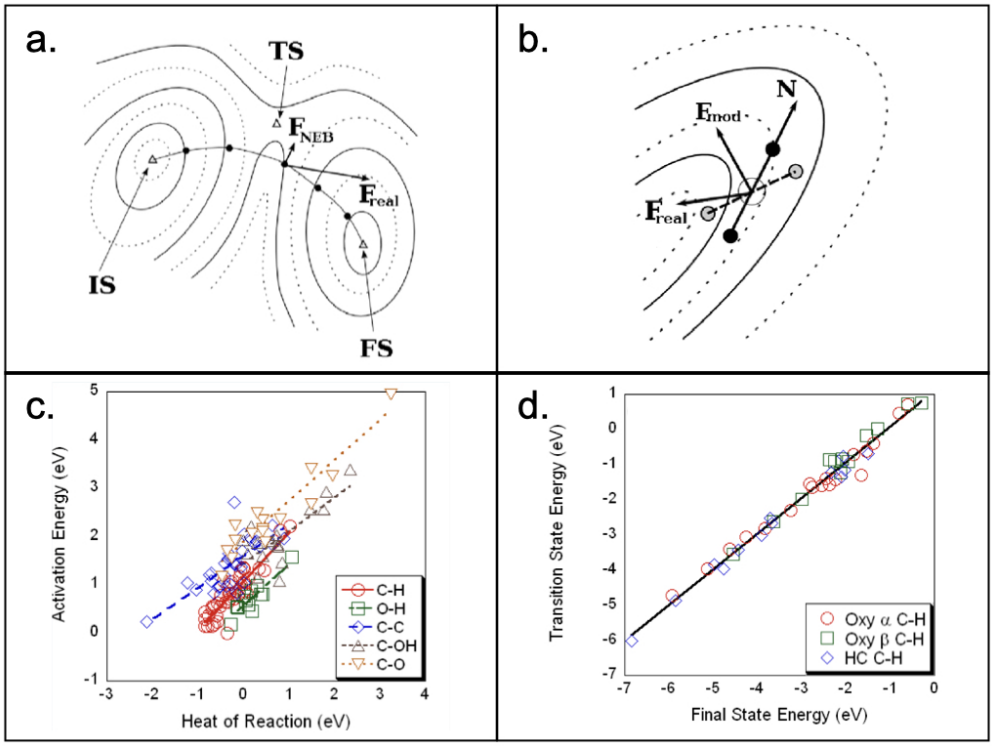

Figure 1.17: Summary of methods to determine transition states and activation barriers. (a) NEB, (b) Dimer, (c) Brønsted - Evans -Polyani (BEP) relationship, and (d) Transistion State Scaling (TSS) relationship. Figs a-b are adapted from Ref[96] and Figs c-d are from Ref[98].

place in the reaction path. The standard NEB method may get close to the actual TS, but does not explicitly optimize the path to find the highest energy state. Commonly, studies using NEB to find a transition state will request an odd number (often 5) of images along the path to increase the likelihood of finding the saddle point. For greater computational efficiency, one may also combine techniques to conduct an initial pathway search using NEB, then refine the pathway with CI-NEB from the optimized pathway found in the initial search.[99,100]

In comparison to the elastic band methods, the dimer method predicts the transition state and reaction pathway from only the initial state image and a closely related image.[97] The pair of images, which are almost identical, are referred to as the "dimer". The dimer is then moved along the potential energy surface assuming that the IS is an energy minima. As the dimer moves, the curvature of the potential energy surface is determined. The motion continues until a minimum curvature is determined and the transition state is found. While this approach may be beneficial in regard to the lack of final state requirement, this is only a local search whereas the NEB approaches are global methods. NEB and CI-NEB would, therefore, have more flexibility to search along a specified path. For any approach, the activation barrier, E_{a} is the difference in energy between the TS, or the highest energy state found along the pathway, and IS.

$$E_{\mathrm{a}} = E_{\mathrm{TS}} - E_{\mathrm{IS}} \tag{1.49}$$

Linear scaling relationships have been developed to generate quick information about the energetics of the activation barriers.[98] Brønsted - Evans -Polyani (BEP) relationships correlate the activation energy to the reaction energy of a given step. Transition state scaling (TSS) relationships correlate the TS energy to the energy of the final state. The relationships of BEP and TSS are defined as, respectively:

$$E_{\mathrm{a}} = \alpha E_{\mathrm{rxn}} + \beta \tag{1.50}$$

$$E_{\mathrm{TS}} = \alpha' E_{\mathrm{FS}} + \beta' \tag{1.51}$$

where α and α' represent linear slopes and the βs are the y-intercept. The two relationships can be combined to establish a unified expression:

$$E_{\mathrm{TS}} = \alpha E_{\mathrm{FS}} + (1-\alpha)E_{\mathrm{IS}} + \beta \tag{1.52}$$

The slopes are equivalent and the y-intercepts are related.

$$\beta' = (1-\alpha)E_{\mathrm{IS}} + \beta \tag{1.53}$$

Application of linear scaling relationships appears straightforward, but it is imperative that constants used in further calculations are consistent with the type of reaction and surface. Initial use of BEP relationships focused primarily on small molecule bonds such as C-O bonds in CO_2, COOH, and CO, and C-H bonds in ethane and methane. Similar systems were also probed with TSS.[98] More recently, relationships have been determined for bonds within more complex molecules such as phenol and furan derivatives.[101–103] These insights are promising for estimation of transition energies, but should be used cautiously in application due to the limited information on less popular surface facets.

Similarly to reaction energies, the implications of variable applied potential on activation barriers can be assessed. This is accomplished through application of Marcus theory where the energy of a transition state references the potential dependence of the proton in electrolyte.[93] The arbitrary elementary steps for the hydrogenation of organic species A are as follows:

$$\mathrm{A}* + \mathrm{H}^+ + \mathrm{e}^- \rightarrow \mathrm{A}* + \mathrm{H}* \tag{1.54}$$

$$\mathrm{A}* + \mathrm{H}* \rightarrow \mathrm{AH}* \tag{1.55}$$

While assuming the CHE method, the equilibrium potential, U_0, is a combination of state free energies.[90,93] The free energy change of the activation barrier, ΔG_{a}, can then be predicted at any potential, U.[93] Details of this analysis are reported in Chapter 4.

1.2.4.2 Computational Predictions of Rate Constants

Once activation barriers are predicted by DFT, the kinetic rate constants can also be predicted. Transition State Theory postulates that a rate constant, k, is related to the activation barrier free energy, ΔG_a, at a given temperature, T.[104,105] Similarly to the activation barriers, potential dependence can also be further considered in kinetics.[104] Chapter 4 extends the work within Chapter 3 by employing DFT activation barriers to predict reaction kinetics in the electrochemical hydrogenation of a furfural and 4-propylphenol binary mixture. Chapter 4 is summarized in Fig 1.19c.

1.3 Manufactured Cell-Laden Tissue Scaffolds

In a further desire to mimic biology for effective engineering solutions, bio-inspired materials are a current focus in medical applications. Development of high-performance materials as a solution to treat bone degradation resulting from osteoporosis has been a prevalent research direction in the biomedical field.[106] A successful material must meet several criteria to be considered for these applications. Tissue-regenerative materials must exhibit biocompatibility, maintain stability in physiological conditions, mimic the extracellular matrix with structure tunablity, and promote cell viability.[107–110] Collagen, and the cheaper alternative, gelatin, meet most of the requirements as a biomaterial.[108]

1.3.1 Bio-ink Development for Tissue Regenerative Materials

While initially attractive, gelatin degrades at physiological temperatures (˜37C).[111] To overcome stability constraints, gelatin methacryloyl (GelMA) was developed to enhance material stability by bonding methacrylate to the gelatin backbone. Chemical modification of gelatin increases the melting point above physiological temperatures.[111] Hydrogels of GelMA also take longer to experience the same degree of mass loss as gelatin.[107,110] To address cell viability, GelMA was further modified by chemical linkage to silver-doped bioactive glass (Ag-BG).[112] Bioactive glass is a traditional component in tissue-regenerative materials with appreciable cell viability properties.[106] Addition of silver has also been shown to increase

antibacterial properties of biomaterials.[109,112] Chemically linked GelMA-AgBG (GAB) is therefore anticipated to have superior cell viability properties to GelMA alone.

1.3.2 Development and Initial Validation of a New Bio-ink for 3D Printed Cell-Laden Tissue Scaffolds

The dissertation work of Marsh sought to develop and validate the use of GAB within 3D cell laden, or 3D Multi-scale (3DBP), tissue regenerative scaffolds.[5] Early work utilized a polymer foam method to support a coat of Ag-BG sol-gel.[113] A follow-up study sintered Ag-BG nanoparticles derived from the sol-gel to a polymer foam base scaffold and compared the performance implications of sintering temperature.[112] A fused filament method was further used to enhance the compressive strength of the Ag-BG-polymer scaffold.[109] Finally, Ag-BG was incorporated with gelatin based inks for 3D bioprinting for enhanced tunablity of scaffold design while protecting the cells from the forces present during printing.[110] Optical and SEM images of the scaffolds produced through Marsh's methods are provided in Figure 1.18. This work is the foreground for further validation reported herein.

The polymer foam supported Ag-BG scaffold incorporated the bioglass to promote antibacterial properties of the scaffold while studying the implications of processing on the structural characteristics (Fig. 1.18a).[113] A polyurethane foam provides can provide a tunable 3D network with a high surface area. An increased surface area is beneficial for methods using a sol-gel application because it enables an increased amount of antibacterial or therapeutic components that increase the bioactivity of the scaffold. The Ag-BG components were found to be homogeneously distributed on the scaffold at the micron-scale. The bioactivity of the scaffold against methicillin-resistant Staphylococcus aureus (MRSA) was also assessed by direct and indirect tests. The direct test where MRSA was exposed to the scaffold showed a decrease of nearly 6 orders of magnitude in bacteria viability within 24 hours. Indirect tests where MRSA was exposed to extracts of the scaffolds also showed decreases in bacteria viability. The bioactivity of the Ag-BG decreased over the 21 day time span of the indirect tests, which is attributed to a decrease in Ag concentration over time. While these scaffolds expressed bioactivity for an extended amount of time, the compressive strength of

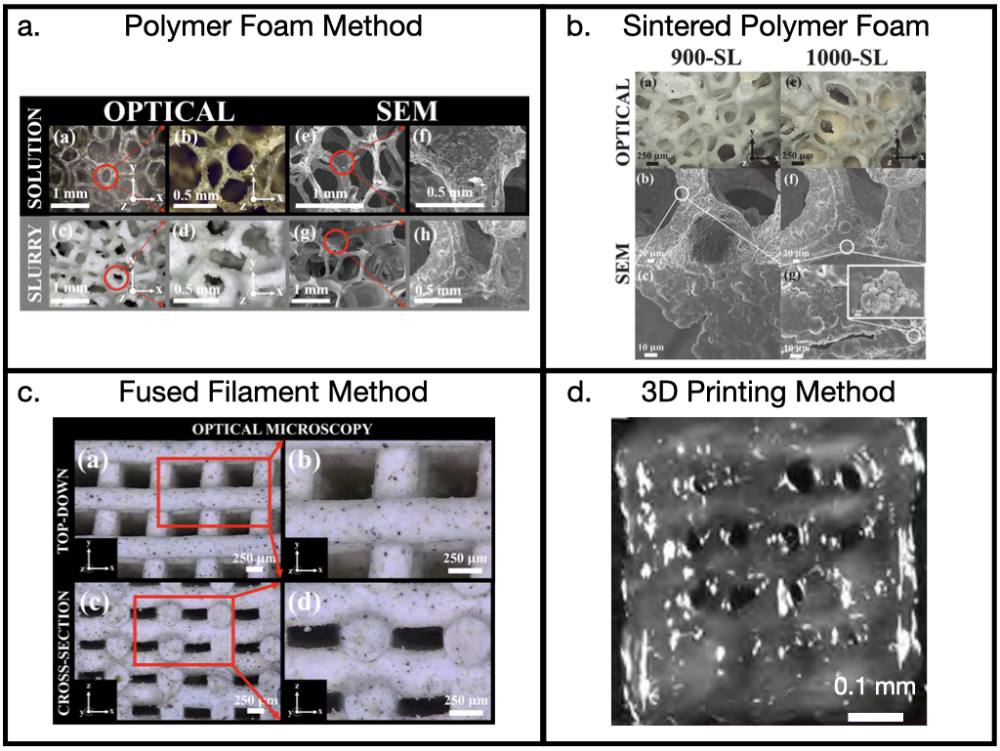

Figure 1.18: Optical and SEM immages of Ag-BG scaffolds produced via (a) polymer foam method, (b) Ag-BG sintered polymer foam, (c) fused filament method, and (d) 3D printing. Image adapted from Marsh.[5]

the Ag-BG scaffold is reported to be low for similar structures, indicating that it may only be viable for low load bearing applications. Nonetheless, this confirms that the inclusion of Ag-BG promotes antibacterial properties when incorporated in to a polymer scaffold.

In the follow up study, particles of Ag-BG were derived from the sol-gel and sintered to the polymer foam(Fig. 1.18b).[112] The sintering temperature was varied from 900C to 1000C and the implications on material and anti-bacterial characteristics were observed. Compared to the unaltered foam, sintering at 900C decreased the pore size and 1000C sintering increased the pore size. The 900C sintered structure could not be assessed for compression strength because it was too brittle and prematurely collapsed. While the 1000C sintered scaffold could be tested for compression, the compression strength was still low. Further, the 1000C sintered scaffolds exhibited slightly better anti-bacterial properties against MRSA than the 900C sintered scaffold. The 1000C scaffolds also expressed the ability to revive antibiotics during the first 24 hours, but did not see significant difference with or without antibiotics present beyond 48 hours. The material and bacterial characteristics of the polymer foam based Ag-BG scaffolds have been shown to be dependent on process variables. These scaffolds show promising results for low load bearing applications, but could be enhanced by improved compression strength.

The fused filament method is a printing method in which a polymer filament is printed to form the desired scaffold (Fig. 1.18c). This method also offers more control over matrix design than the polymer foam. In 2020, Marsh et al. reported using this approach with Ag-BG for the first time.[109] Polyolefin and Ag-BG powder were combined in to the base filament and printed to form a scaffold of approximately 1 cm^3. The scaffolds were determined to have homogenous elemental distribution to the micro-scale, and porosity and compression strength comparable to that of human bone. Similarly to the polymer foam work, MRSA was exposed to the scaffolds for up to 48 hours. At the 24 hour mark, viability of the bacteria had decreased, but only by 2 orders of magnitude compared to the almost 6 order of magnitude decrease of the polymer foam. Some further decrease in bacteria viability was observed at the 48 hour mark, but it was not as substantial as the first 24 hours. Antibacterial properties were present and the scaffolds were found to be comparable to bone in porosity and compression strength, making this approach a viable option for tissue regenerative scaffold

manufacturing.

Synthetic polymer approaches have shown promising results as a support for Ag-BG in antibacterial properties for tissue generation, but synthetic materials are often not compatible with cells. To improve the compatibility with cells for tissue growth, bio-based polymers were explored. In 2021, Marsh et al. reported initial studies of Ag-BG incorporated in to gelatin based bio-inks in 3D bioprinting manufactured scaffolds (Fig. 1.18d).[110] A mixture of GelMA and Ag-BG has limitations in homogeneity of ink composition and may impose further risk to the cells due to extra force from the Ag-BG particle size. Marsh et al.'s work instead chemically linked the Ag-BG to GelMA, forming GAB, to overcome this. The GAB exhibited superior printability and rheological characteristics compared to GelMA alone or a nano-composite blend of GelMA and Ag-BG acting as a control. Specifically, the GAB ink had viscosity, storage modulus, and loss modulus orders of magnitude larger than the GelMA or control. This suggests that GAB is able to absorb and recover from the forces of printing better than the other materials. Combining the ability to protect cells from the forces of printing and the antibacterial properties from the Ag-BG, GAB is predicted to be a superior bio-ink for 3DBP of tissue generative scaffolds. Chapter 5 presents further work toward validation of GAB as a superior bio-ink in 3DBP of tissue scaffolds including 3DBP parameter optimization and some cell viability studies in comparison to GelMA and the nano-composite control. This chapter is summarized by Fig. 1.19d. Necessary future work for complete validation of this approach are also discussed.

1.4 Overview of Included Works

The remainder of this dissertation will discuss three research topics in the area of bioelectrochemical engineering. Chapter 2 presents the first project yielding a manuscript on the topic of electrostatic transport within TCA cycle enzymes.[46] Chapter 3 reports the details of a second project that resulted in a manuscript on the topic of thermodynamic assessment and mechanistic insight in the electrocatalytic upgrading of bio-oil constituents. Chapter 4 adds a kinetic assessment to the system of Chapter 3. The work in Chapter 5 leans more toward biochemical engineering and reports validation work of a new bio-ink material for manu-

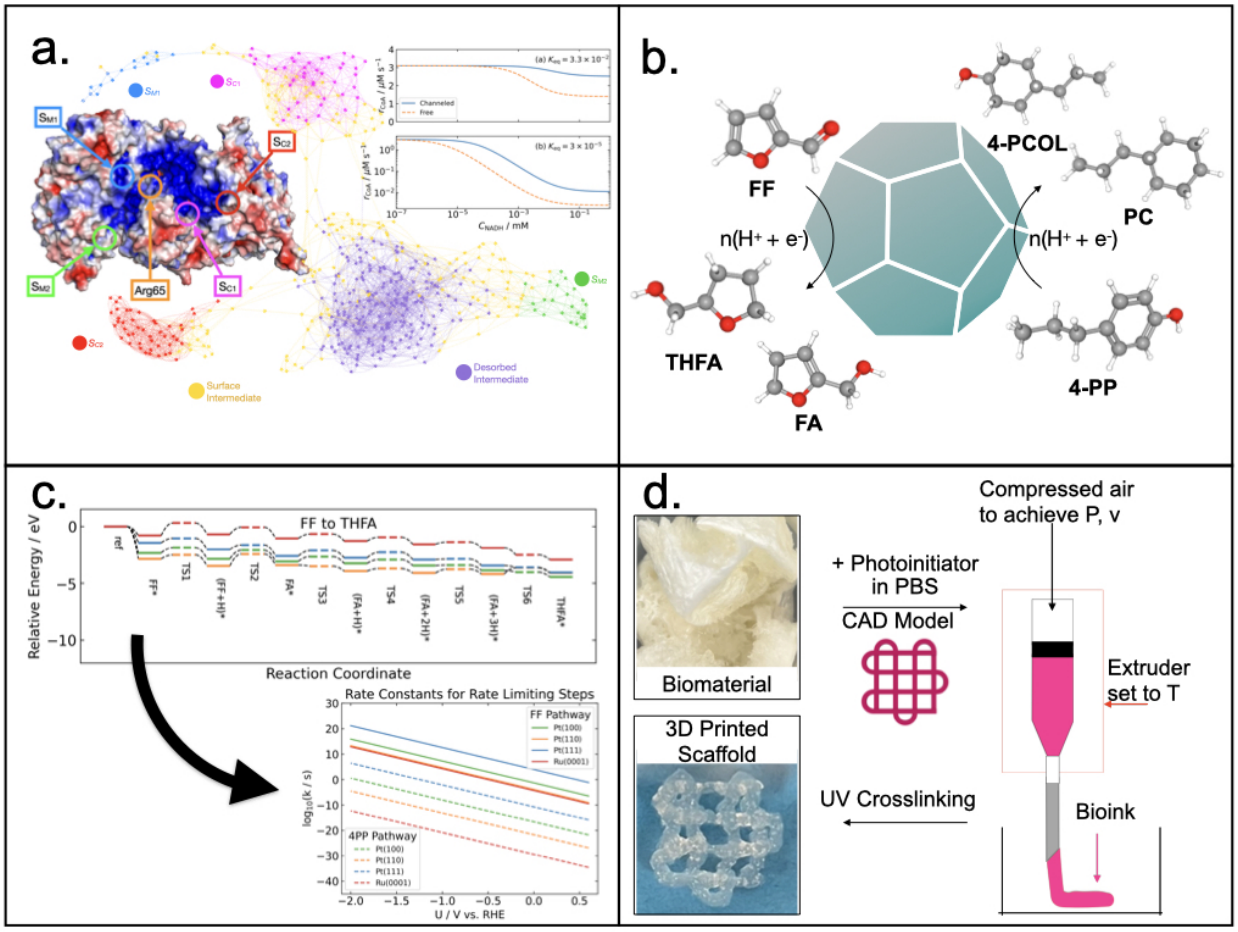

Figure 1.19: Summary of Included Research Projects: (a) Substrate channeling pathways in TCA Cycle enzymes[46], (b) interactions in ECH of Furfural (FF) and 4-Propylphenol (4-PP) binary mixture on a Pt/Ru electrocatalyst, (c) kinetic evaluation of FF and 4-PP ECH on a Pt/Ru electrocatalyst, and (d) extrusion printing of gelatin-hybrid hydrogels.

factured tissue regenerative scaffolds. Chapter 6 summarizes the conclusions of Chapters 2 through 5 and discusses future work directions from this collection of studies.

Chapter 2 (Fig. 1.19a) explores the impact of electrostatic channeling in the conversion of malate conversion to citrate via oxaloacetate (OAA) intermediate on malate dehydrogenase - citrate synthase (MDH-CS).[25] Kinetic parameters determined experimentally[16] and Markov state transition matrices produced by previous molecular dynamics simulations[26] are combined in a finite difference model to calculate time trajectories of surface and bulk occupancies by OAA in the system.[46] Solution of a system of differential mass balance equations, based on surface transport rates, provide occupancy probability at each node in the network. Lag time of MDH-CS was determined computationally to be comparable to experiment for recombinant and mutant complexes.[16] Using the model, dynamics of each of four possible reactiond pathways between two source (MDH) active sites and two sink (CS) sites could be studied independently. This analysis provides a dynamic model for intermediate transport in an electrostatically channeled system, and can be used as a predictive tool to provide mechanistic insight in to path dominance.

Chapters 3 and 4 evaluate the mechanisms in the electrocatalytic hydrogenation (ECH) of a 4-propylphenol (4-PP) and furfural (FF) binary mixture on a Pt/Ru electrocatalyst. In Chapter 3, the thermodynamics of each reactant's reaction pathways are assessed computationally (Fig. 1.19b) . Competitive adsorption between FF and 4-PP along with the respective stable intermediates is assessed with DFT for the FCC (100), (110), and (111) facets of Pt and Ru(0001). The experimental adsorption free energies of select stable intermediates are further explored by organic-blocked hydrogen under potential deposition on Pt. The reaction free energies are also calculated for the experimentally suggested pathways of FF to tetrahydrofurfuryl alcohol (THFA) and 4-PP to propylcyclohexane (PC). The affect of applied potential on the reaction free energies was a further point of exploration. This mechanistic study provides insight into the competition between two bio-oil constituent molecules.

Chapter 4 adds a kinetic analysis from the activation barriers of the energy pathways determined in Chapter 3 (Fig 1.19c). Here, linear scaling relationships for furanics and phenol are used to predict transition state energy from the energy of intermediate states on

the Pt and Ru facets studied in Chapter 3. Through predicting the transition state energy, activation barriers are determined which enable prediction of kinetic rate constants. The implications of variable applied potential are assessed for the transition states and barriers similar to the methods used in the previous work.

Chapter 5 (Fig. 1.19d) compares cell viability in extrusion printed scaffolds of GelMA, GAB, and blended GelMA + AgBG bio-inks toward validation of GAB as a novel bio-ink with enhanced cell viability properties. First, GelMA and GAB materials were synthesized and characterized as reported in literature. Then the extrusion printing parameters were optimized for the three bio-inks. Upon printing parameter optimization, cell viability studies were conducted for GelMA, GAB, and blend bio-inks with fibroblast(3T3) cells. GelMA bionic was the only one to enable cell viability, which lasted less than 24 hours. The poor performance of these bio-inks was attributed to the acidic pH of the materials in inks, resuspension issues resulting from non-optimal lyophilization, and the potential toxicity from residual toluene after synthesis. Correction of these factors are a point of future work.

Chapter 2

Finite Difference Model of Electrostatic Channeling in TCA Cycle Enzymes

2.1 Introduction[1]

Complex living organisms utilize the highly efficient metabolic pathways of biocatalyzed reaction cascades to perform vital functions necessary for survival[3,6,7,114]. These reaction cascades can convert chemicals into energy sources and other materials needed to satisfy metabolic requirements[3,6]. The natural potential of catalytic cascades to produce novel chemicals (*e.g.*, biofuels) at high yields has ignited research efforts aimed at understanding their fundamental mechanisms[3,7].

Within such catalytic cascades, interactions of reaction intermediates with biocatalytic surfaces can control intermediate transmission between active sites, a phenomenon known as channeling[2]. The traversal of charged intermediate species on an oppositely charged surface, or electrostatic channeling, is one channeling mechanism featured in natural cascades[7,27]. Electrostatic interactions maintain short distances between the intermediate and the surface, allowing for the shortest path from one enzyme to another[24]. Transport via surface interactions often occurs quickly, contributing to efficiency[26]. Without these interactions, it can take excessive time for the intermediate to desorb from the first enzyme, diffuse through

[1]This chapter is adapted from Wark, C. M.; Xie, Y.; Calabrese Barton, S. Finite Difference Model of Electrostatic Channeling in TCA Cycle Enzymes. *Electrochimica Acta.* https://doi.org/10.1016/j.electacta.2025.146131.

$$\text{malate} + \text{NAD}^+ \xleftrightarrow{\text{MDH}} \text{OAA} + \text{NADH}$$

$$\text{OAA} + \text{Acetyl}-\text{CoA} \xrightarrow{\text{CS}} \text{CoA} + \text{Citrate}$$

Figure 2.1: Reactions on MDH-CS Complex.

the bulk solution, and adsorb onto the second enzyme before being converted to a product.

The tricarboxylic acid (TCA) cycle, also known as the Krebs cycle, is a biocatalytic cascade vital to efficient energy production in metabolism[115,116]. One step of the TCA cycle involving the malate dehydrogenase - citrate synthase (MDH-CS) complex, is a research focus[117,118]. As shown in Figure 2.1, MDH-CS converts malate to citrate by way of an oxaloacetate (OAA) intermediate and a CoenzymeA (CoA) cofactor[25].

The MDH-catalyzed reaction tends to favor the reverse conversion of OAA back to malate within the reaction equilibrium, contrary to the desired direction[119]. The reverse reaction becomes significant as the concentration of NADH (the reduced form of Nicotinamide adenine dinucleotide ,NAD^+)) increases with OAA generation. This challenge is addressed through electrostatic channeling, utilizing the attractive forces between negatively charged OAA and the positively charged area on the surface of the complex[26,118]. This attraction effectively pulls OAA away from the MDH active site and directs it toward the CS active site[118].

Previously, experimental and computational approaches have increased understanding of the mechanisms of transport and key factors that drive the efficiency of MDH-CS. Bulutoglu and coworkers have shown that the complex does utilize electrostatic channeling, and have reported kinetic parameters[16]. The dynamics of reaction and transport between the two enzymes were characterized by measurement of lag time, which represents the time required for the overall citrate production rate to achieve steady state. For native bovine, commercial wild-type porcine, and recombinant porcine complexes, lag time was determined via transient analysis of CoA concentration. Additionally, a mutated version of the recombinant porcine complex was considered in which a positively-charged arginine residue (Arg65, Fig. 2.2) is replaced with charge-neutral alanine. The native tissue and recombinant complexes had the shortest lag times of 40 and 30 ms, respectively, both lower than that of the commercial complex (290 ms). By mutating the recombinant complex, a substantial increase in lag time to 880 ms was observed. This comparison of lag times suggests that the complex does

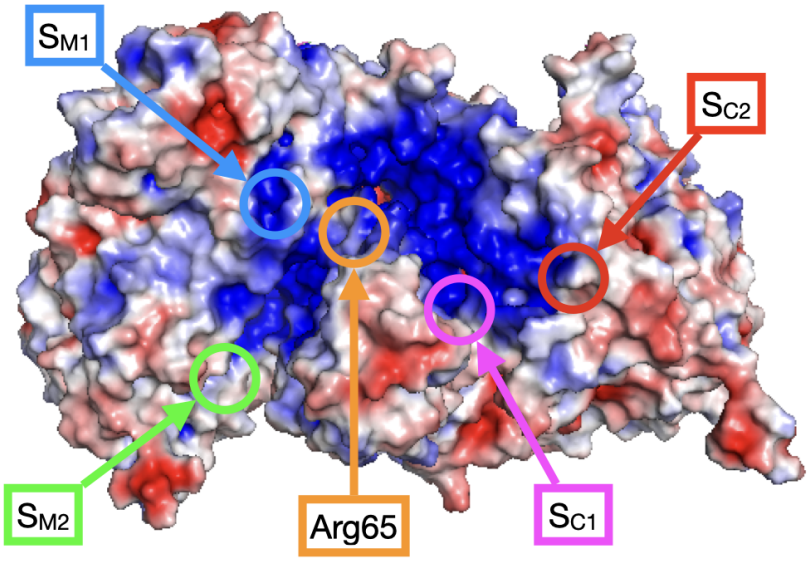

Figure 2.2: Electrostatic potential surface of MDH-CS Complex adapted from Xie et al[26,120]. Positively charged areas are colored blue, negatively charged areas are red, and neutral charges are colored white.

exhibit electrostatic channeling and that modifications to the electrostatic surface is capable of dramatically affecting intermediate transport.

Computationally, molecular and atomistic level simulations have been employed to advance the understanding of mechanisms that occur in catalytic cascades[8,27,39]. The use of these techniques for biological systems is, however, primarily limited to time scales of less than 1 μs[40]. Time scale limitations result in a compromised ability of the simulation to capture transport events and most aspects of chemical reactions having rate constants on the order of 1 second[40,41].

Molecular Dynamics (MD) and Kinetic Monte Carlo (KMC) simulation methods have been used by our group to study transport phenomena at varying time scales in biocatalytic cascades[7,24,26,27,32]. Generally, MD simulations are limited to time frames less than 1 µs, whereas KMC simulations can encompass longer time scales but become slow when the number of rate phenomena or the range of time scales considered becomes large[41,121–124]. We have used KMC to study a bridged enzyme system, namely hexokinase and glucose-6-phosphate dehydrogenase bridged by a polyarginine peptide[7,24,27,32]. This model success-

fully predicted experimental lag time measurements as a function of ionic strength and bridge length. Similarly, ionic strength was found to affect reaction probability in the computational Brownian Dynamics study of OAA transfer mechanisms on MDH-CS by Huang et al.[35]. They also showed that OAA would interact with the surface only if it carried negative charge and that transfer efficiency and reaction probability decreased with increase of ionic strength.

Recently, we have studied the electrostatic channeling of OAA on the MDH-CS complex with a Markov state model (MSM) to determine the dominant pathways and transfer efficiency of OAA[26]. For the MSM, 400,000 frames from MD trajectories of OAA on the MDH-CS surface were clustered into 500 micro-states. The micro-states were grouped into basins to analyze transport efficiency. The basins categorize active site states, desorbed intermediate states, and surface intermediate states. With two active sites on each of the enzymes, four surface paths are possible, each of which was analyzed. The path from the first MDH active site to the first CS active site was found to be the dominant pathway with the lowest probability of desorption for both the recombinant and mutant complexes. Upon mutation, the transfer efficiency from the first MDH active site to either CS active site was found to decrease from 96% to 47% for the recombinant and mutant complexes, respectively.

This previous Markov-state study of MDH-CS only considered equilibrium conditions and did not extend to transient simulations or incorporate reaction rate laws that would enable the prediction of lag time. The KMC approach used previously to model transient conditions is not compatible with an MSM due to the large number of rate phenomena (500^2 to describe transport from the MSM transition matrix alone)[41,121–124]. Alternatively, finite difference methods can be utilized to numerically solve a system of ordinary differential equations derived from the MSM transition matrix, combined with the rate laws describing the kinetics at each active site[42–45]. Solution of this system of equations enables the prediction of intermediate transport dynamics and can provide information on the system's transient behavior, such as lag time.

Here, we study the transient behavior of MDH-CS computationally by calculating the cascade lag time from a finite difference model. The model produces a time record of OAA and CoA concentrations, which are used to extrapolate the lag time after steady state is

achieved. Recombinant and mutated MDH-CS are considered using the MSM transition matrix and basin definitions of Xie et al.[26]. We also utilize the model to study the transport along individual transport paths and estimate their unique lag time. Finally, we explore the implications of reversible reaction at MDH on the recombinant complex under channeling and free enzyme conditions. This approach provides further insight into the cascade's transport efficiency and allows for model results to be compared against experiment[16]. An enhanced understanding of efficient natural systems can then enable the design of reaction cascades for novel chemical processes, such as upconversion of biomass or CO[9,10], biosensors and biofuel cells[12,125], and medical diagnostics[11].

2.2 Methods

Possible positions in the transport of OAA from the MDH source sites, S_{M1} and S_{M2} (Fig. 2.2), to the CS consumption sites, S_{C1} and S_{C2}, are represented by 500 micro-states in a Markov state model (MSM). The probability of the intermediate state of OAA transitioning from state i to state j is described by the transition probability matrix, T_{P}[42,126]. The transition probability matrix is combined with an assumed time scale to generate a set of differential equations describing the mole balance for each state. The kinetic rate law is used at each active site to incorporate the mole balance associated with the reaction into the set of differential equations. The differential equations describing state occupancy by OAA, combined with an assumption of zero initial occupancy, represents an initial value problem that is solved using the initial value problem solver `solve_ivp` from the Python package `SciPy`[127]. The output of `solve_ivp` is a prediction of state occupancy as a function of time.

2.2.1 State Transition Probability and the Network

The transition probability matrix, T_{P}, was generated as described by Xie et al[26]. Briefly, 400,000 MD frames were summarized by the distance between the intermediate and the four active sites, and the intermediate distance to the surface. These frames were clustered into 500 micro-states (or states, used interchangeably). The Python package PyEMMA was then used to calculate the transition probability matrix, T_{P}[128].

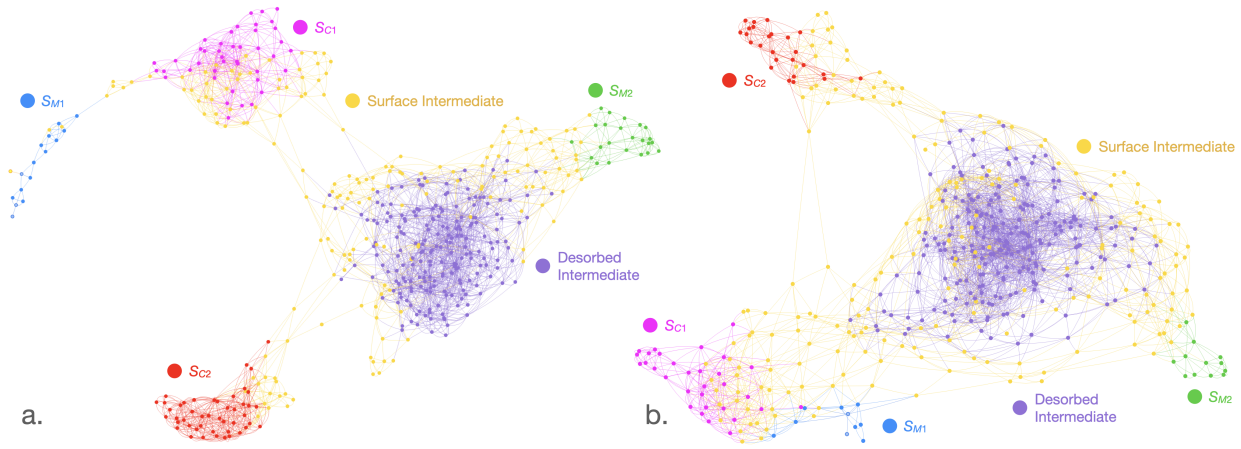

Figure 2.3: Connectivity of the 500 states in the Markov state network for (a) Recombinant and (b) Mutant complex, as defined by the transition probability matrix, T_{P}. Image generated using pyvis[130].

The 500 states are further divided into six basins. Network representations of the transition matrices for the recombinant and mutant complexes are shown in Figure 2.3. Only connections between states where the transition probability is non-zero are shown. The nodes are color-coded according to the basin to which they belong. The probability of remaining in the same state is not represented. This graph was produced using the Python packages NetworkX and pyvis[129,130].

Of the six basins shown in Fig. 2.3, four represent active sites. The active site basins on MDH are named S_{M1} and S_{M2}, and the CS basins are named S_{C1} and S_{C2}. A fifth basin represents OAA desorbed from the surface. A final basin collects states that are neither in the active site basins nor desorbed, denoted as "Surface Intermediate"[26].

2.2.2 System of Equations

The transition probability matrix, T_{P}, is converted to a transition rate matrix, T, according to[126]:

$$T = \frac{T_{\mathrm{P}} - I}{\tau} \tag{2.1}$$

where I is an identity matrix of equal dimension to T_P and τ is a sufficiently small transport time constant such that T_P may be considered a stochastic matrix[126]. Xie et al. determined

a sufficiently small transport time constant, τ, for MDH-CS to be 10 ps[26]. Analysis of the effect of time scale on lag time demonstrates that lag time calculations are unaffected by a τ of up to 100 ns (Appendix A, Figure A.2). Here we assume $\tau = 100$ ns to minimize the time scale difference between surface transport and other phenomena without affecting the lag time. This assumption increases computational efficiency and minimizes problem stiffness, or the need for very small time steps to obtain a smooth solution, by decreasing the difference between transition and reaction time scales. Using the transition rate matrix, the mole balances for the set of states, θ, generally take the form:

$$\frac{d\theta}{dt} = T\theta + r_{\text{rxn}} + r_{\text{ads}} - r_{\text{des}} \tag{2.2}$$

The time-dependent occupancy array, $\theta(t)$, describes the probability that each state is either occupied by OAA ($0 < \theta_i(t) \leq 1$) or vacant ($\theta_i(t) = 0$) as a function of time. Initially, we assume that there is no OAA in the system, $\theta_i|_{t=0} = 0$.

The r_{rxn} term in Eq. 2 represents the rate of OAA generation or consumption via enzymatic reaction, described below. For nodes in the surface or desorbed basins, there is no generation or consumption, so $r_{\text{rxn}} = 0$. At MDH basin nodes, the production of OAA is represented by a reversible reaction rate law. At CS basin nodes, OAA consumption is controlled by an irreversible rate law. The terms r_{ads} and r_{des} represent the intermediate adsorption rate to and desorption rate from bulk concentration, also described below.

The rates of production and consumption of OAA are calculated by rate laws defined at each active site basin. At MDH, OAA can be both produced and consumed. The forward rate of OAA generation, $r_{\text{MDH,f}}$, follows bi-bi kinetics:

$$r_{\text{MDH,f}} = \frac{k_{\text{cat,MDHf}} C_{\text{NAD}^+} C_{\text{L-malate}}}{K_{\text{iNAD}^+} K_{\text{L-malate}} + K_{\text{L-malate}} C_{\text{NAD}^+} + K_{\text{NAD}^+} C_{\text{L-malate}} + C_{\text{NAD}^+} C_{\text{L-malate}}} \tag{2.3}$$

Because $r_{\text{MDH,f}}$ is independent of OAA concentration, this rate represents a zeroth-order rate law in C_{OAA}. The maximum turnover frequency of malate to OAA is $k_{\text{cat,MDHf}}$. The Michaelis Menten constants of the two substrates are $K_{\text{L-malate}}$ and K_{NAD^+}. The enzyme interaction parameter of NAD^+ is K_{iNAD^+}. These parameters are specific to the forward

reaction at MDH and are defined in Table A.1 (Appendix A). Concentrations of substrate L-malate and NAD^+ are provided in Table A.2 (Appendix A).

The reverse reaction rate by which OAA is consumed at MDH, $r_{\mathrm{MDH,r}}$, is also defined by bi-bi kinetics:

$$r_{\mathrm{MDH,r}} = \frac{k_{\mathrm{cat,MDHr}} C_{\mathrm{NADH}} C_{\mathrm{OAA}}}{K_{\mathrm{iNADH}} K_{\mathrm{OAA}} + K_{\mathrm{OAA}} C_{\mathrm{NADH}} + K_{\mathrm{NADH}} C_{\mathrm{OAA}} + C_{\mathrm{NADH}} C_{\mathrm{OAA}}} \tag{2.4}$$

The maximum turnover frequency of OAA back to malate is $k_{\mathrm{cat,MDHr}}$. The Michaelis Menten constants of the two substrates are K_{OAA} and K_{NADH}. The enzyme interaction parameter of NADH is K_{iNADH}. These parameters are specific to the reverse reaction at MDH and are defined in Table A.1 (Appendix A). OAA concentration is initially zero, and accumulation is tracked over time. In the experiments, the initial concentration of NADH is zero, and NADH accumulation is not reported[16]. For this reason, when modeling experimental results, we assume a fixed $C_{\mathrm{NADH}} = 0\ \mu M$.

The combined rate of all MDH sites is given by the difference between $r_{\mathrm{MDH,f}}$ and $r_{\mathrm{MDH,r}}$, and the contribution of each MDH state, accounting for the total enzyme concentration, $C_{\mathrm{MDH-CS}}$, is given by:

$$r_{\mathrm{rxn,MDH}} = \frac{r_{\mathrm{MDH,f}} - r_{\mathrm{MDH,r}}}{C_{\mathrm{MDH-CS}} N_{\mathrm{MDH}}} \tag{2.5}$$

where the total number of states in the two MDH active site basins is represented by N_{MDH}.

The consumption of OAA at CS is described by an applicable rate constant determined from bi-bi kinetics in Bulutoglu's work and reduced to Michaelis Menten kinetics for constant C_{aCoA}[16]. The resulting expression is:

$$r_{\mathrm{CS}} = \frac{k_{\mathrm{cat,CS}} * C_{\mathrm{aCoA}}}{K_{\mathrm{aCoA}} + C_{\mathrm{aCoA}}} \sum_{CS} \theta \tag{2.6}$$

where the maximum turnover frequency of OAA at CS, $k_{\mathrm{cat,CS}}$, and Michaelis Menten constant, K_{aCoA}, are provided in Table A.1 (Appendix A). The concentration of acetyl-Coenzyme A (C_{aCoA}) is provided in Table A.2 (Appendix A). Like the MDH states, the

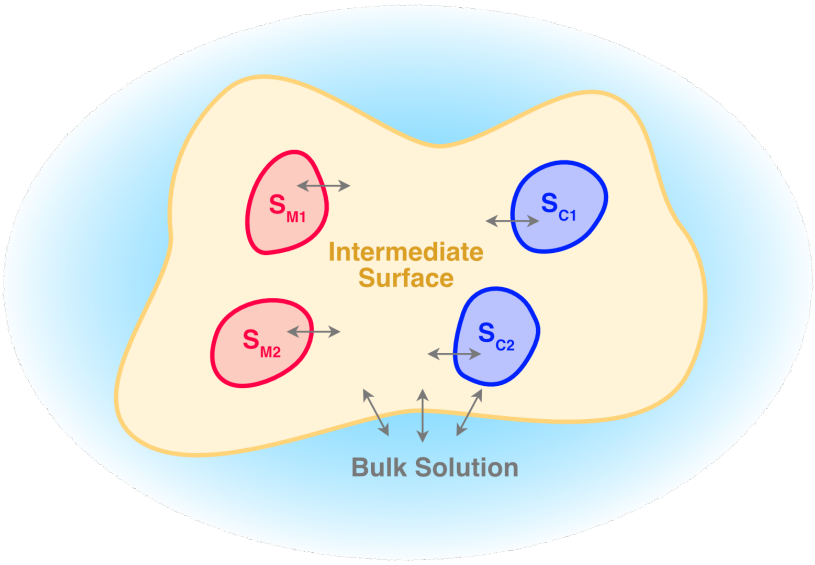

Figure 2.4: Diagram of modified surface network and homogenous bulk interactions.

overall rate law is evenly divided amongst the CS states, numbering to N_{CS}, as:

$$r_{\mathrm{rxn,CS}} = -\frac{r_{\mathrm{CS}}}{N_{\mathrm{CS}}} \tag{2.7}$$

This work uses two approaches to describe the relationship between channeling and desorption. The first utilizes the network directly to account for the transition between the surface and desorbed basins. In this case, the rate terms for adsorption, r_{ads}, and desorption, r_{des}, in Eq. 2.2 are zero, as adsorption and desorption are already considered in the transition rate matrix, T. The second approach considers a single, homogenous bulk concentration instead of a desorbed basin. Interaction between the remaining surface network and the bulk is determined based on surface-bulk terms in the transition matrix. This modification is described in the diagram of Figure 2.4.

Variable adsorption scaling is considered, wherein rate terms for adsorption, r_{ads}, and desorption, r_{des}, describe the state-specific interaction between the surface network and the bulk. However, the adsorption rate constants are scaled by a factor, K_{ads}. These terms are calculated from the transition matrix such that:

$$r_{\mathrm{des},i_{\mathrm{surface}}} = k_{\mathrm{des},i_{\mathrm{surface}}} \cdot \theta_{i_{\mathrm{surface}}} \tag{2.8}$$

$$r_{\text{ads},i_{\text{surface}}} = k_{\text{ads},i_{\text{surface}}}(1 - \theta_{i_{\text{surface}}})\frac{C_{\text{OAA,bulk}}}{C_{\text{MDH-CS}}} \tag{2.9}$$

$$k_{\text{des},i_{\text{surface}}} = \sum_{j_{\text{desorbed}} i \neq j} T_{i_{\text{surface}} j_{\text{desorbed}}} \tag{2.10}$$

$$k_{\text{ads},i_{\text{surface}}} = \frac{1}{K_{\text{ads}}} \sum_{i_{\text{surface}} i \neq j} T_{i_{\text{surface}} j_{\text{desorbed}}} \tag{2.11}$$

In the MSM network model, the bulk concentration of OAA intermediate, $C_{\text{OAA, desorbed}}$, is calculated from the occupancies of nodes in the desorbed basin, $\theta_{i_{\text{desorbed}}}$:

$$C_{\text{OAA,desorbed}} = C_{\text{MDH-CS}} \sum_{i_{\text{desorbed}}} \theta_{i_{\text{desorbed}}} \tag{2.12}$$

In the homogenous bulk model (Fig. 2.4), an additional material balance is required for the bulk concentrations of OAA intermediate, $C_{\text{OAA, bulk}}$, which is dependent on the net rate of desorption of OAA from the surface as:

$$\frac{dC_{\text{OAA,bulk}}}{dt} = C_{\text{MDH-CS}} \sum_{i_{\text{surface}}}^{N_{\text{surface}}} \left(r_{\text{des},i_{\text{surface}}} - r_{\text{ads},i_{\text{surface}}} \right) \tag{2.13}$$

The production rate of CoA is taken by summing the OAA occupancy in all states of both CS active sites. This leads to an additional material balance for product CoA equivalent to r_{CS} in Eq. 2.6:

$$\frac{dC_{\text{CoA}}}{dt} = r_{\text{CS}} \tag{2.14}$$

The system of differential equations to be solved numerically consists of mole balances for each of the 500 micro-states, a mole balance for CoA, and, in the case of the homogenous bulk model (Fig. 2.4), a mole balance for OAA.

2.2.3 Numerical Solution

To solve the system with `solve_ivp`, a function containing the system of differential equations, the initial θ matrix, and the time span are required inputs. The implicit Runge-Kutta method, 'Radau', was chosen to overcome the problem stiffness efficiently[127]. The system of equations is solved by assuming zero presence of OAA or CoA as the initial condition. A repository is available detailing the calculation of concentration profiles and lag times for the homogenous bulk model with fixed adsorption scaling[131].

2.2.4 Lag Time Calculation

Lag time is determined by fitting the final 30% of the CoA concentration profile to a linear function. CoA concentration profiles were predicted for a time span of 40 seconds to ensure that the system achieves steady state within the lag time window. When the CoA concentration profile is curve fit with a slope, m, and y-intercept, b, the concentration of product will be zero at the lag time. The lag time, t_ℓ, is thus calculated as:

$$t_\ell = -\frac{b}{m} \tag{2.15}$$

The lag time, t_ℓ, can also be estimated from the transport efficiency, α, as[20]:

$$t_\ell = t_{\ell 0}(1-\alpha) \tag{2.16}$$

where $t_{\ell 0}$ is the lag time of the uncomplexed, free enzymes. Details on the calculation of free enzyme lag times are provided in the Supplementary Information. Eq. 2.16 was used in our previous work to predict lag times from estimated transport efficiency.[26] It is worth noting that Eq. 2.16 is derived assuming that the enzyme kinetics are pseudo-first order[20]. The pseudo-first-order assumption is valid if the bulk OAA concentration is substantially smaller than the applicable Michaelis Menten constant. For recombinant and mutated free enzymes, the steady-state concentration of bulk OAA is on the order of 1 to 10 μM (Fig. A.1). The applicable Michaelis Menten constant for both complexes is in a similar range (Table A.1). Therefore, pseudo-first-order kinetics cannot be assumed for this system, and the approach

described in this work represents a potential improvement over Eq. 2.16.

2.3 Results and Discussion

The Markov state transition matrix of Xie et al.[26] was combined with the kinetic data obtained by Bulutoglu et al.[16] to produce a transient finite difference model that predicts the prevalence of OAA intermediate molecules on the surface of the MDH-CS complex and in the bulk. The model also calculated transient product CoA concentrations that, once the reaction reached a steady state, were used to calculate the lag time for the overall reaction. The model is applied to conditions wherein both electrostatic channeling and desorption occur. First, the Markov state network (Fig. 2.3), describing the transition between the five surface basins and the desorbed basin, is applied with catalytic reactions occurring at the active site basins. Then, the system is modified to treat the desorbed basin as a single homogenous state with variable concentration. We study the effect of scaled adsorption rate constants to mimic a variable adsorption equilibrium coefficient. We then study the flux through individual transport paths for fixed adsorption rate scaling. Finally, we assess the implications of reversible kinetics at MDH of the recombinant complex under channeled and free enzyme conditions as a function of fixed NADH concentration.

2.3.1 Transport analysis using the Markov state model

To analyze intermediate transport in the complex system, we first employ the Markov state model using the connectivity matrix, T, between surface and desorbed states, as illustrated in Fig. 2.3 for the recombinant and mutant complexes. The resulting CoA and OAA concentration profiles compared to experiment are shown in Fig. 2.5.

When the Markov transition matrix, T, is utilized directly to model transport, the cascade displays near-perfect channeling ($t_\ell \approx 0$ s) for both the mutant and recombinant complexes. Due to fast intermediate transport within the network via both the surface and desorbed basins, the concentration of desorbed OAA (Eq. 2.10) remains near zero. Consequently, no lag time is observed before achieving a steady state.

Previously, Xie et al. predicted an intermediate transport efficiency of 96% for the recom-

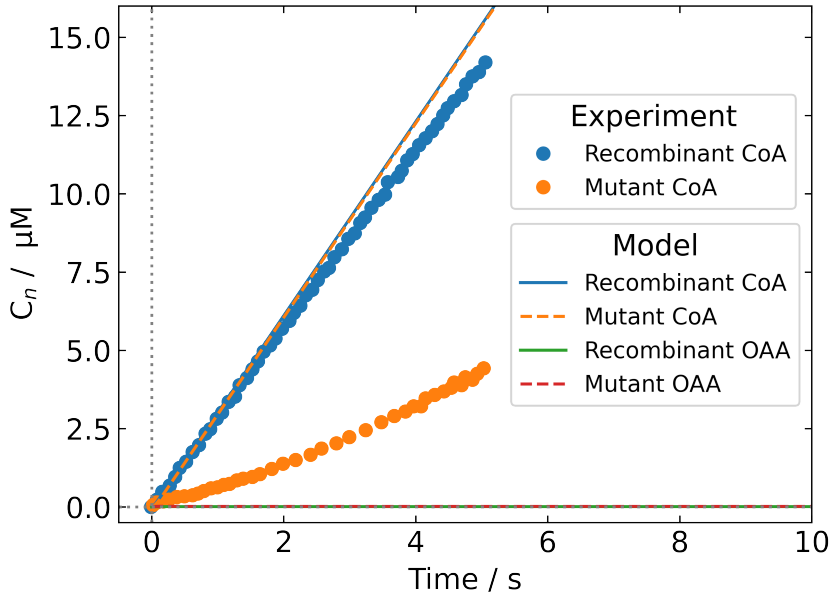

Figure 2.5: Citrate and OAA concentration profiles for the mixed channeling cascade using the network and combined with reaction rate laws.

binant complex but only 47% for the mutant. Based on Eq. 2.16, the lag times associated with Xie's efficiency predictions are 0.24 s and 1.71 s for the recombinant and mutant, respectively (Table 2.1). The unmodified MSM model matches the short lag times of the experiment and Xie's prediction for the recombinant complex, but disagrees with the long lag times for the mutant. This is because transport via the bulk basin of the network does not introduce any time lag. In contrast, Xie's analysis assumed that any intermediate lost to the bulk was lost entirely, introducing significant lag time. To bridge this disagreement, we must, at minimum, add capacitance to the bulk solution that will slow transport through the bulk. This might be expected to increase the lag time of the mutant without affecting that of the recombinant.

2.3.2 Homogenous Bulk Model

To enhance differentiation of transport characteristics between the recombinant and mutant complexes, we modify the network to replace the nodes of the desorbed basin with a single homogenous bulk concentration, $C_{\mathrm{OAA,bulk}}$. The desorption rate constants (Eq. 2.10) describe the interaction between the surface and bulk. Adsorption is considered via a variable

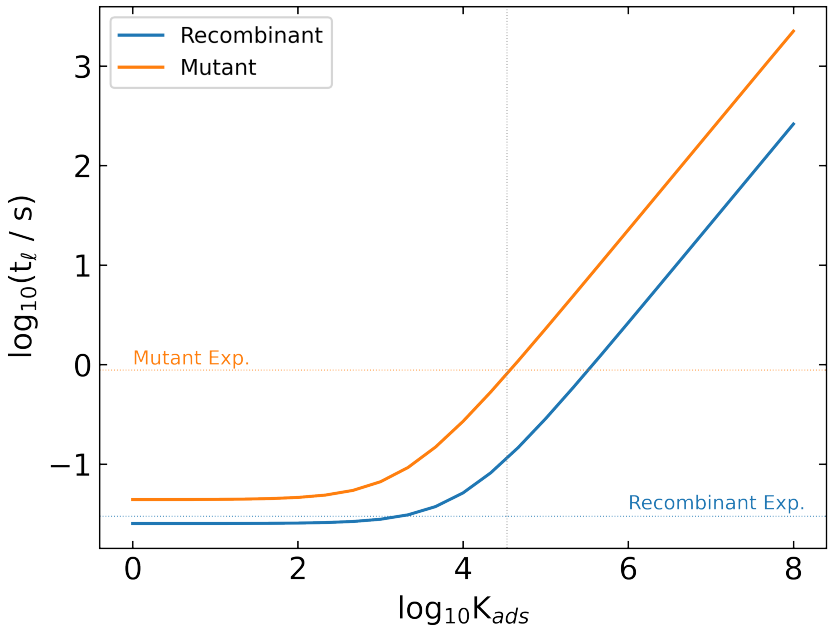

Figure 2.6: Recombinant and Mutant lag times for a range of K_{ads} values. Experimental lag times are marked by horizontal dashed lines and the optimized K_{ads} value is marked by a vertical line.

adsorption scaling (Eq. 2.11). Adsorption scaling factors from the network ($K_{\text{ads}} = 1$) may not capture the energy barrier for OAA to exit the surface to the bulk. Instead, we find a fixed adsorption scaling factor to scale adsorption and capture a more realistic barrier in the desorption of OAA.

2.3.2.1 Effect of Adsorption Scaling Factor, K_{ads}

Lag times for adsorption scaling factor, K_{ads}, ranging from 1 to 10^8 were calculated for both recombinant and mutant complexes. Adsorption rate constants that are defined directly by the transition rate matrix, T, are represented by $K_{\text{ads}} = 1$. However, this results in low lag times that do not exploit the channeling differences between the recombinant and mutant. By increasing the value of K_{ads}, as shown in Fig. 2.6, larger observed lag times and more significant differentiation in lag time between the recombinant and mutant complexes are observed.

The optimal value of K_{ads} is determined by minimizing the total absolute error between experimental and modeled lag times. The point of minimal error exists at a $K_{\text{ads}} = 3.4 \times 10^4$,

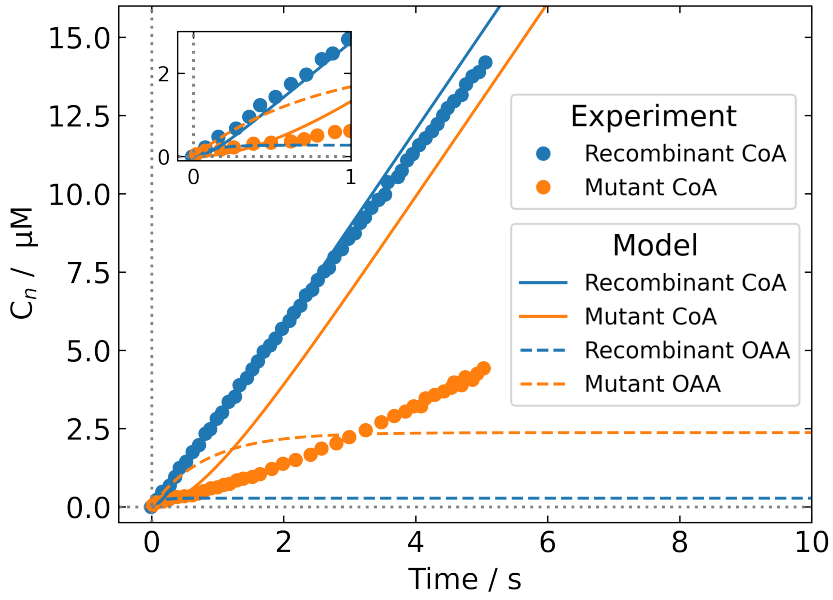

Figure 2.7: Citrate and OAA concentration profiles for the mixed channeling cascade using the bulk concentration model for $K_{\text{ads}} = 3.4 \times 10^4$. The inset figure displays the concentration curves at experiment time less than 1 second.

shown in Fig. 2.6 as a vertical line. This value is assumed in the definition of $k_{\text{ads},i_{\text{surface}}}$ (Eq. 2.11) for the remainder of the analysis.

In our previous work, surface adsorption between enzyme active sites was calculated from an assumed desorption rate constant and an adsorption equilibrium coefficient[7,27]. There, the adsorption equilibrium coefficient ranged from approximately 10^3 to 10^5. Practically, an adsorption equilibrium coefficient scales the adsorption rate constant relative to desorption rate constants in the same fashion as we consider here with a scaling factor.

Assuming a constant adsorption scaling factor, $K_{\text{ads}} = 3.4 \times 10^4$, recombinant and mutant complex behaviors are predicted by OAA and CoA concentration profiles. The simulated concentration profiles are compared to experimental CoA concentration profiles in Fig. 2.7.

Here, the predicted CoA concentration profiles, and resulting lag times, of the modeled complexes are comparable to the experimental outcomes. The recombinant complex model displays faster accumulation of CoA and a lower lag time than the mutant model. The modeled recombinant CoA profile exhibits a steady-state accumulation rate that is similar to the experimental result. However, the mutant's modeled CoA profile only matches the experiment initially ($<$ 1s, Fig. 2.7 inset) but continues accumulating CoA faster than the

experimental counterpart. The steady-state rate of CoA accumulation for the mutant model matches that of the recombinant, as expected because the rate of CoA accumulation depends solely on the MDH reaction rate and is the same ($r_{\mathrm{MDH}} = 3.1\mu\mathrm{M\ s}^{-1}$) for both complexes.

The second key observation is that, in this case, the modeled mutant complex exhibits a higher bulk OAA concentration than the recombinant complex (Fig. 2.7, dashed lines). When operating with $C_{\mathrm{NADH}} = 0\ \mu M$, MDH is operating with a constant velocity, $r_{\mathrm{rxn,MDH}}$ (Eq. 2.5). At these conditions, the steady-state bulk concentration of OAA is proportional to the lag time[20]:

$$t_\ell = \frac{C_{\mathrm{OAA,\ bulk}|\mathrm{steady\ state}}}{r_{\mathrm{rxn,MDH}}} \tag{2.17}$$

Thus, higher bulk OAA concentrations, indicating a greater probability of desorption, lead to longer lag times.

2.3.3 Lag Time Analysis of Recombinant and Mutant MDH-CS

The two extreme cases of (1) enzyme complex with perfect channeling, and (2) free enzymes with no channeling, define the range of lag times that can be expected for each complex, as detailed in Table 2.1. Based on efficiencies predicted by Xie et al., the recombinant lag time should be close to zero, matching the experimental data[16,26]. For the mutant complex, lag time is expected to fall about halfway between the free enzyme and perfect channeling values.

Table 2.1: Recombinant and Mutant Lag Times.

	Recombinant Lag Time, t_ℓ / s	Mutant Lag Time, t_ℓ / s
Experimental[16]	0.03 ± 0.01	0.88 ± 0.06
Free Enzymes[16]†	2.5	0.9
MSM model[26]‡	0.24	1.71
MSM Network Model	0.025 ± 5e-13	0.044 ± 4e-12
Homogenous Bulk Model	0.11 ± 1e-10	0.81 ± 5e-9

†Predicted from kinetic data ‡ Calculated using Eq. 16

When considering adsorption and desorption only as defined by the MSM, a pseudo-perfect channeling case is found in which both complex models exhibit very low lag times (Fig. 2.5). By scaling the adsorption rate constants to minimize absolute lag time errors,

a mixed channeling case is found. In this case, the model predicts a substantially lower lag time for the recombinant than the mutant. This observation aligns with the findings of our previous work and experiment[16,26].

2.3.4 Path Lag Time Analysis

The existence of four active sites, two for each enzyme, suggests four possible paths by which OAA can traverse the surface. Considering OAA source sites on MDH, S_{M1} and S_{M2}, and the OAA consumption sites on CS, S_{C1} and S_{C2}, the paths can be labeled as described previously by Xie et al.: Path 1: $S_{M1} \rightarrow S_{C1}$, Path 2: $S_{M1} \rightarrow S_{C2}$, Path 3: $S_{M2} \rightarrow S_{C1}$, Path 4: $S_{M2} \rightarrow S_{C2}$[26].

The present model includes reaction kinetics at each active site, allowing us to use the model to estimate lag time and, therefore, reaction efficiency for each path. These can be calculated by zeroing the reaction rate at inactive sites. Xie et al. did not calculate individual path efficiencies directly, but the efficiencies of each OAA-producing active site were explored. Here, the parallel operation of paths for sites S_{M1} and S_{M2} are assessed in addition to the study of individual paths.

Transport of OAA from site S_{M1} was predicted by Xie et al. to result in higher transfer efficiency than from S_{M2}[26]. Therefore, Paths 1 and 2 are expected to be more efficient and have lower lag times than Paths 3 and 4. The lag times for each path are compared against the overall models and the origination sites, S_{M1} (Paths 1+2) and S_{M2} (Paths 3+4) as provided in Fig. 2.8. The results in Fig. 2.8 suggest minimal variation exists among the individual paths of the recombinant, and the mutant is much more sensitive to the reaction path. Although there is not much difference between the individual paths of the recombinant, the parallel operation of Paths 1 and 2 results in slightly lower lag times than the parallel operation of Paths 3 and 4. Opposite trends are observed in the mutant. Parallel operation of two paths overcomes the decreased efficiency observed for individual Paths 2 and 4, as shown by much higher lag times for Paths 2 and 4 compared to Paths 1 and 3.

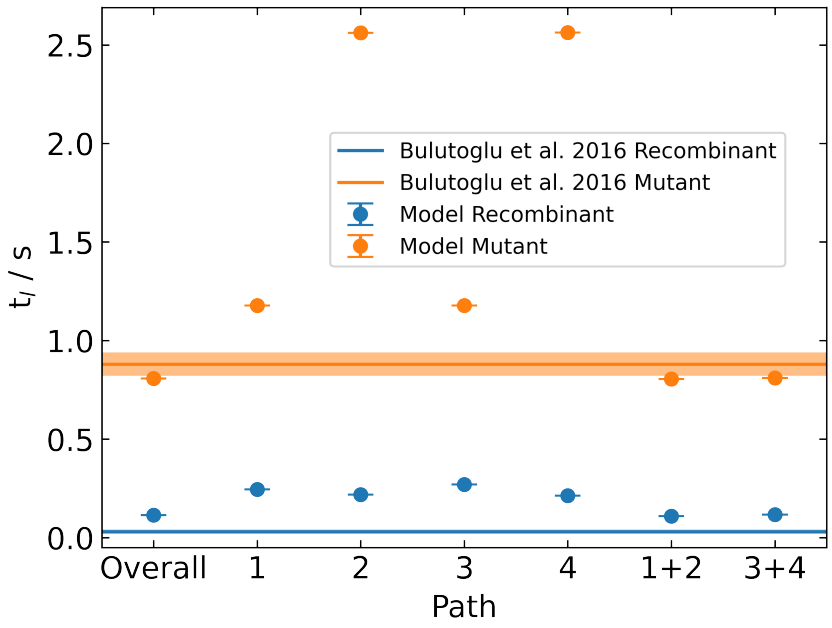

Figure 2.8: Overall complex and path lag times. Error clouds represent the experimental uncertainty in lag times as reported by Bulutoglu et al[16]. Model lag time uncertainties are determined by slope and y-intercept fit error propagation through Eq 2.15. Model results show uncertainty in lag time (vertical axis) and are very small.

2.3.5 State Occupancy Observations

In addition to determining the time to steady state, the numerical model can predict locations of OAA buildup and transport at steady state conditions. Channeling efficiency can be further explored by comparing the amount of bulk, or desorbed, OAA to the amount in the five surface basins. It is important to note that in these analyses, basins and paths can have occupancy greater than unity because each basin has tens of nodes. Therefore, the total occupancy of each basin can have a value up to the number of nodes.

2.3.5.1 Basin Occupancy

To understand the tendency of OAA to transport on the surface versus desorbing off the surface near MDH active sites and adsorbing on to or near CS active sites, the proportionality of basin occupancy can be compared. The steady-state occupancy of each basin for both complexes is provided in Figure 2.9. Less OAA remains on the surface for the recombinant complex than for the mutant complex. The mutant complex has a downstream turnover

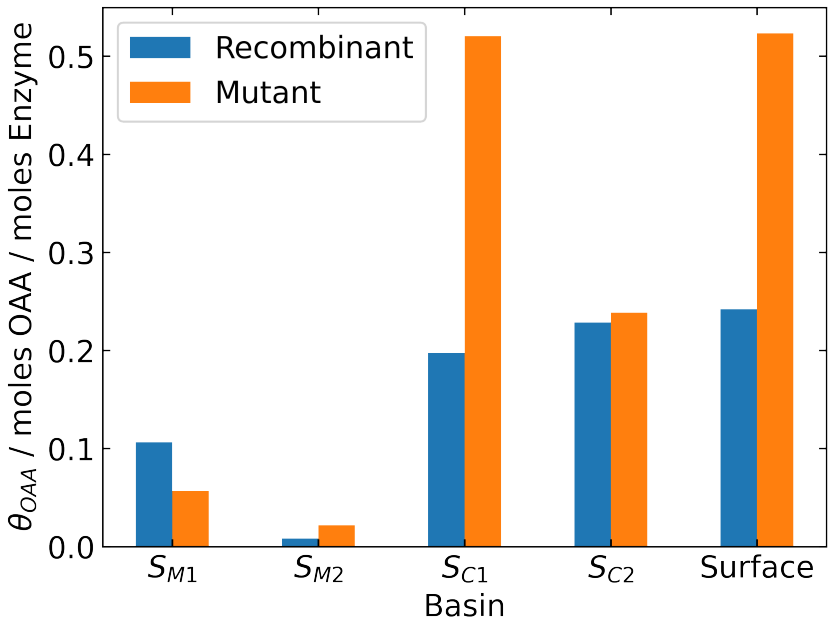

Figure 2.9: Recombinant and Mutant Basin Occupancy by OAA at steady state conditions.

frequency, $k_{\text{cat,CS}}$, half that of the recombinant (Table A.1), so there is expected to be more OAA buildup on that complex. The higher amounts of OAA in CS sites than MDH sites indicate efficient transport.

2.3.5.2 Path Occupancy

The relative channeling efficiency of paths can be elucidated by comparing steady-state total surface occupancy, or path occupancy, and bulk OAA concentrations with only desired active sites "turned on" (Eqs. 2.13 and 2.17).

The total surface occupancy of each path is shown in Figure 2.10a. For the recombinant complex, the amount of OAA on Paths 1 and 2 is lower than on Paths 3 and 4 and is consistent with the expectation that the M1 site is more efficient. The mutant complex has the lowest occupancy on Path 1, followed closely by Path 3. Paths 2 and 4 have nearly double the occupancy. The effect of the reaction path is more distinguishable for the mutant and supports the hypothesis that Path 1 is the most efficient of the four paths. Paths 3 and 4 have higher occupancy than Paths 1 and 2, and indicate higher efficiency of S_{M1} than S_{M2}. The occupancy of dominant trajectories on each path is also assessed in Appendix A (Fig. A.3).

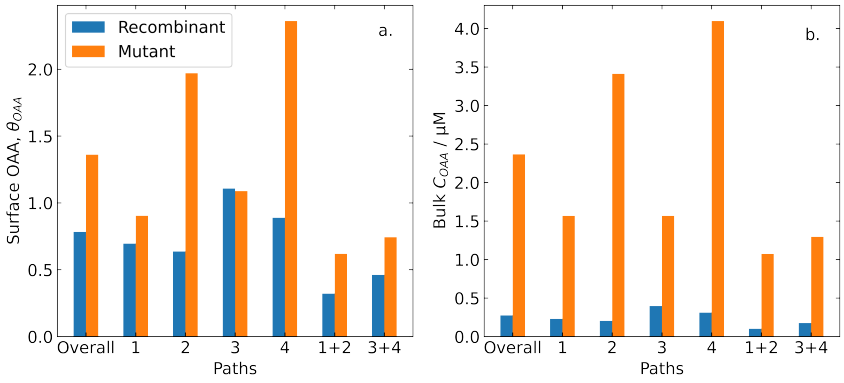

Figure 2.10: Recombinant and Mutant Path Surface Occupancy at steady state by (a) OAA and (b) Path Bulk OAA Concentration.

The bulk OAA concentration resulting from individual activation of each path (Fig. 2.10b) follows a similar trend to that of surface occupancy (Fig. 2.10a). For the recombinant, Paths 1 and 2 generate lower bulk OAA concentration than Paths 3 and 4. The mutant generates comparable concentrations for Paths 1 and 3, which have lower bulk OAA concentrations than either Paths 2 or 4. For all paths, substantially increased bulk OAA concentration was observed for the mutant complex compared to the recombinant, which aligns with previous desorption probability observations[26].

Combining the bulk OAA concentration observations with those of the surface occupancy, the recombinant complex transforms OAA to CoA more efficiently than the mutant, indicated by lower operating concentrations of OAA for the recombinant complex. Transport in the recombinant complex is more sensitive to the origination site than the particular path. Transport in the mutant is most sensitive to the OAA consumption site and is most efficient with Path 1. The effect of the reaction path is most visible on the mutant, confirming Path 1 as the most efficient.

2.3.6 Reversible Kinetics at MDH

The impact of reversible kinetics at MDH is explored for the recombinant complex in channeling and free enzyme conditions. A non-zero, fixed concentration of bulk NADH, C_{NADH}, is specified, representing the ambient condition. In Fig. 2.11, results for the channeled complex are shown in comparison to the free enzymes as a function of bulk NADH concentration,

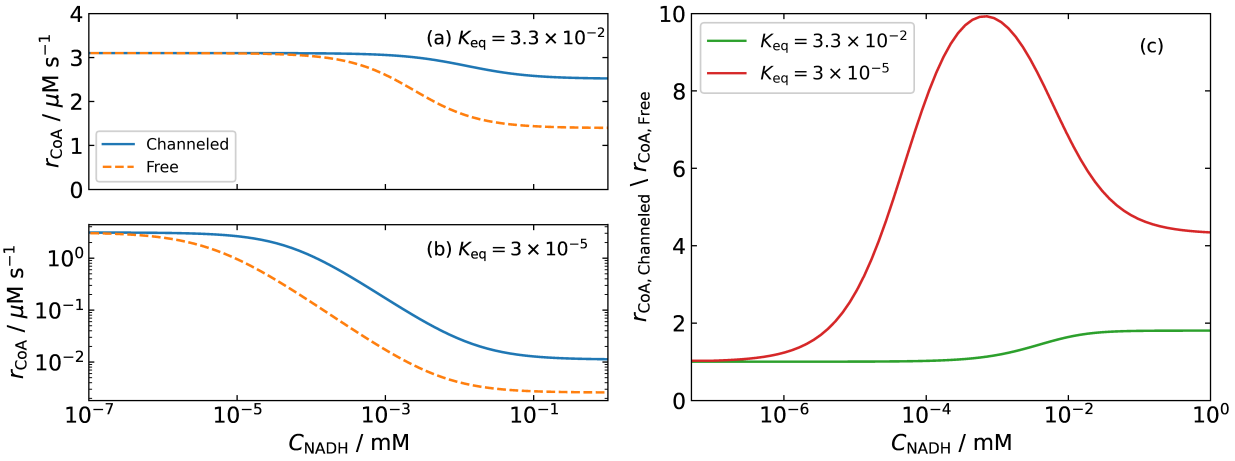

Figure 2.11: Steady state rate of CoA production as a function of fixed NADH concentration for reversible kinetics at MDH. (a) $K_{eq} = 3.3 \times 10^{-2}$, derived from data of Bulutoglu et al[16]. (b) $K_{eq} = 3 \times 10^{-5}$, derived from data of Guynn et al[119]. (c) Amplification factor of CoA generation rates in channeled versus free enzyme conditions.

C_{NADH}, for two values of the NADH equilibrium coefficient, K_{eq}, defined as:

$$K_{eq} = \frac{k_{cat,MDHf}}{k_{cat,MDHr}} \tag{2.18}$$

The case of $K_{eq} = 3.3 \times 10^{-2}$ (Fig. 2.11a), arises from the kinetic values reported by Bulutoglu et al., as listed in Appendix A Table A.1[16]. The case of $K_{eq} = 3 \times 10^{-5}$ is taken from data reported by Guynn et al[119].

In the absence of NADH, represented by the extreme left of Fig. 2.11a-b, the channeled and free enzyme systems produce CoA at the same rate. In the absence of NADH, equivalent rates for channeled and free systems are expected since the reverse reaction at MDH is inactive. At high concentrations of NADH, a constant amplification factor due to channeling is observed (Fig 2.11c) that is independent of C_{NADH}. This amplification increases with K_{eq}, being 1.8 for $K_{eq} = 3.3 \times 10^{-2}$ and 4.3 for $K_{eq} = 3 \times 10^{-5}$. At moderate values of C_{NADH}, reaction rates for both the complex and free enzymes decrease with increasing C_{NADH}, and the amplification factor increases from 1 to its high-concentration value. In the case of the low value of K_{eq}, however, the free enzyme rate decreases more rapidly, and a maximum amplification near 10 arises at an intermediate NADH concentration ($C_{NADH} \approx 0.2$ μM). This intriguing result is likely due to the interplay between electrostatic channeling and the

detailed kinetics at each active site, and will be the subject of future study. In all cases, however, the channeled system's production rate exceeds that of the free enzyme system, demonstrating the impact of channeling in enzyme systems with reversible kinetics.

2.4 Conclusion

In this work, the dynamics of intermediate channeling in the malate dehydrogenase citrate synthase (MDH-CS) complex is modeled using a finite difference approach applied to a Markov state model. The model predicts lag times for the recombinant and mutant complexes of approximately 0.11 seconds and 0.81 seconds, respectively, by assuming a fixed adsorption scaling. These lag times are comparable to their experimental counterpart. Additionally, we explore details of the transport mechanism on the surface through analysis of specific active sites and paths. The recombinant complex was found to have comparable efficiency across the individual paths as marked by similar lag times of the origination site to the overall and amongst individual paths. Transport through the mutant was insensitive to the OAA origination site but exhibited more significant variation in efficiency in the separate paths.

Analysis of surface occupancy identifies Path 1 as the preferred and most efficient path. The recombinant complex's greater efficiency than the mutant is due to its higher preference for Path 1. In contrast, the mutant has a more distributed preference across the paths and an observed tendency to leak OAA. Finally, considering reversible kinetics at the MDH active site, the complex employing electrostatic channeling is demonstrated to be significantly less sensitive to the presence of reaction product NADH than the free enzyme.

The transient model reported here quantitatively relates complex structures to intermediate transport within cascade reactions. While the connectivity network established by the Markov state model enables the model, building the MSM is computationally intensive. Expanding these methods to other biocatalytic cascades may elucidate the generalized behavior of similar systems, allowing for dynamic and rapid prediction of reaction cascade dynamics.

Chapter 3

Quantum Chemical Insight into Electrochemical Upgrading of Bio-oil

3.1 Introduction

With threats of global warming and diminishing supplies of fossil fuels, there exists a strong need for sustainable energy and chemical production.[1] Although alternative energy technology has advanced, society continues to rely on fossil energy supplies.[47] Alternatively, renewable biomass represents a sustainable resource for organic fuels and value-added chemicals. The use of pyrolytic bio-oils derived from plant-based lignocellulosic biomass is a developing option for replacing fossil fuels.[4,47] However, bio-oil, made from lignocellulosic biomass via fast pyrolysis, is highly oxygenated, which leaves it chemically unstable and low in energy density.[48] Recent experimental work and system analysis suggests that electrochemically upgrading bio-oils by hydro-deoxygenation can increase the stability and energy density of pyrolyzed bio-oil.[49–51,57,61,63,132–141]

A sufficient understanding of electrochemical deoxygenation for proper control and optimization requires overcoming two major hurdles. The first lies in the chemical complexity of bio-oil, comprising roughly 25% water and 25% lignin fragments, with the remainder a mix of aldehydes, carboxylic acids, carbohydrates, phenols, furans, alcohols, and ketones. Several deoxygenation/hydrogenation reaction paths can proceed simultaneously and interactively in these systems, leading to a broad selection of possible products.[61,85,132,142,143] Secondly, the electrocatalytic interface plays a large role in product reaction rate and selectivity. The interplay of these factors requires deep mechanistic examination, which, in

conjunction with validating experiments, can be exposed through atomistic and quantum simulations.[67,83,93,142,144–148]

Our previous experimental work investigated the electrochemical conversion of various bio-oil constituent molecules on both single- and mixed-metal electrocatalysts. Oxygenated aromatics, furans, and mixtures were electrocatalytically upgraded on Pt and/or Ru catalysts supported on activated carbon.[55,59,149] Mixed-metal Pt-Ru catalysts were found to improve performance as compared to single-metal catalysts in the conversion of a variety of oxygenated aromatics to cycloalkanes. Specifically, a 75/25 wt% Ru/Pt catalyst supported on activated carbon cloth (Ru/Pt/ACC) produced yields of cyclohexanes greater than 50% and nearly 100% conversion of the associated oxygenated aromatic.[59] Similarly, furfural (FF) conversion to tetrahydrofurfuryl alcohol (THFA) was favored under mildly acidic conditions with moderate yields.[55] However, low carbon mole balances were observed under all conditions, an indication of significant side reactions involving FF, intermediate furfuryl alcohol (FA), and THFA. Nevertheless, by also studying the reduction of 2-methylfuran (MF), FA, and 2-furoic acid, the activity of a Ru catalyst toward furan ring saturation was demonstrated.

Studies of single molecules informed a recent study of a binary mixture of 4-propylphenol (4-PP) and FF on a Ru/Pt/ACC electrocatalyst.[149] Here, 4-PP ECH was performed in the presence of possible inhibitors under a constant current of 60 mA and 50°C. When studied individually, 4-PP produces two major products: 4-propylcyclohexanol (4-PCOL) and propylcyclohexane (PC), in yields of 70% and 20%, respectively.[59] However, when processed in a mixture with FF, product yields are both reduced to less than 10%. Conversely, the yields of 4-PP products are relatively unaffected by the presence of other categories of bio-oil constituent molecules. To understand the factors resulting in inhibition of 4-PP electro reduction by FF and products, mechanistic understanding is required.

The previous work on experimental electrocatalytic hydrotreatment (ECH) of a binary mixture of bio-oil constituents suggests that 4-PP proceeds to 4-PCOL and PC. At the same time, FF proceeds to THFA via a FA intermediate on a Pt/Ru catalyst.[149] These pathways are consistent with other mechanisms studied in the literature.[56,68,145,150] However, FF and product molecules are known to dimerize and produce other products.[53,54] The major side

products that have been studied include the production of methylfuran (MF) from FA along with dimerization of either FF or FA to form furoin (FUI) or hydrofuroin (HF). In the work of Kasad et al., it was suspected that dimers fouled the catalyst surface so mechanistic studies should also consider these byproducts.

Density functional theory (DFT) calculations of various aspects of electrochemical hydrotreatment have been conducted for various single-molecule bio-oil constituents and catalysts. Phenolics[56,57,66,79,83–85,135,140,150–153] and furans[49,59,67,102,137,138,142,145,148,154–159] are popular models given their prevalence in bio-oil and the vast array of value-added chemicals that can be produced[52,53]. Owing to the high activity of platinum electrocatalysts, the Pt(111) surface is a common choice for these models[56,84,85,146,160–163]. More recently, ruthenium and non-precious metal catalysts such as copper and nickel have been considered in DFT models.[50,51,58,62,83,84,135,142,144,155,156] Platinum and ruthenium have both been shown to effectively catalyze the electrochemical hydrotreatment of bio-oil in DFT studies.[57,83,85,156]

This work is a follow-up computational investigation to the previous experimental study aimed at understanding the reaction mechanisms in the hydrotreatment of a furfural and 4-propylphenol mixture on a Ru/Pt electrode. This contrasts with previous works that have focused on single compounds and single metal catalysts. We utilize quantum-scale studies to explore the mechanisms by which model molecules compete in the ECH process, analyzing reaction energetics and rate-limiting steps. Adsorption energetics predicted by the model are validated against experimental results obtained by blocking of hydrogen under potential deposition (H_{upd}). These mechanistic findings suggest possible explanations for the experimentally observed outcomes.

3.2 Methods

The electrocatalytic hydrotreatment reactions of furfural (FF) and 4-propylphenol (4-PP) were assessed computationally by calculation of adsorption energies and reaction energies. The potential dependence of pathway reaction energies was additionally explored. Further, the adsorption energies of some of the molecules are verified experimentally by blocked

hydrogen adsorption on a platinum electrocatalyst under hydrogen underpotential deposition (H_{upd}) conditions.

3.2.1 Reaction Mechanism Energy Calculations

Adsorption and reaction energies are derived from optimized state energy calculations of gas phase organic molecules in vacuum, bare catalyst surfaces, and molecules adsorbed on catalyst surfaces. Each state underwent a geometric relaxation via the plane-wave package Quantum ESPRESSO (QE), version 7.2.[99,100] The Python package Atomic Simulation Environment (ASE) was used to visualize the state structures and write input files for QE calculations.[88] Input parameters were established from reported models exploring the hydrotreatment of organic molecules on platinum catalysts such as benzene on Pt(111) by Shayeghi et al.[66] and furfural on Pt(111) bimetallic surfaces by Khouini and Vahedpour.[156] The Python package PyEnergyDiagrams is used to build the relative energy diagrams.[164]

The relaxations minimized energy and force to a threshold of 0.0001 Ry and 0.001 Ry per Bohr, respectively. Core electrons were described by ultra-soft pseudo-potentials from the SSSP PBE Efficiency v1.3.0 library.[165] Valence electrons are described by Kohn-Sham wave functions expanded to a kinetic energy cutoff of 35 Ry and a charge density cutoff of 279.3 Ry. Cutoffs were selected based on the highest recommended value in the pseudo-potentials for a given atom considered. The Brillouin zone was sampled for the gamma point only for each calculation. The mixing factor for self-consistency was reduced to 0.5 for each calculation. Forces due to van der Waals interactions were corrected through Semi-empirical Grimme's DFT-D3 method[166]. Gas phase species were relaxed with one molecule centered in a 10 x 10 x 10 Å vacuum.

Regarding the bare surfaces, ruthenium is highly stable in the HCP(0001) facet, which is the only surface considered for this metal.[83] Lattice parameters a and c are set to 2.733 Å and 4.314 Å, respectively.[167–169] Platinum, however, is studied in FCC(111), (110), and (100) facets to account for its polycrystalline nature. The experimental lattice parameter of 3.92 Å is used for all platinum slabs.[85,170] Bare slab and adsorbed state structures utilize a 4x4 metal surface with 3 atomic layers. A 10 Å vacuum is placed along the z-axis above the metal surface for all calculations. After a bulk relaxation of the bare metal slab, the bottom

layer is fixed in adsorbed structure calculations to allow the top 2 layers to respond to the adsorbate presence. Fermi-surface effects are treated with Methfessel-Paxton smearing and a degauss factor of 0.1.[171]

Adsorption energies are calculated by comparing the energy of the adsorbed state to that of the bare slab and free organic molecule:

$$E_{ads} = E_{i+slab} - E_i - E_{slab} \tag{3.1}$$

where E_{i+slab} is the energy of the relaxed adsorbed structure, E_i is the energy of the organic in vacuum, and E_{slab} is the energy of the relaxed slab.

The energy of a surface reaction step is:

$$E_{rxn} = E_{FS} - E_{IS} \tag{3.2}$$

where E_{IS} is the energy of the initial state where the reactant molecule and any necessary hydrogen atoms are adsorbed to the metal surface. E_{FS} represents the final state of the adsorbed product(s).

State energies are further corrected for non-zero temperature and pressure to yield Gibbs free energies through vibrational frequency analysis.[93] In doing so, the Gibbs free energy of any state j relative to a chosen reference free energy, G_{ref}, is:

$$\Delta G_j = E_j + E_{\text{ZPE}} - T\Delta S + \Delta H_{0\to T} - G_{\text{ref}} \tag{3.3}$$

where E_j is the relaxed energy of the state such as those used in Eq. 3.1. E_{ZPE} is the zero point energy of the state and represents the vibrational modes of the state at 0K. The terms $T\Delta S$ and $\Delta H_{0\to T}$ represent the change in entropy and enthalpy, respectively, when increasing the temperature to any point above 0K. The reference Gibbs free energies, G_{ref}, for the FF and 4-PP pathways are:

$$G_{\text{ref,FF}} = G_{\text{FF(g)}} + 3G_{\text{H}_2\text{(g)}} + G_{\text{bare slab}} \tag{3.4}$$

$$G_{\text{ref,4PP}} = G_{\text{4PP(g)}} + nG_{\text{H}_2\text{(g)}} + G_{\text{bare slab}} \tag{3.5}$$

where n equivalents of H_2 are considered to represent the maximum number of protons required for the pathways. When 4PP is reduced to 4PCOL, three equivalents of H_2 are consumed, and 3.5 equivalents are consumed when 4PP is reduced to PC.

Vibrational modes and frequencies were calculated for the preferred adsorption configurations via the QE package PHonon.[99,100] The thermochemistry module of ASE was utilized to process the set of vibrational frequencies of each image and calculate E_{ZPE}, $T\Delta S$, and $\Delta H_{0\rightarrow T}$.[88] Gas phase corrections are calculated with the IdealGasThermo function and adsorbed state corrections are calculated by the HarmonicThermo function. The calculations are executed with a pressure of 101,325 Pa and a temperature of 293.15 K, respectively.

3.2.2 Determination of Preferred Adsorption Configurations

Molecules can adsorb on surfaces in multiple configurations. For aromatic molecules, these configurations can be defined by the placement of the ring center in hollow, atop, and bridge configurations. With each ring configuration, the molecules are rotated about the axis perpendicular to the surface to consider the substituent group(s) placement. The configuration of each molecule on each surface with the lowest adsorption energy is considered the preferred geometry. For example, FF is placed onto Pt(111) with 2 aldehyde configurations for each ring configuration, resulting in 8 unique possible adsorption configurations. Of the 8 configurations, the one with the lowest adsorption energy is the preferred geometry. This method was applied to FF and 4-PP on each facet. Adsorbed intermediates and products were relaxed from the preferred configuration of the respective reactant.

3.2.3 Potential Dependent Reaction Thermodynamics

In electrocatalytic hydrotreatment, an applied potential impacts the rate of reaction steps involving electron transfer. The impact of applied potential on the reaction thermodynamics is assessed utilizing the computational hydrogen electrode (CHE) reported by Nørskov et al. as an effective reference electrode.[90] Briefly, the chemical potential of a proton-electron

pair in solvent is assumed to be half the chemical potential of H_2(g) at 0 V vs. RHE. At any applied potential, U_{RHE}, the chemical potential of a proton-electron pair, $H^+ + e^-$, is:

$$\mu(H^+ + e^-) = 0.5\mu(H_2(g)) - |e|U_{RHE} \tag{3.6}$$

where $|e|$ is the elementary charge.

The reactions at the working electrode require an additional term to represent the electrons consumed in electrochemical steps. Eq. 3.3 is modified to Eq. 3.7 account for this where n is the number of electrons consumed up to and including state j[93,142].

$$\Delta G_j = E_j + E_{ZPE} - T\Delta S + \Delta H_{0\rightarrow T} - G_{ref} - n|e|U_{RHE} \tag{3.7}$$

3.2.4 Reaction Mechanisms

A Langmuir-Hinshelwood mechanism is commonly assumed in organic electrochemical hydrotreatment (ECH), where an adsorbed organic compound reacts with a co-adsorbed hydrogen atom.[68] Here, we consider the energy of a hydrogen atom co-adsorbed onto each facet with the organic to be equivalent to the energy of the proton-electron pair in solution per the CHE.[93] The number of electrons consumed in these reactions is also considered as the total consumed in a given state relative to the reference state. Generally, the relative energy of a given organic adsorbed state, j, is represented by:

$$\Delta G_j = G_j + n_{H_2} G_{H_2(g)} + G_* + n|e|U_{RHE} - G_{ref} \tag{3.8}$$

where n_{H_2} and $G_{H_2(g)}$ represent the number and free energy of H_2 molecules that have not yet been consumed from the reference state. G_* represents the free energy of bare slab images, which is only present before adsorption or after desorption of the organic. The mechanisms for FF to THFA, 4-PP to 4-PCOL, and 4-PP to PC, accounting for bare slabs and proton-electron pairs per the CHE, are summarized below.

The net reaction for the reduction of FF to THFA is:

$$\mathrm{FF\,(g)} + 6\,(\mathrm{H^+} + \mathrm{e^-}) + * \longrightarrow \mathrm{THFA\,(g)} + * \tag{3.9}$$

The elementary reaction steps for FF reduction to THFA are:

$$\mathrm{FF\,(g)} + * \longrightarrow \mathrm{FF}* \tag{3.10}$$

$$\mathrm{FF}* + \mathrm{H^+} + \mathrm{e^-} \longrightarrow (\mathrm{FF} + \mathrm{H})* \tag{3.11}$$

$$(\mathrm{FF} + \mathrm{H})* + \mathrm{H^+} + \mathrm{e^-} \longrightarrow \mathrm{FA}* \tag{3.12}$$

$$\mathrm{FA}* + \mathrm{H^+} + \mathrm{e^-} \longrightarrow (\mathrm{FA} + \mathrm{H})* \tag{3.13}$$

$$(\mathrm{FA} + \mathrm{H})* + \mathrm{H^+} + \mathrm{e^-} \longrightarrow (\mathrm{FA} + 2\,\mathrm{H})* \tag{3.14}$$

$$(\mathrm{FA} + 2\,\mathrm{H})* + \mathrm{H^+} + \mathrm{e^-} \longrightarrow (\mathrm{FA} + 3\,\mathrm{H})* \tag{3.15}$$

$$(\mathrm{FA} + 3\,\mathrm{H})* + \mathrm{H^+} + \mathrm{e^-} \longrightarrow \mathrm{THFA}* \tag{3.16}$$

$$\mathrm{THFA}* \longrightarrow \mathrm{THFA\,(g)} + * \tag{3.17}$$

4-PP can either be converted to 4-PCOL or PC. To produce 4-PCOL, the net reaction is:

$$\text{4-PP}\,(\mathrm{g}) + 6\,(\mathrm{H^+} + \mathrm{e^-}) + * \longrightarrow \text{4-PCOL}\,(\mathrm{g}) + * \tag{3.18}$$

The elementary reaction steps are:

$$\text{4-PP}\,(\text{g}) + * \longrightarrow \text{4-PP}* \tag{3.19}$$

$$\text{4-PP} * {}^{+}\,\text{H}^{+} + \text{e}^{-} \longrightarrow (\text{4-PP} + \text{H})* \tag{3.20}$$

$$(\text{4-PP} + \text{H})* + \text{H}^{+} + \text{e}^{-} \longrightarrow (\text{4-PP} + 2\,\text{H})* \tag{3.21}$$

$$(\text{4-PP} + 2\,\text{H})* + \text{H}^{+} + \text{e}^{-} \longrightarrow (\text{4-PP} + 3\,\text{H})* \tag{3.22}$$

$$(\text{4-PP} + 3\,\text{H})* + \text{H}^{+} + \text{e}^{-} \longrightarrow (\text{4-PP} + 4\,\text{H})* \tag{3.23}$$

$$(\text{4-PP} + 4\,\text{H})* + \text{H}^{+} + \text{e}^{-} \longrightarrow (\text{4-PP} + 5\,\text{H})* \tag{3.24}$$

$$(\text{4-PP} + 5\,\text{H})* + \text{H}^{+} + \text{e}^{-} \longrightarrow \text{4-PCOL}* \tag{3.25}$$

$$\text{4-PCOL}* \longrightarrow \text{4-PCOL}\,(\text{g}) + * \tag{3.26}$$

The mechanism to produce PC proceeds through a propylbenzene (PB) intermediate for a net reaction of:

$$\text{4-PP}\,(\text{g}) + 7\,(\text{H}^{+} + \text{e}^{-}) + * \longrightarrow \text{PC}\,(\text{g}) + (\text{OH})* \tag{3.27}$$

The elementary reaction steps are:

$$\text{4-PP}\,(\text{g}) + * \longrightarrow \text{4-PP}* \tag{3.28}$$

$$\text{4-PP}* + \text{H}^{+} + \text{e}^{-} \longrightarrow (\text{PB} + \text{H}, \text{OH})* \tag{3.29}$$

$$(\mathrm{PB} + \mathrm{H}, \mathrm{OH})* + \mathrm{H}^+ + \mathrm{e}^- \longrightarrow (\mathrm{PB} + 2\,\mathrm{H}, \mathrm{OH})* \tag{3.30}$$

$$(\mathrm{PB} + 2\,\mathrm{H}, \mathrm{OH})* + \mathrm{H}^+ + \mathrm{e}^- \longrightarrow (\mathrm{PB} + 3\,\mathrm{H}, \mathrm{OH})* \tag{3.31}$$

$$(\mathrm{PB} + 3\,\mathrm{H}, \mathrm{OH})* + \mathrm{H}^+ + \mathrm{e}^- \longrightarrow (\mathrm{PB} + 4\,\mathrm{H}, \mathrm{OH})* \tag{3.32}$$

$$(\mathrm{PB} + 4\,\mathrm{H}, \mathrm{OH})* + \mathrm{H}^+ + \mathrm{e}^- \longrightarrow (\mathrm{PB} + 5\,\mathrm{H}, \mathrm{OH})* \tag{3.33}$$

$$(\mathrm{PB} + 5\,\mathrm{H}, \mathrm{OH})* + 2\,(\mathrm{H}^+ + \mathrm{e}^-) \longrightarrow (\mathrm{PC}, \mathrm{OH})* \tag{3.34}$$

$$(\mathrm{PC}, \mathrm{OH})* \longrightarrow \mathrm{PC}\,(\mathrm{g}) + (\mathrm{OH})* \tag{3.35}$$

A decision tree method is utilized to predict the radical intermediates in the elementary reaction steps ($i.e.$(FF + H) $*$). Here, adsorbed states for all possible hydrogenation locations on a given ring are relaxed for the first hydrogen addition. For a given hydrogenation step, the state with the lowest energy compared to the others is considered the most surface-stabilized and, therefore, is the most thermodynamically likely. The most stable intermediate of a given step is the basis for defining possible intermediates for the next step. The preferred paths, comprising the most likely intermediates for each hydrogenation step, on each facet, are visualized in Appendix B: Figures B9-B12 for the FF pathway and Figures B13-B16 for the 4-PP pathway. These pathways correspond to the data presented in the reaction energy diagrams. Examples of the decision trees for the FF and 4-PP pathways on Pt(110) are described in Appendix B, Figures B17 and B18. The energies of all possible intermediate states are provided in Appendix B Tables B1-B3.

3.2.5 Hydrogen Underpotential Deposition (H_{upd}) Inhibition by Organic Molecules

The adsorption of organic molecules on a Pt electrode can be experimentally measured by interfering with hydrogen adsorption on the same electrode. The adsorption of organic and hydrogen on a Pt electrode is studied using cyclic voltammetry (CV) and linear sweep voltammetry (LSV) near the hydrogen reversible potential. The experiments yield estimates of the free energy of adsorption for the organic compound, which can then be compared with computed free energies that account for solvation effects expected to be present during the experiments.

3.2.5.1 Materials

The platinum black electrode is prepared with a platinum sheet (Mateck). The platinum black solution contains chloroplatinic acid hydrate (Sigma Aldrich), with lead acetate from ammonium acetate (Sigma Aldrich) and lead sulfate (Sigma Aldrich) as additives for stability. An aqua regia solution, composed of 3:1 hydrochloric acid (Honeywell Fluka) and nitric acid (Fischer Chemical), is used for electrode cleaning. Electrochemical experiments utilized a bare platinum sheet counter electrode and an Ag/AgCl reference electrode in saturated potassium chloride (Sensortechnik Meinsburg). Perchloric acid (0.1 M, Fischer Chemical) is the electrolyte. Furfural (Sigma Aldrich), furfuryl alcohol (Sigma Aldrich), and 2-methylfuran (Sigma Aldrich) are introduced to the electrochemical cell to assess the adsorption free energy.

3.2.5.2 Electrode preparation

Platinum black was galvanostatically deposited on a 3 cm × 2 cm × 0.1 mm platinum sheet. The platinum black precursor solution was prepared as 3.5 wt/wt% Chloroplatinic acid hydrate in DI water. A lead acetate solution was added to the precursor solution in a quantity of 0.005 wt/wt% for stabilization. The lead acetate solution was prepared from 2 moles of ammonium acetate per mole of lead sulfate in DI water. Before the electrode was coated with platinum black, it was cleaned in two steps. First, the bare electrode

was washed in a boiling aqua regia mixture to ensure any previously deposited matter was removed. Then, the electrode was cleaned electrochemically with 0.5 M sulfuric acid while collecting a background cyclic voltammogram (CV).

3.2.5.3 Cell setup and CV parameters

Electrochemical experiments were conducted using a Bio-logic SP-50e Potentiostat with an equally sized bare platinum sheet as a counter electrode and a Ag/AgCl electrode as the reference. A background CV was recorded between 1.2 V and -0.25 V vs. Ag/AgCl at a scan rate of 100 mV/s in 0.1 M $HClO_4$. CVs were collected accordingly unless otherwise noted. To determine the electrochemical surface area (ECSA), cyclic voltammetry (CV) measurements were performed at scan rates of 2, 5, 10, 20, 50, 100, and 200 mV/s.

3.2.5.4 Pt Black Coated Pt Electrode

The platinum sheet working electrode was coated with platinum black through various cycles totaling to 3 minutes of coating time. Chronoamperometric techniques were used for coating at a constant current of -30 mA/cm^2. The coating time variable is detailed in Table 3.1. The 3 electrodes were rinsed and patted dry between coating and collecting CV measurements.

Table 3.1: Pt Electrode Coating Schedule.

Coat	Time per Side (s)	Coat Time (s)	Total Time (s)
1	15	30	30
2	15	30	60
3	30	60	120
4	30	60	180

3.2.5.5 H_{upd} experiments

The heat and free energy of adsorption of an organic molecule on the platinum surface can be determined electrochemically by observing hydrogen adsorption blocked by an organic molecule in the window of hydrogen under potential deposition. Using the electrochemical cell setup, linear potential sweeps are collected after the introduction of various concentrations of organic compounds. Here, the potential was scanned from 0.2 V to -0.3 V

vs. Ag/AgCl at a scan rate of 2 mV/s. Before the introduction of organic, the electrolyte is purged with nitrogen, and an initial cyclic voltammetry (CV) scan was run to verify the potential window associated with hydrogen adsorption.[94]

3.2.5.6 Calculation of Free Energy and Heat of Adsorption

Experimental free energy and heats of adsorption of organic species were calculated by methods previously reported[94,95]. The fraction of H_{upd} inhibited, θ, is first calculated by integrating the hydrogen adsorption curves obtained in the presence and absence of organic species to achieve the charges associated with each case, $Q_{H_{upd}}$ and $Q_{H_{upd}+Organic}$, respectively. The resulting value of θ is

$$\theta = 1 - \frac{Q_{\text{Hupd+Organic}}}{Q_{\text{Hupd}}} \tag{3.36}$$

The aqueous free energy of adsorption is related to coverage in a Frumkin adsorption isotherm.[94,95] This modification provides the advantage of linearly scaling the free energy of adsorption with the organic coverage by the slope α, as described below. The fraction of H_{upd} inhibited as a function of concentration is fit to the isotherm to determine the saturation coverage, θ_{sat}, the free energy of adsorption at zero coverage, $\Delta G^{aq}_{ads,\theta=0}$, and the linear scaling slope for free energy of adsorption, α.[95]

$$\frac{C}{C_0} = \frac{\frac{\theta}{\theta_{sat}}}{1 - \frac{\theta}{\theta_{sat}}} \exp\left[\frac{-\Delta G^{aq}_{ads,\theta=0}}{RT} - \frac{\alpha\frac{\theta}{\theta_{sat}}}{RT}\right] \tag{3.37}$$

The standard state concentration, C_0, is assumed to be 1 M. The free energy of adsorption at any evaluation coverage ($\Delta G_{ads,\theta_{eval}}$) is:

$$\Delta G_{ads,\theta_{eval}} = \Delta G_{ads,\theta=0} + \alpha\theta_{eval} \tag{3.38}$$

The gas-phase free energy of adsorption is calculated from the aqueous-phase free energy of adsorption through coverage-dependent adsorption equilibrium coefficients ($K^{gas}_{eq,\theta}$, $K^{aq}_{eq,\theta}$) and the Henry's constant (K_H) of the organic in water.[172] Henry's constants used

in this analysis are adjusted to account for electrolyte through Setschenow's law.[173–175] By assuming ideal gas behavior, Henry's constant of volatility, K_{H}, in units of bar/M, becomes dimensionless when divided by RT.[95,172] Dimensionless and electrolyte-corrected Henry's constants for each organic are reported in Table 3.3.

$$K_{\mathrm{eq},\theta}^{\mathrm{gas}} = \frac{K_{\mathrm{eq},\theta}^{\mathrm{aq}}}{K_H/(RT)} \tag{3.39}$$

The free energy of adsorption is related to the equilibrium coefficient.

$$K_{\mathrm{eq},\theta} = exp\left(\frac{-\Delta G_\theta}{RT}\right) \tag{3.40}$$

With this equivalence, the value of $\Delta G_{\mathrm{ads},\theta}^{\mathrm{gas}}$ is calculated below and used with α to predict the gas-phase free energy of adsorption at an evaluation coverage (Eq. 3.38).

$$\Delta G_{eq,\theta}^{gas} = \Delta G_{eq,\theta}^{aq} + RTln(K_H/RT) \tag{3.41}$$

The gas-phase free energy of adsorption, calculated from experiments, can then be directly compared to the same value obtained from DFT calculations.

3.3 Results and Discussion

Previous work on experimental electrochemical hydrotreatment (ECH) of a binary mixture of bio-oil constituents suggests that 4-propylphenol (4-PP) proceeds to propylcyclohexane (PC) and 4-propylcyclohexanol (4-PCOL). Furfural (FF) proceeds to tetrahydrofurfuryl alcohol (THFA) via furfuryl alcohol (FA) intermediate on a Pt/Ru catalyst.[149] However, FF and product molecules are known to dimerize and produce other products.[53,54] The main side products that have been studied include the production of methylfuran (MF) from FA along with dimerization of either FF or FA to form furoin (FUI) or hydrofuroin (HF). Previous work suggests that dimers were produced, so the adsorption behavior of these byproducts is considered. However, the production of THFA is the main pathway observed by Kasad et al. and is the only reaction pathway fully explored in this work. A reaction network

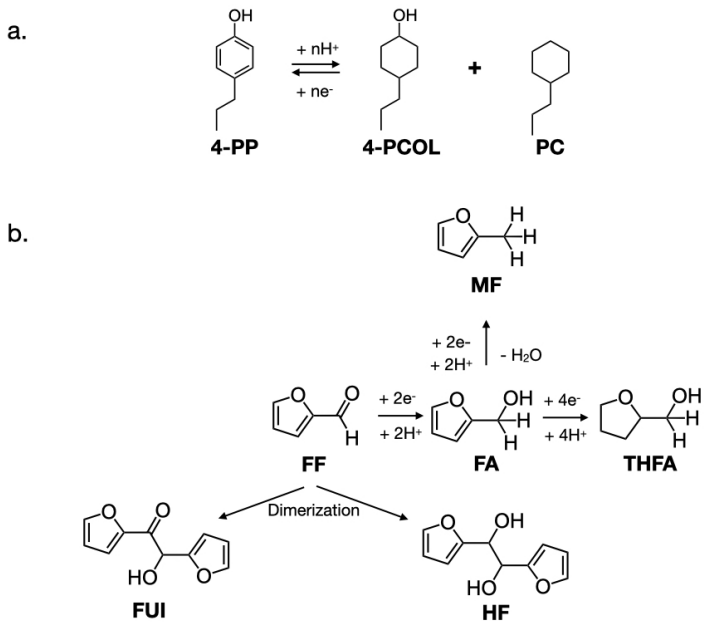

Figure 3.1: Proposed reaction pathways from (a) 4-propylphenol (4-PP) and (b) furfural (FF).

summarizing the species studied in this work is shown in Figure 3.1.

3.3.1 Adsorption Energies by DFT

Upon computing the energies of the adsorbed reactants, FF and 4-PP, the preferred configurations on each surface were determined based on the minimum energy obtained for a range of possible configurations on four metal surface facets. These minimum-energy configurations are shown in Figure 3.2. The remaining non-preferred adsorption configuration images are provided in the Supplementary Information. Configurations of product species are relaxed from the configuration of their respective reactant. The atomic positions of the optimized reactant, stable intermediates, and side product adsorbed states, along with the optimized bare slabs, are available in a repository.[176]

FF molecules prefer a hollow or bridge-type configuration on each of the four surfaces shown in Fig. 3.2, which is consistent with previous models of FF on Pt(111)[102]. Similarly, 4-PP prefers a hollow-type configuration on Ru(0001), Pt(110), and Pt(100), though it prefers an atop-type configuration on Pt(111).

The adsorption energies of the reactants, stable intermediates, and products are reported

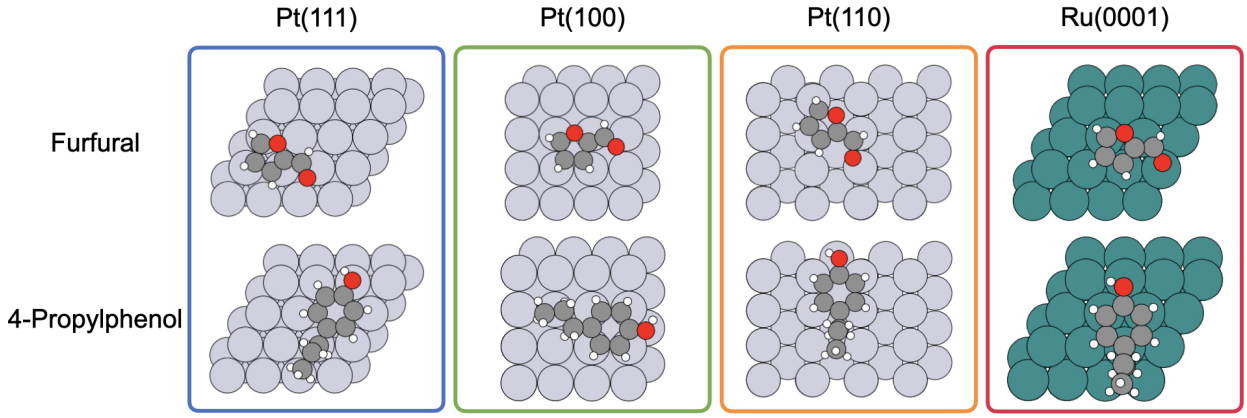

Figure 3.2: Preferred adsorption configurations of furfural and 4-propylphenol on platinum and ruthenium surfaces.

in Figure 3.3 for the four facets studied. Both the electronic adsorption energy and free energy of adsorption are presented. The electronic adsorption energy accounts for the change in chemical potential of the three states, capturing the implications of the surface - organic intermolecular interaction. The free energy of adsorption adds the implications of temperature on the intramolecular interactions to the electronic adsorption energy.

Comparing the electronic adsorption energies of preferred configurations of species in the proposed pathways provided in Fig. 3.3a, we find that 4-PP binds more strongly to all surfaces than FF. However, on Ru and Pt(111), the reactants have comparable electronic binding strengths. This suggests competitive intermolecular surface-organic interactions that can cause competitive adsorption between FF and 4-PP and potential inhibition of active sites by either reactant.

On Ru(0001) and Pt(110) surfaces, intermediate FA exhibits weaker binding than FF or 4-PP at the electronic level. This may explain reclaimed 4-PP product yields in the presence of FA instead of FF. The binding of FF and 4-PP is competitive and strong on Ru and Pt(110), whereas FA binds less strongly on these facets. This computational observation is consistent with the experimental observation that FF inhibited 4-PP ECH more than FA, which suggests that Ru(0001) and Pt(110) are key facets of this process. Finally, intermediates and products with a greater degree of hydrogenation bind more weakly to the surface

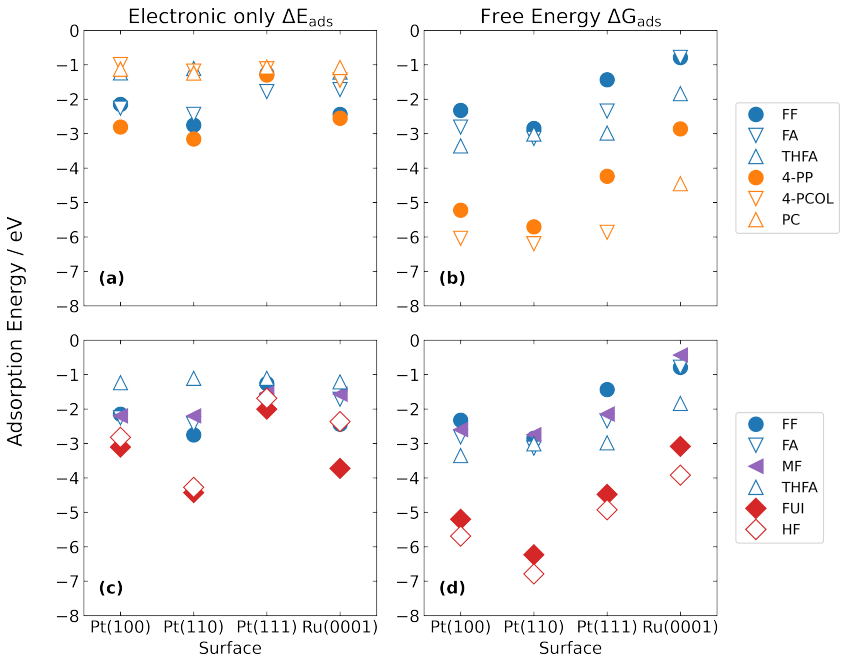

Figure 3.3: Adsorption electronic and free energies of (a,b) molecules involved in the proposed FF and 4-PP pathways and (c,d) other FF products on platinum and ruthenium surfaces.

than the reactants. The carbon atoms of THFA or 4-PCOL and PC have bonds with more hydrogens than their respective reactants, which reduces the availability of the carbon to bind with the surface. Owed to this reduced binding availability, it is expected that the more hydrogenated species would have a weaker adsorption energy.

From the free energy standpoint at 20°C (Fig. 3.3b), the free energies of adsorption of the 4-PP molecules suggest stronger binding than the FF molecules. The contribution of vibrational corrections ($E_{\mathrm{ZPE}} - T\Delta S + \Delta H_{0\to T}$, Eq. 3.7) increase with molecular weight (MW), thus further reducing the free energy of the larger 4-PP molecule as compared to the smaller FF. However, it is worth noting that both pathways have more negative free energies on Pt(100) and Pt(110) than the other facets. This is more apparent from the free energies (Fig. 3.3b) than the electronic energies (Fig. 3.3a). With vibrational corrections, the adsorption energies of FF and 4-PP are also closest on Ru compared to the Pt facets. Thermodynamically, the adsorption of these species on Pt and Ru is favorable, with the same facet comparison trends observed in both electronic and free adsorption energy calculations. While the free energies suggest that the adsorption of 4-PP is more favorable, this effect could be negated by more competitive reaction thermodynamics in the FF pathway, as discussed

in the Reaction Thermodynamics section.

The adsorption of additional intermediates and products of FF hydrogenation were considered, as shown in Fig. 3.3c-d. These include methylfuran (MF) and dimerization products furoin (FUI) and hydrofuroin (HF). MF, a possible hydrogenation product of FA, exhibits stronger binding than THFA at the electronic level (Fig. 3.3c) and is comparable when vibrationally corrected (Fig. 3.3d). Due to this, FA may be converted to MF instead of THFA. Since Kasad did not observe MF experimentally, we do not further consider MF production here. Both dimers (FUI and HF, Fig. 3.3c-d), bind most strongly on all surfaces, likely owing to their high MW. This suggests that dimerization may also be a possible inhibition mechanism in this reaction system. The presence of such dimers was not measurable by Kasad. Therefore, the side reactions producing FUI and HF are not considered below.

3.3.2 Reaction Thermodynamics

The thermodynamics of the FF to THFA and 4-PP to 4-PCOL and PC reactions were assessed and compared. First, an energetic decision tree method developed in this work determined the intermediate states for each hydrogenation step between the stable intermediates. Such intermediate states differed primarily in the position of hydrogen addition. The intermediate state with the lowest energy was considered the preferred intermediate. The pathways were compared on each Pt and Ru facet. Then, the potential was varied to assess the implications of potential dependence on the reaction thermodynamics.

3.3.3 Proposed Pathway Reactions

In addition to binding energies of key species along both FF and 4-PP pathways, the energetics of each hydrogenation step were probed. The energy landscapes in Figure 3.4 comprise the most favorable step determined by the decision tree. An example decision tree for the FF to THFA and 4-PP to 4-PCOL pathways on Pt(110) is provided in Appendix B, Figures B17 and B18. The energies and SMILES notation of all intermediate steps are also provided in Appendix B, Tables B1-B3. Hydrogen presence is also accounted for through the CHE method described in Eq. 3.8.

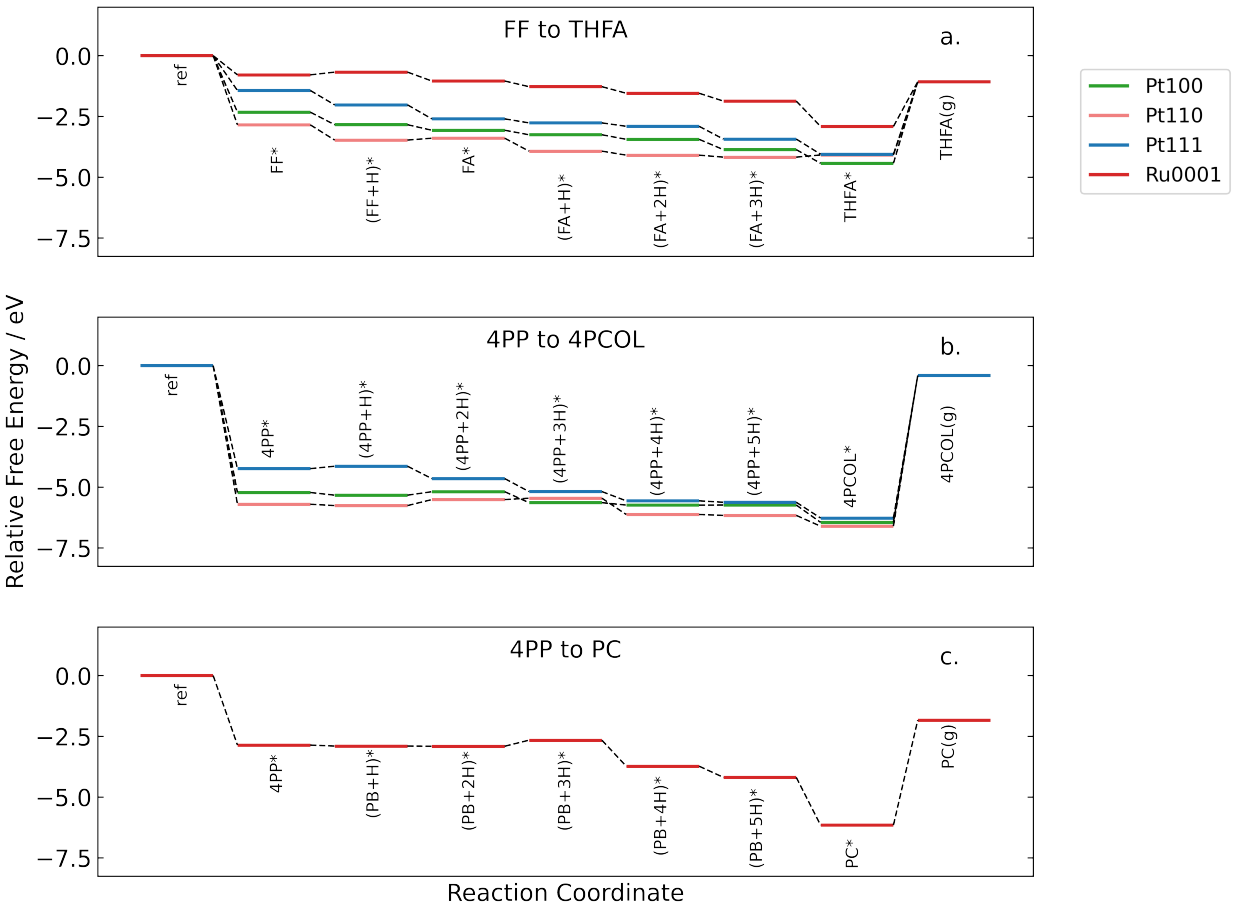

Figure 3.4: Relative free energy landscapes for the (a) FF to THFA pathway with E_{ref} = $E_{FF(g)}$ + $E_{3H_2(g)}$ + E_*, (b) 4-PP to 4-PCOL pathway with E_{ref} = $E_{4-PP(g)}$ + $E_{3H_2(g)}$ + E_* and (c) 4-PP to PC pathway with E_{ref} = $E_{4-PP(g)}$ + $E_{3.5H_2(g)}$ + E_* on Pt(100), Pt(110), Pt(111), and Ru(0001).

The FF to THFA pathway is most favorable on Pt(110) (Fig. 3.4a), as denoted by the lowest energy at every hydrogenation step besides bound THFA. This coincides with FF and FA binding more strongly to Pt(110) than to other surfaces. However, this energy pathway is not strictly downhill, indicating barriers to this transformation. The relative energy of the pathway continually decreases on Pt(111) and Pt(100) until the desorption of THFA. Although both of these surfaces exhibit weaker binding with the three key species than Pt(110), there are no positive reaction energies on Pt(111) or Pt(100). On Pt(110), the reactions to generate FA and THFA both exhibit positive reaction energies. Positive reaction energies indicate that larger activation barriers may exist for that step. To assess activation barriers, a kinetic analysis with transition state barriers is a point of future studies.

On Ru(0001), the FF to THFA pathway exhibits higher state energies than on platinum facets. The high state energies can be attributed to the larger zero point energies compared to those of the platinum facets (SI, Tables S7-S10). A slight barrier exists in the formation of the first radical. However, after the first hydrogenation step, the energy decreases with each proceeding step. Although the state energies are lower on Pt facets, the pathway on Ru(0001) would be competitive due to continually decreasing energy and a more negative net reaction energy than on other facets.

Similar trends are observed for the 4-PP to 4-PCOL pathway on Pt surfaces. Like the FF pathway, state energies of the 4-PP pathways are also lowest on Pt(110), and barriers still exist for the pathway on this facet (Fig. 3.4b). The most significant difference for the 4-PP pathways is also in comparing the pathways on Pt(110) and Ru. On platinum surfaces, 4-PP is converted to 4-PCOL through the hydrogenation of the ring. In contrast, on Ru, the hydroxy group is immediately cleaved from 4-PP, and then the ring is saturated with hydrogen. For the 4-PP to PC pathway on Ru (Fig. 3.4c), reaction energies are initially similar for the adsorption of 4-PP and the first two reaction steps. The third hydrogenation step exhibits a barrier before the state energies rapidly decline for the remaining reaction steps. Considering such reaction energetics, it is plausible that 4-PCOL is preferentially produced on Pt and PC is produced on Ru(0001).

Like the competitive binding observed between FF and 4-PP, the reaction landscapes have the lowest energy on Pt(110). Contrary to the trends in adsorption in which Pt(110)

exhibited the strongest binding, the reaction energies of both pathways are least preferable on Pt(110). This is because, for both the FF and 4-PP pathways on Pt(110), there are the most indications of barriers throughout the transformations, as denoted by upticks in energy throughout the reaction. The FF to THFA pathway generally decreases on all surfaces, whereas the 4-PP pathways on all facets exhibit barriers. While the state energies are lower for the 4-PP pathways, there are more barriers to reaction than for the FF pathway. Therefore, it is conceivable that the FF to FA reaction blocks the transformation of 4-PP to 4-PCOL on Pt and 4-PP to PC on Ru.

3.3.3.1 Potential Dependence

Applied potential also impacts the relative energies of the various states via the potential term in Eq. 3.7. Potential-dependent reaction thermodynamics are predicted for potentials between 0.5 V_{RHE} and -1 V_{RHE}, as shown in Figure 3.5.

The presence of a limiting potential, U_L, or the potential in which the largest barrier is equal to zero, can also help to identify where barriers may have a larger impact on the overall thermodynamic favorability.[177] This implies that if the applied potential is more negative than the limiting potential ($U < U_L$), the reaction pathway will no longer exhibit barriers. Limiting potentials for the pathways on each facet are provided in Table 3.2.

Table 3.2: Limiting Potentials (in V vs. RHE) of FF and 4-PP Pathways on Pt and Ru Facets.

Facet	FF Pathway U_L	4-PP Pathway U_L
Pt(100)	0.19	-0.14
Pt(110)	-0.09	-0.25
Pt(111)	0.14	-0.10
Ru(0001)	-0.11	-0.25

Regarding the FF to THFA pathways on each surface, the limiting potentials are positive on Pt(100) and Pt(111). The Pt(110) and Ru(0001) facets exhibit negative limiting potentials of approximately -0.1 V_{RHE}. The limiting potential for the 4-PP pathway is more negative on all surfaces than for the FF pathway. The limiting potential of the 4-PP pathway is most negative on Pt(110) and Ru(0001) at -0.25 V_{RHE}. On all facets, the limiting

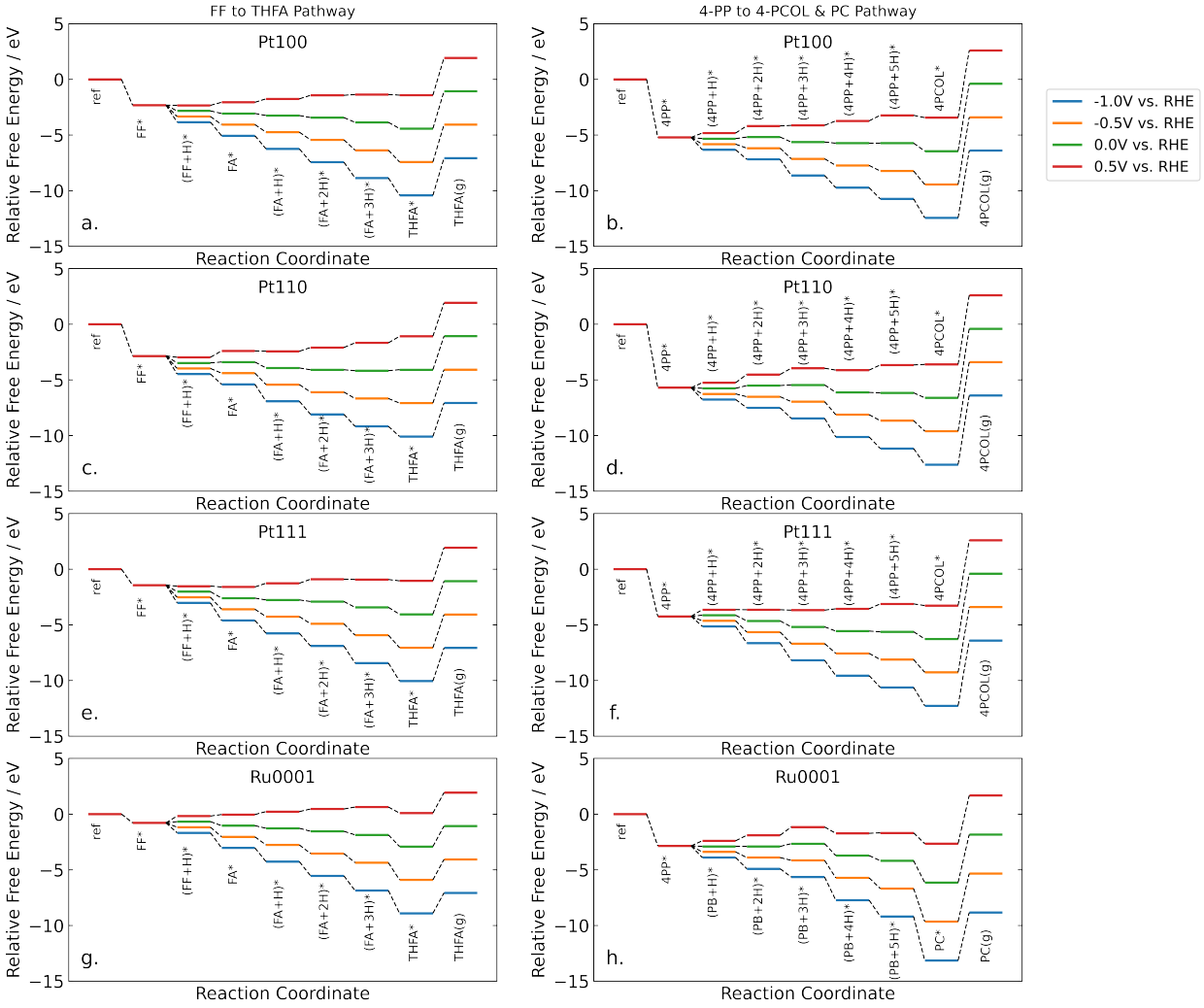

Figure 3.5: Potential dependant relative free energy landscapes for the two proposed pathways on (a and b) Pt(100), (c and d) Pt(110), (e and f) Pt(111), and (g and h) Ru(0001).

potentials of the FF and 4-PP are dissimilar, where the 4-PP potentials are 0.15 to 0.3 V_{RHE} lower than the FF potentials. The more negative limiting potential of 4-PP pathways would require a more negative potential, or greater overpotential, to ensure thermodynamic favorability. Consequently, a more negative applied potential will further drive the FF pathways, resulting in more competition during electrode polarization.

Although Pt(110) and Ru exhibit the strongest binding with the reactants, the pathways on these facets will require the most overpotential. This is due to the larger barriers on these facets compared to Pt(111) or Pt(100). Regarding FF reduction, the only barrier or positive reaction energy on Pt(111) or Pt(100) is the desorption of THFA. On Pt(110), positive reaction energies are observed in the formation of FA and THFA. The FF pathway on Ru exhibits a barrier to the formation of FF radical. The 4-PP pathways exhibit barriers on each of the facets, which require a larger overpotential to overcome. The more negative limiting potentials on Pt(110) and Ru can be attributed to the relatively large barriers in the second and third hydrogenation steps.

3.3.4 Experimental Validation with H_{upd} Experiments

Estimates of adsorption energies for FF, FA, and MF were obtained experimentally by observing hydrogen adsorption inhibition by the organic presence on a Pt electrode.[94,95] First, the clean electrode was used to produce a CV, which represents the normal hydrogen adsorption behavior. Then, varied concentrations of organic molecules were added to the solution and cyclic voltammograms (CVs) were collected for each concentration. CVs are provided in Figure B19 of Appendix B.

Using Eq. 3.36, the fraction of H_{upd} inhibited by an individual organic species, θ, is calculated for varying bulk organic concentration, $C_{Organic}$, as shown in Figure 3.6. The lines in the figure represent the fit of Eq. 3.37. FF and FA exhibit similar fit curves in which H_{upd} is completely inhibited by organic concentrations larger than about 1 mM. MF completely inhibits H_{upd} at concentrations greater than 0.1 mM. Adsorption of hydrogen is most sensitive to the presence of MF, followed by FA, and then FF. From the fit curves in Fig. 3.6, the Gibbs free energy of adsorption is predicted for the aqueous phase and correlated to the gas phase to probe the energy of adsorption in comparison to the DFT

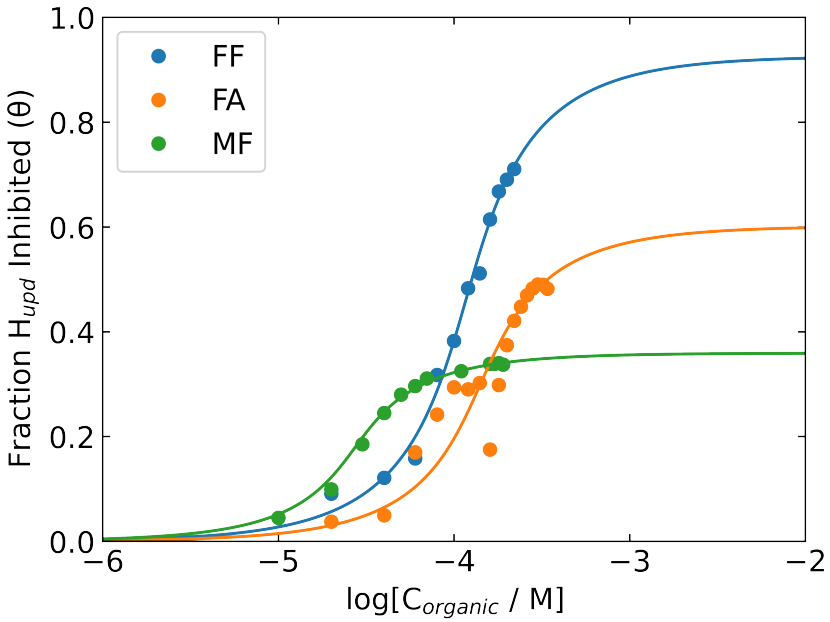

Figure 3.6: Normalized organic coverage as amount of hydrogen blocked versus concentration. The coverage is normalized to the saturation coverage determined for each molecule. Using the coverage profiles from experiments, the parameters in Table 3.3 were fit for concentrations of 1 μM to 1 mM.

calculations presented here.

3.3.4.1 Gibbs free energy of adsorption

For each molecule, the aqueous and gas phase free energies of adsorption for zero coverage, the coverage dependence slope, α, the saturation coverage, θ_{sat}, and the Henry's constant are provided in Table 3.3. Figure 3.6 suggests that FF and FA exhibit similar behavior, with MF binding slightly more strongly due to the complete inhibition of H_{upd} at lower MF concentrations. This is supported by comparable free energies of adsorption on a clean surface in the aqueous phase at approximately -20 kJ/mol. However, these trends do not hold in the extrapolation to the gas phase where MF is predicted to adsorb to a clean surface less strongly than that of FF or FA. The Henry's constant is largest for MF, followed by FF 3 orders of magnitude smaller, then FA. This would cause the gas phase adsorption equilibrium constant to increase the least for MF from the aqueous prediction and subsequently weaken the free energy of adsorption.

Table 3.3: Constants for FF, FA, and MF H_{upd} Inhibition Curves.

Molecule	K_H	$\Delta G_{ad,aq,0}$	$\Delta G_{ad,gas,\theta 0}$	α	θ_{sat}
		kJ/mol	kJ/mol		
FF	1.5E-4 ± 0.2	-19.4 ± 0.2	-40.8 ± 0.2	-5.4 ± 0.6	0.93 ± 0.05
FA	3.3E-6 ± 2E-3	-18.9 ± 0.7	-49.7 ± 0.7	-5.3 ± 1.7	0.60 ± 0.05
MF	0.27	-22.9 ± 1.5	-26.1 ± 1.5	-5.3 ± 1.9	0.36 ± 0.004

The DFT calculations are considered to be a coverage (θ) of 0.0625 to account for the one organic molecule per 16 surface atoms. To appropriately compare the experimental adsorption energies to the computational energies, the free energy and heat of adsorption at $\theta_{\text{eval}} = 0.0625$ must be evaluated. The free energy of adsorption for each molecule at the evaluation coverage are calculated for the aqueous phase and extrapolated to the gas phase to be compared with the computational free energies of adsorption on each Pt facet in Table 3.4.

Table 3.4: Experimental and DFT calculated Gibbs free energy of adsorption of FF, FA, and MF at $\theta_{\text{eval}} = 0.0625$.

Molecule	Experimental $\Delta G_{ad,aq,eval}$	Experimental $\Delta G_{ad,gas,eval}$	DFT - Pt(100) $\Delta G_{ad,gas,eval}$	DFT - Pt(110) $\Delta G_{ad,gas,eval}$	DFT - Pt(111) $\Delta G_{ad,gas,eval}$
	kJ/mol	kJ/mol	kJ/mol	kJ/mol	kJ/mol
FF	-19.7 ± 0.2	-41.1 ± 0.2	-225	-275	-138
FA	-19.3 ± 0.7	-50.0 ± 0.7	-272	-303	-226
MF	-23.3 ± 1.5	-26.4 ± 1.5	-251	-265	-207

In the gas phase, the experimentally predicted free energy follow similar trends at the evaluation coverage as in the case of a clean electrode, provided in Table 3.4. For the three surfaces, the computational adsorption free energies do not align with the experimental free energy prediction. Although, the binding strength trend is similar on Pt(110). Here, and on Pt(110) where the molecules are predicted to adsorb most strongly compared to other facts, FA exhibits the strongest binding, followed by FF, then MF. This opposes the experimentally predicted aqueous phase free energies of adsorption, suggesting that MF binds most strongly, followed by FF and FA. In the DFT calculations and the gas phase experimental extrapolation, MF binds more strongly than FF with the exception of Pt(110) DFT calculations.

Discrepancies between the computational trends and experimental outcomes for MF, specifically, may be due to the higher volatility and hydrophobicity of MF than FF or FA. Experimentally, higher volatility could result in evaporated MF that does not interact with the electrode. Additionally, as the compounds are hydrogenated, they become more hydrophobic. The increased hydrophobicity of an organic compound in an aqueous environment leads to a decrease in solubility, which has been shown to enhance the binding between the organic compound and the surface.[178] This would explain the stronger binding of MF than FF or FA observed experimentally in the aqueous phase. Furthermore, computational free energies are also several hundred kJ/mol more negative than the experimental values. The reasoning behind the discrepancy remains unclear. Still, theories suggest that additional energies are associated with the displacement of water by the organic phase and the solvation between the aqueous and adsorbed phases, which are not accounted for by Henry's Law.[95]

3.4 Conclusions

Computational and experimental methods were utilized to assess and determine a mechanistic explanation for the inhibition of the electrocatalytic hydrotreatment of 4-propylphenol to propylcyclohexane in the presence of furfural on a Pt/Ru electrode. First, DFT methods were used to predict the adsorption energy and reaction free energies of the 4-PP to PC and FF to THFA pathways on Pt(100), Pt(110), Pt(111), and Ru(0001). An electronic energy decision tree determines the hydrogenation intermediate states of each path. Stable intermediates and other intermediate states are considered in reaction energy assessments. Finally, free energies and heats of adsorption are experimentally determined for FF, FA, and MF through competitive binding with hydrogen underpotential deposition on Pt. The aqueous phase results are correlated to the gas phase and 1/16th coverage to compare with the computational free energies of adsorption.

The electronic adsorption energy of reactants 4-PP and FF are most competitive on Pt(110) and Ru(0001) where 4-PP always binds more strongly to a given facet. Vibrational frequency analysis enabled the correction of the internal energies of the adsorption energy calculations to Gibbs free energy, which exhibits stronger binding of the larger molecules.

Namely, where 4-PP and FF were competitive, the free energy of adsorption favors 4-PP. The free energies of reactions along both pathways are further assessed under varied applied potential. The reactions for both pathways are most favorable on Pt(110) and competitive on Pt(100). However, the FF pathway requires less overpotential to have favorable reaction energies than the 4-PP pathway on each of the facets studied. Additionally, there exist more possible barriers in the 4-PP pathways, as indicated by positive reaction energies, than in the FF pathways. These could be elucidated by analysis of activation barriers and kinetics, and is a point of future study.

Furfural is determined to proceed to THFA through an FA intermediate on all four facets studied, as suggested by the previous experimental work. The 4-PP pathway proceeds to 4-PCOL on Pt, and is consistent with previous works. However, on Ru, the hydroxy group is cleaved off of 4-PP to form propylbenzene, which then proceeds to PC. Due to this, 4-PCOL is favored on Pt, but the PC observed in the experiment is likely to form on Ru. The pathway reaction free energies and the adsorption energies of FF and 4-PP are competitive on Ru. Due to this, it is thermodynamically likely that FF would block the adsorption and reaction of 4-PP on Ru, resulting in a decrease in PC product.

Experimental free energies of adsorption on Pt support some of the conclusions determined through the computational assessment. MF, FF, and FA exhibit comparable binding strengths in the aqueous phase, but discrepancies arise in extrapolating to the gas phase. These can be attributed to the variations in Henry's constant for each species, resulting in different shifts in adsorption equilibrium. Experimentally, FA exhibits weaker binding than FF in the aqueous phase, but stronger binding in the gas phase, which is consistent with the computational results that suggest FA would bind more strongly than FF. Further, the isotherms of FF and FA are similar and suggest that either molecule would completely block H_{upd} at higher organic concentrations than MF. Quantitatively, the experimental and computational results are dissimilar, which may be due to effects not accounted for in Henry's Law. Understanding the effects of solvation near the catalyst's surface may correct for some of this, and is a point for future studies.

Ultimately, this work sought to understand the complexities of interacting bio-oil molecules during electrocatalytic hydrogenation processes. Some details have been elucidated which

indicate competitive activity between furans and phenols. However, processing a real bio-oil would have many more molecules and is likely to involve several more interaction effects. In addition to considering activation barriers and solvation effects, there exists a need to scale up the model both in time or space and in the number of interacting reaction pathways. An immediate expansion of this work involves the prediction of reaction rate constants from the potential dependent activation barriers, which experiments utilizing a rotating disk electrode could validate. By similar studies of other bio-oil constituents, it would become possible to predict the behavior of a real bio-oil, but would be time intensive. Prediction of adsorption energies and reaction barriers by high-throughput means would expedite the prediction of reaction rate constants that enable larger-scale models of interacting constituent molecules.

Chapter 4

Kinetic Evaluation of Electrochemical Upgrading of Bio-oil

4.1 Introduction

In Chapter 3, an evaluation of adsorption and reaction energies in the competitive electrocatalytic hydrogenation (ECH) of furfural (FF) and 4-propylphenol (4-PP) on a Pt/Ru electrocatalyst was performed. The mechanisms of FF to tetrahydrofurfuryl alcohol (THFA) via furfuryl alcohol (FA) intermediate and 4-PP to propyl cyclohexane (PC) via 4-propyl cyclohexanol (4-PCOL) intermediate were assessed on the fcc facets of platinum and an hcp facet of ruthenium. The electronic adsorption energies of the species indicate competitive adsorption mechanisms, and that dimerization of FF may further block the surface, inhibiting the 4-PP reaction. Further, the reaction energies of the FF pathway are more thermodynamically favored than the 4-PP pathway. Comparing each path on the facets studied, the reactions are most favored on the Pt(110) surface, as marked by the low relative free energies of the states. However, the FF pathway may be more favored due to fewer barriers along the reaction coordinates than the 4-PP pathway.

Within the FF to THFA and 4-PP to PC pathways on each Pt and Ru facet (Chapter 3, Figure 3.4), most paths experience at least one unfavorable reaction energy of positive value, indicating locations of potentially high barriers. To computationally determine activation barriers of reactions, the transition state (TS) must be determined for each reaction step. Through DFT methods, the TS can be determined by a search of the reaction path to find the highest energy state between an initial state (IS) and final state (FS). Some of these

methods include nudged elastic band (NEB), climbing image NEB (CI-NEB), and the dimer method.[96,97] The elastic band methods search for a TS along a pathway between an initial state (IS) and final state (FS). The subsequent images are connected via "springs" with spring constants to set the forces that determine how stiff the pathway is, or how far apart images are from each other. CI-NEB offers the advantage of optimizing the details of the highest energy state, which NEB does not do.[96] The dimer method moves a pair of images consisting of the IS and an image closely related to the IS, called the "dimer", along the potential energy surface.[97] The curvature of the potential energy surface is calculated with the motion of the dimer. The transition state exists at the point of minimum curvature.

Although transition state search methods are effective, they can become prohibitively computationally demanding for complex reaction systems. To overcome this, linear scaling relationships have been developed to correlate the energy of a TS or activation barrier to the IS or FS.[98] This approach offers the advantage of quick estimation of transition state energy where the relationship has been defined for a specific reaction type using a method like NEB, CI-NEB, or the dimer method. Two methods of linear scaling relationships include Brønsted - Evans -Polyani (BEP) and Transition state scaling (TSS). BEP relationships correlate the activation energy to the reaction energy of a given step. TSS relationships correlate the TS energy to the energy of the final state.

Linear scaling relationships are only viable if trends have been determined for the class of molecules, bond break or formation, and catalyst to ensure that implications of these factors are accurately captured. Initially, BEP and TSS relationships were primarily determined for small molecule bonds, such as C-O bonds in CO_2, COOH, and CO, and C-H bonds in ethane and methane.[98] More recently, relationships have been determined for bonds within more complex molecules such as phenol and furan derivatives.[101–103] Kanchan and Banerjee report a TSS relationship for furan ring hydrogenation on Pt(111) and Ru(0001). Other surfaces and ring-opening reactions were also assessed.[101] Liu et al. also determined a TSS relationship for hydrogenating FF's aldehyde group to form FA on noble metal catalysts.[102] Finally, Mao et al. determined BEP relationships for cleavage of the C-O bond and hydrogenation of the ring for phenol.[103] There are limited studies of scaling relationships for 4-PP, mainly because the propyl group is unreactive, as demonstrated in Chapter 3. Therefore, we will

use the scaling data for phenol here.

Thermodynamic evaluation of hydrogenation reactions provides substantial information for understanding competing mechanisms. However, reaction kinetics may be a further cause of competitive mechanisms and inhibition of certain pathways. Computationally, reaction rate constants can be calculated from the free energy reaction barriers, per Transition State Theory.[104,105] Similarly to the state energies, the potential dependence of activation barriers and, by extension, rate constants may be calculated by applying Butler-Volmer type kinetics.[93]

The work herein extends that reported in Chapter 3 by calculating facet-dependent rate constants for the transformation of FF to THFA and 4-PP to PC. The activation free energies are first calculated from the initial and final state free energies of Chapter 3 using previously reported linear scaling relationships. Then, zeroth-order reaction rate constants are calculated for each reaction step on the three facets of Pt and the one Ru facet. Finally, the potential dependence of the rate constants is predicted. These results lay the groundwork for predicting transient product concentration profiles for the two pathways independently and in competition.

4.2 Methods

The free energies of initial, intermediate, and final states are predicted for the FF to THFA and 4-PP to 4-PCOL or PC reactions on Pt(100), Pt(110), Pt(111), and Ru(0001) in Chapter 3. The activation-free energies are predicted by combining these energies with linear scaling relationships for transition state or activation barrier energies reported in the literature. Transition state theory is applied to calculate the zeroth-order reaction rate constants for each reaction step from the activation free energies. The activation energies of the pathways on the four facets and the resulting rate constants are compared for a given pathway and across the two pathways. A Butler-Volmer type expression is utilized to further predict the potential dependence of these parameters by first determining an equilibrium potential for each reaction step, then predicting potential-dependent rate constants.

4.2.1 Activation Barrier

As discussed in Chapter 1, the energy of a reaction is defined as the difference between the energy of the initial state (IS) and final state (FS).

$$E_{\text{rxn}} = E_{\text{FS}} - E_{\text{IS}} \tag{4.1}$$

The activation barrier of the reaction, E_{a} is the difference in energy between the TS, or the highest energy state found along the pathway, and IS.

$$E_{\text{a}} = E_{\text{TS}} - E_{\text{IS}} \tag{4.2}$$

Activation barriers or TS energies are predicted by a combination of BEP and TSS linear relationships. BEP predicts the activation energy, E_{a}, from reaction energy:

$$E_a = \alpha E_{rxn} + \beta \tag{4.3}$$

A TSS relationship correlates the TS energy to the eneergy of the FS:

$$E_{\text{TS}} = \alpha' E_{\text{FS}} + \beta' \tag{4.4}$$

Where α and α' represent linear slopes and the βs are the y-intercept. The constants for each reaction type are summarized in Table 4.1. Parameter errors were not reported, but goodness of fit measures were provided, which are included in the Table.

Table 4.1: Linear scaling constants for FF and phenol hydrogenation, and C-OH bond cleavage of phenol.

Reaction Type	Relationship Type	α	α'	β	β'	Goodness of Fit
furan ring hydrogenation[101]	TSS		1.192		1.226	$R^2 = 0.73$
FF aldehyde hydrogenation[102]	TSS		1.01		1.01	SE = 0.13 eV
phenol hydrogenation[103]	BEP	-3.94		-1.00		$R^2 = 0.93$
phenol C-OH bond cleavage[103]	BEP	0.31		0.64		$R^2 = 0.96$

The phenol hydrogenation is a slight deviation from the equations reported above. Here,

the activation energy of hydrogenation is instead correlated to the adsorption energy of hydrogen.[103]

$$E_{\mathrm{a,Ph+H}} = \alpha E_{\mathrm{ads,H}} - \beta \tag{4.5}$$

Free energies along the reaction pathways are also considered from Chapter 3. For the transition states, the correction of the respective FS is applied to the TS for simplicity.

4.2.2 Computational Predictions of Rate Constants

Once activation barriers are predicted using computational approaches or scaling relationships, the kinetic rate constants can also be predicted. Transistion State Theory postulates that a zeroth-order rate constant, k_0, is related to the activation barrier free energy, ΔG_a, at a given temperature, T, and the reaction specific equilibrium potential, U_0.[90,93,104,105]

$$k_0 = \frac{k_{\mathrm{B}}T}{h} exp\left(\frac{-\Delta G_a}{k_{\mathrm{B}}T}\right) \tag{4.6}$$

Where k_B is the Boltzmann constant and h is Planck's constant.

The zeroth order rate constants predicted here are independent of reactant concentration and reactant concentration would increase linearly. As calculated here, a generation rate for some product concentration, C_{P}would look like:

$$\frac{dC_{\mathrm{P}}}{dt} = k_0 \tag{4.7}$$

However, non-zeroth order reactions are possible in experiment. To fit these conversions to first or second order rate laws that are dependent on concentration, experimental insight is required. Specifically, concentration profiles over time for generated products must be fit to determine turnover of reactants and realistic reaction orders.

4.2.3 Potential Dependence

Similarly to reaction energies, the implications of variable applied potential on activation barriers can be assessed. This is accomplished through application of Marcus theory and

Butler-Volmer kinetics where the energy of a transition state references the potential dependence of the proton in electrolyte.[93] The reversible hydrogenation reaction of some organic species A is:

$$\mathrm{A}* + \mathrm{H}^+ + \mathrm{e}^- \underset{k_r}{\overset{k_f}{\rightleftharpoons}} \mathrm{AH}* \tag{4.8}$$

Using the computational hydrogen electrode (CHE) method, the equilibrium potential, U_0, is a combination of free energies and the elementary charge, e.[90,93]:

$$U_0 = \frac{G_{\mathrm{AH}*} - G_{\mathrm{A}*} - 0.5G_{\mathrm{H_2(g)}}}{|e|} \tag{4.9}$$

The free energy change of the activation barrier, ΔG_{a}, at any potential, U, is[93]:

$$\Delta G_{\mathrm{a}}(U) = \Delta G_{\mathrm{a}}(U_0) + \beta F(U - U_0) \tag{4.10}$$

where F is Faraday's constant and β is the symmetry factor, generally assumed to be 0.5 for highly reversible (i.e. fast) reactions.

To impose potential dependence for some potential, U, the rate constant is defined as a function of the equilibrium potential and rate constant, U_0 and k_0.[104] When $U < U_0$, the reductive, or forward, reaction is favored. The oxidative, or reverse, reaction is favored when $U > U_0$. The forward and reverse rate constants, k_f and k_r, are defined below:

$$k_f = k_0 exp\left(\frac{-\beta|e|(U - U_0)}{k_{\mathrm{B}}T}\right) \tag{4.11}$$

$$k_r = k_0 exp\left(\frac{(1-\beta)|e|(U - U_0)}{k_{\mathrm{B}}T}\right) \tag{4.12}$$

where k_0 is defined by Eq. 4.6 and is the same for both Eqs. 4.11 and 4.12. By assuming that the reaction is symmetric ($\beta = 0.5$), the reverse rate constant is equivalent to the forward rate constant.

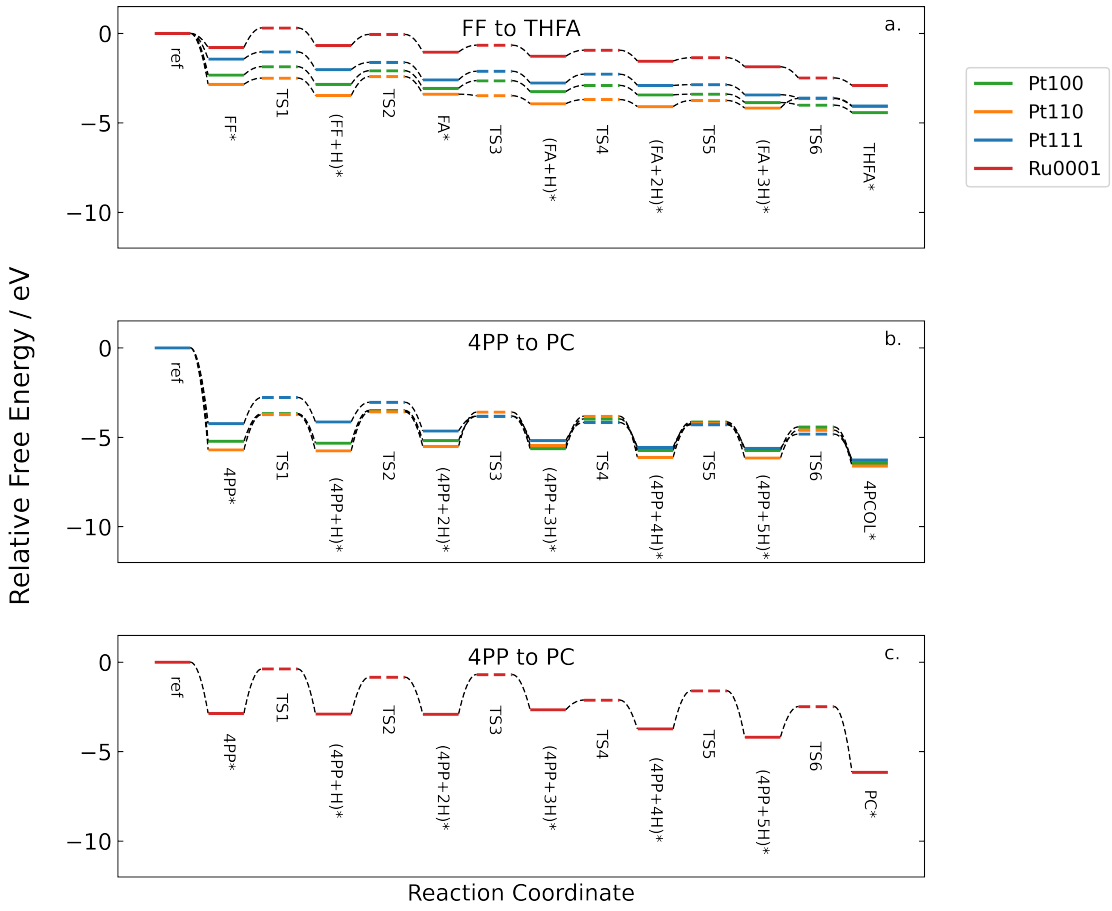

Figure 4.1: Reaction Free Energy diagram for (a) FF to THFA on the four facets (b) 4-PP to PC on platinum facets and (c) 4-PP to PC on ruthenium.

4.3 Results and Discussions

4.3.1 Reaction Free Energy and Activation Barriers

To predict kinetics computationally, the reaction free energies must first be extended to include the activation barriers. Activation free energy barriers (G_a) are predicted as described in Eqs. 4.3-4.5 with constants for each reaction type in Table 4.1. Figure 4.1 presents the relative free energy diagrams of the pathways at 20°C from Chapter 3, which are updated with the transistion state energies, denoted by "TSX".

Fig 4.1 suggests that the barriers are generally lower for the FF pathways than those of 4-PP on each surface. The two steps in FF hydrogenation to FA exhibit notably higher bar-

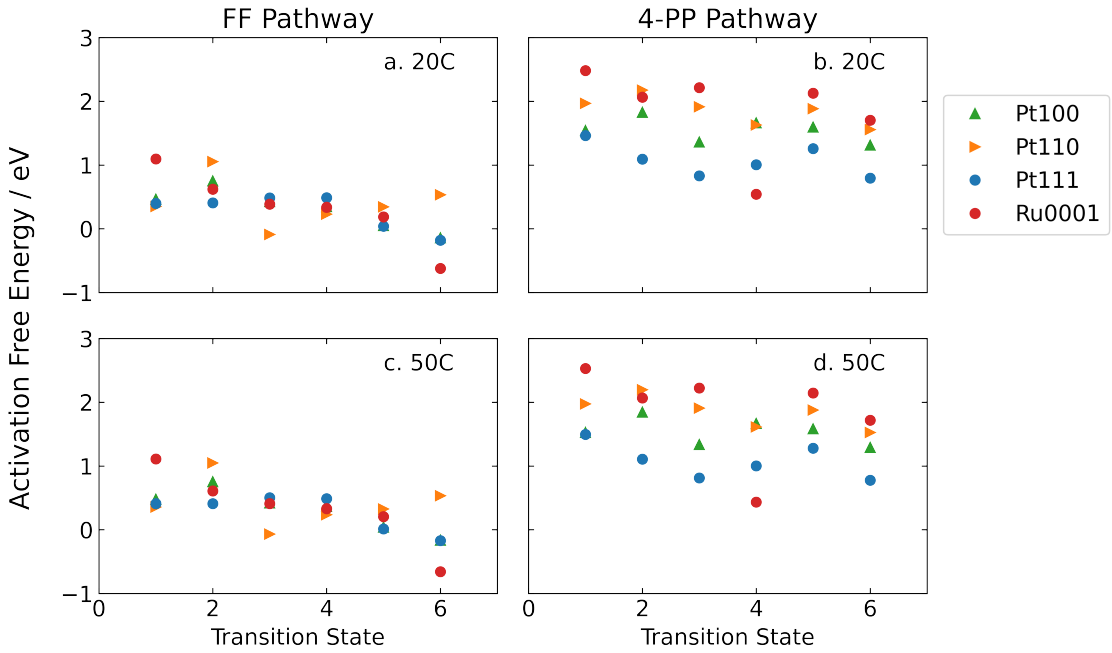

Figure 4.2: Activation Barrier Free Energies at 20°C and 50°C for (a,c) FF to THFA and (b,d) 4-PP to PC on the four surface facets.

riers than the remaining hydrogenation steps. In the 4-PP pathways, barriers are relatively consistent along the reaction on platinum and also large for most steps on ruthenium. A comparison of activation free energies is provided in Fig 4.2 for temperatures of 20°C and 50°C, the two temperatures used in the experiments of Chapter 3 and in the previous work, respectively.

The activation free energies of both pathways are on the order of 0 to 3 eV and are comparable with others reported in literature calculated from traditional methods (i.e. NEB, dimer method).[104,142,145] Comparison of ΔG_a values also confirms that the FF pathways exhibit lower barries than those of the 4-PP pathways by approximately 1 eV. There is also a sizeable decrease in the FF pathway barriers to nearly 0 eV for the hydrogenation steps of FA. Conversely, the 4-PP barriers are relatively consistent for the platinum facets. However, while the initial deoxygenation step of 4-PP on Ru has a higher barrier, there is a consistent decrease during the hydrogenation steps on ruthenium. Although the barriers of the 4-PP reaction on Ru are still higher than those on FF, there may be competition amongst the various pathways due to the shift in favorability of 4-PP to PC on Ru. Finally, the barriers are not substantially impacted by increase of temperature from 20°C to 50°C, suggesting that

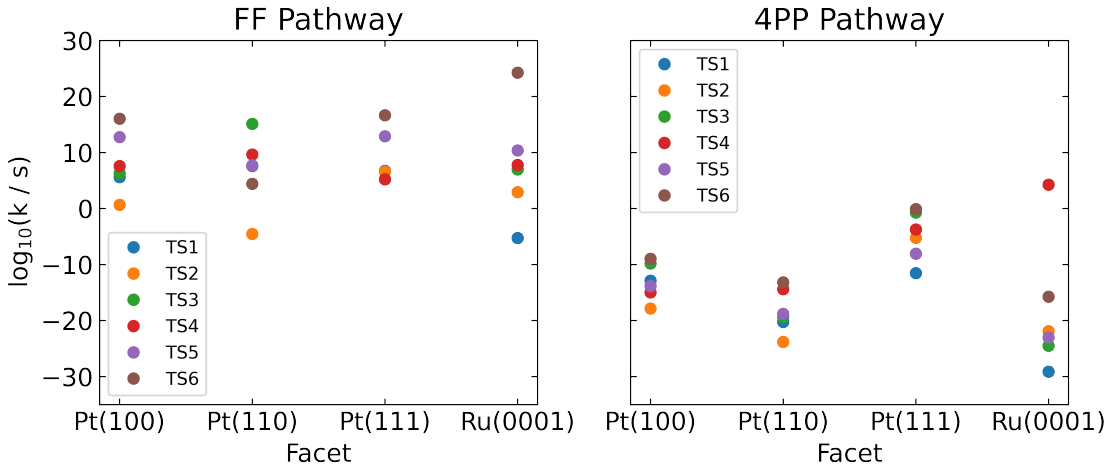

Figure 4.3: Zeorth order rate constants at 20°C for (a) FF to THFA and (b) 4-PP to PC on the four surface facets.

the thermodynamics of these reactions would be minimally impacted in that temperature range. The remainder of the analysis will only be conducted at 20°C.

4.3.2 Rate Constants

Rate constants were further calculated from the activation barriers via Eq. 4.6. The constants provided in Figure 4.3 are tabulated for each TS, as labeled in Fig 4.1, and facet for the FF and 4-PP pathways, respectively. The FF pathway rate constants (Fig. 4.3a) vary from a minimum of 5.4E-06 s^{-1} (Ru(0001) TS1) to a maximum of 1.8E24 s^{-1} (Ru(0001) TS6). Most constants are between approximately 1E4 and 1E15 s^{-1}. Due to the larger activation barriers, the rate constants of the 4-PP pathway are much smaller than those of the FF pathway. In Fig. 4.3b, the minimum is as low as 7.7E-30 s^{-1} (Ru(0001) TS1) and the maximum for platinum surfaces is 0.79 s^{-1} (Pt(111) TS6). Ruthenium sees a maximum rate of 1.8E04 s^{-1} (TS4), but is an outlier due to the relatively small activation barrier for that step. Most rate constants are smaller than 1E-10 s^{-1}.

As in discussed in Chapter 3 and observing the intermediate state free energies of Fig. 4.1, the FF and 4-PP reaction free energies are comparable. The lower state free energies of the 4-PP pathway than those of the FF pathway would initially suggest thermodynamic favorability. However, combining the tendancy of the 4-PP pathways to increase in energy

along the reaction and the larger barriers, the FF pathway is predicted to be more thermodynamically favored on the Pt/Ru catalyst.

The rate constants of the FF pathway are generally also predicted to be higher than those of the 4-PP pathway. The minimum constant in 4-PP to PC is 24 orders of magnitude smaller than the minimum in FF to THFA. The maximum constant in FF to THFA is also more than 20 orders of magnitude larger than that of the 4-PP pathway. The median rate constant across the facets is similarly larger for the FF pathway than the 4-PP pathway. These comparisons suggest that in addition to thermodynamic favorability of the FF to THFA path, it is also kinetically favored.

4.3.3 Potential Dependence

In the electrochemical hydrogenation reactions, there can be further implications from applied potential on the reaction pathways. First, the equilibrium potential of the reactions were determined. A reaction's equilibrium potential, U_0, is the potential at which the reversible electrochemical reaction is in equilibrium. An equilibrium potential is calculated for each reaction step.[93] At a potential of U_0, the forward and reverse reactions proceed at a rate of k_0 s^{-1}. These values are further used to predict potential dependent rate constants. In Figure 4.4, the rate constants are provided as a function of potential for each reaction step on the facets, as calculated by Eq. 4.11. The equilibrium potential and rate constant of each step is presented as a point.

On Pt facets, U_0 for FF reactions is generally around 0 V_{RHE} with a handful of reactions finding equilibrium around -0.5 V_{RHE}. 4-PP reactions exhibit equilibrium around similar potentials, but are slightly more negative than that of FF reactions. On Ru, most equilibrium potentials occur near the same potential as the same reaction on Pt, but some steps exhibit substantially more negative equilibrium potentials as low as -2 V_{RHE}. This indicates that around an applied potential of 0 V_{RHE}, the reactions on platinum will be pushed forward in their equilibrium while a more negative applied potential is required to have the same effect on Ru. While the FF pathway reactions have a slightly more positive equilibrium potential than those of the 4-PP reactions, equilibrium conditions are close for most steps indicating that some competition may be expected between the pathways at moderately

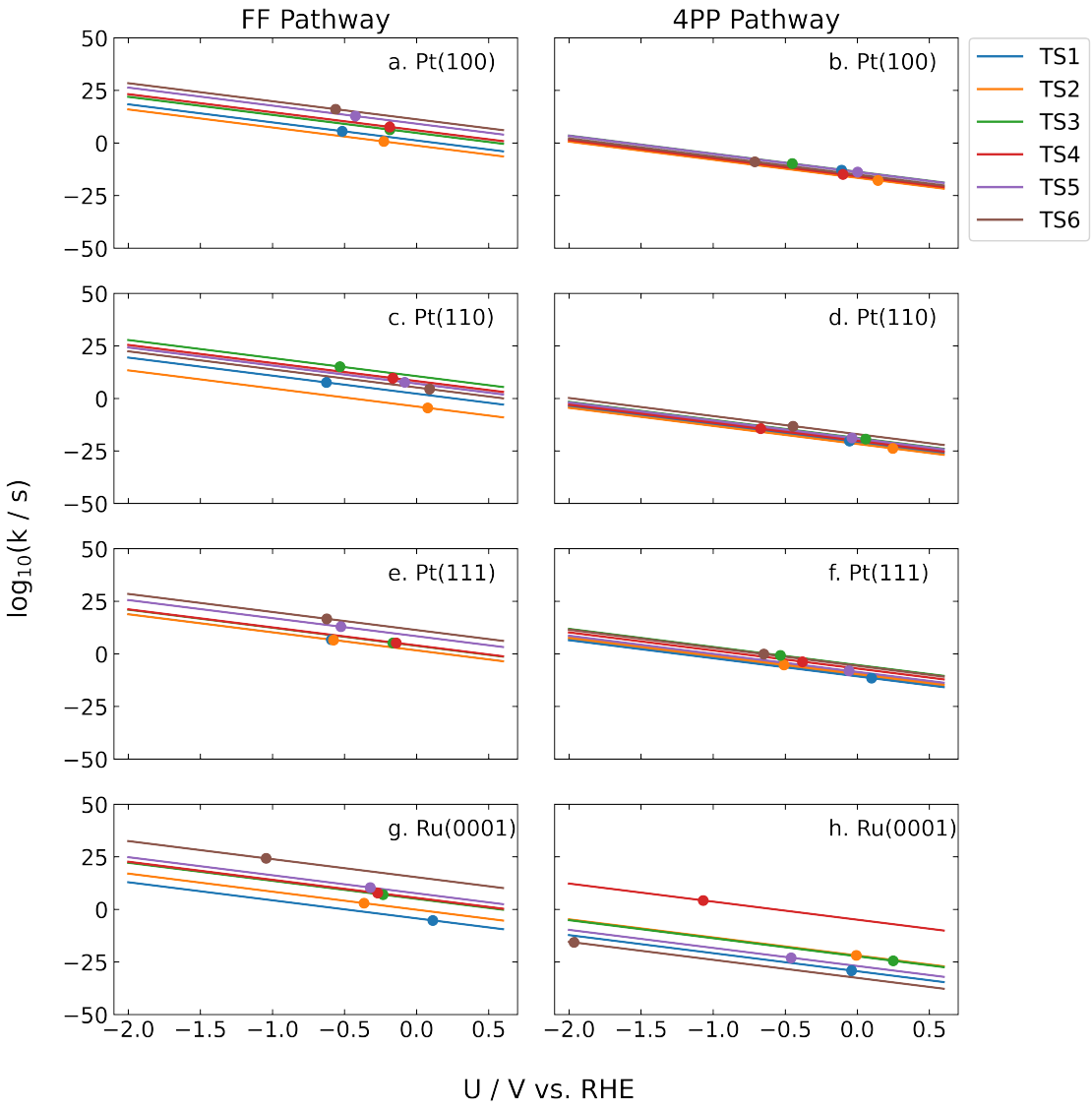

Figure 4.4: Potential dependent rate constants at 20°C for (a,c,e,g) FF to THFA and (b,d,f,h) 4-PP to PC on the four surface facets.

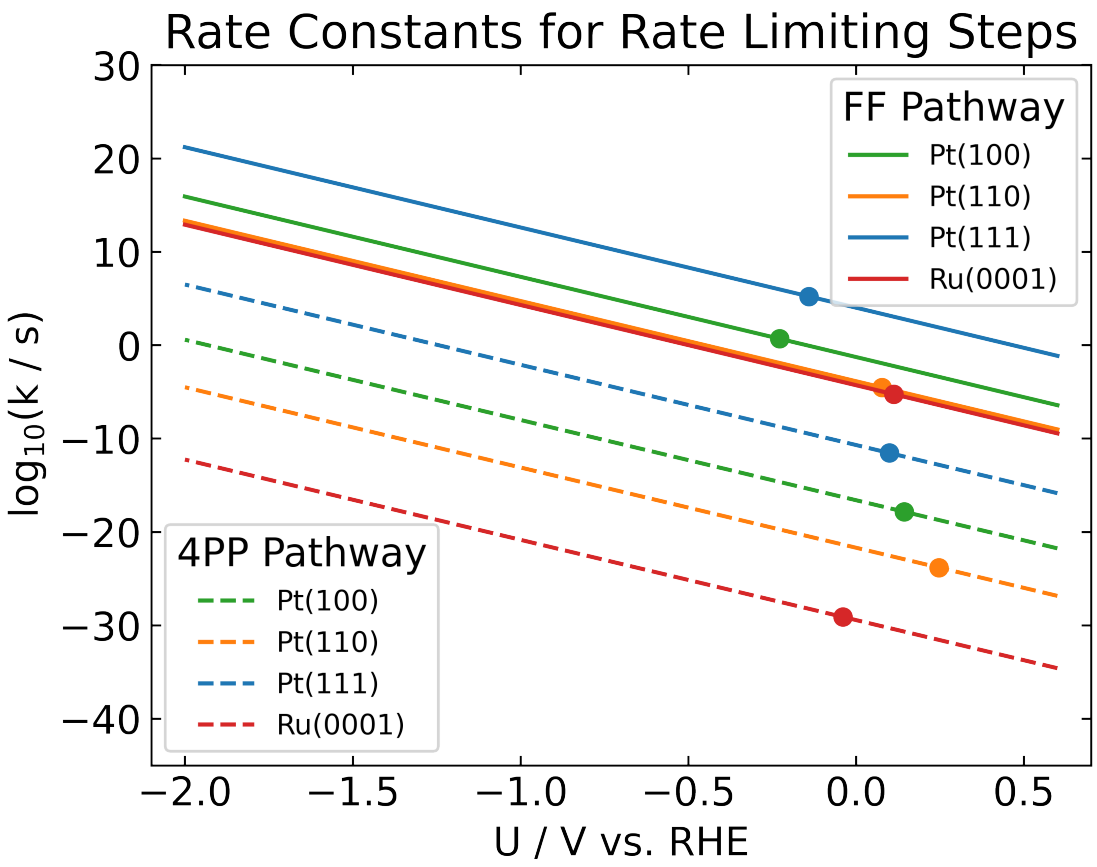

Figure 4.5: Effect of potential on the zeroth-order rate constant of the rate limiting steps at 20C in the FF pathways (solid lines) and 4-PP (dashed lines) pathways on the four surface facets. Equilibrium for each rate limiting step is marked as a point.

negative applied potentials. At any given potential, the rate constants are larger for FF reactions, and may be sufficient to overcome the competition with 4-PP reactions near equilibrium conditions.

The favorability of a given net reaction will be dictated by the rate limiting step (RLS) within that mechanism. For the FF and 4-PP pathways on a given facet, the rate limiting steps are the transition states that exhibit the lowest rate constant or slowest reaction. The rate constants of rate limiting steps for the FF (solid lines) and 4-PP (dashed lines) pathways on each facet are compared in Figure 4.5. On all of the facets, the FF pathway RLS are faster than those of the 4-PP pathway by 10 to 20 orders of magnitude. If these reactions were experimentally zeroth-order, this would indicate that, across a range of applied potentials, the FF pathway is kinetically favored over 4-PP reactions.

4.4 Conclusions

The thermodynamic investigation on the inhibitionary effect of furfural presence on 4-propylphenol ECH was further probed here by addition of activation barrier calculation. Linear scaling relationships were utilized to make rapid predictions of the reaction barriers in the hydrogenation of FF to tetrahydrofurfuryl alcohol and the hydrodeoxygenation of 4-PP to propylcyclohexane. The 4-PP pathway exhibits large barriers and positive reaction energies. While the FF to THFA also has some positive reaction energies, the barriers are lower of that than the 4-PP path. Additionally, the FF barriers generally decrease along the reaction, whereas the 4-PP path barriers stay relatively consistent. Due to the lower barriers and more favorable reaction energies, the FF to THFA reaction is predicted to be more thermodynamically favorable than the 4-PP to PC reaction on the Pt/Ru catalyst.

Thermodynamic analysis was complemented by an analysis of kinetic rate constants. Here, the zeroth order rate constants corresponding to each transition state were calculated from the respective activation free energy. Generally, the 4-PP reactions exhibit smaller rate constants than the FF reactions. The difference in rate constants between the two pathways are as large as 20 orders of magnitude with those of the FF path being closer to 10^{10} s^{-1} and the 4-PP path constants are lower than 10^{-10} s^{-1}. Therefore, the FF to THFA reaction is predicted to also be more kinetically favorable than the 4-PP to PC pathway.

Through calculation of equilibrium potentials for each reaction step, potential dependent rate constants and rate limiting steps (RLS) are determined. Most equilibrium potentials occur near the range of 0 V_{RHE} and -0.5 V_{RHE} for the FF reactions. Equilibrium potentials of 4-PP reactions are generally similar, but slightly more negative. For a given pathway on a given facet, the rate limiting step is the transition state with the slowest rate constant across the potential range of -2 V_{RHE} to 0.6 V_{RHE}. For both FF and 4-PP pathways, the rate limiting step is either the first or second reaction step. Comparing RLS of FF and 4-PP pathways on a given facet, the FF pathways exhibit faster rates by up to 20 orders of magnitude. This further suggests the kinetic favorability of FF reduction to THFA over 4-PP ECH.

This work lays the groundwork toward a dynamic model of the inhibition of 4-PP ECH

by FF ECH. The predicted potential dependent rate constants may be applied to a potential dependent dynamic micro-kinetic model. To further scale up the model, dimensionality due to non-zeroth order reactions would need to be considered. In line with this ambition, reaction rates should be validated through experimental methods.

Chapter 5

Toward Validation of a New Bioink for 3D Printed Cell-Laden Tissue Scaffolds

5.1 Introduction[1]

Engineered biomaterials are a current focus in medical applications to enhance the success of the treatments. One approach is in the development of high-performance materials to treat bone degradation resulting from osteoporosis.[106] Traditional methods for bone tissue generation take healthy tissue from elsewhere in the body to artificially produce new tissue.[179] This leaves the patient with further physical trauma in multiple locations. Alternatively, biomaterials may be developed that promote tissue generation without requiring additional extraction from the patient's bone.[106] Suitable materials must meet several criteria to be viable options for these applications, especially if the material will be implanted in humans. Tissue-regenerative materials must exhibit biocompatibility, maintain stability in physiological conditions, mimic the extracellular matrix with structure tunability, and promote cell viability.[107–110] Collagen, and the cheaper alternative, gelatin, meet most of the requirements as a biomaterial.[108]

While initially attractive, gelatin degrades at physiological temperatures (˜37C).[111] To overcome stability constraints, gelatin methacryloyl (GelMA) was developed to enhance ma-

[1]This work was completed in collaboration with Victoria Toomajian, Anthony Tundo, Nureddin Ashammakhi, Christopher Contag

terial stability by bonding methacrylate to the gelatin backbone in place of lysine groups. Chemical modification of gelatin increases the melting point above physiological temperatures.[111] GelMA is stable at physiological temperatures (37C)[111], whereas gelatin melts around 32C.[180] Hydrogels of GelMA also take longer to experience the same degree of mass loss as gelatin.[107,110] To address cell viability, GelMA was further modified by chemical linkage to silver-doped bioactive glass (Ag-BG).[112] Bioactive glass is a traditional component in tissue-regenerative materials with appreciable cell viability properties.[106] The addition of silver has also been shown to increase the antibacterial properties of biomaterials.[109,112] Chemically linked GelMA-AgBG (GAB) is therefore hypothesized to have superior cell viability properties to GelMA alone.

In tissue engineering, a three-dimensional (3D) template, termed "scaffolds", can help guide and support the growth of tissue.[106] Additive manufacturing enables customized scaffold design - making this solution more versatile. Some of these methods are fused filament fabrication (FFF)[109], polymer foam, and extrusion printing.[106] Currently, extrusion printing of bio inks is a prevalent approach to obtaining cell-laden scaffolds.[181–185] Extrusion printing enables control of scaffold structure while also allowing for an environment capable of cell viability in terms of media presence through the extrusion process.[183,186,187] In extrusion printing applications, some substrates can also be further strengthened through photo polymerization, or UV cross linking. In these cases, the polymer structures become linked by a photo-initiator which creates a more complex matrix structure and a scaffold with enhanced mechanical properties.[188]

Previously, GAB was developed for 3D printing applications to leverage the photopolymerization capabilities of GelMA and antibacterial properties of Ag-BG.[110,188] In 2021, Marsh et al. reported rheological and degredation properties of the GAB bioink in comparison to inks of GelMA alone and a nanocomposite of GelMA and Ag-BG nanoparticles.[110] The viscosity, and storage and loss moduli determined for GAB suggest that the material is a viable option for a bioink in 3D printing applications. The rehological parameters of GAB were also higher than that of GelMA alone, suggesting that GAB will be more resistant to shear forces and better suited to protect the cells than GelMA. Further, the GAB was shown to swell less and retain more mass over time than the GelMA or nanocomposite. These char-

acteristics lead to the hypothesis that GAB will be a superior polymer for 3D bioprinting applications. However, 3D bioprinting with a cell-laden GAB bioink was not reported.

Beyond generation of stable scaffolds, biomaterials must be assessed for biocompatibility. This is accomplished by tracking the viability of cells incorporated in to the bioinks through extrusion printing and in the time following. In bone tissue regeneration applications, fibroblast (3T3) cells can be incorporated for validation purposes. Fibroblasts are useful because they are very stable and have been engineered to express biolumiesence while alive. Specifically, 3T3 cells express firefly bioluminescence (fLuc2), in which live cells will emit light at a wave length of approximately 560 nm.[189,190] Luminesence is the result of the fLuc2 catalyzed D-Luciferin oxidation in the presence of ATP from the cells and oxygen.[189] The D-Luciferin and cell media are added to the well of a printed scaffold immediately after printing to initiate the reaction. Radience measurements are collected at multiple time points spanning from a few minutes post print to multiple days post print to assess the time dependence of cell viability. The magnitude of the radiance indicates the number of live cells within a scaffold as a direct correlation to the amount of ATP present.

This work aims to extend that of Marsh et al. through comparison of cell viability in extrusion printing of GelMA and GAB against a control of blended GelMA + AgBG bio-inks. GelMA and GAB materials were first synthesized and characterized as reported in the literature. Then, extrusion printing parameters for the three bio-inks were optimized. Upon printing parameter optimization, cell viability studies were executed with 3T3 cells in GelMA, GAB, and blend bio-inks. GAB bio-ink is hypothesized to exhibit enhanced cell viability during extrusion printing compared to GelMA and blend bio-inks. Enhanced properties of GAB will exemplify its superiority as a novel biomaterial. Here, however, a combination of rheological inconsistencies and material acidity resulted in a non-viable cellular environment across the GelMA, GAB, and Blend inks. Future work requires improvement of material synthesis protocols to improve the ability to be reconstituted into an ink with a pH closer to 7. Nevertheless, the work herein reports optimization of printing parameters and cell viability studies for the prepared materials. Additional methods utilized in efforts to overcome the challenges of the current materials are also reported.

5.2 Methods

5.2.1 Material Synthesis

Scaffold generation by 3D bio-printing (3DBP) uses two synthesized materials, GelMA and GAB. The benefits of chemically linking AgBG to GelMA are elucidated by a standard blend of GelMA and AgBG ink. GelMA and GAB are synthesized following previously established protocols.[110] Briefly, GelMA was synthesized by the addition of methacrylic anhydride (MAA) to Type A, 300G bloom strength gelatin dissolved in DMSO. GelMA was precipitated from DMSO using toluene in an amount of three times the DMSO volume. The precipitate was rinsed three times and then dissolved in one liter of DI water for 24 hours. Water and any remaining solvent were removed by lyophilization (i.e. freeze-drying). We deviate from reported protocols[110] by using a -84C lyophilizer instead of operating at -50C for the materials used in these studies.

GAB synthesis adds Ag-BG sol steps to the GelMA protocol. Ag-BG sol is comprised of methanol (MeOH), tetraethyl orthosilicate (TEOS), and triethyl phosphate (TEP) solvents. Upon combination of solvent, solids are added in order: aluminum nitrate nonahydrate (AlNT), silver nitrate (AgNT), and calcium nitrate tetrahydrate (CaNT). GelMA synthesis through the addition of MAA is done separately during the Ag-BG sol process. Chemical linker (3-Glycidyloxypropyl)trimethoxysilane (GPTMS) is added to the GelMA solution after MAA is allowed ample time to react with gelatin. Ag-BG sol is added with water to the GelMA solution, allowing a day for the reaction. The resulting GAB solution is precipitated, rinsed, and lyophilized as previously described. The overall scheme is shown in Fig 5.1.

5.2.2 Material Characterization

GelMA and GAB materials are characterized via several means. The chemical structures of each material are characterized by Fourier-transformed infrared spectroscopy (FTIR; Jasco FT/IR-4600) and proton nuclear magnetic resonance (H-NMR; Agilent DirectDrive2 500 MHz NMR spectrometer)[110]. FTIR spectra were collected on reflected chemical bonds present in the materials. H-NMR is primarily used to observe the degree of substitution of

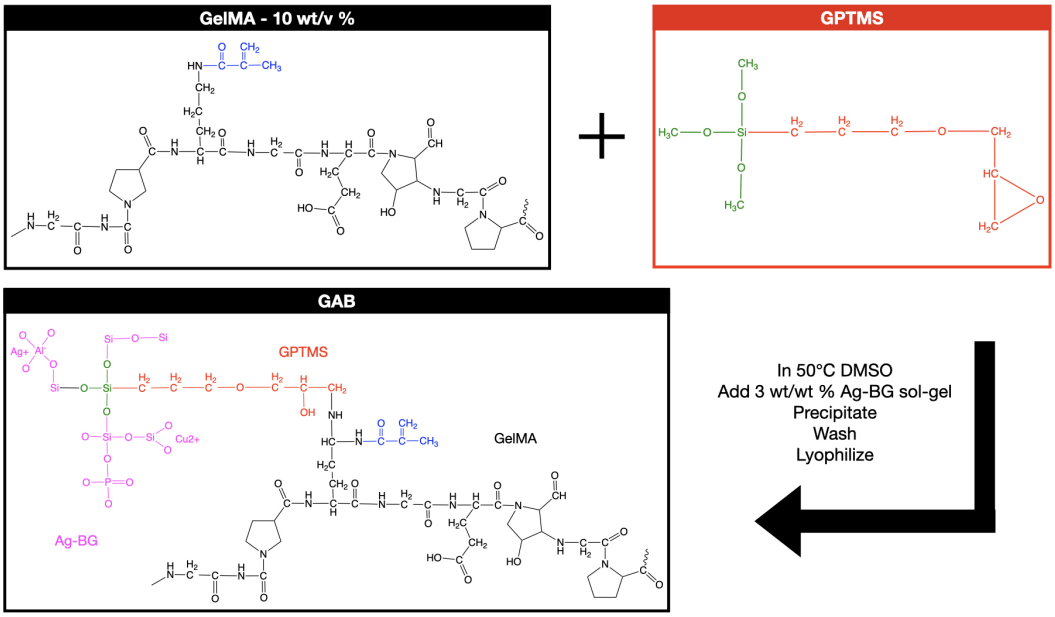

Figure 5.1: GAB Synthesis by reaction of GelMA and GPTMS with AgBG solution.

lysine by methacryloyl groups. To collect the spectra, 50 mg of each material was dissolved in 1 mL of deuterium oxide samples.

Microscopic morphology and distribution of elements are assessed by scanning electron microscopy and energy dispersive spectroscopy (SEM-EDS). Samples were prepared for imaging, as reported previously[110]. Briefly, the solid materials first underwent graded ethanol dehydration. Then, the solids were further dried by critical point liquid CO_2. Once dehydration was complete, the solids were mounted and coated with Osmium. SEM (JEOL 6610LV) images were collected using a 5 kV beam voltage. EDS (Oxford EDS) spectra were collected at a 20 kV beam voltage.

5.2.3 3D Printing and Bio-Printing

This project's printing consists of two phases using an Allevi 3 printer. Phase 1 includes parameter optimization for printing synthesized GelMA, GAB and a control blend of GelMA with Ag-BG nanoparticles. To enhance the mechanical properties of the scaffolds, photo-polymerization of the substrate material was introduced via a photo-initiator component and applied UV light during the printing process. Allevi recommends lithium phenyl (2,4,6-trimethyl benzoyl) phosphonate (LAP) as a photo-initiator, so Allevi GelMA is also printed

with LAP for validation purposes.[1,191] Synthesized materials are printed with VA-086 photo initiator, as in previous work.[110] Phase two consists of incorporating cells into inks and executing cell viability tests on printed scaffolds.

Bioinks were initially prepared as Allevi recommends.[1] Briefly, 0.1 g/mL GelMA is suspended in 0.1 M N-[2-Hydroxyethyl]piperazine-N-[2-ethanesulfonic acid] (HEPES) buffer with 5 mg/mL photoinitiator. Upon consistent suspension, inks were collected in a capped syringe and left to rest either at room temperature for at least 2 hours or placed on ice for 15 minutes. Before extruding, the syringes were given a minimum of 15 minutes to equilibrate at 22C in the printer extruder. Initially, inks were printed using recommended and reported values for details of the extrusion mechanism and print. Regarding the extrusion process, tunable parameters include the velocity of the tip during printing, or print speed, temperature of the extruder body which is held constant during prints, and the pressure applied to extrude the ink. Print specific parameters include the height of each print layer, and UV crosslinking intensity and time. As trials proceeded, other optimum parameters were determined. Recommended, reported, and optimized parameters are compared in Table 5.1.

Table 5.1: 3D Printing Parameter Comparison.

Parameter	Allevi Recommendation[1]	Reported[5]	Optimized Parameters
Layer Height (mm)	0.45	0.5	0.5
Print Speed (mm/s)	5	4	10
Extruder Temperature (C)	22	27	22-27
Pneumatic Pressure (psi)	18-28	12	5-15
UV Crosslinking Conditions	15% intensity for 10s	120s	45% intensity for 60s
Nozzle Gauge	27	27	27
Bioink Concentration (g/mL)	0.1	0.1	0.15

To mimic an extracellular matrix, scaffolds are printed as 10 mm by 10 mm grids. In this work, only one layer is printed with a height of 0.5 mm, as defined in Table 5.1. However, many layers of the grid may be stacked to produce a 1 cm^3 cube scaffold. The template in Fig 5.2 was provided to the Allevi software as an additional input for printing.

In 3DBP trials, Fibroblast (3T3) cells were incorporated into the bio-inks in a quantity of approximately 1.5×10^6 cells per mL of bio-ink. The solvent was 0.1 M HEPES. Cell viability was assessed via bioluminescence measurements. The radiance was read via a Perkin-Elmer

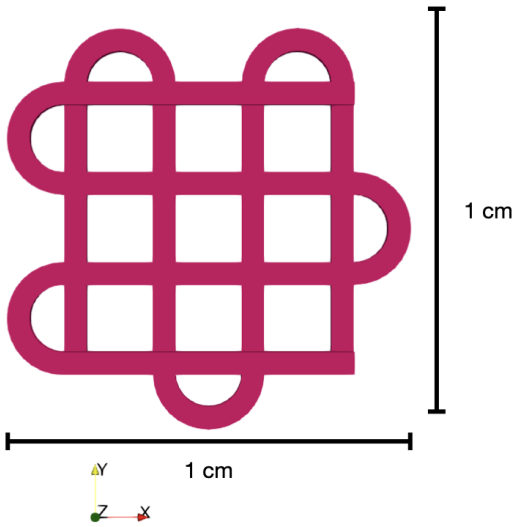

Figure 5.2: Matrix template used for 3DP and 3DBP.

in vitro imaging system (IVIS). A the light was filtered to collect luminesence readings around 560 nm.[189] Samples were imaged 5 and 10 minutes after D-luciferin addition immediately after printing and at the 24-hour mark.

5.3 Results and Discussion

5.3.1 Material Characterization

Chemical structures of gelatin, GelMA, and GAB were characterized by FTIR and H-NMR.[110] NMR Spectra are provided in Figure 5.3a. The figure inset zooms in on the location of the lysine peak around 2.8 ppm. The absence of the lysine peak around a chemical shift of 2.8 ppm indicates complete substitution.[110] Both GelMA and GAB lack lysine peaks, indicating nearly 100% substitution. Additionally, a peak just above 3 ppm appears in gelatin and is reduced in the synthesized materials. This peak is suspected to be proline and hydroxyproline amino acids, which may also be involved in the reaction.[192,193]

Characterization of the materials by FTIR (Figure 5.3b) determines if solvents were removed, confirms that GAB maintains the base GelMA structure, and confirms characteristic peaks of Ag-BG sol in GAB.[110,113] Some characteristics of DMSO and MAA appear most prominently in both GelMA and GAB. Namely, two additional peaks around 1015 cm^{-1} and

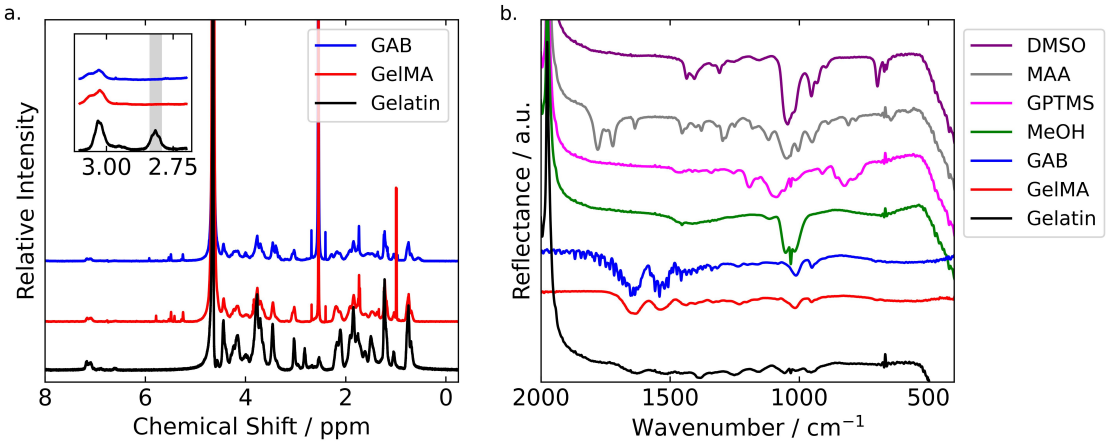

Figure 5.3: (a) NMR Spectra of synthesized GelMA and GAB, and gelatin.

950 cm^{-1} appear in both materials that were not reported in the literature.[110]. This may be indicative of insufficient solvent extraction during toluene precipitation and lyophilization. Ideally, any residual solvent not extracted during precipitation would evaporate while dissolving the precipitate in water to prepare for lyophilization. The presence of DMSO and MAA peaks indicates that insufficient solvent extraction occurred during these syntheses. It is, however, promising that the GAB has maintained the characteristic amide I-III peaks near 1650 cm^{-1}, 1500 cm^{-1}, and 1450 cm^{-1}, which indicates that the GelMA structure is preserved.[110] Additionally, there are hints of a broad peak around 800 cm^{-1} for GAB. That peak represents a Si-O bond and is indicative of Ag-BG.[113]

The surface morphology and distribution of elements within the GelMA and GAB materials were assessed by SEM-EDS. As shown in Fig 5.4a, GelMA has pores in the material visible at the micron level. The presence of the pores is crucial for dissolving or suspending the finished solid material to produce a bioink. Conversely, the GAB does not have visible pores at the 50 or 5 μm scales. The lack of pores may prevent the complete dissolution of the GAB because pores enable more rapid incorporation of solvent into the bulk material. Instead, a suspension of GAB particles in the HEPES buffer could be expected.

The EDS analyses of GelMA (Fig 5.4c&e) and GAB (Fig 5.4d&f) suggest that, in both materials, elements are homogenously distributed to the micron level. The GelMA has a homogenous distribution of C, N, and O, which is maintained with similar relative counts in the GAB. Additionally, the GAB has uniformly distributed Si and Ag with noteable counts

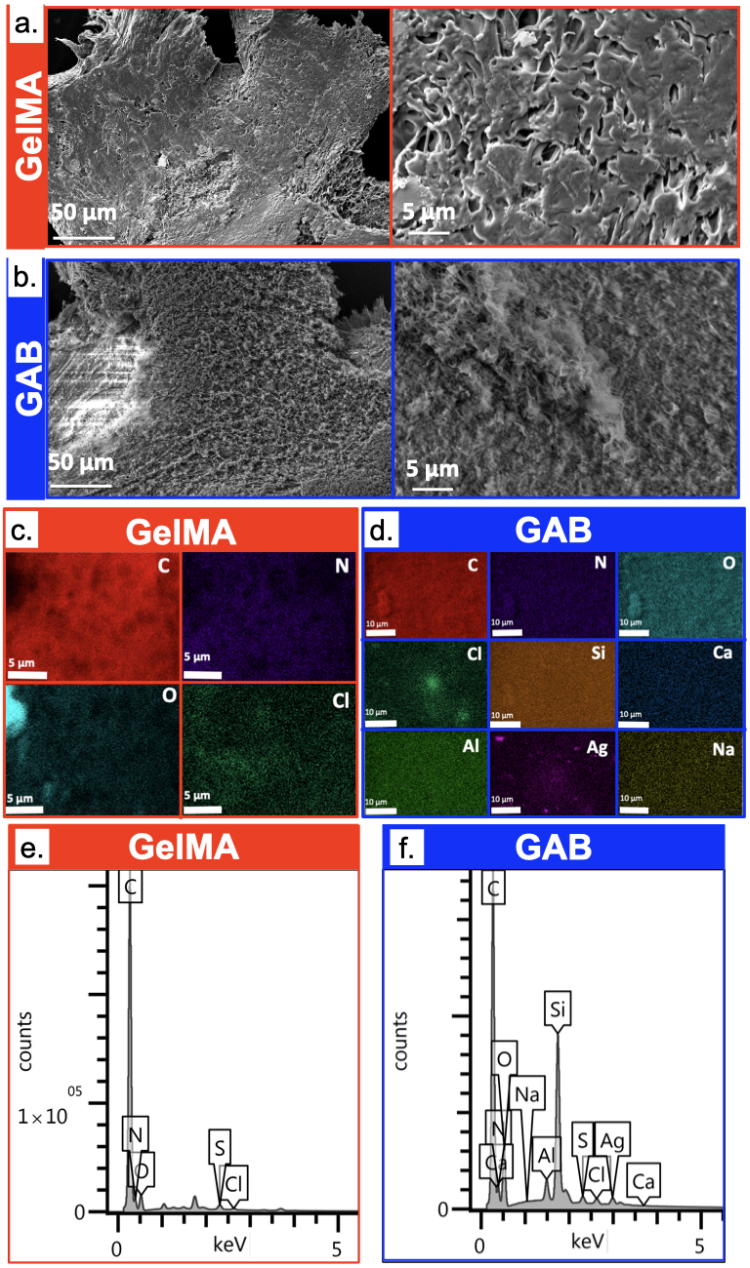

Figure 5.4: SEM (a,b), EDS imaging (c,d), and EDS spectra (e,f) of synthesized GelMA and GAB.

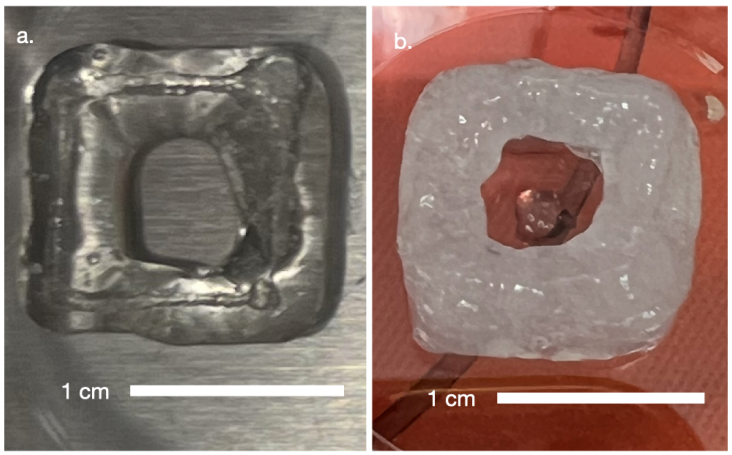

Figure 5.5: 1cm by 1cm squares 3D printed with optimized prrinting parameters and 0.1 mg/mL concentrations for (a) Allevi GelMA and (b) Synthesized GelMA bioinks.

of Si, specifically. This indicates a homogenous linkage of AgBG to the GelMA backbone.

5.3.2 Optimization of 3D Printing Parameters

Optimization of biomaterials in extrusion printing included trials of purchased and synthesized GelMA at concentrations of 10 wt/v%. During printing trials, suspensions had low viscosities which caused immediate release of syringe contents with applied pressures greater than 10 psi instead of shaped prints. To compensate for liquid behavior, specific deviations from printing parameters in the literature were made. Namely, a combination of low pressures and faster printing speeds produced a more controlled shape print. Sample prints of Allevi GelMA and synthesized GelMA at specified parameters are shown in Figure 5.5.

Printed Allevi GelMA served as initial validation on a handful of parameters such as print speed, pneumatic pressure, and extruder temperature. However, the inks of synthesized materials were less viscous than the purchased GelMA ink which resulted in low resolution of prints. While the print in Fig 5.5a exhibits some spreading of the ink, the shape is overall consistent with comparable wall widths. The wall widths of the synthesized GelMA print in Fig 5.5b are not as consistent marked by the jagged inner square shape. Some synthesized GelMA ink was also prematurely released in the center of the square shape, further indicating

low viscosity of the ink. To obtain greater control over the print resolution, concentration and UV Crosslinking conditions were further optimized. Additionally, the purchased GelMA produced a transparent bioink whereas the synthesized GelMA was more opaque. This indicates that the synthesized materials do not completely dissolve, but are a suspension of polymer particles in the HEPES buffer.

As shown in Fig 5.6a, a matrix was achieved by increasing ink concentration to 15 mg/mL and UV intensity to 45%. These optimized parameters allowed the synthesized GelMA and the GelMA + AgBG Blend control to print a mesh successfully. However, when the printing temperature was also increased to 27C, the GAB material was not printable and continuously clogged the needle tip due to inconsistent suspension. To overcome this, GAB inks were produced with a 1:1 ratio of GAB and GelMA with the intent of improving the printability of GAB without substantially affecting the cell viability properties. While extrusion of ink was made possible for GAB in this mixture, these scaffolds did not have mesh resolution like GelMA alone or the Blend control. Imaged of the most optimal prints of GelMA, Blend, and GAB+GelMA are provided in Fig 5.6.

The printing issues for GAB bio-inks resulted from an inability of the material to be reconstituted into the HEPES buffer. The remaining solids clogged the tip during printing. The material's pores can collapse when the frozen solid melts during the lyophilization process. This results in a stiff plastic that becomes difficult to dissolve. Addition of HCl in amounts between 10 and 48 μL per mL solvent was used to improve GAB dissolution. The acid helped to some extent in dissolving the GAB, but was not a complete solution. A more careful lyophilization of a fresh synthesis of GAB could produce a porous structure, but was not possible within the time frame of this project. Printing and bioprinting proceeded with the parameters detailed in Table 5.1 for GelMA, Blend, and GAB+GelMA mixture inks.

5.3.3 3D Bioprinting

3D Bioprinting (3DBP) describes conditions in which cell-laden inks are extruded. These trials incorporated fibroblast (3T3) cells into the bio-inks, and initial 3DBP trials utilized otherwise unmodified bio-inks. The HEPES buffer doubles as a pH indicator: A pink color indicates approximately neutral conditions, but it turns yellow when the media is acidic.

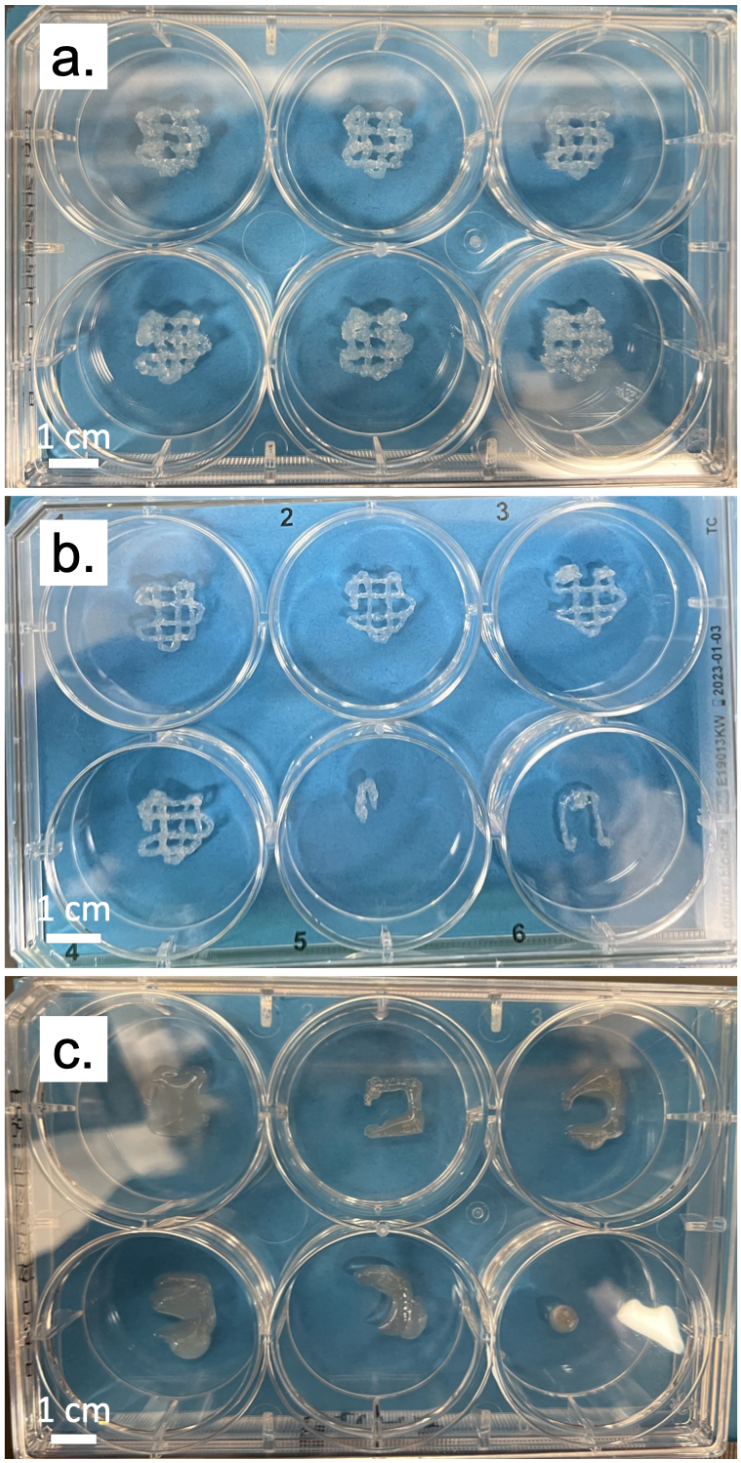

Figure 5.6: 3D prints under 15 mg/mL concentration and 45% UV Intesity conditions of (a) GelMA, (b) GelMA + AgBG Blend, and (c) GAB + GelMA Blend.

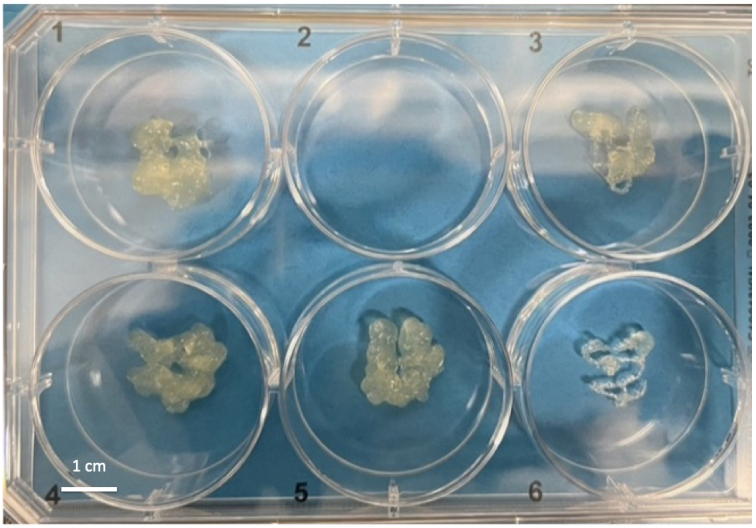

Figure 5.7: Initial 3DBP Samples of 3T3 Cells in a GelMA + AgBG Blend bio ink.

The media must be maintained around neutral conditions for cell viability. When acidic media were detected, the inks were neutralized by adding sodium bicarbonate.

5.3.3.1 Initial 3DBP with Blend Bioink

Initial trials of 3DBP were done with the GelMA + AgBG blend bioink. The scaffolds shown in Fig 5.7 are noticeably yellow, indicating acidic media. In these trials, the blend, GelMA, and GAB+GelMA were all measured to have a pH of approximately 6. The 3T3 cells prefer an environment pH in the range of 7.0 - 7.6.[194] No viability was recorded among these samples, likely because of ink acidity.

5.3.3.2 3DBP with Neutralized Bioinks

To return the inks to a neutral pH, 1 to 5 mg increments of sodium bicarbonate were added before cell incorporation. The pH was measured after each addition. Neutralization continued until pH 7 was achieved, as measured by pH strips. For the GelMA and blend inks, approximately 25 mg of sodium bicarbonate was required to achieve neutral conditions. The GAB+GelMA ink required up to 50 mg of sodium bicarbonate. Cells were incorporated upon neutralization, and the inks were prepared for printing.

Sample prints of neutralized inks are shown in Fig 5.8. As shown in Fig 5.8a&b, the

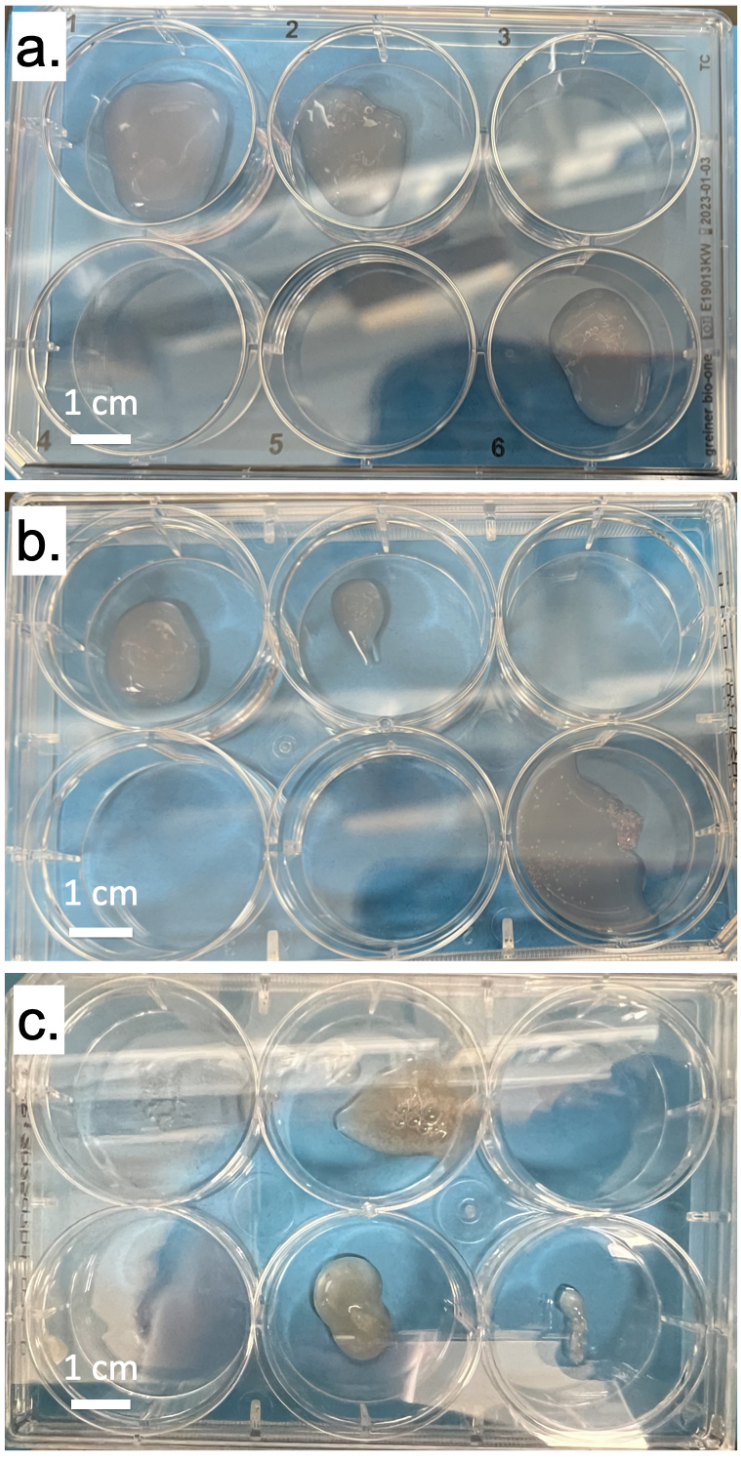

Figure 5.8: 3DBP Samples of 3T3 cells in neutralized (a) GelMA, (b) GelMA + AgBG Blend, and (c) GAB + GelMA Blend.

GelMA and GelMA + AgBG blend prints are pink, but the mesh resolution was lost. There is a finite window of time and temperature in which the gelling of the inks is optimal for printing.[1,110] The prrinting window may have been surpassed due to the processing required for neutralization, cell incorporation, and cooling. This would result in a low-viscosity fluid that would print like the samples shown. The GAB+GelMA blend performs consistently with the acellular GAB trials in which the GAB does not suspend completely and clogs prevent consistent printing. Like the GelMA and control blend, the GAB+GelMA was less viscous after neutralization. The GAB+GelMA ink also still had a yellow hue, which indicates a non-neutral pH. Although initial pH strip readings suggested a pH of approximately 7, double the amount of sodium bicarbonate was required for neutralization compared to the GelMA and blend inks. The buffing capacity of HEPES may have been overwhelmed by the excess sodium bicarbonate once equilibrium was achieved.

5.3.4 Cell Viability

The cell-laden samples in neutralized ink were assessed for cell viability immediately after printing and 24 hours later. The luminescence readings are summarized in Figure 5.9. Only the GelMA samples express viability immediately after printing (Figure 5.9a-c). Some of the cells survived the first day, but viability was substantially diminished after 24 hours (Figure 5.9d).

The lack of cell viability in these materials could be due to a combination of factors. The first, and most apparent, is the acidic nature of the acellular inks. The materials themselves could also be toxic due to residual toluene present from the synthesis process. These factors alone can kill cells but also may contribute to non-optimal rheology for printing. The inks were capable of achieving a gel-like consistency. However, if printing was delayed or extended over four or so hours from the time that the ink was print ready, the viscosity was notably decreased. Although the low viscosity of the inks required less than standard printing pressures, the extrusion still exhibits a large force on the inks and could be an additional contributor to the cellular demise. Further work would need to tease apart the interplay of material and process complications. In particular, the synthesis process should be reevaluated to remove toluene and adjust the pH to a neutral level.

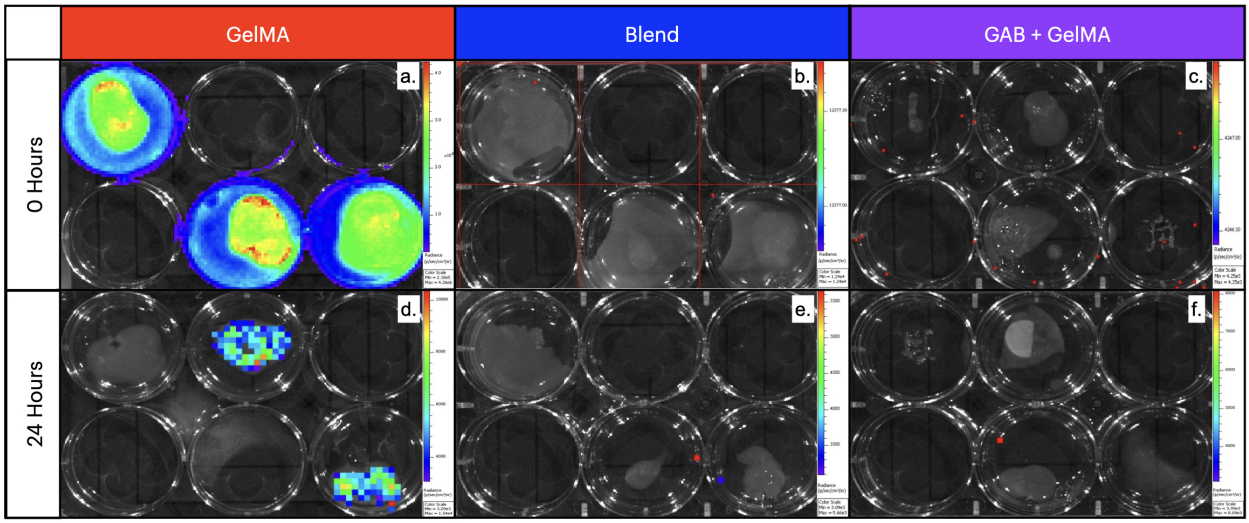

Figure 5.9: Luminesence readings of 3T3 cells immediately after printing bioinks of (a) GelMA, (b) GelMA + AgBG Blend, and (c) GAB + GelMA Blend and after 24 hours (d-f).

5.4 Conclusions

In conclusion, GelMA and GAB were synthesized and enabled some inks that were 3D printable in acellular trials. Most characteristics of the materials were consistent with those previously reported, but synthesized GAB did not have visible pores at the micron level. This is suspected to cause challenges during resuspension as a bio-ink. The materials were further found to produce acidic inks and may also be toxic due to residual toluene. Both factors are suspected to have resulted in little to no cell viability

Initial extrusion printing trials of Allevi GelMA and synthesized GelMA suggest that 3D printing is viable. However, cellular printing with synthesized materials exposed several points of improvement. While GelMA and the Blend were printable in acellular trials, introducing cellular media resulted in lower viscosity inks that did not allow for mesh resolution. The rheology of the ink further changed upon neutralization before the incorporation of cells and resulted in an even lower resolution 3DBP. Rheological issues may be overcome by ensuring pH-neutral materials and careful lyophilization to enable more porous structures during synthesis. Revised material synthesis protocols and re-optimizing printing parameters are required for future work. More recent revisions to the material synthesis and printing protocols show promising results toward improved cell viability with GAB.

Chapter 6

Conclusions

This work takes a multi-scale approach to understanding engineering challenges in producing and optimizing biomaterials for versatile applications. Biomaterials can be broadly applied to enable advancements in medical treatments, energy production, and consumer products. Chapter 2 presents a finite difference model to predict transient behavior in the biocatalytic reaction cascade of the MDH-CS enzyme complex. Chapter 3 employs a first-principles thermodynamic analysis to assess the reaction mechanisms and cause of inhibition involved in the electrochemical upgrading of a binary mixture of bio-oil constituents furfural and 4-propylphenol. Chapter 4 utilizes linear scaling relationships to determine activation barriers and kinetic rate constants for the system presented in Chapter 3. Chapter 5 sought to validate a new gelatin-based bio-ink for the 3D printing of cell-laden scaffolds in tissue regenerative applications. Each topic demonstrates how we can learn from nature to engineer efficient solutions for various applications.

6.1 Enzyme-inspired Efficient Reaction Cascades

In Chapter 2, the dynamics of intermediate channeling in the malate dehydrogenase citrate synthase (MDH-CS) complex is modeled using a finite difference approach applied to a Markov state model. The model predicts lag times for the recombinant and mutant complexes comparable to their experimental counterpart. Surface transport was further assessed through analysis of specific active sites and paths. The paths on the recombinant complex exhibited comparable lag times, indicating similar efficiencies and insensitivity to path specifics. The mutant complex, however, exhibited more sensitivity to the reaction path and was predicted to have more significant variation in path efficiencies.

Previous work identified Path 1 from S_{M1} to S_{C1} as the most efficient path, which we have confirmed by analysis of surface occupancy. A path preference is more distinct in the mutant than the recombinant, where the surface occupancy and bulk OAA are higher for the mutant than the recombinant. The greater efficiency of the recombinant than the mutant is attributed to the recombinant's preference for Path 1 and a lower amount of OAA leaked to the bulk.

We conclude this work by briefly investigating the implications of reversible kinetics at MDH active sites in the recombinant complex. For a fixed concentration of reaction product NADH, the rate of CoA generation is predicted in channeling and free enzyme systems. The channeling system was significantly less sensitive to NADH presence than free enzymes. This is marked by a minimal change in CoA generation rate at high NADH concentration for the channeling system compared to the free enzymes.

6.1.1 Future Work

The model presented in Chapter 2 can handle many reaction and transport events efficiently while predicting the transient behavior of MDH-CS. However, some further development of this system, more broadly, may extend this approach to rapid and dynamic prediction of reaction cascade behavior. Regarding the MDH-CS system directly, intriguing results were determined while investigating the implications of the reversible reaction at MDH. Specifically, a maximum amplification of the CoA generation rate for the channeled system compared to free enzymes existed around moderate NADH concentrations. This may be attributed to the interplay of transport and reaction kinetics. Compared to the mutant, which has different MDH kinetic rates, a more thorough investigation of this aspect may reveal a reason for the maximum amplification of product generation. The design of efficient artificial cascades is promoted by understanding how to accurately tune this system to the highest performance.

Broad application of this technique for studying biocatalytic cascades still requires overcoming some computational limitations. The connectivity network describing intermediate transport calculated by a Markov state model enables consideration of transport in the finite difference model. However, building a MSM is computationally demanding. By applying

these methods to other biocatalytic cascades, one may be able to predict the general behavior of electrostatically channeling enzyme systems. Generalizing transport to overcome the computational demand of MSMs would enable a more rapid prediction of the interplay between cascade kinetics and surface transport for the design of efficient reaction cascades.[195]

6.2 Multiscale Modeling of Electrochemical Conversion of Biomass

In Chapters 3 and 4, computational and experimental methods were employed to assess the mechanisms that may cause inhibition of the electrocatalytic hydrogenation of 4-propylphenol to propylcyclohexane in the presence of furfural on a Pt/Ru electrode. Chapter 3 primarily targets the thermodynamics of adsorption and intermediate reaction states. DFT methods were used to predict the adsorption energy and reaction free energies of the 4-PP to PC and FF to THFA pathways stable and radical intermediates on Pt(100), Pt(110), Pt(111), and Ru(0001). Free energies and heats of adsorption were also determined experimentally for FF, FA, and MF by blocked hydrogen under potential deposition on a Pt electrocatalyst. The aqueous phase results are correlated to the gas phase and 1/16th coverage to compare with the free energies of adsorption predicted by DFT.

Computationally, the electronic adsorption energy of reactants 4-PP and FF are most competitive on Pt(110) and Ru(0001), and 4-PP always binds more strongly to a given facet. Where 4-PP and FF were competitive, the free energy of adsorption further favors 4-PP because of the increase in Zero Point Energy for larger molecules. Experimental free energies of adsorption on Pt support some conclusions determined through the computational assessment. MF, FF, and FA exhibit comparable binding strengths in the aqueous phase, but discrepancies arise when extrapolating to the gas phase. The isotherms of FF and FA are nearly identical and suggest that either molecule would completely block Hupd at higher organic concentrations than MF. Quantitatively, the experimental and computational results are dissimilar, which may be due to effects not accounted for in Henry's Law.

Predicted free energies of reactions along both pathways were further assessed for variable

applied potential. Reactions for both paths are most favorable on Pt(110) and competitive on Pt(100). The FF pathway requires less potential to have favorable reaction energies than the 4-PP pathway on each of the facets studied. Finally, FF proceeds to THFA via FA on all facets, as previous experiments suggested. The 4PP pathway also proceeds as expected on Pt facets but deviates to a propylbenzene derivative instead of the 4-propylcyclohexanol intermediate on Ru. The pathway reaction free energies and the adsorption energies of FF and 4-PP are competitive on Ru. Due to this, it is thermodynamically likely that FF would block the adsorption and reaction of 4-PP on Ru, resulting in a decrease in PC product.

Positive reaction energies suggest that more barriers exist in the 4-PP pathways than in the FF pathways. In Chapter 4, the activation free energy barriers are assessed. Linear scaling relationships correlate intermediate state energies to the activation energy to enable rapid prediction of transition state energy. The 4PP pathway exhibits larger barriers and more positive reaction energies than the FF to THFA path. The FF to THFA reaction is predicted to be more thermodynamically favorable than the 4PP to PC reaction on the Pt/Ru catalyst. The thermodynamic analysis was complemented by an analysis of potential-dependent kinetic rate constants calculated from the activation free energy of each transition state. Generally, the 4PP reactions exhibit smaller rate constants than the FF reactions. Therefore, the FF to THFA reaction is also predicted to be more kinetically favorable than the 4PP to PC pathway.

6.2.1 Future Work

The work presented in Chapters 3 and 4 sought to understand the complexities of interacting bio-oil molecules during electrocatalytic hydrogenation processes. Some details have been elucidated, which indicate competitive activity between furans and phenols. However, real bio-oil contains a much broader range of molecular species and likely involves several more interaction effects. In addition to considering activation barriers and solvation effects, the model needs to be scaled in time or space and in the number of interacting reaction pathways. Continually considering factors such as potential dependence might enable greater synergy between computational predictions and experimental results.

In Chapter 4, future research directions were initiated by predicting reaction rate con-

stants from activation barriers. This approach was also expanded to include potential dependence, enabling a transient FF and 4PP competitive reactions model. Experimental methods may also be considered to validate the predicted rate constants.[104] However, further considerations may need to compensate for the ability of computational methods to predict radical formation, whereas experiments target stable intermediates.

Similar studies of other bio-oil constituents would make it possible to predict the behavior of a real bio-oil, but it would be time-intensive. Predicting adsorption energies and reaction barriers by high-throughput means would expedite the prediction of reaction rate constants, enabling larger-scale models of interacting constituent molecules.

6.3 Manufactured Cell-Laden Tissue Scaffolds

In Chapter 5, validation of GAB as a new biomaterial was pursued in anticipation that GAB bioink has superior cell viability in 3D printed scaffolds for tissue regeneration applications. Initially, GelMA and GAB were synthesized in a consistent way with the literature. Most characteristics of the materials were consistent with those previously reported, but synthesized GAB did not have visible pores at the micron level. The lack of micropores in GAB may have contributed to the challenges faced during resuspension to produce bio-inks. The materials further resulted in acidic inks that may be additionally toxic because of residual toluene from the synthesis. These factors are suspected of causing little to no cell viability within the cell-laden scaffolds.

Initial extrusion printing trials of Allevi GelMA and synthesized GelMA suggest that 3D printing is a viable approach. Comparable mesh resolution was achieved with synthesized GelMA compared to the purchased GelMA. Similarly, the control GelMA - AgBG blend ink yielded mesh resolution. Due to the reconstitution challenges with the GAB material, some resolution was only achieved when GAB was mixed with GelMA. In acellular trials, nearly optimal printing parameters were determined for the GelMA, but the GAB presented challenges that required further optimization. Cellular printing with synthesized materials exposed several more points of improvement.

6.3.1 Future Work

Several aspects of further work are required to validate GAB as a viable and more effective bio-ink. Many of these items may be related to the synthesis process. The acidic and toxic nature of the materials was hypothesized to have caused low cell viability. This may be overcome by incorporating a dialysis process within the synthesis to exchange potentially problematic residual reagents with water. Further, lyophilization should be executed carefully to ensure a more porous structure. A porous and more pH-neutral material may better enable cellular printing because the neutralization process of Chapter 5 reduced the viscosity, resulting in an inability to achieve mesh resolution.

While GelMA and the Blend were printable in acellular trials, the introduction of cellular media also resulted in lower viscosity inks that did not allow for mesh resolution. Using any of these materials as a bioink requires further optimization of printing parameters. Alternative scaffold manufacturing techniques may also yield desirable results. An example includes electrospinning, where a very fine-resolution mesh is built by drawing a thread of the bioink along an electric field.[196,197] A grounded collector will gather the micron-scale fibers by applying high voltage at the discharge point of the bioink. This approach may overcome the rheological challenges of 3D printing while producing a fine mesh.

Beyond cell viability, the longevity of cells within the scaffolds is also an important parameter to consider. The presence of oxygen during early tissue generation stages may enable longer cell viability. Oxygen generation techniques, such as incorporating calcium peroxide[198,199] or electrochemical water splitting[200,201], could further aid in cell longevity.

More recent work revised the material synthesis protocol of GAB and GelMA to address concerns due to pH and the use of toluene. Recent cellular printing also used mesenchymal stem cells (MSCs) instead of fibroblasts. These adjustments show promising improvements in printibility and cell viability.

6.4 Conclusion

Current and future work strives to advance the understanding of bio-inspired materials for various engineering challenges and solutions. Systematic, multi-scale studies are employed to understand and develop bio-inspired materials from medical treatment to chemical and energy production. First, a finite difference model of TCA cycle enzyme aims to understand mechanisms within a naturally occurring reaction cascade to develop efficient artificial reaction cascades. Then, thermodynamic and kinetic analysis of electrocatalytic upgrading of bio-oil constituent mixtures was executed to understand the underlying mechanisms contributing to the complexities in bio-oil upgrading to commodity chemicals. Finally, validation of a new gelatin-based bio-ink for tissue regeneration was reported to establish a more bio-compatible engineered solution to tissue regenerative materials. In conclusion, nature presents ample opportunities for bio-inspired materials and processing to produce alternative resources. The work herein established a greater mechanistic understanding of bioelectrochemical systems for designing efficient solutions in energy, commodity chemicals, and medical applications.

BIBLIOGRAPHY

[1] World Energy Outlook 2022 shows the global energy crisis can be a historic turning point towards a cleaner and more secure future - News. https://www.iea.org/news/world-energy-outlook-2022-shows-the-global-energy-crisis-can-be-a-historic-turning-point-towards-a-cleaner-and-more-secure-future, October 2022.

[2] Ian Wheeldon, Shelley D. Minteer, Scott Banta, Scott Calabrese Barton, Plamen Atanassov, and Matthew Sigman. Substrate channelling as an approach to cascade reactions. *Nat. Chem.*, 8(4):299–309, April 2016.

[3] Yoo Seok Lee, Koun Lim, and Shelley D. Minteer. Cascaded Biocatalysis and Bioelectrocatalysis: Overview and Recent Advances. *Annu. Rev. Phys. Chem.*, January 2021.

[4] Tony Bridgwater. Biomass for energy. *Journal of the Science of Food and Agriculture*, 86(12):1755–1768, 2006.

[5] Adam Christoph Marsh. *DEVELOPMENT OF 3D BIOACTIVE AND ANTIBACTERIAL SILICATE-BASED SCAFFOLDS FOR BONE TISSUE REGENERATION IN LOAD-BEARING APPLICATIONS*. PhD thesis, Michigan State University, 2021.

[6] Kanchan Suklal Chavan and Scott Calabrese Barton. Simulation of Intermediate Channeling by Nanoscale Confinement. *The Journal of Physical Chemistry C*, 122(26):14474–14480, July 2018.

[7] Yuanchao Liu, Ivana Matanovic, David P. Hickey, Shelley D. Minteer, Plamen Atanassov, and Scott Calabrese Barton. Cascade Kinetics of an Artificial Metabolon by Molecular Dynamics and Kinetic Monte Carlo. *ACS Catalysis*, 8(8):7719–7726, August 2018.

[8] Jia-Wei Shen, Tao Wu, Qi Wang, and Hai-Hua Pan. Molecular simulation of protein adsorption and desorption on hydroxyapatite surfaces. *Biomaterials*, 29(5):513–532, February 2008.

[9] Adrie J. J. Straathof. Transformation of Biomass into Commodity Chemicals Using Enzymes or Cells. *Chem. Rev.*, 114(3):1871–1908, February 2014.

[10] Su Keun Kuk, Raushan K Singh, Dong Heon Nam, Ranjitha Singh, Jung-Kul Lee, and Chan Beum Park. Photoelectrochemical Reduction of Carbon Dioxide to Methanol through a Highly Efficient Enzyme Cascade. *Angew Chem Int Ed*, 56(14):3827–3832, March 2017.

[11] Junfa Yin, Tian Xu, Ning Zhang, and Hailin Wang. Three-Enzyme Cascade Bioreactor for Rapid Digestion of Genomic DNA into Single Nucleosides. *Anal. Chem.*, 88(15):7730–7737, August 2016.

[12] Florika C. Macazo and Shelley D. Minteer. Enzyme cascades in biofuel cells. *Curr. Opin. Electrochem.*, 5(1):114–120, October 2017.

[13] H. Scott Fogler. *Elements of Chemical Reaction Engineering.* Prentice Hall, fifth edition, 2016.

[14] Athel Cornish-Bowden. One hundred years of Michaelis–Menten kinetics. *Perspectives in Science*, 4:3–9, March 2015.

[15] Leonor Michaelis and Maud Leonora Menten. Die Kinetik der Invertinwirkung. *Biochemische Zeitschrift*, 49:333–369, 1913.

[16] Beyza Bulutoglu, Kristen E. Garcia, Fei Wu, Shelley D. Minteer, and Scott Banta. Direct Evidence for Metabolon Formation and Substrate Channeling in Recombinant TCA Cycle Enzymes. *ACS Chem. Biol.*, 11(10):2847–2853, 2016.

[17] Yun Wang and Anthony K. Mittermaier. Characterizing Bi-substrate Enzyme Kinetics at High Resolution by 2D-ITC. *Anal. Chem.*, 93(37):12723–12732, September 2021.

[18] Athel Cornish-Bowden. Chapter 6 - Two-substrate reactions. In Athel Cornish-Bowden, editor, *Fundamentals of Enzyme Kinetics*, pages 99–129. Butterworth-Heinemann, January 1979.

[19] Matthew J. Kummer, Yoo Seok Lee, Mengwei Yuan, Bassam Alkotaini, John Zhao, Emmy Blumenthal, and Shelley D. Minteer. Substrate Channeling by a Rationally Designed Fusion Protein in a Biocatalytic Cascade. *JACS Au*, 1(8):1187–1197, August 2021.

[20] Adrian H. Elcock, Gary A. Huber, and J. Andrew McCammon. Electrostatic channeling of substrates between enzyme active sites: Comparison of simulation and experiment. *Biochem.*, 36(51):16049–16058, 1997.

[21] Changsun Eun, Peter M Kekenes-Huskey, Vincent T Metzger, and J Andrew McCammon. A model study of sequential enzyme reactions and electrostatic channeling. *Journal of Chemical Physics*, 140(10):105101, March 2014.

[22] Mario Milani, Alessandra Pesce, Martino Bolognesi, Alessio Bocedi, and Paolo Ascenzi. Substrate channeling: Molecular bases. *Biochemistry and Molecular Biology Education*, 31(4):228–233, July 2003.

[23] Setare Mostajabi Sarhangi and Dmitry V. Matyushov. Electron Tunneling in Biology: When Does it Matter? *ACS Omega*, 8(30):27355–27365, August 2023.

[24] Yuanchao Liu, David P. Hickey, Shelley D. Minteer, Alex Dickson, and Scott Calabrese Barton. Markov-State Transition Path Analysis of Electrostatic Channeling. *J. Phys. Chem. C*, 123(24):15284–15292, June 2019.

[25] Konstantin Shatalin, Sandrine Lebreton, Magali Rault-Leonardon, Christian Vélot, and Paul A. Srere. Electrostatic Channeling of Oxaloacetate in a Fusion Protein of Porcine Citrate Synthase and Porcine Mitochondrial Malate Dehydrogenase. *Biochem.*, 38(3):881–889, January 1999.

[26] Yan Xie, Shelley D. Minteer, Scott Banta, and Scott Calabrese Barton. Markov State Study of Electrostatic Channeling within the Tricarboxylic Acid Cycle Supercomplex. *ACS Nanosci. Au*, 2(5):414–421, October 2022.

[27] Yan Xie and Scott Calabrese Barton. Infrequent metadynamics study of rare-event electrostatic channeling. *Phys. Chem. Chem. Phys.*, 23(23):13381–13388, 2021.

[28] V. Ásgeirsson, H. Jónsson, and K. T. Wikfeldt. Long-Time Scale Simulations of Tunneling-Assisted Diffusion of Hydrogen on Ice Surfaces at Low Temperature. *J. Phys. Chem. C*, 121(3):1648–1657, January 2017.

[29] Kanchan Suklal Chavan and Scott Calabrese Barton. Confinement and Diffusion of Small Molecules in a Molecular-Scale Tunnel. *J. Electrochem. Soc.*, 167(2):023505, February 2020.

[30] Yubo Fan, Liliya Lund, Qiang Shao, Yi-Qin Gao, and Frank M. Raushel. A Combined Theoretical and Experimental Study of the Ammonia Tunnel in Carbamoyl Phosphate Synthetase. *J. Am. Chem. Soc.*, 131(29):10211–10219, July 2009.

[31] Frank M. Raushel, James B. Thoden, and Hazel M. Holden. Enzymes with Molecular Tunnels. *Acc. Chem. Res.*, 36(7):539–548, July 2003.

[32] Yuanchao Liu, David P. Hickey, Jing-Yao Guo, Erica Earl, Sofiene Abdellaoui, Ross D. Milton, Matthew S. Sigman, Shelley D. Minteer, and Scott Calabrese Barton. Substrate Channeling in an Artificial Metabolon: A Molecular Dynamics Blueprint for an Experimental Peptide Bridge. *ACS Catalysis*, 7(4):2486–2493, April 2017.

[33] Erica Earl and Scott Calabrese Barton. Simulation of intermediate transport in nanoscale scaffolds for multistep catalytic reactions. *Phys. Chem. Chem. Phys.*, 19(23):15463–15470, 2017.

[34] Da-Jiang Liu, Jing Wang, David M. Ackerman, Igor I. Slowing, Marek Pruski, Hung-Ting Chen, Victor S.-Y. Lin, and James W. Evans. Interplay between Anomalous Transport and Catalytic Reaction Kinetics in Single-File Nanoporous Systems. *ACS Catal.*, 1(7):751–763, July 2011.

[35] Yu-ming M. Huang, Gary A. Huber, Nuo Wang, Shelley D. Minteer, and J. Andrew McCammon. Brownian dynamic study of an enzyme metabolon in the TCA cycle: Substrate kinetics and channeling. *Protein Sci.*, 27(2):463–471, 2018.

[36] Xue Bin and Peter D. Pawelek. Evidence of isochorismate channeling between the Escherichia coli enterobactin biosynthetic enzymes EntC and EntB. *Protein Science*, 33(8):e5122, 2024.

[37] Sylvie Ouellette, Paknoosh Pakarian, Xue Bin, and Peter D. Pawelek. Evidence of an intracellular interaction between the *Escherichia coli* enzymes EntC and EntB and identification of a potential electrostatic channeling surface. *Biochimie*, 202:159–165, November 2022.

[38] Asha Kumari. Chapter 2 - Citric Acid Cycle. In Asha Kumari, editor, *Sweet Biochemistry*, pages 7–11. Academic Press, January 2018.

[39] Arieh Warshel. Molecular Dynamics Simulations of Biological Reactions. *Acc. Chem. Res.*, 35(6):385–395, June 2002.

[40] Mie Andersen, Chiara Panosetti, and Karsten Reuter. A Practical Guide to Surface Kinetic Monte Carlo Simulations. *Front. Chem.*, 7, 2019.

[41] Abhijit Chatterjee and Dionisios G. Vlachos. An overview of spatial microscopic and accelerated kinetic Monte Carlo methods. *J Computer-Aided Mater Des*, 14(2):253–308, July 2007.

[42] Arti Bhoutekar, Susmita Ghosh, Swati Bhattacharya, and Abhijit Chatterjee. A new class of enhanced kinetic sampling methods for building Markov state models. *J. Chem. Phys.*, 147(15):152702, June 2017.

[43] Yang Cao, Linda R. Petzold, Muruhan Rathinam, and Daniel T. Gillespie. The numerical stability of leaping methods for stochastic simulation of chemically reacting systems. *J. Chem. Phys.*, 121(24):12169, 2004.

[44] Sherly Rusli, Janna Grabowski, Anja Drews, and Matthias Kraume. A Multi-Scale Approach to Modeling the Interfacial Reaction Kinetics of Lipases with Emphasis on Enzyme Adsorption at Water-Oil Interfaces. *Processes*, 8(9):1082, 2020.

[45] Hèctor Prats, Francesc Illas, and Ramón Sayós. General concepts, assumptions, drawbacks, and misuses in kinetic Monte Carlo and microkinetic modeling simulations applied to computational heterogeneous catalysis. *Int. J. Quantum Chem.*, 118(9):e25518, 2018.

[46] Christina M. Wark, Yan Xie, and Scott Calabrese Barton. Finite difference model of electrostatic channeling in TCA cycle enzymes. *Electrochim. Acta*, 528:146131, July 2025.

[47] Fayaz A. Malla, Suhaib A. Bandh, Shahid A. Wani, Anh Tuan Hoang, and Nazir Ahmad Sofi. Biofuels: Potential Alternatives to Fossil Fuels. In Suhaib A. Bandh and Fayaz A. Malla, editors, *Biofuels in Circular Economy*, pages 1–15. Springer Nature, Singapore, 2022.

[48] Guangcan Su, Hwai Chyuan Ong, M. Mofijur, T. M. Indra Mahlia, and Yong Sik Ok. Pyrolysis of waste oils for the production of biofuels: A critical review. *Journal of Hazardous Materials*, 424:127396, February 2022.

[49] Manali S. Dhawan, Ganapati D. Yadav, and Scott Calabrese Barton. Zinc-electrocatalyzed hydrogenation of furfural in near-neutral electrolytes. *Sustainable Energy Fuels*, 5(11):2972–2984, 2021.

[50] Pengchao Hao. Electrocatalytic Hydrogenation of Monomeric, Dimeric, and Polymeric Lignin Model Compounds With Raney Nickel: Chemistry, Mechanistic, and Product Toxicity Studies - ProQuest. https://www.proquest.com/docview/2036629929/fulltextPDF/B2E002C3B2074166PQ/1?accountid

[51] Chun Ho Lam, Christy B. Lowe, Zhenglong Li, Kelsey N. Longe, Jordan T. Rayburn, Michael A. Caldwell, Carly E. Houdek, Jack B. Maguire, Christopher M. Saffron, Dennis J. Miller, and James E. Jackson. Electrocatalytic upgrading of model lignin monomers with earth abundant metal electrodes. *Green Chem.*, 17(1):601–609, 2015.

[52] Dekui Shen, Wei Jin, Jun Hu, Rui Xiao, and Kaihong Luo. An overview on fast pyrolysis of the main constituents in lignocellulosic biomass to valued-added chemicals: Structures, pathways and interactions. *Renewable and Sustainable Energy Reviews*, 51:761–774, November 2015.

[53] Furkan H. Isikgor and C. Remzi Becer. Lignocellulosic biomass: A sustainable platform for the production of bio-based chemicals and polymers. *Polymer Chemistry*, 6(25):4497–4559, 2015.

[54] Maria Temnikova, Jury Medvedev, Xenia Medvedeva, Nyhenflore H. Delva, Evgeniia Khairullina, Elena Krivoshapkina, and Anna Klinkova. Electrochemical Hydrodimerization of Furfural in Organic Media as an Efficient Route to Jet Fuel Precursor. *ChemElectroChem*, 10(2):e202200865, 2023.

[55] Meheryar R. Kasad, James E. Jackson, and Christopher M. Saffron. Electrocatalytic hydrogenation of the formyl group and heteroaromatic ring in furfural on activated carbon cloth-supported ruthenium. *RSC Sustain.*, 2(10):3001–3013, October 2024.

[56] Eveliina Mäkelä, José Luis González Escobedo, Jouni Neuvonen, Jouko Lahtinen, Marina Lindblad, Ulla Lassi, Reetta Karinen, and Riikka L. Puurunen. Liquid-phase Hydrodeoxygenation of 4-Propylphenol to Propylbenzene: Reducible Supports for Pt Catalysts. *ChemCatChem*, 12(16):4090–4104, August 2020.

[57] Jeffrey R. Page, Amol Pophali, Taejin Kim, Juan A. Lopez-Ruiz, Stoyan Bliznakov, and Julia A. Valla. Effect of Pt and Ru-based catalysts on the electrochemical hydrodeoxygenation of phenol to cyclohexane. *Catal. Sci. Technol.*, 14(19):5559–5573, 2024.

[58] Shyam Deo and Michael J. Janik. Predicting an optimal oxide/metal catalytic interface for hydrodeoxygenation chemistry of biomass derivatives. *Catal. Sci. Technol.*, 11(16):5606–5618, 2021.

[59] Meheryar R. Kasad, James E. Jackson, and Christopher M. Saffron. Electrocatalytic conversion of biomass-derived oxygenated aromatics to cycloalkanes. *Sustainable Energy Fuels*, November 2024.

[60] Tao Peng, Wenbin Zhang, Baiyao Liang, Guanwu Lian, Yun Zhang, and Wei Zhao. Electrocatalytic valorization of lignocellulose-derived aromatics at industrial-scale current densities. *Nat Commun*, 14(1):7229, November 2023.

[61] Mudasir Akbar Shah, Wasif Farooq, Tasrin Shahnaz, and Muthumariappan Akilarasan. Bioenergy and Value-Added Chemicals Derived Through Electrocatalytic Upgradation of Biomass: A Critical Review. *Bioenerg. Res.*, August 2024.

[62] Yuting Zhou, Grace E. Klinger, Eric L. Hegg, Christopher M. Saffron, and James E. Jackson. Multiple Mechanisms Mapped in Aryl Alkyl Ether Cleavage via Aqueous Electrocatalytic Hydrogenation over Skeletal Nickel. *J. Am. Chem. Soc.*, 142(8):4037–4050, February 2020.

[63] Jeffrey R. Page, Zachary Manfredi, Stoyan Bliznakov, and Julia A. Valla. Recent Progress in Electrochemical Upgrading of Bio-Oil Model Compounds and Bio-Oils to Renewable Fuels and Platform Chemicals. *Materials (Basel)*, 16(1):394, January 2023.

[64] Allen J Bard, Larry R Faulkner, New York, Chichester @bullet, Weinheim Brisbane, and Singapore E Toronto. *ELECTROCHEMICAL METHODS Fundamentals and Applications*. Wiley, 1944.

[65] Martin Z. Bazant. Unified quantum theory of electrochemical kinetics by coupled ion–electron transfer. *Faraday Discuss.*, 246:60–124, 2023.

[66] A. Shayeghi, S. Krähling, P. Hörtz, R. L. Johnston, C. J. Heard, and R. Schäfer. Adsorption of Acetonitrile, Benzene, and Benzonitrile on Pt(111): Single Crystal Adsorption Calorimetry and Density Functional Theory. *J. Phys. Chem. C*, 121(39):21354–21363, October 2017.

[67] Yun Shi, Yulei Zhu, Yong Yang, Yong-Wang Li, and Haijun Jiao. Exploring Furfural Catalytic Conversion on Cu(111) from Computation. *ACS Catal.*, 5(7):4020–4032, July 2015.

[68] Yang Song, Udishnu Sanyal, Dhananjai Pangotra, Jamie D. Holladay, Donald M. Camaioni, Oliver Y. Gutiérrez, and Johannes A. Lercher. Hydrogenation of benzaldehyde via electrocatalysis and thermal catalysis on carbon-supported metals. *Journal of Catalysis*, 359:68–75, March 2018.

[69] Juan A. Lopez-Ruiz, Udishnu Sanyal, Jonathan Egbert, Oliver Y. Gutiérrez, and Jamie Holladay. Kinetic Investigation of the Sustainable Electrocatalytic Hydrogenation of Benzaldehyde on Pd/C: Effect of Electrolyte Composition and Half-Cell Potentials. *ACS Sustainable Chem. Eng.*, 6(12):16073–16085, December 2018.

[70] Andrzej Lasia. Mechanism and kinetics of the hydrogen evolution reaction. *International Journal of Hydrogen Energy*, 44(36):19484–19518, July 2019.

[71] Anthony R. Kucernak and Christopher Zalitis. General Models for the Electrochemical Hydrogen Oxidation and Hydrogen Evolution Reactions: Theoretical Derivation and

Experimental Results under Near Mass-Transport Free Conditions. *J. Phys. Chem. C*, 120(20):10721–10745, May 2016.

[72] Ana L. Santos, Maria-João Cebola, and Diogo M. F. Santos. Towards the Hydrogen Economy—A Review of the Parameters That Influence the Efficiency of Alkaline Water Electrolyzers. *Energies*, 14(11):3193, May 2021.

[73] Renato Seeber, Chiara Zanardi, and György Inzelt. Links between electrochemical thermodynamics and kinetics. *ChemTexts*, 1(4):18, December 2015.

[74] David S. Sholl and Janice Steckel. Frontmatter. In *Density Functional Theory*, pages i–xii. John Wiley & Sons, Ltd, 2009.

[75] W. Kohn and L. J. Sham. Self-Consistent Equations Including Exchange and Correlation Effects. *Phys. Rev.*, 140(4A):A1133–A1138, November 1965.

[76] Shyue Ping Ong, William Davidson Richards, Anubhav Jain, Geoffroy Hautier, Michael Kocher, Shreyas Cholia, Dan Gunter, Vincent L. Chevrier, Kristin A. Persson, and Gerbrand Ceder. Python Materials Genomics (pymatgen): A robust, open-source python library for materials analysis. *Computational Materials Science*, 68:314–319, February 2013.

[77] Jürgen Hafner. Ab-initio simulations of materials using VASP: Density-functional theory and beyond. *Journal of Computational Chemistry*, 29(13):2044–2078, 2008.

[78] Markus Bursch, Jan-Michael Mewes, Andreas Hansen, and Stefan Grimme. Best-Practice DFT Protocols for Basic Molecular Computational Chemistry**. *Angew Chem Int Ed*, 61(42):e202205735, October 2022.

[79] Renqin Zhang, Alyssa J. Hensley, Jean-Sabin McEwen, Sandra Wickert, Erik Darlatt, Kristina Fischer, Matthias Schöppke, Reinhard Denecke, Regine Streber, Michael Lorenz, Christian Papp, and Hans-Peter Steinrück. Integrated X-ray photoelectron spectroscopy and DFT characterization of benzene adsorption on Pt(111), Pt(355) and Pt(322) surfaces. *Physical Chemistry Chemical Physics*, 15(47):20662–20671, 2013.

[80] Karsten Reuter. Ab Initio Thermodynamics and First-Principles Microkinetics for Surface Catalysis. In Joost Frenken and Irene Groot, editors, *Operando Research in Heterogeneous Catalysis*, Springer Series in Chemical Physics, pages 151–188. Springer International Publishing, Cham, 2017.

[81] Sunghwan Kim, Jie Chen, Tiejun Cheng, Asta Gindulyte, Jia He, Siqian He, Qingliang Li, Benjamin A Shoemaker, Paul A Thiessen, Bo Yu, Leonid Zaslavsky, Jian Zhang, and Evan E Bolton. PubChem 2025 update. *Nucleic Acids Research*, 53(D1):D1516–D1525, January 2025.

[82] Gabriel A. Bramley, Manh-Thuong Nguyen, Vassiliki-Alexandra Glezakou, Roger Rousseau, and Chris-Kriton Skylaris. Understanding Adsorption of Organics on

Pt(111) in the Aqueous Phase: Insights from DFT Based Implicit Solvent and Statistical Thermodynamics Models. *J. Chem. Theory Comput.*, 18(3):1849–1861, March 2022.

[83] Cheng-chau Chiu, Alexander Genest, Armando Borgna, and Notker Rösch. Hydrodeoxygenation of Guaiacol over Ru(0001): A DFT Study. *ACS Catal.*, 4(11):4178–4188, November 2014.

[84] L. Delle Site, A. Alavi, and C. F. Abrams. Adsorption energies and geometries of phenol on the (111) surface of nickel: An *ab initio* study. *Phys. Rev. B*, 67(19):193406, May 2003.

[85] Kyungtae Lee, Geun Ho Gu, Charles A. Mullen, Akwasi A. Boateng, and Dionisios G. Vlachos. Guaiacol Hydrodeoxygenation Mechanism on Pt(111): Insights from Density Functional Theory and Linear Free Energy Relations. *ChemSusChem*, 8(2):315–322, January 2015.

[86] David Loffreda. Theoretical insight of adsorption thermodynamics of multifunctional molecules on metal surfaces. *Surface Science*, 600(10):2103–2112, May 2006.

[87] Michelle J.S. Spencer and Graeme L. Nyberg. DFT modelling of hydrogen on Cu(110)- and (111)-type clusters. *Molecular Simulation*, 28(8-9):807–825, August 2002.

[88] Ask Hjorth Larsen, Jens Jørgen Mortensen, Jakob Blomqvist, Ivano E. Castelli, Rune Christensen, Marcin Dułak, Jesper Friis, Michael N. Groves, Bjørk Hammer, Cory Hargus, Eric D. Hermes, Paul C. Jennings, Peter Bjerre Jensen, James Kermode, John R. Kitchin, Esben Leonhard Kolsbjerg, Joseph Kubal, Kristen Kaasbjerg, Steen Lysgaard, Jón Bergmann Maronsson, Tristan Maxson, Thomas Olsen, Lars Pastewka, Andrew Peterson, Carsten Rostgaard, Jakob Schiøtz, Ole Schütt, Mikkel Strange, Kristian S. Thygesen, Tejs Vegge, Lasse Vilhelmsen, Michael Walter, Zhenhua Zeng, and Karsten W. Jacobsen. The atomic simulation environment-a Python library for working with atoms. *J Phys Condens Matter*, 29(27):273002, July 2017.

[89] Joseph W Ochterski. Thermochemistry in Gaussian, 2000.

[90] J. K. Nørskov, J. Rossmeisl, A. Logadottir, L. Lindqvist, J. R. Kitchin, T. Bligaard, and H. Jónsson. Origin of the Overpotential for Oxygen Reduction at a Fuel-Cell Cathode. *J. Phys. Chem. B*, 108(46):17886–17892, November 2004.

[91] Robert E. Warburton, Alexander V. Soudackov, and Sharon Hammes-Schiffer. Theoretical Modeling of Electrochemical Proton-Coupled Electron Transfer. *Chem. Rev.*, 122(12):10599–10650, June 2022.

[92] David R. Weinberg, Christopher J. Gagliardi, Jonathan F. Hull, Christine Fecenko Murphy, Caleb A. Kent, Brittany C. Westlake, Amit Paul, Daniel H. Ess, Dewey Granville McCafferty, and Thomas J. Meyer. Proton-Coupled Electron Transfer. *Chem. Rev.*, 112(7):4016–4093, July 2012.

[93] Sneha A. Akhade, Nicole J. Bernstein, Monica R. Esopi, Michael J. Regula, and Michael J. Janik. A simple method to approximate electrode potential-dependent activation energies using density functional theory. *Catalysis Today*, 288:63–73, June 2017.

[94] Ruslan M. Mensharapov, Dmitry D. Spasov, Nataliya A. Ivanova, Adelina A. Zasypkina, Sergey A. Smirnov, and Sergey A. Grigoriev. Screening of Carbon-Supported Platinum Electrocatalysts Using Frumkin Adsorption Isotherms. *Inorganics*, 11(3):103, March 2023.

[95] Nirala Singh, Udishnu Sanyal, John L. Fulton, Oliver Y. Gutiérrez, Johannes A. Lercher, and Charles T. Campbell. Quantifying Adsorption of Organic Molecules on Platinum in Aqueous Phase by Hydrogen Site Blocking and in Situ X-ray Absorption Spectroscopy. *ACS Catal.*, 9(8):6869–6881, August 2019.

[96] Jiří Klimeš, David R Bowler, and Angelos Michaelides. A critical assessment of theoretical methods for finding reaction pathways and transition states of surface processes. *J. Phys.: Condens. Matter*, 22(7):074203, February 2010.

[97] Graeme Henkelman and Hannes Jónsson. A dimer method for finding saddle points on high dimensional potential surfaces using only first derivatives. *The Journal of Chemical Physics*, 111(15):7010–7022, October 1999.

[98] Jonathan E. Sutton and Dionisios G. Vlachos. A Theoretical and Computational Analysis of Linear Free Energy Relations for the Estimation of Activation Energies. *ACS Catal.*, 2(8):1624–1634, August 2012.

[99] Paolo Giannozzi, Stefano Baroni, Nicola Bonini, Matteo Calandra, Roberto Car, Carlo Cavazzoni, Davide Ceresoli, Guido L. Chiarotti, Matteo Cococcioni, Ismaila Dabo, Andrea Dal Corso, Stefano de Gironcoli, Stefano Fabris, Guido Fratesi, Ralph Gebauer, Uwe Gerstmann, Christos Gougoussis, Anton Kokalj, Michele Lazzeri, Layla Martin-Samos, Nicola Marzari, Francesco Mauri, Riccardo Mazzarello, Stefano Paolini, Alfredo Pasquarello, Lorenzo Paulatto, Carlo Sbraccia, Sandro Scandolo, Gabriele Sclauzero, Ari P. Seitsonen, Alexander Smogunov, Paolo Umari, and Renata M. Wentzcovitch. QUANTUM ESPRESSO: A modular and open-source software project for quantum simulations of materials. *J. Phys.: Condens. Matter*, 21(39):395502, September 2009.

[100] P. Giannozzi, O. Andreussi, T. Brumme, O. Bunau, M. Buongiorno Nardelli, M. Calandra, R. Car, C. Cavazzoni, D. Ceresoli, M. Cococcioni, N. Colonna, I. Carnimeo, A. Dal Corso, S. de Gironcoli, P. Delugas, R. A. DiStasio, A. Ferretti, A. Floris, G. Fratesi, G. Fugallo, R. Gebauer, U. Gerstmann, F. Giustino, T. Gorni, J. Jia, M. Kawamura, H.-Y. Ko, A. Kokalj, E. Küçükbenli, M. Lazzeri, M. Marsili, N. Marzari, F. Mauri, N. L. Nguyen, H.-V. Nguyen, A. Otero-de-la-Roza, L. Paulatto, S. Poncé, D. Rocca, R. Sabatini, B. Santra, M. Schlipf, A. P. Seitsonen, A. Smogunov, I. Timrov, T. Thonhauser, P. Umari, N. Vast, X. Wu, and S. Baroni. Advanced capabilities for materials modelling with Quantum ESPRESSO. *J. Phys.: Condens. Matter*, 29(46):465901, October 2017.

[101] Dipika Rajendra Kanchan and Arghya Banerjee. Linear Scaling Relationships for Furan Hydrodeoxygenation over Transition Metal and Bimetallic Surfaces. *ChemSusChem*, 16(18):e202300491, 2023.

[102] Bin Liu, Lei Cheng, Larry Curtiss, and Jeffrey Greeley. Effects of van der Waals density functional corrections on trends in furfural adsorption and hydrogenation on close-packed transition metal surfaces. *Surface Science*, 622:51–59, April 2014.

[103] Shanjun Mao, Zhe Wang, Zhirong Chen, Kejun Wu, Kaichao Zhang, Qichuan Li, Huihuan Yan, Guofeng Lü, Guodong Huang, and Yong Wang. Towards the selectivity distinction of phenol hydrogenation on noble metal catalysts. *Nano Materials Science*, 5(1):91–100, March 2023.

[104] Heine A. Hansen, Venkatasubramanian Viswanathan, and Jens K. Nørskov. Unifying Kinetic and Thermodynamic Analysis of 2 e^- and 4 e^- Reduction of Oxygen on Metal Surfaces. *J. Phys. Chem. C*, 118(13):6706–6718, April 2014.

[105] Kelth J Laidler' and M Chrlstlne Klng. The Development of Transition-State Theory. *J Phys Chem*, 1983.

[106] Julian R. Jones. Review of bioactive glass: From Hench to hybrids. *Acta Biomaterialia*, 9(1):4457–4486, January 2013.

[107] Jean-Pierre Draye, Bernard Delaey, André Van de Voorde, An Van Den Bulcke, Bepke De Reu, and Etienne Schacht. In vitro and in vivo biocompatibility of dextran dialdehyde cross-linked gelatin hydrogel films. *Biomaterials*, 19(18):1677–1687, September 1998.

[108] K. Panduranga Rao. Recent developments of collagen-based materials for medical applications and drug delivery systems. *Journal of Biomaterials Science, Polymer Edition*, 7(7):623–645, January 1996.

[109] Adam C. Marsh, Yaozhong Zhang, Lucrezia Poli, Neal Hammer, Aljoscha Roch, Martin Crimp, and Xanthippi Chatzistavrou. 3D printed bioactive and antibacterial silicate glass-ceramic scaffold by fused filament fabrication. *Materials Science and Engineering: C*, 118:111516, January 2021.

[110] Adam C. Marsh, Ehsanul Hoque Apu, Marcus Bunn, Christopher H. Contag, Nureddin Ashammakhi, and Xanthippi Chatzistavrou. A New Bioink for Improved 3D Bioprinting of Bone-Like Constructs. Preprint, Bioengineering, November 2021.

[111] An I. Van Den Bulcke, Bogdan Bogdanov, Nadine De Rooze, Etienne H. Schacht, Maria Cornelissen, and Hugo Berghmans. Structural and Rheological Properties of Methacrylamide Modified Gelatin Hydrogels. *Biomacromolecules*, 1(1):31–38, March 2000.

[112] Adam C. Marsh, Nathan P. Mellott, Martin Crimp, Anthony Wren, Neal Hammer, and Xanthippi Chatzistavrou. Ag-doped Bioactive Glass-Ceramic 3D Scaffolds: Microstructural, Antibacterial, and Biological Properties. *Journal of the European Ceramic Society*, 41(6):3717–3730, June 2021.

[113] Adam C. Marsh, Nathan P. Mellott, Natalia Pajares-Chamorro, Martin Crimp, Anthony Wren, Neal D. Hammer, and Xanthippi Chatzistavrou. Fabrication and multiscale characterization of 3D silver containing bioactive glass-ceramic scaffolds. *Bioactive Materials*, 4:215–223, December 2019.

[114] Qing Tang, Sujiao Cao, Tian Ma, Xi Xiang, Hongrong Luo, Pavel Borovskikh, Raul D. Rodriguez, Quanyi Guo, Li Qiu, and Chong Cheng. Engineering Biofunctional Enzyme-Mimics for Catalytic Therapeutics and Diagnostics. *Adv. Funct. Mater.*, 31(7):2007475, 2021.

[115] Alisdair R Fernie, Fernando Carrari, and Lee J Sweetlove. Respiratory metabolism: Glycolysis, the TCA cycle and mitochondrial electron transport. *Curr. Opin. Plant Biol.*, 7(3):254–261, June 2004.

[116] Fei Wu and Shelley Minteer. Krebs Cycle Metabolon: Structural Evidence of Substrate Channeling Revealed by Cross-Linking and Mass Spectrometry. *Angew. Chem. Int. Ed.*, 54(6):1851–1854, 2015.

[117] Davide M. Ferraris, Ralf Spallek, Wulf Oehlmann, Mahavir Singh, and Menico Rizzi. Structures of citrate synthase and malate dehydrogenase of Mycobacterium tuberculosis. *Proteins*, 83(2):389–394, 2015.

[118] Joy Omini, Izabela Wojciechowska, Aleksandra Skirycz, Hideaki Moriyama, and Toshihiro Obata. Association of the malate dehydrogenase-citrate synthase metabolon is modulated by intermediates of the Krebs tricarboxylic acid cycle. *Sci Rep*, 11(1):18770, September 2021.

[119] Robert W. Guynn, Harris J. Gelberg, and Richard L. Veech. Equilibrium Constants of the Malate Dehydrogenase, Citrate Synthase, Citrate Lyase, and Acetyl Coenzyme A Hydrolysis Reactions under Physiological Conditions. *J. Biol. Chem.*, 248(20):6957–6965, October 1973.

[120] Elizabeth Jurrus, Dave Engel, Keith Star, Kyle Monson, Juan Brandi, Lisa E. Felberg, David H. Brookes, Leighton Wilson, Jiahui Chen, Karina Liles, Minju Chun, Peter Li, David W. Gohara, Todd Dolinsky, Robert Konecny, David R. Koes, Jens Erik Nielsen, Teresa Head-Gordon, Weihua Geng, Robert Krasny, Guo-Wei Wei, Michael J. Holst, J. Andrew McCammon, and Nathan A. Baker. Improvements to the APBS biomolecular solvation software suite. *Protein Sci.*, 27(1):112–128, 2018.

[121] Michail Stamatakis and Dionisios G. Vlachos. A graph-theoretical kinetic Monte Carlo framework for on-lattice chemical kinetics. *J. Chem. Phys.*, 134(21):214115, June 2011.

[122] Michail Stamatakis and Dionisios G. Vlachos. Unraveling the complexity of catalytic reactions via kinetic monte carlo simulation: Current status and frontiers. *ACS Catalysis*, 2(12):2648–2663, 2012.

[123] Luca Messina, Nicolas Castin, Christophe Domain, and Pär Olsson. Introducing ab initio based neural networks for transition-rate prediction in kinetic Monte Carlo simulations. *Phys. Rev. B*, 95(6):064112, February 2017.

[124] Haobo Li, Yan Jiao, Kenneth Davey, and Shi-Zhang Qiao. Data-Driven Machine Learning for Understanding Surface Structures of Heterogeneous Catalysts. *Angew. Chem. Int. Ed.*, 62(9):e202216383, 2023.

[125] Ruiqi Zou, Hongxia Li, Junxiao Shi, Chunyan Sun, Geyu Lu, and Xu Yan. Dual-enhanced enzyme cascade hybrid hydrogel for the construction of optical biosensor. *Biosens. Bioelectron.*, 263:116613, November 2024.

[126] Bernard Philippe, Youcef Saad, and William J. Stewart. Numerical Methods in Markov Chain Modeling. *Oper. Res.*, 40(6):1156–1179, 1992.

[127] Pauli Virtanen, Ralf Gommers, Travis E. Oliphant, Matt Haberland, Tyler Reddy, David Cournapeau, Evgeni Burovski, Pearu Peterson, Warren Weckesser, Jonathan Bright, Stéfan J. van der Walt, Matthew Brett, Joshua Wilson, K. Jarrod Millman, Nikolay Mayorov, Andrew R. J. Nelson, Eric Jones, Robert Kern, Eric Larson, C. J. Carey, İlhan Polat, Yu Feng, Eric W. Moore, Jake VanderPlas, Denis Laxalde, Josef Perktold, Robert Cimrman, Ian Henriksen, E. A. Quintero, Charles R. Harris, Anne M. Archibald, Antônio H. Ribeiro, Fabian Pedregosa, and Paul van Mulbregt. SciPy 1.0: Fundamental algorithms for scientific computing in Python. *Nat Methods*, 17(3):261–272, March 2020.

[128] Martin K. Scherer, Benjamin Trendelkamp-Schroer, Fabian Paul, Guillermo Pérez-Hernández, Moritz Hoffmann, Nuria Plattner, Christoph Wehmeyer, Jan-Hendrik Prinz, and Frank Noé. PyEMMA 2: A Software Package for Estimation, Validation, and Analysis of Markov Models. *J. Chem. Theory Comput.*, 11(11):5525–5542, November 2015.

[129] Aric A Hagberg, Daniel A Schult, and Pieter J Swart. Exploring Network Structure, Dynamics, and Function using NetworkX. *Proceedings of the 7th Python in Science Conference*, 2008.

[130] Giancarlo Perrone, Jose Unpingco, and Haw-minn Lu. Network visualizations with Pyvis and VisJS, June 2020.

[131] Christina M. Wark and Scott Calabrese Barton. Electrostatic_Channeling_MDH-CS. https://github.com/scbgroup/Electrostatic_Channeling_MDH-CS, 2024.

[132] Jia Wu, Jinli Chen, Tianqi Yu, Zhixiang Zhai, Yumei Zhu, Xizi Wu, and Shibin Yin. Boosting Electrochemical Kinetics of NiCo2 via MoO2 Modification for Biomass Upgrading Assisted Hydrogen Evolution. *ACS Catal.*, 13(20):13257–13266, October 2023.

[133] Mahlet Garedew, Chun Ho Lam, Laurene Petitjean, Shuquan Huang, Bing Song, Fang Lin, James E. Jackson, Christopher M. Saffron, and Paul T. Anastas. Electrochemical upgrading of depolymerized lignin: A review of model compound studies. *Green Chem.*, 23(8):2868–2899, 2021.

[134] Tedd E. Lister, Luis A. Diaz, Michael A. Lilga, Asanga B. Padmaperuma, YuPo Lin, Varada Menon Palakkal, and Christopher G. Arges. Low-Temperature Electrochemical Upgrading of Bio-oils Using Polymer Electrolyte Membranes. *Energy Fuels*, 32(5):5944–5950, May 2018.

[135] Wei Liu, Wenqin You, Yutao Gong, and Yulin Deng. High-efficiency electrochemical hydrodeoxygenation of bio-phenols to hydrocarbon fuels by a superacid-noble metal particle dual-catalyst system. *Energy Environ. Sci.*, 13(3):917–927, 2020.

[136] Francisco W. S. Lucas, R. Gary Grim, Sean A. Tacey, Courtney A. Downes, Joseph Hasse, Alex M. Roman, Carrie A. Farberow, Joshua A. Schaidle, and Adam Holewinski. Electrochemical Routes for the Valorization of Biomass-Derived Feedstocks: From Chemistry to Application. *ACS Energy Lett.*, 6(4):1205–1270, April 2021.

[137] Peter Nilges and Uwe Schröder. Electrochemistry for biofuel generation: Production of furans by electrocatalytic hydrogenation of furfurals. *Energy Environ. Sci.*, 6(10):2925, 2013.

[138] Alex Román. *Electrochemical Upgrading of Biomass to Sustainable Chemicals: Mechanistic Insights into the Electrocatalytic Oxidation of Furfural and Related Compounds - ProQuest*. PhD thesis, University of Colorado, 2020.

[139] Mia D. Stankovic, Jessica F. Sperryn, Roxanna S. Delima, Connor C. Rupnow, Michael B. Rooney, Monika Stolar, and Curtis P. Berlinguette. Electrochemical production of methyltetrahydrofuran, a biofuel for diesel engines. *Energy Environ. Sci.*, 16(8):3453–3461, 2023.

[140] Peng Zhou, Si-Xuan Guo, Linbo Li, Tadaharu Ueda, Yoshinori Nishiwaki, Liang Huang, Zehui Zhang, and Jie Zhang. Selective Electrochemical Hydrogenation of Phenol with Earth-abundant Ni-MoO2 Heterostructured Catalysts: Effect of Oxygen Vacancy on Product Selectivity. *Angewandte Chemie International Edition*, 62(8):e202214881, 2023.

[141] Sabyasachi Das, James E. Anderson, Robert De Kleine, Timothy J. Wallington, James E. Jackson, and Christopher M. Saffron. Technoeconomic analysis of corn stover conversion by decentralized pyrolysis and electrocatalysis. *Sustainable Energy Fuels*, 6(11):2823–2834, 2022.

[142] Yingying Li, Gen Huang, Yimin Jiang, Chongyang Ma, Yuxuan Lu, Shuangyin Wang, and Yuqin Zou. Theoretical Insights into Facet-Dependent Activity and Selectivity of Cu Catalysts in Electrochemical Furfural Reduction. *J. Phys. Chem. C*, 127(45):21989–21998, November 2023.

[143] Hengzhou Liu, Deep M. Patel, Yifu Chen, Jungkuk Lee, Ting-Han Lee, Sarah D. Cady, Eric W. Cochran, Luke T. Roling, and Wenzhen Li. Unraveling Electroreductive Mechanisms of Biomass-Derived Aldehydes via Tailoring Interfacial Environments. *ACS Catal.*, 12(22):14072–14085, November 2022.

[144] Amani O. Alghamdi, Abdesslem Jedidi, Saadullah G. Aziz, Kazuhiro Takanabe, and Luigi Cavallo. Theoretical insights into dehydrogenative chemisorption of alkylaromatics on Pt(1 0 0) and Ni(1 0 0). *Journal of Catalysis*, 363:197–203, July 2018.

[145] Arghya Banerjee and Samir H. Mushrif. Reaction Pathways for the Deoxygenation of Biomass-Pyrolysis-Derived Bio-oil on Ru: A DFT Study using Furfural as a Model Compound. *ChemCatChem*, 9(14):2828–2838, July 2017.

[146] Cecil N. M. Ouma, Phillimon M. Modisha, and Dmitri Bessarabov. Catalytic dehydrogenation of the liquid organic hydrogen carrier octahydroindole on Pt (1 1 1) surface: *Ab initio* insights from density functional theory calculations. *Applied Surface Science*, 471:1034–1040, March 2019.

[147] Christopher D. Taylor, Sally A. Wasileski, Jean-Sebastien Filhol, and Matthew Neurock. First principles reaction modeling of the electrochemical interface: Consideration and calculation of a tunable surface potential from atomic and electronic structure. *Phys. Rev. B*, 73(16):165402, April 2006.

[148] Shengguang Wang, Vassili Vorotnikov, Jonathan E. Sutton, and Dionisios G. Vlachos. Brønsted–Evans–Polanyi and Transition State Scaling Relations of Furan Derivatives on Pd(111) and Their Relation to Those of Small Molecules. *ACS Catal.*, 4(2):604–612, February 2014.

[149] Meheryar R. Kasad, James E. Jackson, Scott Calabrese Barton, Calvin Mukarakate, Uwe Schröder, and Christopher M. Saffron. Electrocatalytic hydrotreatment of bio-oil: Exploring interactions between functional groups. *In Preparation*, 2025.

[150] Meng-Yuan Chen, Yao-Bing Huang, Huan Pang, Xin-Xin Liu, and Yao Fu. Hydrodeoxygenation of lignin-derived phenols into alkanes over carbon nanotube supported Ru catalysts in biphasic systems. *Green Chemistry*, 17(3):1710–1717, 2015.

[151] C Mirodatos. Steady-state and isotopic transient kinetics of benzene hydrogenation on nickel catalysts. *Journal of Catalysis*, 105(2):405–415, June 1987.

[152] F Montilla, F Huerta, E Morallon, and J. L Vazquez. Electrochemical behaviour of benzene on platinum electrodes. *Electrochimica Acta*, 45(25):4271–4277, August 2000.

[153] Yeohoon Yoon, Roger Rousseau, Robert S. Weber, Donghai Mei, and Johannes A. Lercher. First-Principles Study of Phenol Hydrogenation on Pt and Ni Catalysts in Aqueous Phase. *J. Am. Chem. Soc.*, 136(29):10287–10298, July 2014.

[154] Jacob Anibal. *UNDERSTANDING THE ELECTROCHEMICAL REDUCTION AND COUPLING OF BIOMASS DERIVED CARBONYL SPECIES*. PhD thesis, University of Delaware, 2021.

[155] Qiuju Fu, Wenpeng Xie, Lingzhi Yang, Liting Yan, and Xuebo Zhao. Recent advances in electrocatalytic upgrading of biomass-derived furfural. *Chemical Engineering Journal*, 485:150083, April 2024.

[156] Fahime Khouini and Morteza Vahedpour. New Platinum Bimetallic Surfaces, M/Pt(111) and Pt/M/Pt(111) (M = Mo, Zn, and Co), for Furfural Adsorption. *J. Phys. Chem. C*, 128(22):8961–8973, June 2024.

[157] Martin J. Taylor, Li Jiang, Joachim Reichert, Anthoula C. Papageorgiou, Simon K. Beaumont, Karen Wilson, Adam F. Lee, Johannes V. Barth, and Georgios Kyriakou. Catalytic Hydrogenation and Hydrodeoxygenation of Furfural over Pt(111): A Model System for the Rational Design and Operation of Practical Biomass Conversion Catalysts. *J. Phys. Chem. C*, 121(15):8490–8497, April 2017.

[158] M. Soledad Zanuttini, Martin Gross, Gustavo Marchetti, and Carlos Querini. Furfural hydrodeoxygenation on iron and platinum catalysts. *Applied Catalysis A: General*, 587:117217, October 2019.

[159] Bo zhao, Mengyuan Chen, Qingxiang Guo, and Yao Fu. Electrocatalytic hydrogenation of furfural to furfuryl alcohol using platinum supported on activated carbon fibers. *Electrochimica Acta*, 135:139–146, July 2014.

[160] James Akinola, Isaiah Barth, Bryan R. Goldsmith, and Nirala Singh. Adsorption Energies of Oxygenated Aromatics and Organics on Rhodium and Platinum in Aqueous Phase. *ACS Catal.*, 10(9):4929–4941, May 2020.

[161] Ş. C. Bădescu, P. Salo, T. Ala-Nissila, S. C. Ying, K. Jacobi, Y. Wang, K. Bedürftig, and G. Ertl. Energetics and Vibrational States for Hydrogen on Pt(111). *Phys. Rev. Lett.*, 88(13):136101, March 2002.

[162] K Christmann, G Ertl, and T Pignet. Adsorption of hydrogen on a Pt(111) surface. *Surface Science*, 54(2):365–392, February 1976.

[163] Griffin Ruehl, S. Elizabeth Harman, Líney Árnadóttir, and Charles T. Campbell. Acetonitrile Adsorption and Adhesion Energies onto the Pt(111) Surface by Calorimetry. *ACS Catal.*, 12(1):156–163, January 2022.

[164] Giacomo Marchioro, Samuel Young, Gvina Bulgarit, and Raz-Hemo. Giacomomarchioro/PyEnergyDiagrams: New features and pypi. Zenodo, September 2022.

[165] Gianluca Prandini, Antimo Marrazzo, Ivano E. Castelli, Nicolas Mounet, and Nicola Marzari. Precision and efficiency in solid-state pseudopotential calculations. *npj Comput Mater*, 4(1):1–13, December 2018.

[166] Stefan Grimme, Jens Antony, Stephan Ehrlich, and Helge Krieg. A Consistent and Accurate Ab Initio Parametrization of Density Functional Dispersion Correction (DFT-D) for the 94 Elements H-Pu. *The Journal of chemical physics*, 132:154104, April 2010.

[167] E.A. Owen, L. Pickup, and J.O. Roberts. Lattice constants of five elements possessing hexagonal structure. *Zeitschrift fuer Kristallographie, Kristallgeometrie, Kristallphysik, Kristallchemie (-144,1977)*, 91:70–76, 1935.

[168] E.A. Owen and E.W. Roberts. The crystal parameters of osmium and ruthenium at different temperatures. *Zeitschrift fuer Kristallographie, Kristallgeometrie, Kristallphysik, Kristallchemie (-144,1977)*, 96:497–498, 1937.

[169] Y. Urashima, T. Wakabayashi, T. Masaki, and Y. Teresaki. Ruthenium, a new mineral from horokanai, hokkaido, japan. *Mineralogical Journal (Japan)*, 7:438–444, 1974.

[170] Charles Kittel. *Introduction to Solid State Physics*. Wiley, Hoboken, NJ, 8. ed., [repr.] edition, 20.

[171] M. Methfessel and A. T. Paxton. High-precision sampling for Brillouin-zone integration in metals. *Phys. Rev. B*, 40(6):3616–3621, August 1989.

[172] Rolf Sander. Compilation of Henry's law constants (version 5.0.0) for water as solvent. *Atmospheric Chemistry and Physics*, 23(19):10901–12440, October 2023.

[173] Nina Ni and Samuel H. Yalkowsky. Prediction of Setschenow constants. *International Journal of Pharmaceutics*, 254(2):167–172, March 2003.

[174] S. Weisenberger and A. Schumpe. Estimation of gas solubilities in salt solutions at temperatures from 273 K to 363 K. *AIChE Journal*, 42(1):298–300, January 1996.

[175] Chemeo - chemical and physical properties. https://www.chemeo.com.

[176] Christina M. Wark and Scott Calabrese Barton. CMW_diss_code. https://github.com/scbgroup/CMW_diss_code.git, 2025.

[177] Colin F. Dickens, Charlotte Kirk, and Jens K. Nørskov. Insights into the Electrochemical Oxygen Evolution Reaction with ab Initio Calculations and Microkinetic Modeling: Beyond the Limiting Potential Volcano. *J. Phys. Chem. C*, 123(31):18960–18977, August 2019.

[178] Kaiyue Zhao, Ningyao Xiang, Yu-Qi Wang, Jinyu Ye, Zihan Jin, Linke Fu, Xiaoxia Chang, Dong Wang, Hai Xiao, and Bingjun Xu. A molecular design strategy to enhance hydrogen evolution on platinum electrocatalysts. *Nat Energy*, April 2025.

[179] Tomas Kucera, Karel Urban, and Stavroula Ragkou. Healing of cavitary bone defects. *Eur J Orthop Surg Traumatol*, 22(2):123–128, February 2012.

[180] Sulaiman Mad-Ali, Soottawat Benjakul, Thummanoon Prodpran, and Sajid Maqsood. Characteristics and gelling properties of gelatin from goat skin as affected by drying methods. *J Food Sci Technol*, 54(6):1646–1654, May 2017.

[181] Batzaya Byambaa, Nasim Annabi, Kan Yue, Grissel Trujillo-de Santiago, Mario Moisés Alvarez, Weitao Jia, Mehdi Kazemzadeh-Narbat, Su Ryon Shin, Ali Tamayol, and Ali Khademhosseini. Bioprinted Osteogenic and Vasculogenic Patterns for Engineering 3D Bone Tissue. *Adv. Healthcare Mater.*, 6(16):1700015, August 2017.

[182] Zhen Jiang, Broden Diggle, Ming Li Tan, Jekaterina Viktorova, Christopher W Bennett, and Luke A. Connal. Extrusion 3D Printing of Polymeric Materials with Advanced Properties. *Advanced Science*, 7(17):2001379, 2020.

[183] Stephanie Knowlton, Chu Hsiang Yu, Fulya Ersoy, Sharareh Emadi, Ali Khademhosseini, and Savas Tasoglu. 3D-printed microfluidic chips with patterned, cell-laden hydrogel constructs. *Biofabrication*, 8(2):025019, June 2016.

[184] Sean V Murphy and Anthony Atala. 3D bioprinting of tissues and organs. *Nat Biotechnol*, 32(8):773–785, August 2014.

[185] Guoliang Ying, Nan Jiang, Cunjiang Yu, and Yu Shrike Zhang. Three-dimensional bioprinting of gelatin methacryloyl (GelMA). *Bio-des. Manuf.*, 1(4):215–224, December 2018.

[186] Ahmet Erdem, Mohammad Ali Darabi, Rohollah Nasiri, Sivakoti Sangabathuni, Yavuz Nuri Ertas, Halima Alem, Vahid Hosseini, Amir Shamloo, Ali S. Nasr, Samad Ahadian, Mehmet R. Dokmeci, Ali Khademhosseini, and Nureddin Ashammakhi. 3D Bioprinting of Oxygenated Cell-Laden Gelatin Methacryloyl Constructs. *Adv. Healthcare Mater.*, 9(15):1901794, August 2020.

[187] Jingyi Liu, Liang Li, Hairui Suo, Mengling Yan, Jun Yin, and Jianzhong Fu. 3D printing of biomimetic multi-layered GelMA/nHA scaffold for osteochondral defect repair. *Materials & Design*, 171:107708, June 2019.

[188] Paola Occhetta, Roberta Visone, Laura Russo, Laura Cipolla, Matteo Moretti, and Marco Rasponi. VA-086 methacrylate gelatine photopolymerizable hydrogels: A parametric study for highly biocompatible 3D cell embedding: VA-086 GelMA Photopolymerizable Hydrogels. *J. Biomed. Mater. Res.*, 103(6):2109–2117, June 2015.

[189] Bioluminescent Firefly Luciferase Assays. https://www.sigmaaldrich.com/US/en/technical-documents/technical-article/cell-culture-and-cell-culture-analysis/imaging-analysis-and-live-cell-imaging/firefly-luciferase-assays, 2023.

[190] Claudia Coronnello, Rosalia Busà, Luca Cicero, Albert Comelli, and Ester Badami. A Radioactive-Free Method for the Thorough Analysis of the Kinetics of Cell Cytotoxicity. *J Imaging*, 7(11):222, October 2021.

[191] Alexander K. Nguyen, Peter L. Goering, Rosalie K. Elespuru, Srilekha Sarkar Das, and Roger J. Narayan. The Photoinitiator Lithium Phenyl (2,4,6-Trimethylbenzoyl) Phosphinate with Exposure to 405 nm Light Is Cytotoxic to Mammalian Cells but Not Mutagenic in Bacterial Reverse Mutation Assays. *Polymers (Basel)*, 12(7):1489, July 2020.

[192] Gregory R. Fulmer, Alexander J. M. Miller, Nathaniel H. Sherden, Hugo E. Gottlieb, Abraham Nudelman, Brian M. Stoltz, John E. Bercaw, and Karen I. Goldberg. NMR Chemical Shifts of Trace Impurities: Common Laboratory Solvents, Organics, and Gases in Deuterated Solvents Relevant to the Organometallic Chemist. *Organometallics*, 29(9):2176–2179, May 2010.

[193] John Josse and William F. Harrington. Role of pyrrolidine residues in the structure and stabilization of collagen. *Journal of Molecular Biology*, 9(2):269–287, August 1964.

[194] NIH/3T3 - CRL-1658 | ATCC. https://www.atcc.org/products/crl-1658.

[195] Aashutosh Mistry, Alejandro A. Franco, Samuel J. Cooper, Scott A. Roberts, and Venkatasubramanian Viswanathan. How Machine Learning Will Revolutionize Electrochemical Sciences. *ACS Energy Lett.*, pages 1422–1431, March 2021.

[196] Annabel L. Butcher, Ching Theng Koh, and Michelle L. Oyen. Systematic mechanical evaluation of electrospun gelatin meshes. *Journal of the Mechanical Behavior of Biomedical Materials*, 69:412–419, May 2017.

[197] Yanzhong Zhang, Hongwei Ouyang, Chwee Teck Lim, Seeram Ramakrishna, and Zheng-Ming Huang. Electrospinning of gelatin fibers and gelatin/PCL composite fibrous scaffolds. *Journal of Biomedical Materials Research Part B: Applied Biomaterials*, 72B(1):156–165, 2005.

[198] Neslihan Alemdar. Oxygen-Generating Photocrosslinkable Hydrogel. In Peter Ertl and Mario Rothbauer, editors, *Cell-Based Microarrays: Methods and Protocols*, Methods in Molecular Biology, pages 241–250. Springer, New York, NY, 2018.

[199] Hanna Hanna, Lluis M. Mir, and Franck M. Andre. In vitro osteoblastic differentiation of mesenchymal stem cells generates cell layers with distinct properties. *Stem Cell Research & Therapy*, 9(1):203, July 2018.

[200] Francesca M. Toma, Andrea Sartorel, Matteo Iurlo, Mauro Carraro, Pietro Parisse, Chiara Maccato, Stefania Rapino, Benito Rodriguez Gonzalez, Heinz Amenitsch, Tatiana Da Ros, Loredana Casalis, Andrea Goldoni, Massimo Marcaccio, Gianfranco Scorrano, Giacinto Scoles, Francesco Paolucci, Maurizio Prato, and Marcella Bonchio. Efficient water oxidation at carbon nanotube–polyoxometalate electrocatalytic interfaces. *Nature Chem*, 2(10):826–831, October 2010.

[201] Chao Wei and Zhichuan J. Xu. The Comprehensive Understanding of as an Evaluation Parameter for Electrochemical Water Splitting. *Small Methods*, 2(11):1800168, 2018.

[202] Gábor I. Csonka, Adrienn Ruzsinszky, and John P. Perdew. Estimation, Computation, and Experimental Correction of Molecular Zero-Point Vibrational Energies. *J. Phys. Chem. A*, 109(30):6779–6789, August 2005.

APPENDIX A

SUPPLEMENTARY INFORMATION FOR CHAPTER 2: FINITE DIFFERENCE MODEL OF ELECTROSTATIC CHANNELING IN TCA CYCLE ENZYMES

A.1 Rate Constants

Kinetic parameters and composition are taken from experimental work by Bulutoglu, et al[16]. The reaction rate constants for the enzymes are shown in Table A.1. Substrate concentrations are shown in Table A.2.

Table A.1: Reaction Rate Constants.[16]

	$k_{cat}(s^{-1})$	$K_{iA}(\mu M)$	$K_A(\mu M)$	$K_B(\mu M)$
MDH Forward	31	0.42	0.13	0.83
MDH Reverse	870	15	87	33
CS Recombinant	88	4.6	7.9	21
CS Mutant	44	1.7	1.1	7.8

For MDH forward, substrate A is NAD^+ and substrate B is L-malate. For MDH reverse, substrate A is NADH and substrate B is OAA. At CS, substrate A is OAA and substrate B is a-CoA.

Table A.2: Substrate and Complex Concentrations.[16]

Species	Concentration (mM)
aCoA	0.1
NAD+	2
L-malate	1
NADH	0
MDH-CS	1×10^{-4}

A.2 Free Standing Enzymes

In the case where no channeling occurs, rates at each enzyme active site can be calculated from the kinetic expressions with no reference to the transition state matrix. This calculation is comparable to the model result of Bulutoglu et al.[16], but in this case we extend the

simulation time and consider the possibility of reverse reaction at MDH by a variable NADH concentration, initially set to 100 μM.

Concentration profiles for product Coenzyme A and intermediate OAA are shown in Figure A1, for both the reversible and irreversible cases of MDH kinetics. CoA generation is slightly faster for the mutant than for the recombinant free enzymes, consistent with Bulutoglu et al., who only modeled the irreversible case. As expected, inclusion of the reverse reaction suppresses CoA generation due to decreased reaction rate at MDH. The decreased reversible rate also suppresses intermediate OAA concentrations (Fig. A.1b). In contrast to Fig. A.1a, however, mutant OAA concentrations are higher than for the recombinant enzymes, again due to faster mutant CS kinetics.

Lag time is estimated by fitting a straight line to the product concentration profiles of Fig. A.1a, in the 10–20 s time frame where the generation rate is approximately steady-state. Note that true steady state would require constant OAA concentration, which as shown in Fig. A.1b remains transient in the 10–20 s time frame.

Table A.3: Lag Times for the Free Enzyme Cascade.

	Recombinant Lag Time (t_ℓ / s)	Mutant Lag Time (t_ℓ / s)
Reversible	1.1 $\pm$ 0.008	0.49 $\pm$ 0.004
Irreversible	5.4 $\pm$ 0.003	3.2 $\pm$ 0.002
Bulutoglu et al.[16]	2.5	0.9

Due to extrapolation procedure, lag times are highly sensitive to the details of the calculation. However, all of the lag times in Table A.3 are of order 1s. Also, the effect of mutation appears to be ˜50% decrease in lag time and is consistent with the free enzyme calculations of Bulutoglu[16]. Irreversible kinetics at MDH also lead to substantially longer lag times than reversible kinetics, due to the higher bulk OAA concentration in the case of irreversible kinetics.

A.3 Effect of Time Scale on Lag Time

The transport time constant, τ, is an assumed parameter in the model. Xie et al. estimated τ = 10 ps in building the Markov state model[26]. The time scale of transport ultimately

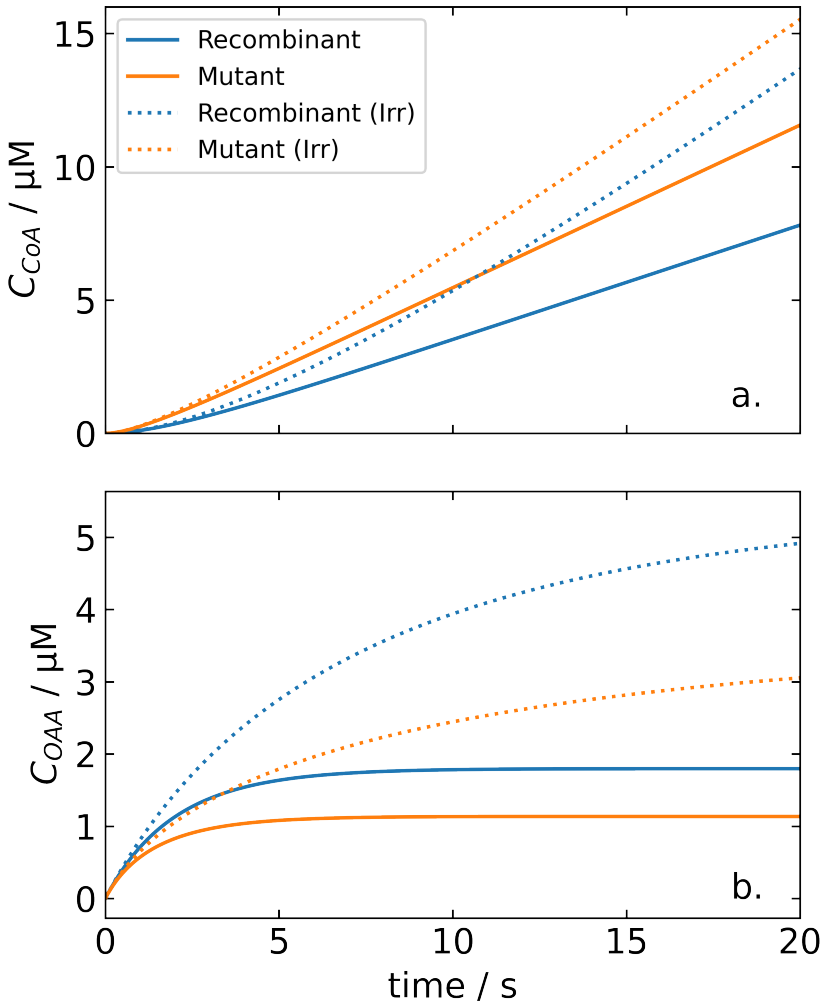

Figure A.1: Concentration Profiles of Coenzyme A and OAA in a 20 second Simulation of Free Enzymes.

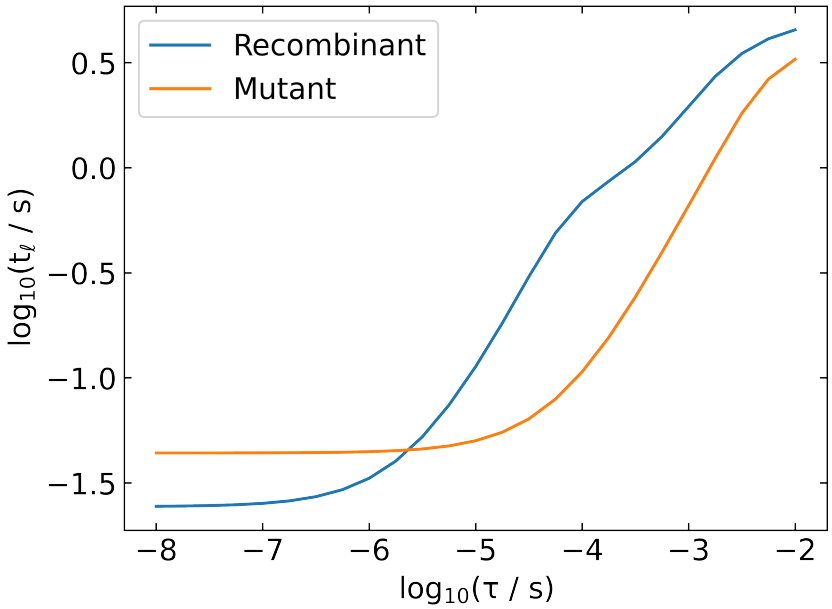

Figure A.2: Effect of Transport Time Scale on Lag Time.

determines whether the system is limited by intermediate transport or by kinetics. To identify a feasible range of transport time scales, τ was varied, from 10 ns to 10 ms, for both recombinant and mutant complexes under MSM network model conditions, as shown in Figure A.2.

Analysis of the change in lag time with transport time constant shows that for both complexes, lag time is virtually unaffected by transport time scales below $1{\times}10^{-7}$ s. Larger time scales lead to an exponential increase in lag time. This observation holds true for both complexes, but the recombinant complex is more sensitive to larger transport time constants. This is attributed to larger difference between the turnover frequency at MDH and at CS for the recombinant, making the recombinant complex more sensitive to diffusion. In either case, large differences in rates cause stiffness in the problem. Reducing the magnitude difference between time scales can increase the computational efficiency by decreasing the stiffness of the system of equations. For this reason, $\tau = 100$ ns was chosen for the finite difference model.

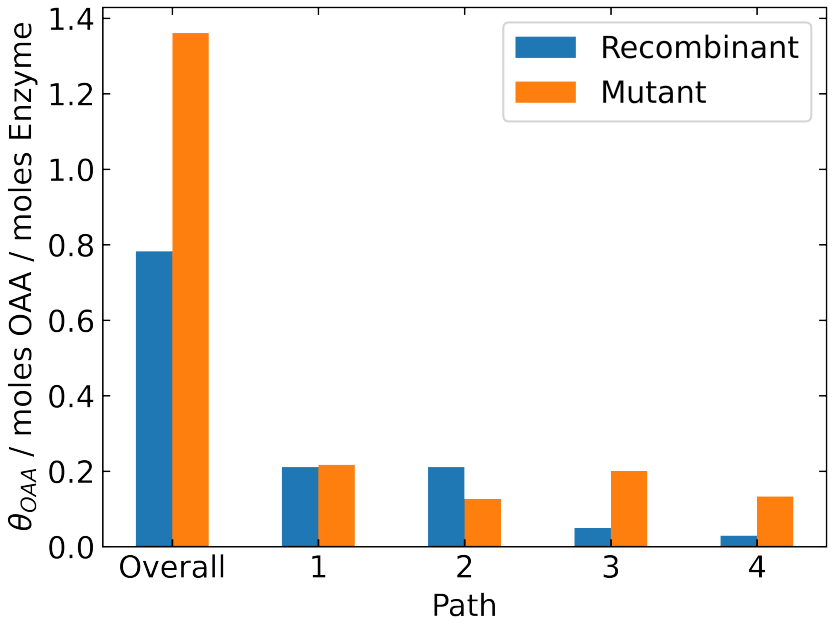

Figure A.3: Recombinant and Mutant Path Dominant Trajectory Occupancy.

A.4 Path Dominant Trajectory Occupancy

Each path has a corresponding series of nodes that exist on a dominant trajectory. The dominant trajectories were identified by Xie et al. to display the highest relative probability compared to the other trajectories in the same path[26]. Path to path comparison against the overall model provides insight to the preferences of OAA transport on the complex. Steady state occupancy of each path's dominant trajectory and the overall surface occupancy are given in Fig A.3.

The recombinant complex has a clear preference for Paths 1 and 2 with the respective dominant trajectories having more than triple the occupancy of OAA than Paths 3 or 4. For the recombinant complex, combination of the 4 dominant trajectories make up most of the overall surface occupancy, consistent with the previously reported deep free energy basins along the dominant trajectories[26]. Conversely, the mutant complex did not display as deep of free energy basins as the recombinant, so the dominant trajectories do not contribute as strongly to the overall occupancy. The mutant complex sees comparable occupancy of Paths 1 and 3 dominant trajectories that are higher than the occupancy of Paths 2 or 4. This observation is consistent with the lag time observations in the path analysis (Fig. 2.8).

Whereas the recombinant primarily utilizes dominant and efficient paths, low relative probabilities of the mutant's dominant trajectories compared to the overall occupancy suggests that the mutant complex utilizes less efficient means of transport. It is possible that OAA traverses non-dominant paths on the surface of the mutant complex in addition to those studied, but increased desorption is likely the cause of lower dominant trajectory occupancy. The increased likelihood of taking less efficient paths, especially through the bulk instead of channeling, is the driving force behind the lowered efficiency of the mutant complex compared to the recombinant complex.

APPENDIX B

SUPPLEMENTARY INFORMATION FOR CHAPTER 3: QUANTUM CHEMICAL INSIGHT INTO ELECTROCHEMICAL UPGRADING OF BIO-OIL

B.1 Adsorption Configurations

To establish possible adsorption configurations, we consider those in which the molecule ring is parallel to the surface. At low coverages, furfural and guaiacol have been shown to prefer these "ring down" configurations[83,85,102,145]. On each of the platinum and ruthenium facets, configurations are initially classified by the FF or 4-PP ring center placement. The relaxed configurations of FF and 4PP on each surface are shown in Figs B.1-B.4 (FF) and Figs B.5-B.8 (4-PP). The configurations in these figures are labeled by their starting configuration. Both FF and 4-PP on Pt and Ru generally relax to configurations where the ring is either in a bridge or hollow. Nearly all configurations maintain a ring-down configuration where the ring is bound to the surface and the substituent group(s) turn up away from the surface.

B.2 Reaction Pathways

For each hydrogenation step in the two pathways, possible intermediate states were explored. A decision tree was utilized to decide the proceeding step. For example, three possible intermediate steps exist for the first hydrogenation of FF to FA. Of those three options, each relaxed on the surface, the state with the lowest energy was deemed the most probable intermediate. For steps involving multiple hydrogenation steps, the potential second intermediate states are only those from the lowest energy first hydrogenation intermediate. As such, the possibilities for the third hydrogenation are determined from the lowest energy second intermediate state, and so on. The relaxed configurations in the pathway of FF to THFA via FA on each surface are provided in Figs B.9-B.12. The relaxed pathway states of 4PP to 4PCOL on each surface are shown in Figs B.13-B.16.

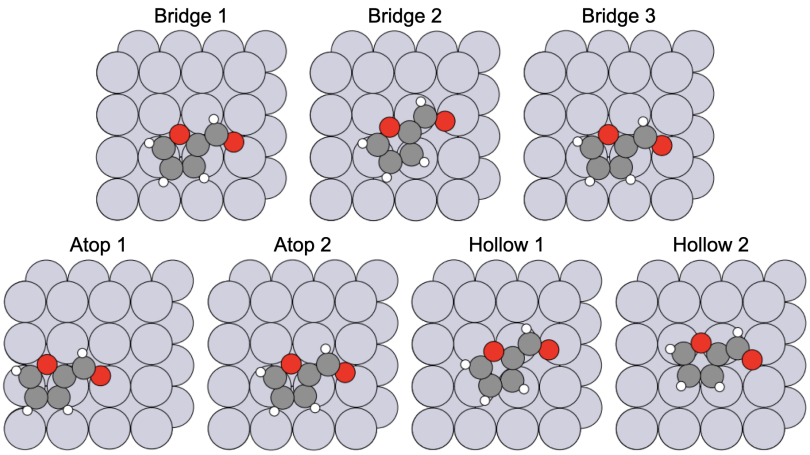

Figure B.1: Relaxed positions of Furfural on Pt(100) by starting configuration label.

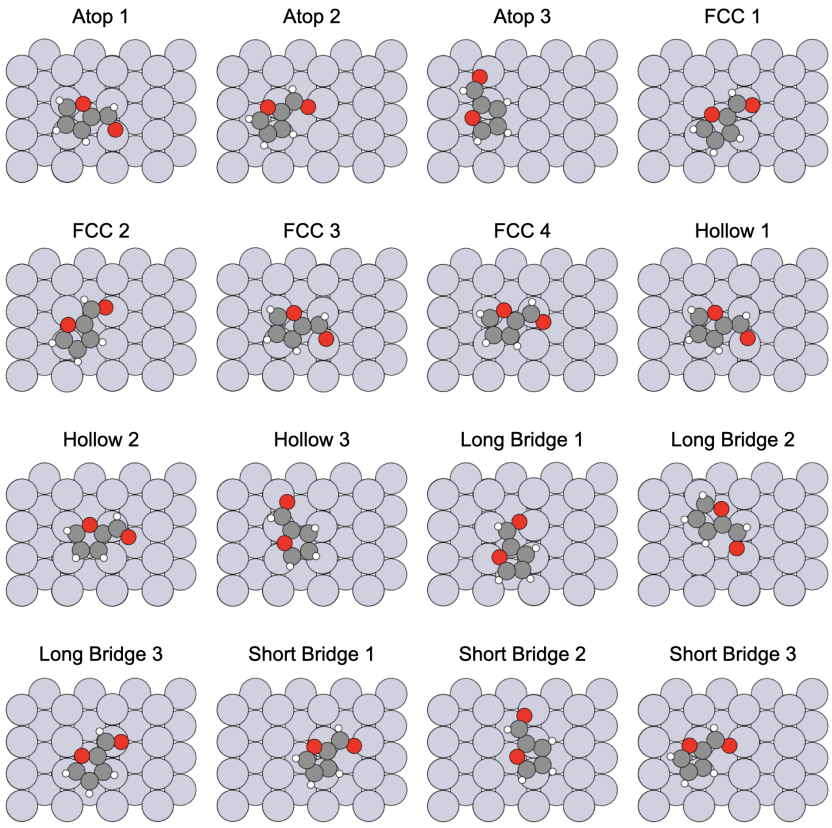

Figure B.2: Relaxed positions of Furfural on Pt(110) by starting configuration label.

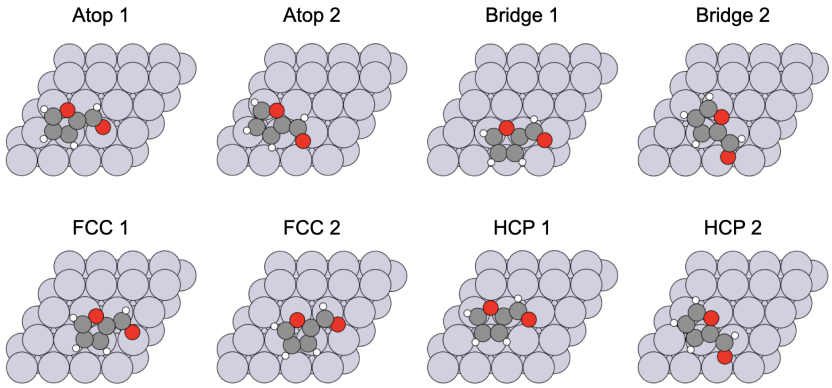

Figure B.3: Relaxed positions of Furfural on Pt(111) by starting configuration label.

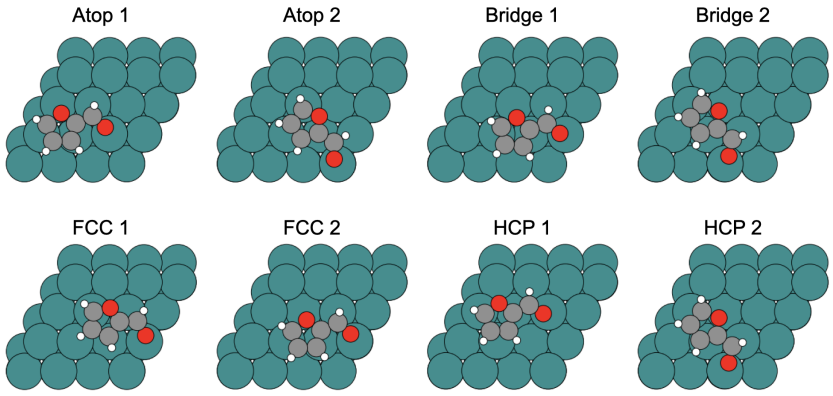

Figure B.4: Relaxed positions of Furfural on Ru by starting configuration label.

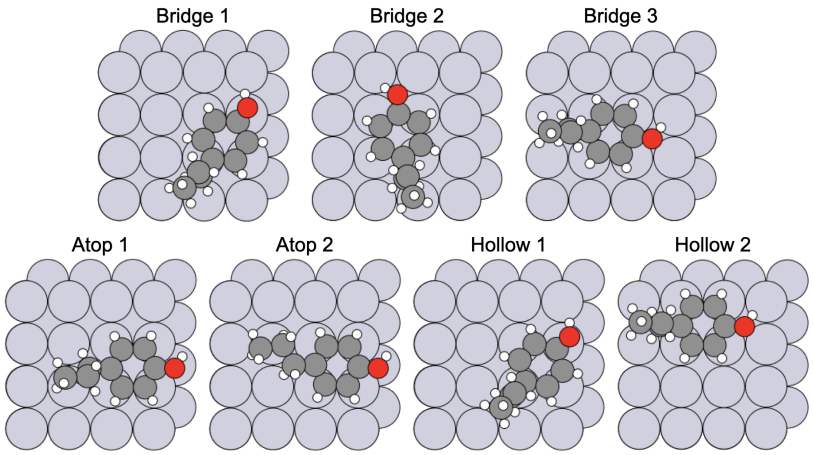

Figure B.5: Relaxed positions of 4-Propylphenol on Pt(100) by starting configuration label.

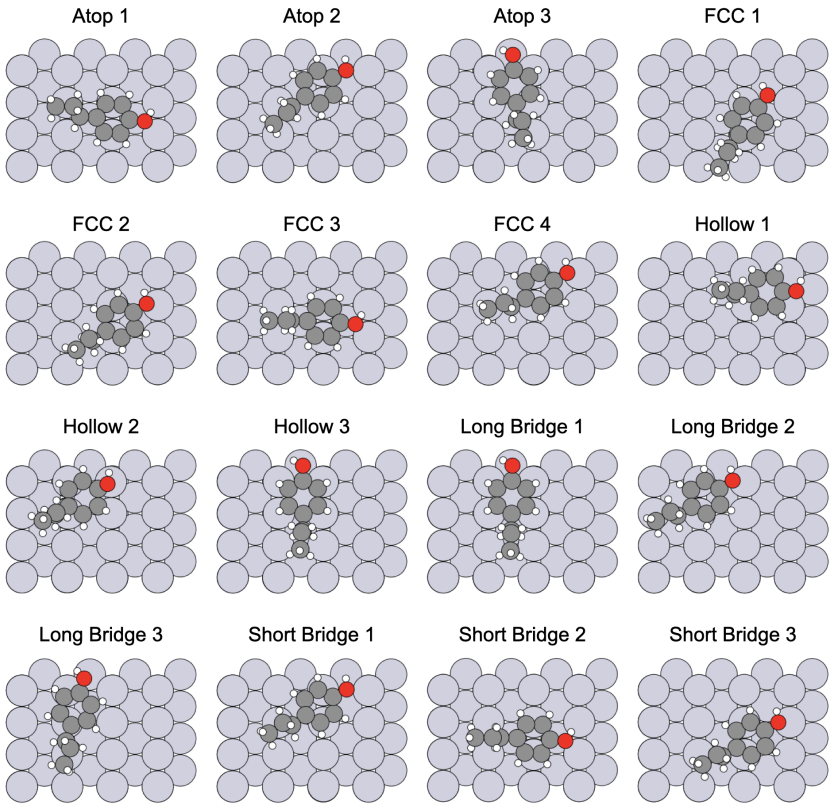

Figure B.6: Relaxed positions of 4-Propylphenol on Pt(110) by starting configuration label.

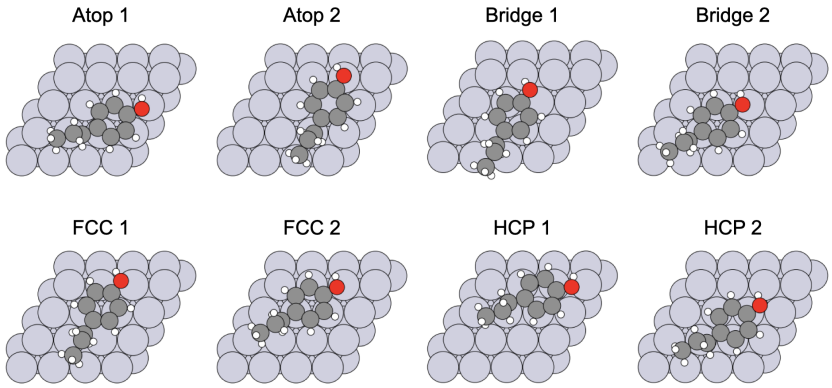

Figure B.7: Relaxed positions of 4-Propylphenol on Pt(111) by starting configuration label.

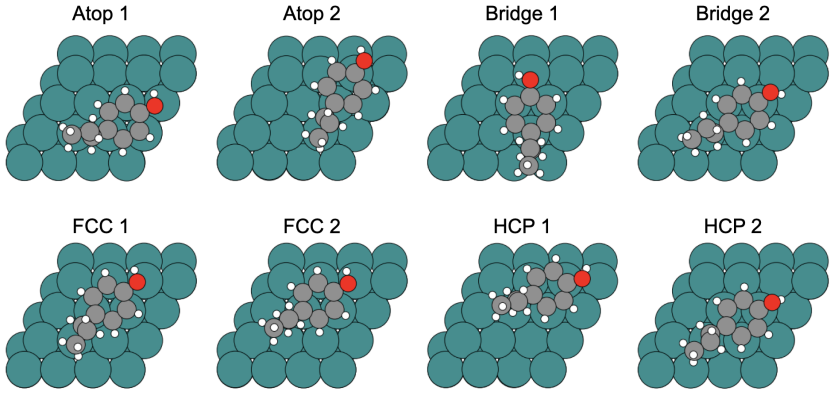

Figure B.8: Relaxed positions of 4-Propylphenol on Ru by starting configuration label.

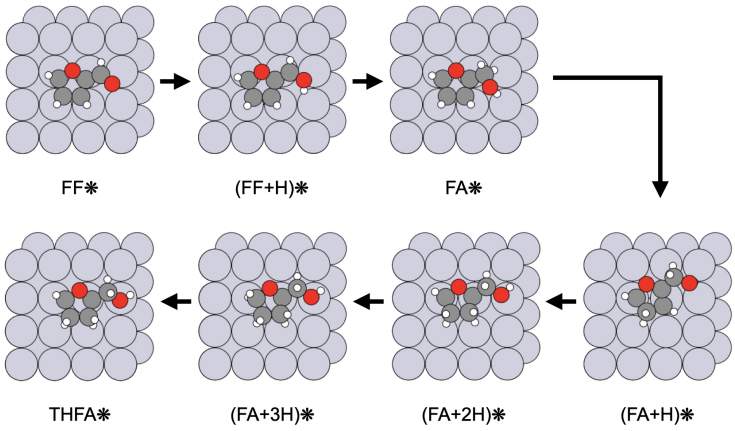

Figure B.9: Reaction path intermediate states in the transformation of FF to THFA via FA on Pt(100).

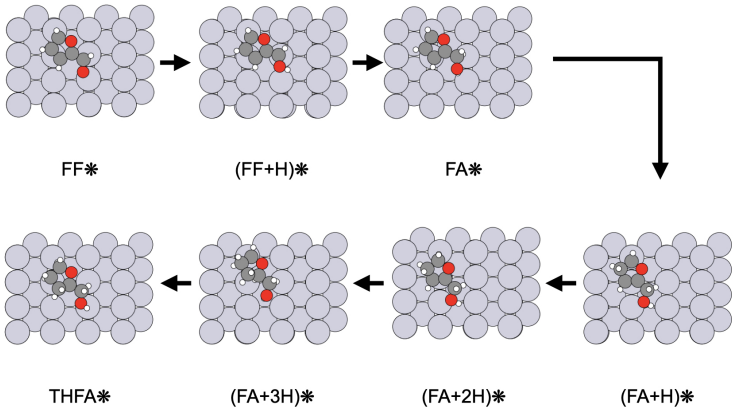

Figure B.10: Reaction path intermediate states in the transformation of FF to THFA via FA on Pt(110).

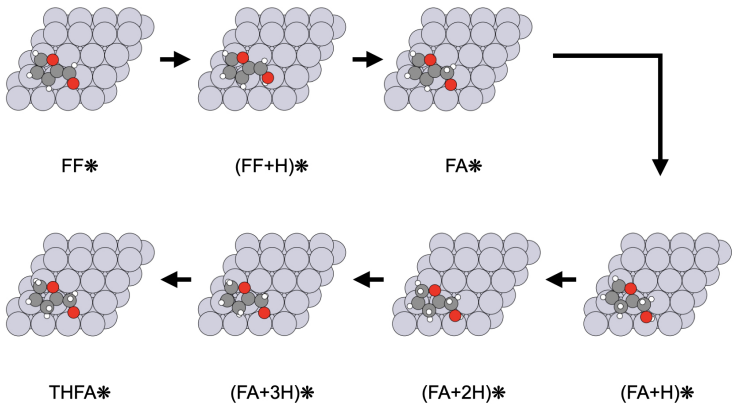

Figure B.11: Reaction path intermediate states in the transformation of FF to THFA via FA on Pt(111).

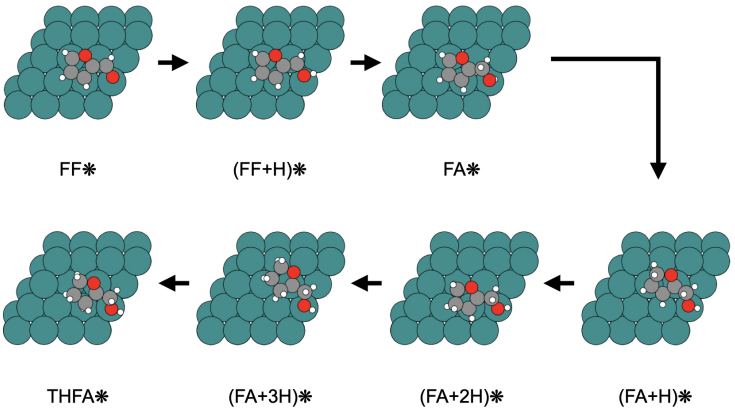

Figure B.12: Reaction path intermediate states in the transformation of FF to THFA via FA on Ru.

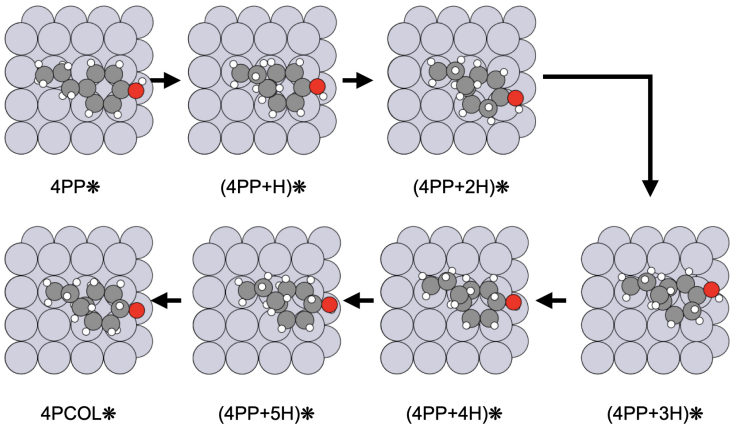

Figure B.13: Reaction path intermediate states in thee transformation of 4PP to 4PCOL on Pt(100).

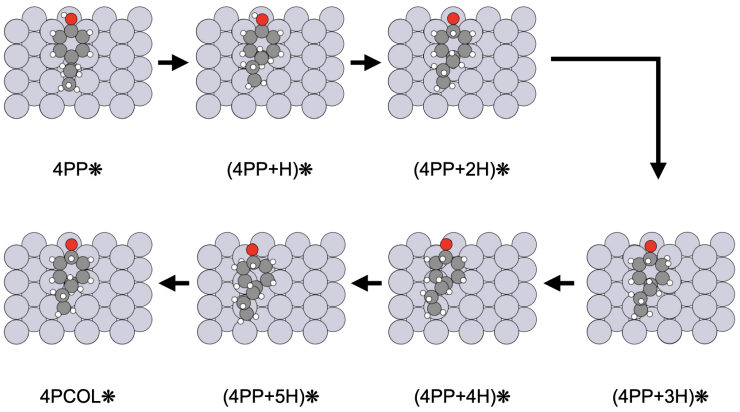

Figure B.14: Reaction path intermediate states in the transformation of 4PP to 4PCOL on Pt(110).

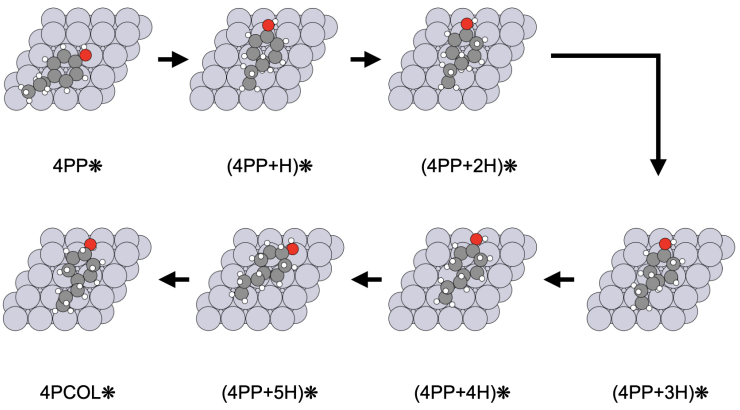

Figure B.15: Reaction path intermediate states in the transformation of 4PP to 4PCOL on Pt(111).

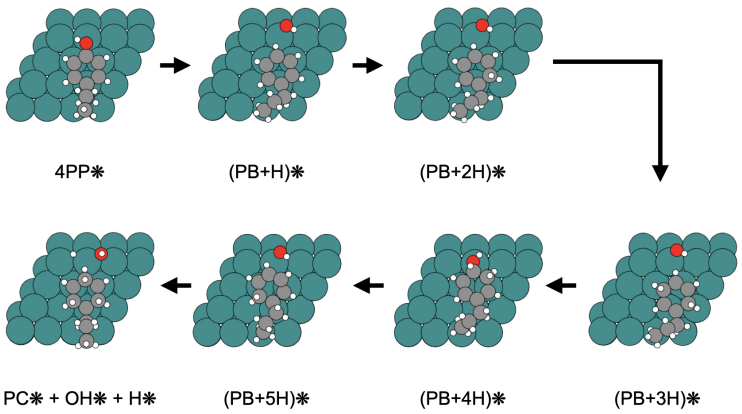

Figure B.16: Reaction path intermediate states in the transformation of 4PP to 4PCOL on Ru.

B.2.1 Energies of all Reaction Intermediates

To determine the reaction pathways, the energies of various possible states for a given hydrogenation step were compared. The one with the lowest energy was chosen as the intermediate state for a given facet. Summaries of the data and SMILES label of all intermediate states considered are provided in Table B.1 for FF to FA, Table B.2 for FA to THFA, and Table B.3 for 4-PP to PC. An example of the decision tree for the FF to THFA pathway and 4PP to 4PCOL pathway on Pt(110) are provided in Figures B.17 and Figure B.18.

Table B.1: Intermediate State Energies for the 2 step hydrogenation of FF to FA.

H #	State #	SMILES	Pt(100) Energy - E(State 0) / eV	Pt(110) Energy - E(State 0) / eV	Pt(111) Energy - E(State 0) / eV	Ru(0001) Energy - E(State 0) / eV
0	FF	O=Cc1ccco1	44472.75	-44452.81	-44482.82	-130481.84
1	1	[O-]c1ccco1	-16.38	-15.62	-16.13	-15.88
1	2	OCc1ccco1	-16.52	-16.60	-16.54	-15.96
1	3	[O-]c1ccco1	-16.59	-16.56	-16.65	-15.84

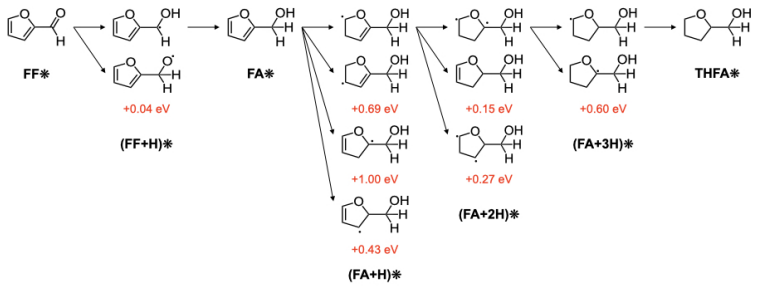

Figure B.17: Reaction Intermediate Decision Tree for FF to THFA on Pt(110).

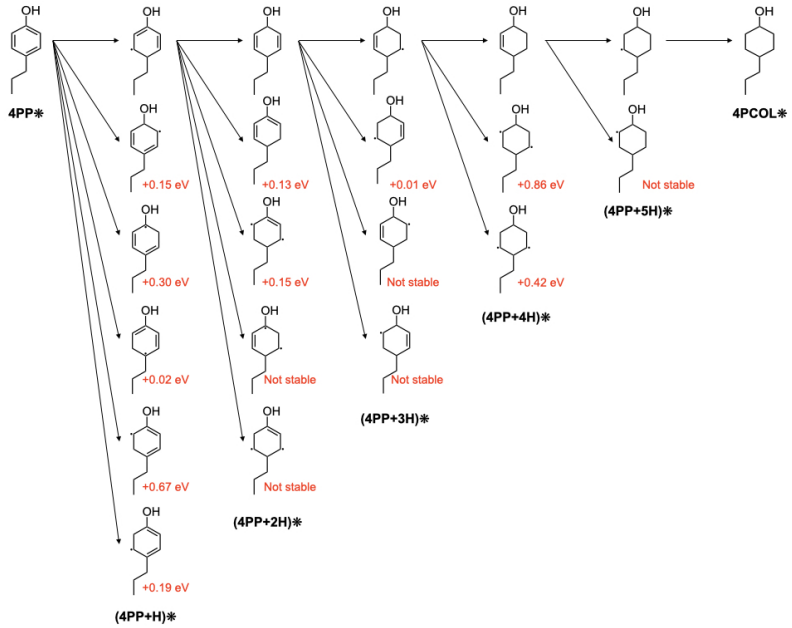

Figure B.18: Reaction Intermediate Decision Tree for 4PP to 4PCOL on Pt(110).

Table B.2: Intermediate State Energies for the 4 step hydrogenation of FA to THFA.

H #	State #	SMILES	Pt(100) Energy - E(State 0) / eV	Pt(110) Energy - E(State 0) / eV	Pt(111) Energy - E(State 0) / eV	Ru(0001) Energy - E(State 0) / eV
2	FA	OCc1ccco1	-44505.45	-44485.09	-44515.93	-130513.70
3	1	OCC1=C[CH-]CO1	-15.89	-15.94	-15.54	-16.43
3	2	OCC1=CC[CH-]O1	-15.94	-16.63	-15.94	-16.19
3	3	OC[C-]1CC=CO1	-15.80	-15.63	-16.20	-16.13
3	4	OCC1[CH-]C=CO1	-15.14	-16.19	-15.46	-16.18
4	5	OCC1=CCCO1	-32.10	-32.59		-32.34
4	6	OC[C-]1C[CH-]CO1			-32.18	-31.53
4	7	OCC1[CH-][CH-]CO1				-31.66
4	8	OC[C-]1CC[CH-]O1	-32.18	-32.74	-31.70	
4	9	OCC1[CH-]C[CH-]O1	-31.65	-32.47		
4	10	OCC1CC=CO1			-32.16	
5	11	OC[C-]1CCCO1	-48.36	-47.83	-48.36	-48.72
5	12	OCC1[CH-]CCO1		-47.83		-48.60
5	13	OCC1C[CH-]CO1			-48.28	
5	14	OCC1CC[CH-]O1	-48.23	-48.43		
6	THFA	OCC1CCCO1				

Table B.3: Intermediate State Energies for the hydrogenation of 4-PP to 4-PCOL and PC.

H #	**State #**	**SMILES**	**Pt100 Energy - E(State 0) / eV**	**Pt110 Energy - E(State 0) / eV**	**Pt111 Energy - E(State 0) / eV**	**Ru0001 Energy - E(State 0) / eV**
0	4-PP	CCCc1ccc(O)cc1	-44839.58	-44819.38	-44849.03	-130848.12
1	1	CCCC1=C[CH-]C(O)C=C1	-15.59	-15.80	-16.14	-16.52
1	2	CCCC1=CCC-C=C1	-15.08	-15.65	Not stable	-16.26

Table B.3: (cont'd)

H #	State #	SMILES	Pt100 Energy - E(State 0) / eV	Pt110 Energy - E(State 0) / eV	Pt111 Energy - E(State 0) / eV	Ru0001 Energy - E(State 0) / eV
1	3	CCC[C-]1C=CC(O)=CC1	-15.32	-15.93	-14.70	-15.90
1	4	CCCC1C=CC(O)=C[C-]1	-15.79	-15.95	-16.15	-15.65
1	5	CCCC1=CC=C(O)[C-]C1	-15.16	-15.28	Not stable	-15.71
1	6	CCCC1=CC=C(O)C=[C-]1	-15.23	-15.76	Not stable	-15.27
2	7	CCCC1=CCC(O)C=C1				-31.63
2	8	CCC[C-]1C=CC(O)[CH-]C1				-32.39
2	9	CCCC1C=CC(O)[CH-][CH-]1	-31.48	-31.76	-32.21	-31.70
2	10	CCCC1=C[CH-]C(O)[CH-]C1				-31.77
2	11	CCCC1=C[CH-]C(O)C[CH-]1				-31.56
2	12	CCC[C-]1C=CC-CC1				
2	13	CCCC1C=CC-C[CH-]1	-31.64	Not stable	-32.64	
2	14	CCCC1=CCC-[CH-]C1				
2	15	CCCC1=CCC-C[CH-]1				
2	16	CCCC1C=CC(O)=C[C-]1	-31.57	-31.63	-31.81	
2	17	CCC[C-]1CC=C(O)[CH-]C1				
2	18	CCC[C-]1CC=C(O)C[CH-]1				
2	19	CCCC1C[CH-]C(O)=C[CH-]1	-31.51	-31.60	-32.56	
2	20	CCCC1[CH-]C=C(O)C[CH-]1	-31.14	Not stable	Not stable	
2	21	CCCC1=CC=C(O)CC1				
3	22	CCCC1C=CC(O)C[C-]1	-47.30	-47.46	-48.61	

Table B.3: (cont'd)

H #	State #	SMILES	Pt100 Energy - E(State 0) / eV	Pt110 Energy - E(State 0) / eV	Pt111 Energy - E(State 0) / eV	Ru0001 Energy - E(State 0) / eV
3	23	CCCC1C=CC-CC1	-47.67		-48.79	
3	24	CCCC1C[CH-][C-](O)C[CH-]1	-47.67		-48.63	
3	25	CCCC1[CH-]CC-C[CH-]1	-47.56		Not stable	
3	26	CCCC1C[CH-]C(O)[CH-][CH-]1		Not stable		
3	27	CCCC1CC=C(O)[CH-]C1				
3	28	CCCC1CCC(O)=C[CH-]1				
3	29	CCCC1[CH-]CC(O)[CH-][CH-]1		-47.45		
3	30	CCCC1CC=C(O)C[CH-]1				
3	31	CCC[C-]1C=CC(O)CC1				-47.58
3	32	CCCC1=CCC(O)[CH-]C1				
3	33	CCCC1=CCC(O)C[CH-]1				
3	34	CCCC1C=CC(O)[CH-]C1		Not stable		-47.69
3	35	CCC[C-]1C[CH-]C(O)[CH-]C1				-46.46
3	36	CCC[C-]1C[CH-]C(O)C[CH-]1				-48.10
3	37	CCCC1=C[CH-]C(O)CC1				
4	38	CCCC1C=CC(O)CC1	-63.63	-63.81	-64.61	
4	39	CCCC1CCC-[CH-]C1	-63.57		-64.97	
4	40	CCCC1CCC-C[CH-]1	-62.65		Not stable	
4	41	CCCC1C[CH-]C(O)[CH-]C1				
4	42	CCCC1CC=C(O)CC1				

Table B.3: (cont'd)

H #	State #	SMILES	Pt100 Energy - E(State 0) / eV	Pt110 Energy - E(State 0) / eV	Pt111 Energy - E(State 0) / eV	Ru0001 Energy - E(State 0) / eV
4	46	CCCC1CCC(O)[CH-][CH-]1				
4	47	CCCC1CCC-C[CH-]1				
4	48	CCC[C-]1CCC(O)C[CH-]1				-63.30
4	49	CCCC1C[CH-]C(O)C[CH-]1				Not stable
4	50	CCC[C-]1CCC(O)[CH-]C1				-62.82
4	54	CCCC1C[CH-]C(O)C[CH-]1		-62.94		
4	55	CCCC1[CH-]CC(O)C[CH-]1		-63.39		
5	43	CCCC1CCC(O)[CH-]C1	-79.34	Not stable	-81.05	
5	44	CCCC1CCC(O)C[CH-]1	-78.74	-79.60		-78.77
5	45	CCCC1CCC-CC1			-80.98	
5	51	CCCC1CCC(O)C[CH-]1				
5	52	CCCC1CCC(O)[CH-]C1				
5	53	CCC[C-]1CCC(O)CC1				-79.91
6	4-PCOL	CCCC1CCC(O)CC1				
7		CCCC1CCCCC1				

B.3 Gibbs Correction Terms

Gibbs free energy correction terms were calculated for each gas phase and the preferred adsorbed states, including intermediate states. The total correction includes the ZPE, an entropic contribution, and an enthalpic contribution. The following tables provide the correc-

tional terms for the gas phases of all stable intermediates and hydrogen, and the corrections for each reaction state on each surface at 20°C.

Each correctional term is calculated through some combination of all of the vibrational energies. The Gibbs free energies reported here utilize Atomic Simulation Environment's (ASE) `Thermochemistry` package to calculate the correctional terms[88]. Gas phase molecule corrections are determined by the `IdealGasThermo` function and corrections of an adsorbate on some surface are calculated with the `HarmonicThermo` function. The zero point energy for both types of calculations is simply a summation of vibrational frequencies[202].

$$E_{\mathrm{ZPE}} = \frac{h}{2}\sum_i \nu_i \tag{B.1}$$

Where h is Planck's constant in eV/Hz and ν_i is the vibrational frequency of vibrational mode i in Hz.

The remaining terms are more complex for gas phase calculations than adsorbed state calculations due to a greater number of degrees of freedom (DOF). For the gas phase, assuming ideal gas, the entropy term at some temperature, T, and some pressure, P, is[88,89]:

$$TS = T(S_{\mathrm{trans}} + S_{\mathrm{rot}} + S_{\mathrm{elec}} + S_{\mathrm{vib}}) \tag{B.2}$$

Where the entropy is a combination of translational, rotational, electronic, and vibrational terms, as defined below, and a term to account for the change in pressure from the vacuum calculation.

$$S_{\mathrm{trans}} = k_{\mathrm{B}}\left(\ln\left[\left(\frac{2\pi m k_{\mathrm{B}}}{h^2}\right)^{3/2}\frac{k_{\mathrm{B}}T}{P}\right] + 5/2\right) \tag{B.3}$$

The Boltzmann constant is k_B and m is the mass.

$$S_{\mathrm{rot}} = \begin{cases} k_{\mathrm{B}}\left[\ln\left(\frac{8\pi^2 I k_{\mathrm{B}}T}{\sigma h^2}\right) + 1\right] & \text{if linear} \\ k_{\mathrm{B}}\left[\ln\left[\frac{\sqrt{\pi I_{\mathrm{A}} I_{\mathrm{B}} I_{\mathrm{C}}}}{\sigma}\left(\frac{8\pi^2 I k_{\mathrm{B}}T}{\sigma h^2}\right)^{3/2}\right] + 3/2\right] & \text{if nonlinear} \end{cases} \tag{B.4}$$

The moment(s) of inertia are represented by I, I_{A}, I_{B}, and I_{C}. These are determined within

the analysis package based on the provided symmetry number of the molecule, σ.

$$S_{\text{vib}} = k_{\text{B}} \sum_{i}^{vibDOF} \left[\frac{\epsilon_i}{k_{\text{B}}T \left(e^{\epsilon_i / k_{\text{B}}T} - 1 \right)} - \ln \left(1 - e^{-\epsilon_i / k_{\text{B}}T} \right) \right]$$

The vibrational entropy contribution is a function of the vibrational energies, defined by $\epsilon_i = h\nu_i$.

$$S_{\text{elec}} = k_{\text{B}} \ln \left[1 + 2 \sum (\text{spin}) \right]$$

The electronic entropy contribution accounts for the total spin of the molecule. Here, the spin is either 0 if all electrons are paired, 0.5 if there is a single unpaired electron, or 1 if there are two unpaired electrons.

The additional enthalpic correction is[88,89]:

$$H_{0 \to \text{T}} = \int_0^T C_P dT = \int_0^T (k_{\text{B}} + C_{V,\text{trans}} + C_{V,\text{rot}} + C_{V,\text{vib}} + C_{V,\text{elec}}) dT$$

Where $C_{V,\text{trans}}$, the translational heat capacity, is equal to $\frac{3}{2}k_{\text{B}}$, $C_{V,\text{rot}}$ is the rotational heat capacity equal to k_{B} for linear gas molecules or $\frac{3}{2}k_{\text{B}}$ for non-linear gas molecules, the electronic heat capacity $C_{V,\text{elec}}$ is assumed to be zero, and the vibrational heat capacity, $C_{V,\text{vib}}$, is a function of vibrational frequencies.

$$\int_0^T C_{V,\text{vib}} dT = \sum_{i}^{\text{vib DOF}} \frac{\epsilon_i}{e^{\epsilon_i / k_{\text{B}}T} - 1}$$

Adsorbed state vibrations and free energy corrections are treated somewhat differently due to the reduced degrees of freedom in the adsorbate. For these analyses, the vibrations are treated harmonically and the enthalpy is assumed to be equivalent to the internal energy in order to predict the Gibbs free energy from the Helmholtz energy calculated by `HarmonicThermo`[88]. Additionally, by considering the adsorbed state free energy correction as a combined correction of the adsorbate and the surface, the vibrations of the surface can be ignored because they will cancel out in any reaction change in free energy calculation.

The entropic and enthalpic contributions are calculated for the adsorbate in a similar

way to those calculated for the gas phase. The primary difference is that translational and rotational contributions are assumed to be negligible, so only the vibrational contributions are considered. The Helmholtz energy is calculated from the internal energy and entropic vibrational contribution for a given adsorbed state, j[88].

$$F_j = E_j + E_{\mathrm{ZPE}} + \int_0^T C_{V,\mathrm{vib}} dT - TS_{\mathrm{vib}}$$

The Gibbs free energy is then a function of the Helmholtz energy and a pressure-volume term. The volume is assumed to be the cell size from the geometric optimization and the pressure can be any arbitrary value.

$$G_j = F_j + PV$$

B.3.1 Gas Phase Corrections

Table B.4: Gibbs Corrections of Gas Phase Molecules.

Molecule	$\mathrm{E_{ZPE}}$ / eV	TS / eV	$\Delta \mathrm{H_{0\rightarrow T}}$ / eV	Total Correction / eV
FF	2.10	0.98	0.18	1.29
FA	2.71	1.04	0.21	1.87
THFA	3.93	1.10	0.23	3.06
4PP	5.00	1.27	0.30	4.03
4PCOL	6.85	1.34	0.34	5.85
PC	6.74	1.25	0.30	5.79
H2	0.27	0.40	0.09	-0.05

B.3.2 Adsorbed $\mathrm{H_2(g)}$ and H Corrections

Table B.5: Gibbs Corrections of H on each surface.

Surface	$\mathrm{E_{ZPE}}$ / eV	TS / eV	$\Delta \mathrm{H_{0\rightarrow T}}$ / eV	Total Correction / eV
Pt(100)	0.73	8.70e-09	8.27e-09	0.73
Pt(110)	0.34	1.68e-04	1.49e-04	0.34
Pt(111)	0.31	2.90e-04	2.53e-04	0.31
Ru(0001)	0.73	8.70e-09	8.27e-09	0.73

Table B.6: Gibbs Corrections of H_2(g) on each surface.

Surface	E_{ZPE} / eV	TS / eV	$\Delta H_{0\rightarrow T}$ / eV	Total Correction / eV
Pt(100)	1.07	1.31e-04	1.17e-04	1.07
Pt(110)	0.63	3.70e-03	2.99e-03	0.63
Pt(111)	0.50	7.07e-03	5.52e-03	0.50
Ru(0001)	1.07	1.31e-04	1.17e-04	1.07

B.3.3 Adsorbed State Corrections of the Furfural to THFA pathway

Table B.7: Gibbs Corrections of FF to THFA States on Pt(100).

Adsorbate	E_{ZPE} / eV	TS / eV	$\Delta H_{0\rightarrow T}$ / eV	Total Correction / eV
FF	1.54	0.70	0.30	1.13
IS	1.79	0.77	0.31	1.33
FA	1.94	0.96	0.35	1.34
IS1	2.00	1.21	0.42	1.21
IS2	2.19	1.24	0.43	1.39
IS3	2.29	1.51	0.48	1.27
THFA	2.33	1.92	0.56	0.96

Table B.8: Gibbs Corrections of FF to THFA States on Pt(110).

Adsorbate	E_{ZPE} / eV	TS / eV	$\Delta H_{0\rightarrow T}$ / eV	Total Correction / eV
FF	1.62	0.70	0.29	1.22
IS	1.82	0.84	0.33	1.32
FA	1.89	1.09	0.39	1.19
IS1	2.09	1.09	0.40	1.40
IS2	2.25	1.21	0.43	1.47
IS3	2.28	1.57	0.50	1.21
THFA	2.40	1.77	0.55	1.18

Table B.9: Gibbs Corrections of FF to THFA States on Pt(111).

Adsorbate	E_{ZPE} / eV	TS / eV	$\Delta H_{0\rightarrow T}$ / eV	Total Correction / eV
FF	1.58	0.75	0.30	1.14
IS	1.82	0.83	0.33	1.31
FA	1.97	1.01	0.36	1.32
IS1	2.13	1.04	0.38	1.48
IS2	2.22	1.22	0.43	1.44
IS3	2.40	1.67	0.49	1.22
THFA	2.49	1.80	0.52	1.21

Table B.10: Gibbs Corrections of FF to THFA States on Ru(0001).

Adsorbate	E_{ZPE} / eV	TS / eV	$\Delta H_{0\rightarrow T}$ / eV	Total Correction / eV
FF	3.11	0.32	0.17	2.96
IS	3.35	0.39	0.19	3.15
FA	3.22	0.69	0.28	2.82
IS1	3.49	0.64	0.28	3.14
IS2	3.46	0.92	0.36	2.90
IS3	3.64	0.94	0.38	3.08
THFA	3.49	1.52	0.48	2.45

B.3.4 Adsorbed State Corrections of the 4-PP to 4-PCOL and PC pathways

Table B.11: Gibbs Corrections of 4-PP to 4-PCOL States on Pt(100).

Adsorbate	E_{ZPE} / eV	TS / eV	$\Delta H_{0\rightarrow T}$ / eV	Total Correction / eV
4-PP	3.13	2.17	0.67	1.64
IS1	3.22	2.51	0.73	1.45
IS2	3.37	2.56	0.75	1.56
IS3	3.44	3.01	0.83	1.26
IS4	3.54	3.16	0.86	1.24
IS5	3.63	3.47	0.92	1.07
4-PCOL	3.72	3.87	0.97	0.82

Table B.12: Gibbs Corrections of 4-PP to 4-PCOL States on Pt(110).

Adsorbate	E_{ZPE} / eV	TS / eV	$\Delta H_{0\rightarrow T}$ / eV	Total Correction / eV
4-PP	3.07	2.26	0.70	1.51
IS1	3.21	2.42	0.73	1.52
IS2	3.36	2.41	0.74	1.70
IS3	3.45	2.67	0.80	1.58
IS4	3.55	3.03	0.85	1.38
IS5	3.65	3.29	0.90	1.26
4-PCOL	3.66	3.79	0.98	0.85

Table B.13: Gibbs Corrections of 4-PP to 4-PCOL States on Pt(111).

Adsorbate	E_{ZPE} / eV	TS / eV	$\Delta H_{0\rightarrow T}$ / eV	Total Correction / eV
4-PP	3.02	2.66	0.74	1.11
IS1	3.27	2.53	0.73	1.48
IS2	3.43	2.60	0.75	1.58
IS3	3.49	2.99	0.82	1.32
IS4	3.62	3.24	0.86	1.24
IS5	3.76	3.25	0.87	1.38
4-PCOL	3.83	3.64	0.93	1.12

Table B.14: Gibbs Corrections of 4-PP to PC States on Ru(0001).

Adsorbate	E_{ZPE} / eV	TS / eV	$\Delta H_{0\rightarrow T}$ / eV	Total Correction / eV
4-PP	4.82	1.61	0.54	3.74
IS1	5.20	1.37	0.52	4.35
IS2	5.29	1.52	0.56	4.33
IS3	5.45	1.63	0.59	4.41
IS4	4.75	2.90	0.81	2.66
IS5	5.05	2.93	0.82	2.94
PC + OH	5.73	3.39	0.90	3.24

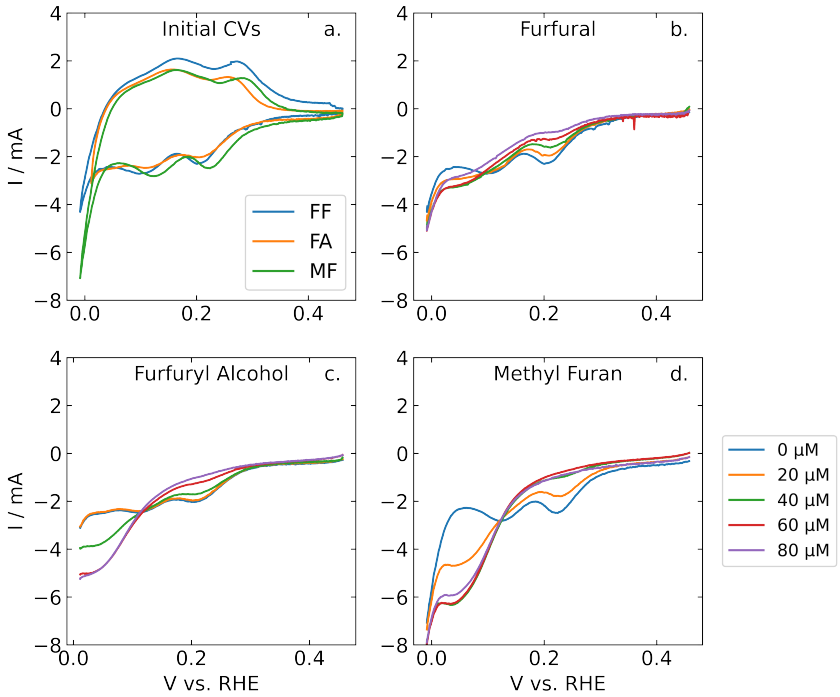

Figure B.19: Initial CVs taken before each Hupd experiment (a) and the LSVs acquired during addition of varied concentrations of (b) furfural, (c) furfuryl Alcohol, and (d) methyl furan.

B.4 Organic-blocked Hydrogen Under Potential Deposition

For Hupd experiments of FF, FA, andMF, an initial CV was collected before the addition of any organic material. The initial CVs to understand unihbitied hydrogen deposition are shown in Figure B.19a. The linear sweeps of potential with each concentration of organic added are shown in Fig. B.19b-d.

The LSV data shown corresponds to the data used in analyzing adsorption parameters. The window is set to focus on the area of Hupd.